E. A. M. HUSSAIN

AN ELECTROCHEMICAL INVESTIGATION OF EROSION CORROSION OF DUPLEX STAINLESS STEEL IN SEA WATER CONTAINING SAND PARTICLES

SCHOOL OF INDUSTRIAL AND MANUFACTURING SCIENCE

Ph.D. Thesis

CRANFIELD UNIVERSITY

SCHOOL OF INDUSTRIAL AND
MANUFACTURING SCIENCE

ESSAM A. M. HUSSAIN

AN ELECTROCHEMICAL INVESTIGATION OF EROSION CORROSION OF DUPLEX STAINLESS STEEL IN SEA WATER CONTAINING SAND PARTICLES

PhD THESIS

Academic Year 2000 - 2001

Supervisor: Dr M. J. Robinson

CONTENTS

ABSTRACT

Passive metals, like stainless steels, are usually protected from corrosion by a thin oxide film on the surface. If the film is stable it will reform spontaneously when it becomes damaged. Erosion-corrosion of passive metals proceeds by the repeated removal and repair of the oxide film.

Erosion corrosion behaviour studies were carried out on UNS 31803 grade of duplex stainless steel in seawater using a water jet impingement apparatus. Electrochemical polarisation scans and optical film thickness measurements were utilised to measure the rate of repair of the passive film while varying the fluid flow velocity in seawater with and without the addition of sand particles.

The value of the passive current density revealed the severity of the attack, as the fluid velocity was changed on the surface of the material. This demonstrated the pitting of the ferrite phase at 380 mV and breakdown of the austenitic phase at 880 mV. With the presence of sand particles, the passive current density was significantly enhanced and increased up to 7.5 $\mu A/cm^2$ for 3 grams and the value stayed constant as the sand concentration increased to 4 grams. Both the current and potential versus time measurements supported the polarisation results. In general, the passive film produced an interface colour of the first or second order.

Modelling of the erosion-corrosion behaviour under particle impingement was characterised by developing a relationship between passive film colour thickness, sand particle energy from the water jet impingement system and the electrochemical scans. It was possible to show that the mean charge passed for a single particle impact of 0.01 impact was 6×10^{-12} coulombs and the corresponding absolute current was 6×10^{-12} Ampere.

Overall, the conclusion drawn from this work was that the UNS31803 duplex stainless steel would exhibit a good resistance to erosion corrosion if used in ship power plants and offshore piping giving a depth of attack between 0.07 and 0.08 mm/year.

ACKNOWLEDGEMENTS

A deep sincere thanks to Dr Mike Robinson for his sustained technical guidance and social support during my research study at Cranfield University. Also I would like to thank most of the staff and technicians in the school of industrial and manufacturing science who participated through their technical knowledge and physical effort to make this research study complete. Last but not least warm thanks for my beloved family.

TABLE OF FIGURES

1.0 INTRODUCTION

The word *erosion* derives from the Latin verb 'rodene' which means to gnaw, or to wear away gradually[1]. The term is used in a diverse number of technologies, ranging from the geologist's loss of land or beach or mountain to the politician's loss of support to the engineer's loss of wall thickness. In all of these meanings, the process defies efforts to model it and thereby the ability to predict accurately the amount of loss that will occur in a particular set of conditions. It is therefore important to understand the nature and mechanisms of erosive loss to effectively minimise its effects.

Erosion-material wastage is dependent on many interrelated factors that include the properties and structure of the target materials, for example in duplex stainless steels, the integrity of the oxide film is a function of the metal composition and microstructure and the presence of stresses. It is also a function of the solution composition, the electrochemical potential and its distribution across the interface, and frequently of the hydrodynamic conditions, and the physical and chemical characteristics of the erodent particles. Combined erosion-corrosion at various temperatures is also a function of the chemical environment of the surface. The combination of all of these factors, sometimes exceeding 20 in number, results in material wastage rates that are peculiar to specific sets of conditions.

Duplex stainless steels are one of the most conventional and important groups of corrosion resistant alloys in many marine production and manufacturing fields. As the name 'dual' clearly shows, this material has a high resistance to erosion-corrosion. The UNS 31803 (21.9 % Cr, 5.4 % Ni, 3.1 % Mo) containing a high chromium content, exhibited a passive chromium rich oxide film for their corrosion protection. The material is very widely used in marine applications such as pipelines, pumps and water cooling systems and from the economic side, this material has a good cost performance. The duplex stainless steels have a high resistance to pitting corrosion, a low thermal expansion coefficient compared to the austenitic stainless steels and the yield strength is almost 65% larger than the austenitic grades.

From the electrochemical point of view, the biggest problem that limits the applicability of this alloy is its susceptibility to crevice and localised corrosion. Also the galvanic effect between the ferrite and austenite of the material leads to a significant increase in active dissolution of the ferrite phase. Many attempts at applying different treatments to resolve crevice corrosion effect have been made, but still optimum results have not been achieved.

The stability of the duplex stainless steels with respect to aqueous environments depends on the presence of an oxide film, which covers the surface completely. Such oxide films are usually thin, compact and adherent to the metal substrate. In aqueous solutions the material is governed by its dissolution rate into the environment and by the rate at which the film can conduct ions. If these are low, the metal is regarded as passive although its erosion corrosion rate is still finite. If the oxide film is partially damaged, the damaged region will often be repassivated quickly. However, if the oxide film failed to repassivate then this could result in some form of deep penetration into the metal, pitting and crevice corrosion, the consequences of which are severe.

When the metal is subjected to erosive condition (sand particle impact), each mechanical event will cause rupture or removal of the oxide film in a localised region of the surface thereby exposing bare metal to environment. Because of the synergistic effect of both the mechanical and chemical processes exhibited in such type of localised corrosion, the accurate predication of the mechanism related to the mechanical degradation in the erosion corrosion is still difficult.

Studies on the oxide colouring techniques of stainless steels have been carried out extensively using hot acidic solutions[2] or applying different electrochemical potentials. The nature of the oxide film growth on metals is of great importance in understanding the mechanism of erosion corrosion. Despite this there is still disagreement on how oxides are nucleated in specific electrolytes and how the film develop to form a steady state passive film.

By understanding the influence of some of the erosion factors on the microstructure and the characteristic of the alloy, the resultant behaviour is essential for the resistance of erosion corrosion in aqueous environments, adding to the complex nature of this form of corrosion and to simulate the condition of the erosion corrosion of pipelines, marine pumps and water cooling systems. Accelerated test methods based on electrochemistry such as rotating cylinder and disc electrode was performed, thus, to be able to fully reproduce the condition in laboratory scale. However, there are only few results, which were successfully correlated to the mass loss and depth of attack experienced in the real industrial plants.

In the present study, a water jet impingement system was designed and assembled for evaluating the electrochemical behaviour of the duplex stainless steel (UNS 31803) during erosion-corrosion in a flowing electrolyte containing 275 microns sand particles. The fabricated jet system simulates the fluid flow, characteristics, the electrochemical reactions and mass loss exhibited on the surface of the material as in a real marine system. Microscopic analysis was employed and the mechanisms and extent of attack under various fluid velocities in seawater with sand impingement were defined and assessed. Passive film colour fringe thickness measurement and sand particle measurements were determined to assess the material evaluation.

Upon the completion of the erosion experiment, a theoretical erosion model was promoted to determine the current developed from a single particle sand impact on the surface of the duplex stainless which resulted from the charge passed per second and the number of particle impacts on 1 cm^2 per second.

2.0 STAINLESS STEELS

2.1 Introduction

A historical review of stainless steels is carried out in order to place the current study on duplex stainless steel in context. Stainless steel production started in the 1910s. Stainless steels are alloys of iron based materials containing a minimum of approximately 11% chromium (Cr). This percentage of Cr prevents the formation of rust in unpolluted atmospheres, which in turn gives them the popular designation name 'stainless', due to their corrosion resistance and enhanced rust resistance. Thus, their corrosion resistance is provided by a very thin surface film which is self-healing in a wide variety of environments[3].

Nearly every year a new modification of the existing stainless steels is made. McLoone[4] pointed out that in some steels Cr content now approaches 30% and many other elements are added to provide specific properties or ease of fabrication. For example, nickel (Ni) and molybdenum (Mo) are added for corrosion resistance, sulphur (S) and selenium (Se) for machinability, and carbon (C), nitrogen (N), Mo, titanium (Ti), aluminium (Al) and copper (Cu) for strength, although C must be kept low for weldability and Ni for formability and toughness. Similarly, the current investigated UNS 31083 duplex stainless steel exhibits similar characteristic behaviour and element additions in its chemical composition.

Sedrick[3] reported that austenitic stainless steels are designated as the AISI-300 series and represent by far the largest category of stainless steels produced. An example is the classic 18/8 (18%Cr-8% Ni) type 304 stainless steel. Among the most important compositional modifications in this category of stainless steels are: improved corrosion resistance to pitting and crevices due to Mo addition, and reduction of intergranular corrosion due to low C content stabilising with either Ti or Ni plus talium (Ta). The addition of Ni and Cr improve high temperature oxidation resistance and strength, and lastly the improved stress corrosion cracking resistance due to the Ni.

The next category of stainless steels is the ferritic steels (AISI-400). Their ferritic structure of Cr is approximately 12%, with the addition of 0.2% Al and low C of about 0.05%. In the past, type 430 with a Cr content of between 14% and 18% gave the user a choice of properties. Low Cr provides improved weldability, impact resistance, strength and hardness, but with some sacrifice in corrosion resistance. A high Cr content provides a gain in corrosion resistance, especially in nitric acid, but mechanical properties are lost, particularly impact strength. With the addition of N, Al and Ti, grain growth is restricted at higher Cr content grades, but ferritic structure suffers a number of complications such as sigma phase formation, sensitisation and 475 embrittlement[3].

The martensitic stainless steels (AISI -400 series) have a Cr content of 11.5-18% and have an austenitic structure at elevated temperatures that can be transformed into martensite by suitable cooling to room temperature. 410 type is the classic 12% Cr martenitic stainless steel, and is the most popular martensitic grade produced today. Free machining grade is obtained with the addition of S and Se, Ni gives rise to higher

toughness and corrosion resistance and is used in aircraft fittings, pumps and valves. Also high hardness and wear resistance are gained with high Cr grades [3].

Duplex stainless steel grades are a product of the basic Fe-Cr-Ni alloy system of stainless steels. The duplex microstructure of most commercially available steels consists of approximately equal proportions of ferrite and austenite in the microstructure. The ferrite –austenite structure is achieved by means of a suitable alloy chemical composition and the application of an appropriate thermo-mechanical treatment. Atamert et al[5] acknowledged that duplex steels exhibit an impressive combination of properties that would prove difficult to achieve in conventional austenitic or ferritic stainless steel. These steels demonstrate good weldability, high strength, high toughness, good corrosion protection and pitting resistance and excellent stress corrosion cracking resistance[5].

Related to the use of duplex stainless steel in seawater, Varol et al[6] considered that owing to its high strength and corrosion resistance, duplex stainless steel has been employed in both the onshore and offshore oil and gas industry, as well as the petrochemical pulp, paper, chemical and food industries.

The accuracy and reproducibility of its chemical composition enables the amounts of the two phases α and γ to be closely adjusted. Increased control of N levels make it possible to improve the corrosion resistance and the high temperature stability of the duplex structure. Finally, the reduction in the levels of residuals has resulted in a marked beneficial effect on hot workability. All improvements have led to a significant reduction in production costs; making more and more cost saving materials. This explains why they have increased in popularity[8].

Nevertheless, in the early 1970s, the 22% Cr duplex grade was developed in Germany and Sweden, i.e. DIN 1.4462 or UNS S31803 (table **2.1**). As reported by Gunn[9], this new steel was not sensitive to intergranular corrosion (IGC) upon welding due to a balanced chemistry (i.e. Cr/Ni equivalent ratio)[7]. During the 1980s, more highly alloyed duplex grades were developed to withstand more aggressive environments. These are the so-called super-duplex grades (table **2.1**). These grades have pitting resistance equivalent numbers (PRE_N) greater than 40, where:

$$PRE_N = \%\,Cr + 3.3 \times (\%\,Mo) + 16 \times (\%\,N) \qquad (1)$$

Another development during the 1980s was a lean alloy grade exemplified by S32304. The lower alloy content, in particular of Mo, than the standard grade S31803 means that it is cheaper to produce, but has lower pitting resistance. In this respect, it competes with the high production austenitic grades such as 304L and 316L on the grounds of its higher strength, similar pitting resistance in chloride media and better resistance to chloride stress corrosion cracking (SCC)[9]. In 1980 Creusot-Loire was the first steel company to introduce duplex stainless steels for the manufacture of the cargo tank of chemical tankers. Since that time the steel industry has made continuous developments in its processes. Many authors have studied the exhibited nature of self-healing passive films in stainless steels[13-16], erosion-corrosion behaviour in various environments[17-21] and their chemical and mechanical properties using simulated electrochemical

techniques in laboratories[22, 23]. This has led to a significant improvement in the control of residual elements such as O_2, S and N in the steel industry's process[8]. Since then there has been a continuous drive to develop stronger and more corrosion resistant grades.

UNS	Element, wt% C	S	P	Si	Mn	Ni	Cr	Mo	Cu	W	N
Alloy lean											
S31500 (3RE60)	0.030	0.030	0.030	1.40–2.00	1.20–2.00	4.25–5.25	18.0–19.0	2.50–3.00	–	–	–
S32304 (2304)	0.030	0.040	0.040	1.0	2.50	3.0–5.5	21.5–24.5	–	0.05–0.60	–	0.05–0.20
S32404 (Uranus 50)	0.04	0.010	0.030	1.0	2.0	5.5–8.5	20.5–22.5	2.0–3.0	1.0–2.0	–	0.20
Standard 22% Cr											
S31803 (2205)	0.030	0.020	0.030	1.00	2.00	4.50–6.50	21.0–23.0	2.50–3.50	–	–	0.08–0.20
S32205	0.030	0.020	0.030	1.00	2.00	4.50–6.50	22.0–23.0	3.00–3.50	–	–	0.14–0.20
High alloy											
S31200 (44LN)	0.030	0.030	0.045	1.00	2.00	5.50–6.50	24.0–26.0	1.20–2.00	–	–	0.14–0.20
S31260 (DP3)	0.03	0.030	0.030	0.75	1.00	5.50–7.50	24.0–26.0	2.50–3.50	0.20–0.80	0.10–0.50	0.10–0.30
S32550 (Ferralium)	0.04	0.030	0.04	1.00	1.5	4.50–6.50	24.0–27.0	2.9–3.9	1.50–2.50	–	0.10–0.25
S32900 (329)	0.08	0.030	0.040	0.75	1.00	2.50–5.00	23.0–28.0	1.00–2.00	–	–	–
S32950 (7-Mo Plus)	0.03	0.010	0.035	0.60	2.00	3.50–5.20	26.0–29.0	1.00–2.50	–	–	0.15–0.35
Superduplex											
S32520 (Uranus 52N+)	0.030	0.020	0.035	0.8	1.5	5.5–8.0	24.0–26.0	3.0–5.0	0.50–3.00	–	0.20–0.35
S32750 (2507)	0.030	0.020	0.035	0.8	1.20	6.0–8.0	24.0–26.0	3.0–5.0	0.5	–	0.24–0.32
S32760 (Zeron 100)	0.03	0.01	0.03	1.0	1.0	6.0–8.0	24.0–26.0	3.0–4.0	0.5–1.0	0.5–1.0	0.2–0.3
S39226	0.030	0.030	0.030	0.75	1.00	5.50–7.50	24.0–26.0	2.50–3.50	0.20–0.80	0.10–0.50	0.10–0.30
S39274 (DP3W)	0.030	0.020	0.030	0.80	1.0	6.0–8.0	24.0–26.0	2.50–3.50	0.20–0.80	1.50–2.50	0.24–0.32
S39277 (AF918)	0.025	0.002	0.025	0.80	–	6.5–8.0	24.0–26.0	3.0–4.0	1.2–2.0	0.80–1.20	0.23–0.33

The chemical compositions listed are for information purposes only. After metal and alloys in the Unified Numbering System , SAE/ASTM, September 1996. Values are maxima unless range given.

Table **2.1**, Wrought duplex grades listed in the Unified Numbering System[9].

2.2 Types

Sedrick[3] divided the common stainless steels into three groups according to metallurgical structure; austenitic (face centred cubic), ferritic (body centred cubic), and martensitic (body centred tetragonal). The American Iron and Steel Institute (AISI) designates the wrought standard grades of stainless steel using 3 digit numbers. The austenite grades are identified by numbers in the 200 and 300 series, whereas the ferrite and martensitic grades are designated by numbers in the 400 series. Duplex (austenitic/ferritic) alloys, precipitation hardening stainless steels, and higher alloys containing less than 50% Fe are generally known by proprietary designations or trademarks or the Unified Numbering System (UNS)[3].

A modification summary from the basic 18/8 (304) grade stainless steel is shown in figure **2.1**. Among the more important compositional modifications that improve corrosion resistance are:

(a) The addition of Mo to improve pitting and crevice corrosion resistance.
(b) Lowering C content or stabilising with either Ti or niobium (Nb) plus Ta to reduce intergranular corrosion in welded materials.
(c) Addition of Ni and Cr to improve high temperature oxidation resistance and strength.
(d) Addition of Ni to improve stress corrosion cracking resistance.
(e) S and Se for machinability.

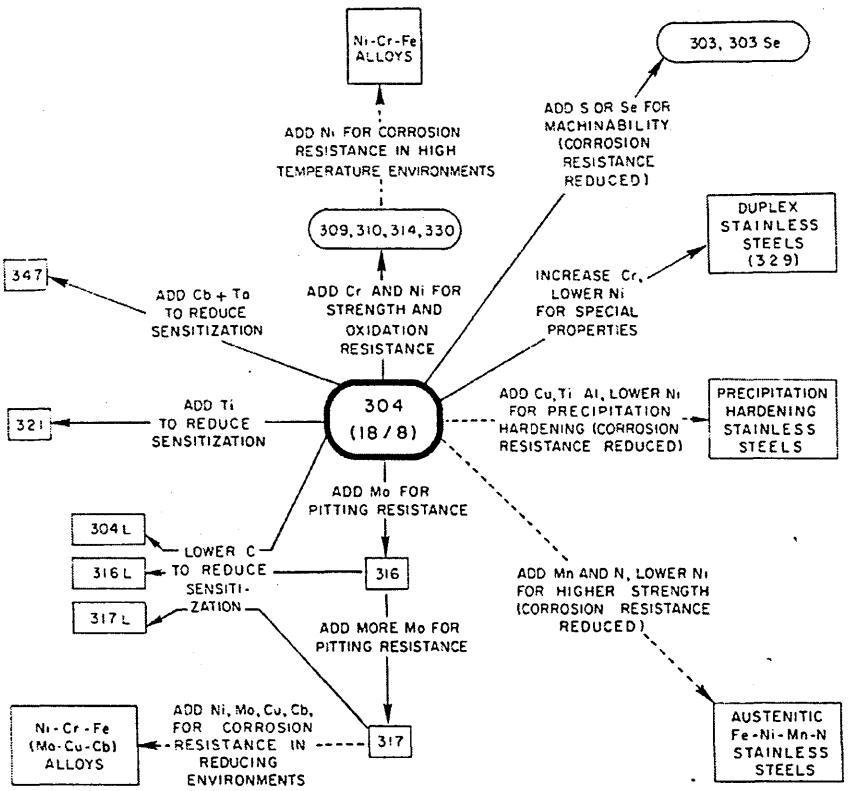

Figure **2.1**, Compositional modification to 18/8 stainless steel[3]

A simple way to relate metallurgical structure with the composition of stainless steel is by means of a Schaeffler diagram, as shown in figure **2.2.** This diagram indicates the structure obtained after rapid cooling to room temperature from 1050°C. It was established to estimate the delta ferrite content of welds in austenitic steels. The alloying elements found in stainless steels act either as austenite stabilisers or delta ferrite stabilisers, each element being expressed in terms of either equivalence to Ni (austenite stabiliser) or Cr (ferrite stabiliser) on a weight percentage basis, which form the two axes of the Schaeffler diagram[3]. Chromium content in excess of 12% can be estimated from the equations below:-

% Ni equivalent = (% Ni) + (% Co) + 30 (% C) + 25 (% N) + 0.5 (% Mn) + 0.3 (% Cu)
% Cr equivalent = (% Cr) + 2 (% Si) + 1.5 (% Mo) + 5 (% V) + 5.5 (% Al) + 1.75 (% Nb) + 1.5 (% Ti) + 0.75 (% W) (2,3)

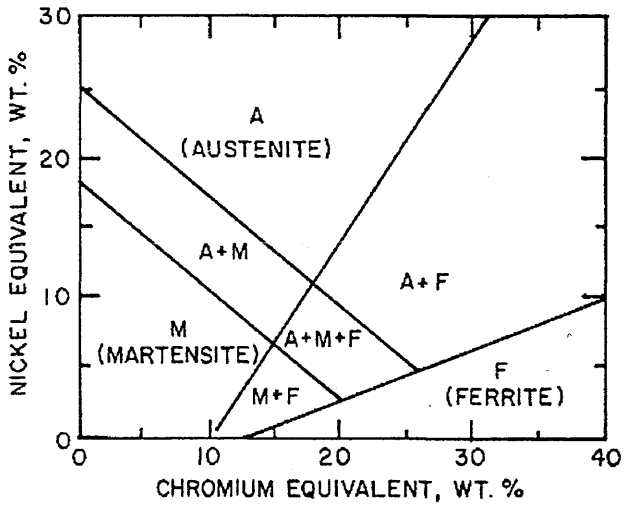

Figure **2.2,** Schaeffler diagram including modifications by Schneider[3].

2.3 Austenitic stainless steel

This is represented by the 300 series steels. When related to the Schaeffler diagram, their compositions are shown to be balanced to minimise the formation of delta ferrite. This phase is rich in Cr and other ferrite stabilising elements and lean in Ni and austenite stabilising elements. It requires hot working and the presence of delta ferrite is known to decrease pitting resistance. However, in duplex stainless steels it improves resistance to sensitisation and SCC. Long term exposure of delta ferrite at elevated temperatures can lead to its transformation to sigma - a hard brittle phase that can reduce ductility and toughness[3].

Sulphur is present in austenitic stainless steels as an impurity to improve machinability, (0.01% solubility of sulphur in stainless steels) and exists as metal sulphide, usually manganese sulphide. The sulphides are detrimental to pitting resistance in all grades of stainless steels, although the extent to which they act as pit sites depends on their manganese and Cr content. Chemical heat treatments can be used to remove them from the surface layer[3].

2.4 Duplex stainless steels

As duplex stainless steel (UNS31803) is a relatively new material in comparison with the published research literature of other stainless steels, the literature about other grades of stainless steel was included in this literature survey to clarify and bring out the critical aspects of duplex stainless steel.

As postulated by Haynes[24] in figure **2.3**, there is a region in which alloy compositions will produce mixed two phase microstructures with varying amounts of ferrite and austenite (marked $\delta+\gamma$). These are known as the two phase alloys-duplex series of stainless steels. It is seen that alloys solidify as ferrite and remain as such down to 1200°C and probably below. Under near equilibrium conditions (very slow cooling or prolonged holding at temperature) some of the ferrite will start to transform to austenite at about 1200°C and progressively more austenite will continue to form down to about 700°C. The aim is to produce 30-70% of either phase in duplex stainless steels, and such mixtures are obtained after 'equilibrium' solution annealing in the range 920-1120°C, depending on the steel composition.

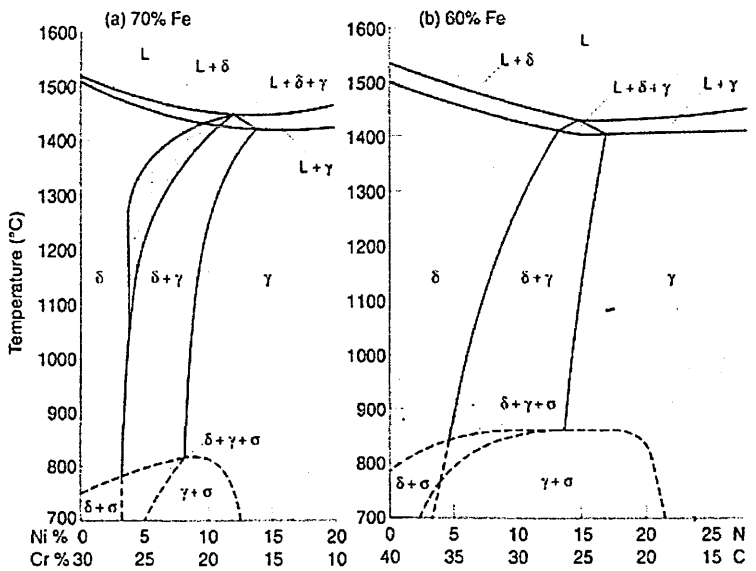

Figure **2.3**, Concentration profiles in the ternary Fe-Cr-Ni constitution diagram at 70% and 60%Fe. The schematic effect of nitrogen additions is shown in (a)[24].

The effect of N is to promote more rapid austenite formation, hence a microstructure of high ferrite content is to be avoided due to lower toughness, less corrosion resistance and a higher susceptibility to hydrogen embrittlement. In addition, the use of higher Ni and N contents to control heat affected zone (HAZ) microstructure will tend to promote more than the desired amount of austenite in the annealed base steel[24]. During a solution anneal, even though the solubility of N in ferrite may increase a little, the volume fraction of austenite decreases markedly. This leads to enrichment of N in the remaining austenite[9]. N as Garner[132] reported, has a multiple effect on stainless steels by increasing pitting resistance, austenite content and strength, moving pitting potential (E_p) in the noble direction and thus increasing the passive potential range.

Gunn[9] observed that N content is highest next to the ferrite austenite interface, just within the austenite, due to phase boundary displacement. However, on cooling, austenite formation occurs and the ferrite becomes rapidly saturated with N, with the excess N diffusing into the austenite (0.03-0.05% N being the equilibrium solubility limit in ferrite at ambient temperatures[33]). As N has a significant beneficial influence on pitting corrosion resistance, this balances the preferential partitioning of Cr and Mo to the ferrite. For instance, during heat treatment if the temperature is too high, then primary austenite dissolves, encouraging secondary austenite on cooling. This has inherently lower N, Mo and Cr contents than primary austenite, with inferior pitting resistance. On the other hand, if the heat treatment temperature is too low, then the substitutional amount of the elements can partition and lead to intermetallic phase formation.

Gojkovic et al[25] confirmed that duplex stainless steels consisting of austenite and ferrite as the main phases have a significantly larger surface of the phase boundaries and, therefore, lower density of non-metallic inclusions and secondary phases. These are mostly located at the main phase boundaries and inside the ferrite. Hence, Koren et al[26] expected that duplex stainless steel has a higher corrosion resistance than austenitic or ferritic steels. This leads to a galvanic interaction between the two phases, due to the additions of element percentages such as Co, C, N, Mn and Cu in the austenite phase and Cr, Si, Mo, V, Al and Nb in the ferrite phase.

As pointed out by Gupta et al[154], in order to improve wear resistance in stainless steels, one approach adopted in recent years is to add N to cast stainless steels to improve their resistance to sensitisation corrosion and adhesive wear resistance[10]. Lu et al[100] confirmed that N enhances the anodic segregation of beneficial alloying elements, such as chromium in austenitic stainless steels, when local attack takes place and significantly prevents the transpassive dissolution of Mo. The effects of alloying elements such as Cr, Mo and N all improve the localised corrosion resistance of stainless steels by inhibiting the anodic processes.

2.4.1 Physical and mechanical properties

The most interesting characteristics of the alloys include[8]:

- A low thermal expansion coefficient when compared with that of the austenitic stainless steels.
- Thermal conductivity similar to that of austenitic stainless steels but lower than that of structural steel (C.Mn steel).
- Strongly magnetic behaviour when compared to a non magnetic austenitic stainless steel, enabling the use of magnetic clamps during machining.

The mechanical properties of duplex stainless steels compared with those of austenitic stainless steel are shown in table **2.2**. The yield strength of the duplex stainless steels is almost 65% larger than that of the austenitic grades[8]. The yield stress of S31803 is an important parameter in this study especially in the mathematical modelling section when determining the type of damage on the surface of the material sustained from sand particle impact.

	Tensile test results				
	YS 0.2%		UTS		EL %
	MPa	KSI	MPa	KSI	
304 LN	290	42	590	86	40
Duplex 3204	400	58	600	87	25
316 LN 2.5 Mo	300	43	600	87	40
Duplex 31803	480	69	680	98	25

Table **2.2** Mechanical properties of duplex and austenitic stainless steels[8]

Karimi[27] pointed out that cavitation erosion of duplex stainless steel is initiated from the austenite-ferrite boundaries and propagates more rapidly into the ferrite grains than into the austenite grains. Potgieter et al[133] reported that SAF 2205 has good resistance to chloride stress corrosion cracking, strength and excellent corrosion resistance.

2.4.2 Microstructure stability

Haynes[24] showed that extra corrosion resistance is conferred on the ferrite by the extra Cr and Mo and may be largely balanced by the benefit of N to the austenite phase. An increase in the Mo and Cr content makes the alloy more prone to intermetallic phase precipitations which result in a decrease in the mechanical properties[8], thus ductility may decrease but strength is expected to increase. Charles[32] stated that all agree that the ferrite is enriched in P, W, Mo, Si and Cr and the austenite in N, Ni, Cu and Mn.

2.4.2.1 Characteristics and morphology of precipitates

(a) Sigma (σ)

The deleterious Cr and Mo rich σ-phase is a hard embrittling precipitate which forms between 650-1000°C and is often associated with a reduction in both impact properties and corrosion resistance. At the peak temperature of around 900°C, ferrite decomposition to sigma may take as little as two minutes in superduplex alloys. Certainly, σ-phase has been found by Redjamimia[34] to nucleate at temperatures above 750°C in association with such pre-existing $M_{23}C_6$ particles in duplex stainless steels, with the following order of preference: δ/γ phase boundaries, austenitised δ/δ sub-grain boundaries and high energy δ/δ grain boundaries. On the other hand, Yutaka et al[35], mentioned that an increase in annealing time increases the sigma content. Sigma phase forms preferentially at one side of the ferrite/austenite along intergranular austenite in a duplex stainless steel weld metal annealed at 1100°K.

(b) Carbides and nitrides

At high temperatures (ca 1000-1400°C) both high Cr ferrite and Cr-Ni austenite phases may dissolve up to about 0.2% C. However, on cooling down super-saturation leads to the precipitation of Cr carbides. The solubility of nitrogen in molten steel at 1600°C is reported as about 0.3-0.6% for ferrite 20-30% Cr and decreases to about 0.25-0.5% when 5% Ni is added (duplex). However, upon solidification and cooling to room temperature, the austenite can retain much of the N in solution whereas much of that in the ferrite is lost by precipitation as Cr nitride[24].

2.4.3 Marine applications of stainless steels

Some of the important marine applications of UNS 31803 duplex stainless steel were reported by Francis[36] and Farrar[124] who demonstrated that duplex stainless steels are increasingly used in oil, gas, chemical, petrochemical, pulp and paper, and flue gas desulphurisation applications. Duplex stainless steel castings used for pumps, valves, and other components are economical alternatives to forging or fabrication. Similarly, Haynes[24] and Angelini et al[122] pointed out that SAF2205 (UNS31803) is used extensively in the marine environment for applications such as heat exchangers, pumps handling seawater, gas production, transportation and offshore drilling. With the worldwide increase in the production of chemicals, about 100 km of duplex stainless steels have been used or specified as subsea pipe work in the North Sea fields. It has also been used in 24 chemical tankers being built in Italy, which involved 112,000 tones of plate, pipe, fittings and bar of Avesta 2205.

Equally, Zhang et al[99] reported the use of duplex stainless steel in phosphoric fertiliser production and Ravindranath et al[43] suggested that SAF 2205 is immune to IGC after aging treatment at 1173K, and has better resistance to it in copper-copper sulphide-sulphuric acid solution than in ferric suphate-sulphuric acid solution. Research by Symniotis[106] showed that duplex stainless steels have very good corrosion resistance in a number of environments and they are proposed to replace standard austenitic stainless steel. The Bjordal et al[101] study revealed that SAF2205 is quite resistant to erosion-corrosion in seawater solution systems because of its good corrosion properties.

Neville et al[152] reported that SAF 2205 is a reliable material for seawater handling systems in industries ranging from the petrochemical to desalination. The majority of equipment exposed to moving fluids is subject to erosion corrosion. Examples of these are piping systems, particularly bends, elbows, and tees, valves, pumps, blowers, centrifugal, propellers, agitators, orifices, turbine blades, nozzles, ducts, cutters, wear plates and equipment subject to spray. As anticipated by Kwok et al[21], thanks to their excellent corrosion resistance, S31803 stainless steels are widely used both in the marine, urban water, chemical and food industries. Levin et al[147] conveyed Lammarre's findings that damage associated with solid particle erosion (SPE) costs the utility industry at least $150 million annually in reduced efficiency of power generation. One method to combact SPE as mentioned in previous section is the design and proper selection of erosion resistant materials.

2.5 Influence of alloy element additions

The existence of various alloys in the chemical composition of UNS31803 duplex stainless steel is of great importance, especially under erosion-corrosion conditions in seawater environments. Many elements are added to stainless steel to provide specific properties or ease of fabrication. Charles[8] observed that the duplex alloys have a lower nickel content, whilst the addition of Cr, Mo and N contributes to corrosion resistance properties. These elements are as follows:

2.5.1 Chromium

Chromium is defined as a ferrite (α) stabiliser and a predominantly ferrite structure is stable for Cr contents in excess of 12%, about the amount necessary to establish passivity. Studies by Hashimoto et al[39] and Olefjord et al[40] showed that Cr addition to

steel improves localised corrosion resistance by the formation of a passive Cr rich oxy-hydroxide film and by improving their tenacity, rendering pitting corrosion less likely in chloride solution.

The study by Gunn[9] was cited by Sedriks[41] and showed this electrochemically, by extending the passive range in the stainless steel as shown in figure **2.4** and reducing the rate of general corrosion (i_{pass}). However, a higher level of Cr is negated by the enhanced precipitation of intermetallic phases, such as sigma. These phases often lead to a reduction in ductility, toughness and corrosion properties. Intergranular corrosion in the SAF 2205 duplex stainless steel was controlled to a great extent by Cr depletion around the precipitated sigma phase at the grain boundaries (Ravindranath et al[43]). Wanklyn[44] addresses studies by other worker[39]which showed that Cr and Mo act co-operatively, as below a certain Cr content Mo ceases to be beneficial.

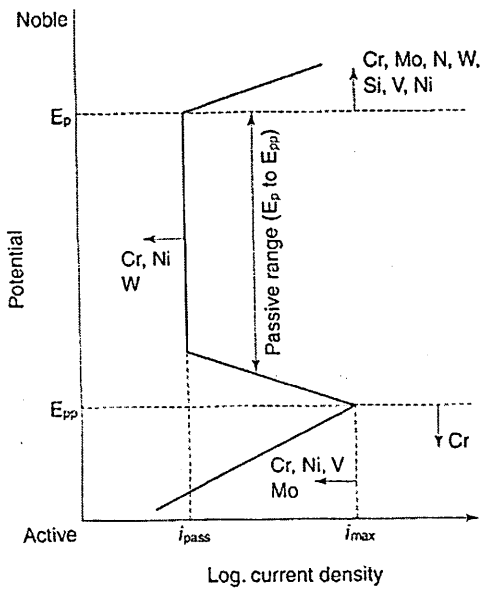

Figure **2.4**, Schematic summary of the effect of alloying elements on the anodic polarisation curve[9].

However, Belfrouth et al[47] suggested that in the passive region, Cr is responsible for a very low dissolution rate and Mo plays an important role in increasing Cr enrichment in pre-passive film development. Asami et al[45] pointed out that a decrease in the Mo content of the alloy led to a decrease in the content of beneficial Cr in the passive film and to an increase in the content of unstable Mo in the film. McLoone[4] reported the effect of Cr content on the active-passive behaviour of steel. During polarisation scans, at high Cr values, the anodic and cathodic curves intersect within the passive range whereas at low levels of Cr the two curves intersect in the active range.

Crsitofaro et al[50] noted that all the passive films were Cr enriched with respect to bulk composition. Hong et al[51] showed a significant enrichment of Cr in the surface film formed on 430 stainless steel by HNO_3 surface treatment. The higher the Cr enrichment the higher the pitting potential (E_p), corrosion potential (E_c), and polarisation resistance

(R_p). In figure **2.5** the increase in Cr reduces the corrosion rate difference between Cr-bearing weldment and the X65 line pipe steels in an immersion test of CO_2 gas saturated 10% NaCl solution with an addition of 0.3% Cr. This effect may be attributable to the cathodic polarisation curve polarised[49].

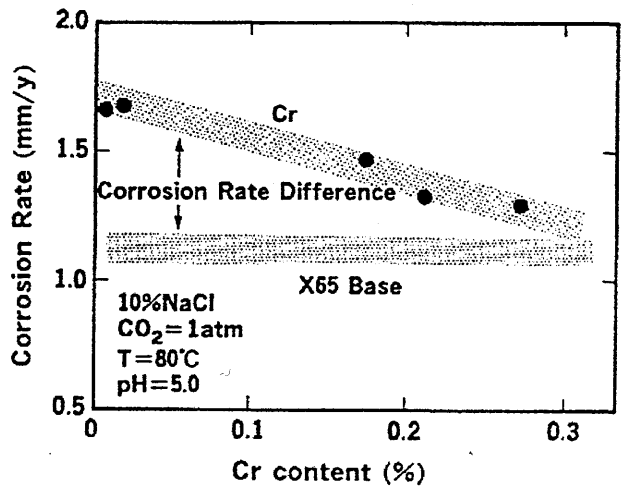

Figure **2.5**, The effect of Cr content on corrosion rate of line pipe steel[49].

2.5.2 Nickel

The essentials of Ni addition to the properties of duplex stainless steel are reviewed by Kotecki et al[53]. They showed that the main purpose of Ni is to promote the formation of austenite, i.e. Ni is (γ) former and imparts toughness and ductility. In order to maintain about 40% to 60% ferrite, the balance being austenite, the ferrite stabilising elements need to be balanced with the austenite stabilisers. For this reason, the level of Ni addition to a given duplex alloy will depend primarily on the Cr content. At excessive Ni contents, the austenite level increases to well above 50%, the consequence being that Cr and Mo are enriched in the remaining ferrite.

Further, Solomon et al[55] stated that high Ni content accelerates the alpha prime formation which is an embrittling intermetallic phase in the ferrite phase. For instance in figure **2.4** Ni moves the pitting potential (E_p) in the noble direction and reduces i_{pass}, and yet it appears that the main role of Ni is to control phase balance and element partitioning. Similarly, Denpo et al[49] suggested that Ni depolarises the anodic polarisation curves in the weld metal, whilst the addition of chromium to the weld metal polarises the cathodic polarisation curves. On the other hand, Wang et al[120] developed nickel-free duplex stainless steels, which have high strength and toughness, good corrosion resistance and low alloy element cost.

Figure **2.6** shows the difference between the Ni-bearing weld metal in an immersion test of CO_2 gas saturated 10% NaCl solution compared with base metal X65 line pipe steels. In the early stage of immersion, Ni kept the corrosion rate constant up to 1% Ni in the weld metal. Beyond 1% Ni content the corrosion rate increased and the corrosion rate difference increased compared with the base metal. Denpo[49] cited the study by Endo et al[56] who showed that the addition of Ni and Mo can improve the uneven corrosion of weldment and heat affected zones.

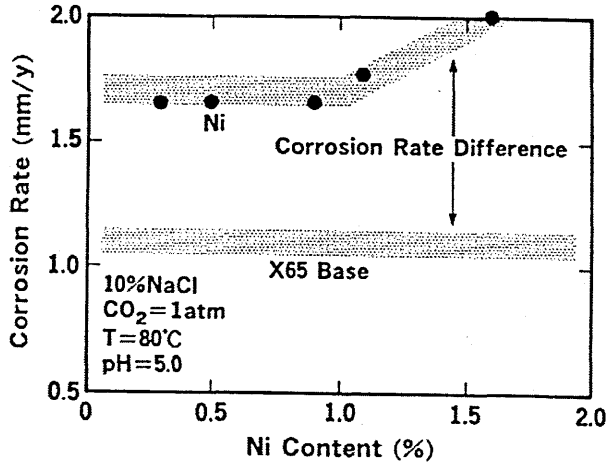

Figure **2.6**, The effect of Ni content on corrosion rate of linepipe steel[49].

2.5.3 Molybdenum

The beneficial influence of Mo on the pitting and crevice corrosion resistance of stainless steel in chloride solutions has been recognised for many years (Fig. **2.4**). As with Cr, Mo extends the passive potential range and reduces the corrosion current density (i_{max}) in the active range, whilst it has a similar effect on ferrite stability as Cr. A recent study by Montemor et al[62] shows that the oxide films formed on the AISI 304 and AISI 316 stainless steels at temperatures between 250°C to 450°C are composed of an outer iron oxide region and an inner Cr oxide region. Mo was not detected in the former region, whereas the latter region reveals the presence of Mo. Whenever Mo is present in the alloy there is an enrichment of Cr oxide in the film[45, 64]. The film thickness is practically independent of the presence and content of Mo.

Nilsson[60] stated that the addition of Mo causes a reduction in toughness and SCC resistance because Mo enhances precipitation of brittle σ and χ phases. Nagano et al[58] showed that Mo suppresses active sites via the formation of an oxyhydroxide or molybdate ion. In high temperature sea water, the addition of 3% Mo is recommended to prevent crevice corrosion, while an upper limit of about 4% Mo has enhanced sigma forming which must be avoided, i.e. above 1000°C[9].

The beneficial effects of Mo as stated by Sugimoto et al[63] in the corrosion resistance of stainless steels are attributed to several factors such as an enrichment of Mo in the passive film or in the alloy layer just below the passive film as reported by Tan et al[64]. Enrichment of Cr in the oxide layer led to thickening of the passive film and stabilisation of the Cr oxide[63] by the presence of Mo^{6+}. It also tends to eliminate the active surface sites through the formation of Mo oxides or oxyhydroxides[39]. Frankel[94] found that one effect of Mo in stainless steel is to ennoble the anodic dissolution reaction in the pit environment, which diminishes the breakdown of passivity, especially in chloride containing media[59]. A variant view suggested by Defranoux[167] that Mo prevents depassivation by the increasingly aggressive conditions that develop within crevices.

According to Heymann[162] improved erosion resistance has been associated with alloying elements such as Cr, Mn and Nb. The effect of Ni was inconsistent, as some studies have found nickel deleterious. Fine microstructure is advantageous and so is the ability of the surface layer to work harden as a result of impact induced deformation.

2.5.4 Manganese

The current understanding is that Mn has little effect on duplex phase balance. Roscoe et al[71] suggested that Mn can increase the temperature range and formation rate of the detrimental sigma phase. Manganese additions to stainless steel increase tensile properties without loss of ductility[71]. Furthermore, Mn increases the solid solubility of N and significantly decreases the critical pitting temperature (CPT), probably due to the increase of MnS inclusions. Nevertheless, Chance et al[70] demonstrated that the combined addition of Mn and N in modern duplex alloys improves the pitting resistance and counteracts the singular problems associated with Mn.

2.5.5 Copper

Guha et al[73] described that in some 25% duplex alloys, 1.5% Cu is added to obtain the optimum corrosion resistance in 70% H_2SO_4 at 60°C, while for boiling HCl, an addition of 0.5% Cu decreases both the active dissolution and crevice corrosion rates. Gunn[9] reported that in general, the addition of Cu to duplex stainless steels is limited to about 2%, since higher levels reduce hot ductility and can lead to precipitation hardening. However, Cu additions to high alloy austenitic stainless steel are used to reduce the corrosion rate in non-oxidising environments such as sulphuric acid.

The results of Pini et al[74] and Heubner[75] suggested that under high velocity conditions where cavitation erosion in H_2S-contaminated seawater is found, Cu appears to be beneficial, due to the formation of a Cu rich layer on the surface during active dissolution. Improved machinability in low oxygen and S materials leads to hardening after exposure to a temperature range of 300-600°C.

2.5.6 Tungsten

Okamoto[76] showed that tungsten (W) additions of up to 2% have been made to duplex stainless steels to improve pitting resistance, i.e. extending the passive potential range and reducing i_{pass}, (Fig.**2.4**). Also when W is added to austenitic stainless steel it improves pitting resistance in acid or in neutral Cl^- solutions[61]. Similarly, Nagano et al[58] stated that W increases crevice resistance in heated chloride solutions. This is thought by Bui et al[81] to be due to the adsorption of W into the passive layer without modification of its oxide state. In acid chloride solutions tungsten passes from the substrate into the passive film by interaction with water to form soluble WO_3.

Nilsson et al[79] revealed that W encourages intermetallic formation in temperature ranges from 700 to 1000°C and encourages secondary austenite formation in weld metal. However, levels between 1% and 3% restrict formation of sigma at the phase boundaries and, instead, precipitation occurs at intergranular sites. This is thought to be due to the large W atom influencing the diffusion of Mo and W at the phase boundaries and thus nucleation of sigma. Notwithstanding this, W alloyed weld metal forms the chi phase more rapidly.

As Kim et al[59] found the addition of W to duplex stainless steel equivalent to SAF 2507, one homogenized (h) and the other aged (a) is known to suppress formation of the brittle secondary phases that may have a negative effect on general corrosion and SCC properties. On ageing, W addition reduced the amount of the α-phase precipitation, while enhancing precipitation of the χ phase. In figure **2.7** at room temperature, the tungsten effect became apparent when Cl^- concentration was increased to 50.000 ppm. The passive current density of Alloy *C*(h) and *C*(a), which did not contain tungsten, increased to about 10 times higher than alloys *E* (h) of 4.4% W, *F*(h) and *F*(a) of 3.6% W. Bui, et al[81], showed that interaction of W oxide (WO_3) with other oxides in neutral Cl^- solution, led to enhanced stability and improved bonding of the oxide layers of the base metal.

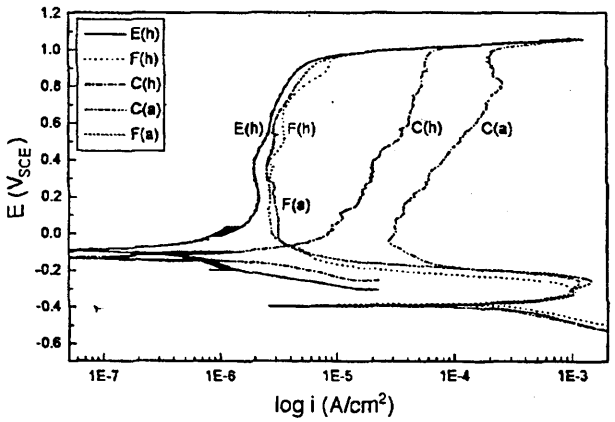

Figure **2.7** The effect of tungesten addition to homogenized C(h) and aged C(a) duplex stainless steel in 10% H_2SO_4 + 50,000 ppm Cl^- at 25 °C[59].

2.5.7 Silicon

Silicon is beneficial for concentrated nitric acid applications and also enhances high temperature oxidation resistance and it increases pitting resistance in stainless steel (figure. **2.4**). Despite this, Si enhances sigma formation; hence its addition is generally limited to a level of 1%. Kim et al[83] pointed out that the addition of Si results in competitive grain boundary segregation between S and C or N and causes a decrease in S content at the grain boundaries below 700°C in pure iron. The intergranular brittleness was mainly caused by the S segregated at grain boundaries, and a decrease in S content at the grain boundaries with increasing Si content.

2.5.8 Carbon and sulphur

The C content of most wrought duplex stainless steels is limited from 0.02% to 0.03%, primarily to suppress the precipitation of Cr-rich carbides. Elbiache et al[116], concluded that S shifts the corrosion potential to a more negative potential and accelerates the dissolution of the alloy in the active region and shows a catalytic effect on the dissolution. Thus it clearly showed that Mo is responsible for the desorption of S at the corrosion potential.

2.6 The corrosion resistance properties of duplex stainless steels

A review of the effect of general, pitting and crevice corrosion on duplex stainless steel material is discussed in this section. As pointed out by Bjordal et al[101], Johnsen[52] and Charles[8], SAF 2205 and other high chromium duplex stainless steels[78] perform better in certain seawater applications than standard austenitic grades when different corrosion mechanisms are considered. In some conditions the duplex stainless steel has to be cathodically protected to prevent corrosion, in the contrary. On the contrary, Symniotis[106] concluded that SAF2205 has a better corrosion resistance in terms of galvanic action between the ferrite and austenite phases than the 316L austenitic alloy in acidic solutions.

2.6.1 General corrosion

Various caustic & acid media

As Charles[8] stated, the general corrosion resistance properties of duplex stainless steel AISI 31803-SAF2205 are generally much better than the austenitic grades, even at the high chloride level encountered in 54% P_2O_5 industrial solutions. This is explained by the high Cr and Mo contents of the duplex grades. As the chlorides and fluorides can lead to high corrosion rates, the behaviour of UR45N is also good when comparing the alloys with classic austenite grades for sulphuric acid transportation. For concentrated solutions of more than 95% H_2SO_4 as shown in figure **2.8**, and where the chloride concentration is up to 40%, UR 45N shows better behaviour than the 316LN and 316L alloys.

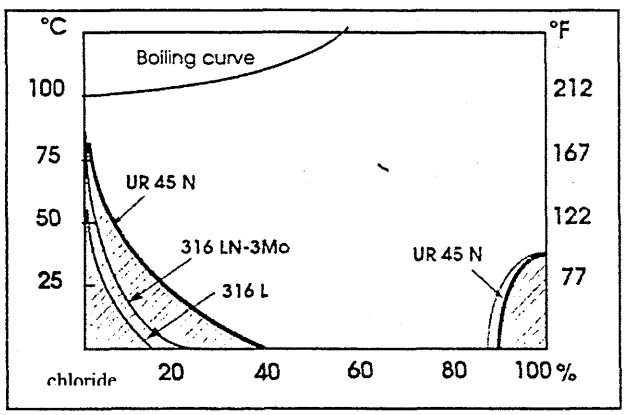

Figure **2.8**, Compare UR45N duplex stainless steel with austenitic grades alloys in H_2SO_4 solution at different chloride concentrartions.[8]

Under concentrated nitric acid, the duplex steels exhibit dramatically different behaviour. In this environment Mo has a strong negative effect, while Cr is beneficial[9]. Horn et al[87] showed that different duplex grades can be applied successfully in caustic environments at low concentrations and Gelder et al[118] found out that duplex stainless steel at its free corrosion potential is susceptible to SCC in H_2S, CO_2 and Cl^- media only at temperatures higher than 80°C.

2.6.2 Pitting corrosion

This literature survey clarifies the pitting corrosion of duplex stainless. Haynes[24] showed that pitting occurs in stainless steels when the passive film is penetrated by

selective electrochemical attack. The penetrated region will remain active until it is healed by oxidation from the corrosive media. When stainless steel is placed in a corrosive solution which approaches the limit of its corrosion resistance, pit initiation and pit repassivation processes occur. Electrochemical testing accelerates pit initiation - when the voltage applied is progressively increased to a critical level, anodic current (e.g. 0.01-0.1 mA/cm^2) will flow. This is indicative of local pit initiation. This critical level is known as the pitting potential (E_p) or the breakdown potential (E_b). Pitting corrosion has been studied for several decades by many researchers[88, 89, 90-94] on stainless steels and other alloys. The fundamental studies focused on the following stages:

Passive film breakdown. Frankel[94] conveyed Stehblow findings and pointed out that theories for passive film breakdown in stainless steels and pit initiation have been categorized into three main mechanisms that focus on passive film penetration, film breaking, or adsorption. However, pits in real alloys are most often associated with inclusions or second phase particles.

Penetration mechanisms for pit initiation. (Figure **2.9a**), involve the transportion of the aggressive anions through the passive film to the metal/oxide interface where aggressive dissolution is promoted[96]. Anion migration would be assisted by the high electric field in the film. The existence of an induction time for pitting - when a critical concentration of chloride in the passive film is reached - film breakdown and pit initiation begin. Others such as Stehblow found no evidence of chloride in passive films.

Adsorption theories of initiation. According to Uhlig which was cited by Frankel[94] (figure **2.9b**), these theories were based on the competitive adsorption of chloride ions and O_2. Stehblow pointed out that the passive film is at least several monolayers thick rather than just an adsorbed oxygen layer. For instance, exposure of iron to chloride causes thinning of the passive film based on X-ray Proton Spectroscopy (XPS) measurements, as a result of catalytical transfer of cations from the oxide to the electrolyte. Interestingly, Hoar[96] reported that no Cl^- was found incorporated into the oxide. When thinning occurs locally because of some local adsorbed species, the local electric field strength will increase, which may eventually lead to complete breakdown and the formation of a pit.

Pit initiation by a film breaking mechanism. (figure. **2.9c**). Mechanical stresses at weak sites resulting from surface tension effects may cause local breakdown events, which rapidly heal in non-aggressive environments. In fact, the background passive current density may come from many such breakdown and repair events. However, there is a lower likelihood for such a breakdown to heal because of the inhibition of repassivation by chloride[94]. One theory of initiation that combines film breaking with film penetration[98] proposes that chloride migrates to the metal/oxide interface and forms a metal chloride phase that cracks the overlying oxide as a result of its larger specific volume. Frankel[94] concluded that the chloride phase would then provide a ready source of chloride ions to stabilise pit growth from the very outset of pit development.

Metastable pitting. Metastable pits initiate and grow for a limited period before repassivating. Pits can form at potentials far below the pitting potential, and during the induction time before the onset of stable pitting at potentials above the pitting potential. These events are characterised by potential transients in the active direction at an open circuit or under an applied anodic current. According to Pessal and Hisamatsu studies were conveyed by Frankel[94] and reported that in stainless steel; stable pits survive the metastable stage and continue to grow, whereas metastable pits repassivate and stop growing for some reason.

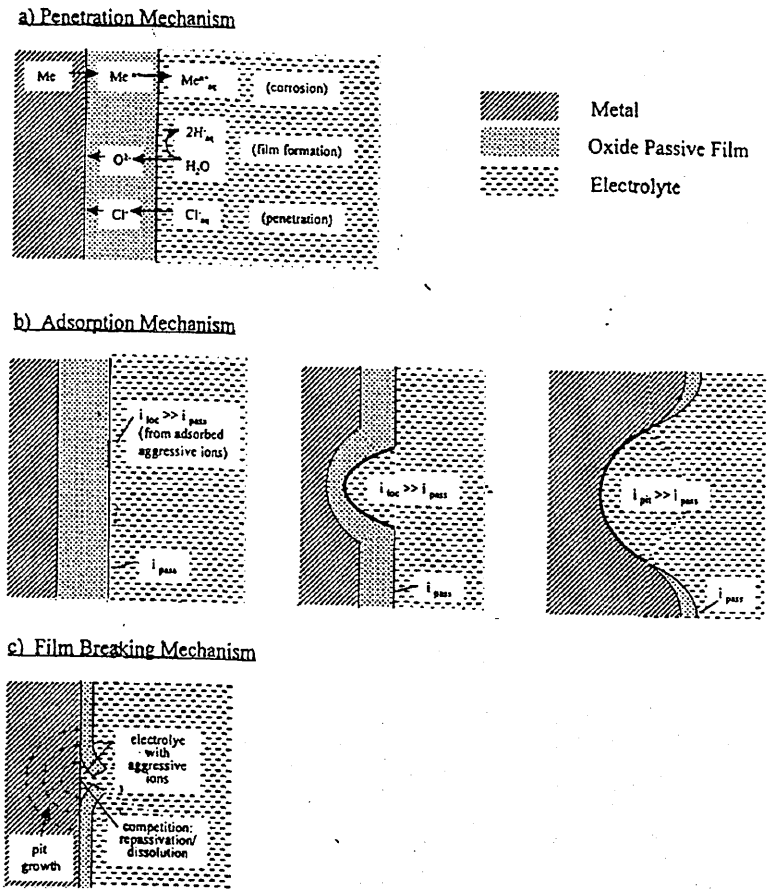

Figure **2.9**, Schematic diagrams representing pit initiation by (a) penetration, (b) adsorption and thinning, and (c) film breaking[94].

Pit growth. Frankel[94] stated that pit growth depends on material composition, pit elecrolyte concentration, and pit bottom potential. These parameters are at least severe enough to prevent repassivation of the dissolving metal surface at the pit bottom.

Kim et al[59] reported that as duplex stainless steels are well known for their higher resistance to pitting corrosion and SCC, as a result of their dual phase structures, they are proposed as replacements to the standard austenitic stainless steel in many applications, especially in chloride (Cl^-) environments. Solomon[102] demonstrated that thiosulphate pitting in stainless steel occurs over a narrow range of ionic concentrations, and over a limited range of potentials. If the potential is too oxidizing, the adsorbed species is not enough for pitting to occur. The same thing happened at low Cl^-

concentration. If the thiosulphate concentration is too high, this tends to neutralise the acidic pit solution. When potential and concentration are within a critical range, thiosulphate will sustain active pitting by delivering sulphur to the pit.

2.6.3 Crevice corrosion

Stainless steels are well known for their tendency to develop crevice corrosion. Many researchers investigating crevice corrosion treatment in stainless steel materials including Suleiman et al[177] used disc specimens for stainless steel type 304L mounted in epoxy resin after treating the edges with a primer in 0.1M or 0.005M NaCl solutions. Neville et al[20] reported Gartland's[135] work which demonstrated the beneficial aging of the passive film which can reduce susceptibility to breakdown of the passive film. Berslin's[68] study which involved altering only the surface layers of a material also showed this. This enhanced the corrosion resistance of many materials. Cerium-treated UNS S31603 stainless steel in seawater solution was observed by Lu and Ives[85, 119], resulting in a reduction in oxygen which inhibited the cathodic reaction by precipitating cerium oxides or hydroxides over cathodic sites.

Nash et al[175] coated the epoxy and stainless steel interface with Turco-Lacquer to prevent crevice occurrence. Hakkarainen[84] described a method to avoid crevice corrosion tape in AISI 304 AND 316 commercial stainless steel in chloride solutions by using a multilayer textile. Similarly, Laycock et al[103] confirmed that crevice corrosion in 316L stainless steel shows many similarities with pitting in 1M NaCl solution, such as an increase in likelihood with increasing potential or chloride concentration, and the existence of critical crevice temperatures (CCT) analogous to the critical pitting temperature.

A study by Hayes[24] showed that crevice corrosion is created when a solution covers a junction between the subject metal and another material which may be another piece of the same metal. The interfaces which produce crevice corrosion include shafts, bearings, beneath washers, nuts, bolt heads and deposits in tanks and pipelines. The crevice traps some solution which is not easily replenished by fresh solution outside the crevice. This stagnant solution has a lower O_2 content than the one outside. This creates a differential oxygen cell that becomes the driving force for the corrosion process. Within the crevice more acid and chloride concentrations are developed, leading to a breakdown of the stainless steel passive film. On the other hand, Oldfield et al[104] modelled the various stages of crevice corrosion and related these to the passive current density measurements, the pH, and chloride levels to the initiation of a crevice attack. The mechanism of crevice corrosion reveals the four stages in the process, outlined in table **2.3**.

Stage 1	Depletion of oxygen within the crevice solution
Stage 2	Increase in acidity and chloride content of the crevice solution
Stage 3	Permanent breakdown of the passive film and the onset of rapid corrosion
Stage 4	Propagation of crevice corrosion

Table **2.3**, The mechanism of crevice corrosion[104]

The passive current produced represents the rate at which metal ions pass through the passive film, and is essential during the induction period leading up to the onset of rapid

corrosion. Hydrolysis of these metal ions causes the pH in the crevice to fall whilst mass transfer causes the concentration of Cl^- ions in the crevice to rise. Eventually the composition of the crevice may become sufficiently aggressive to break down the passive film; this composition is known as critical crevice solution (CCS).

In a recent study, Turnbull[107] paid particular attention to the internal cathodic reaction kinetics inside the crevice for stainless steel. If the kinetics of the internal cathodic reactions could be simulated, the consequent increase in pH could, in principle, act to prevent the onset of crevice corrosion. The coupling of stainless steel to the more noble material would result in a more noble potential than the potential in the crevice prior to breakdown. However, according to Oldfield and Sutton's[108] model of stainless steel in a neutral chloride solution, since the kinetic of the cathodic reaction in the crevice is greater, the pH in the crevice would go alkaline and would inhibit passivity breakdown.

2.7 Electrochemical mixed potential theory

Reviewing the basic electrochemistry of duplex stainless steel in this section will assist in evaluating the mechanism of erosion-corrosion of the material in a seawater environment. Sedriks[3] indicates that the theoretical basis for electrochemical corrosion testing is derived from mixed potential theory, the formulation of which in its modern form is usually attributed to Wagner and Traud, which was cited by Sedriks[3]. Mixed potential theory has proven to be useful in corrosion studies because:

(1) It permits predictions of complex corrosion behaviour.
(2) It has been used to develop new corrosion prevention methods.
(3) It has been used as a basis for new rapid corrosion rate measurement techniques.

In essence this theory separates the oxidation and reduction reactions of corrosion and postulates that the total rates of all oxidation reactions must equal the total rates of all the reduction reactions on a corroding surface[3]. That is, the sum of the anodic oxidation currents must be equal to the sum of the cathodic reduction currents. This must be true to avoid accumulating charges in the electrode[111]. The anodic reaction for metal corrosion is of the general form:

$$M \rightarrow M^{n+} + ne^- \qquad (4)$$

This anodic reaction represents the dissolution of metal M (oxidation), in which metal atoms are converted to metal ions. At the same time the releasing electrons are equal in number to the valence of the metal produced. According to the mixed potential theory, all electrons generated by the anodic reactions are consumed by corresponding reduction reactions. Reduction reactions are known as cathodic, hence they occur at the cathodic site of a corroding metal, or at the cathode of an electrochemical cell. Common cathodic (electron consuming) reactions encountered in aqueous corrosion are as follows[3, 110, 111].

Reduction of hydrogen ions and hydrogen evolution:

$$2H^+ + 2e^- \rightarrow H_2 \qquad \text{(de-aerated acid solutions)} \qquad (5)$$

$$2H_2O + 2e^- \rightarrow H_2 + 2OH^- \qquad \text{(neutral and alkaline solutions)} \qquad (6)$$

Oxygen reduction:

$$O_2 + 4H^+ + 4e^- \rightarrow 2H_2O \qquad \text{(aerated acid solutions)} \qquad (7)$$

Oxygen reduction:

$$O_2 + 2H_2O + 4e^- \rightarrow 4OH^- \qquad \text{(basic or neutral solutions)} \qquad (8)$$

Metal ion reduction:

$$M^n + e \rightarrow M^{(n-1)} \qquad (90)$$

OR, reduction of a dissolved oxidizer in a redox reaction such as:

$$Fe^{+3} + e^- \rightarrow Fe^{+2} \qquad (10)$$

Metal deposition:

$$M^n + ne \rightarrow M \qquad \text{(plating)} \qquad (11)$$

During the corrosion process more than one anodic and more than one cathodic reaction may be operative. Figure **2.10**[112] shows the mixed potential itself, which is the potential between that of the separate anode and cathode corrosion reactions. This is commonly referred to as the corrosion potential E_{corr}. The exchange of electrons results in currents between microscopic anodes and cathodes on the surface of the metal. The driving force of this current is the difference in potential of the two electrode reactions. This is called corrosion current density potential i_{corr} and is a measure of the corrosion rate.

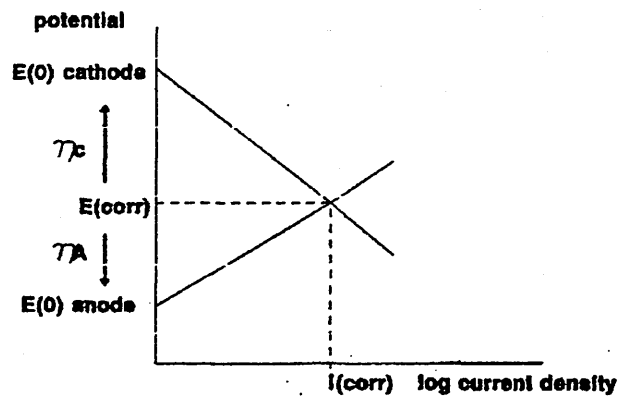

Figure **2.10**, Evans diagram, illustrating mixed corrosion potential[112].

2.7.1 Electrochemical polarisation measurement

Polarisation, η, is the potential change, E-e, from the equilibrium half cell electrode potential, e. This is caused by a net surface reaction supplied to the surface, and a build-up in the metal due to the slow reaction rate causing the surface potential, E, to become negative to e. Hence, ηc is negative by definition. For anodic polarisation, electrons are

removed from the metal, a deficiency results in a positive charge due to the slow liberation of electrons by the surface reaction, and ηa must be positive[111]. Fontana[110] and Hirooka[113] reported that at the corrosion potential, the rates of the oxidation and reduction reaction are equal and the change of state is called polarisation. This results in the change of the potential of the material.

As suggested by Jones[111], polarisation is classified into two types- *activation* and *concentration*. The term *activation polarisation* is used to indicate retarding factors which are inherent in the reaction itself. These factors include the speed of electron transfer to the hydrogen ion at the metal surface, depending on the inherent rate of a particular metal, hydrogen ion concentration, and the temperature of the system. Also activition polarisation occurs when a step in the half-cell reaction controls the rate of charge (electron) flow. The reaction is said to be under activation or charge transfer control. For example, consider the hydrogen gas evolution in the equation:

$$2H^+ + 2e \rightarrow H_2\uparrow \qquad (12)$$

This occurs at the metal surface in three major steps. Firstly, H^+ reacts with an electron from the metal:

$$H^+ + e^- \rightarrow H_{ads}, \qquad (13)$$

to form an adsorbed hydrogen atom, H_{ads}, at the surface. Secondly, two of these adsorbed atoms must react in the second step to form the hydrogen molecule:

$$H_{ads} + H_{ads} \rightarrow H_2 \qquad (14)$$

Thirdly sufficient molecules are required to combine and nucleate a hydrogen bubble on the surface. Any one of the steps can control the rate of reaction:

$$2H^+ + 2e^- \rightarrow H_2\uparrow \qquad (15)$$

In contrast, *concentration polarisation* refers to the retardation of an electrochemical process in the solution adjacent to the metal surface. In other words, at high rates cathodic reduction reactions deplete the adjacent solution of the dissolved species being reduced.

Therefore, activation polarisation is usually the controlling factor during corrosion in strong acids. Concentration polarisation usually predominates when the concentration of the active species is low; for example, in dilute acids and in aerated water and salt solutions. Knowing the type of polarisation is very helpful in predicting the characteristics of the corroding system.

Poulson[115] found that electrochemical measurements in flowing solutions can provide data on:

(a) Corrosion rates in general and the possibility of other forms of attack.
(b) Corrosion mechanism.
(c) The characteristic hydrodynamic parameters, e.g. the rate of mass transfer, the degree of turbulence or the surface shear stress.

(d) The composition of the solution by electro- analytically monitoring compositions or measuring redox potentials and pH's.

Nowadays a potentiostat is used to generate a typical form of potential/current electrochemical plot as shown in figure **2.11.** The potential difference between the specimen and a reference electrode (saturated calomel) being controlled so that any deviation in potential from a chosen value is corrected via a D.C. amplifier, the output from which feeds a third auxiliary electrode (usually platinum electrode).

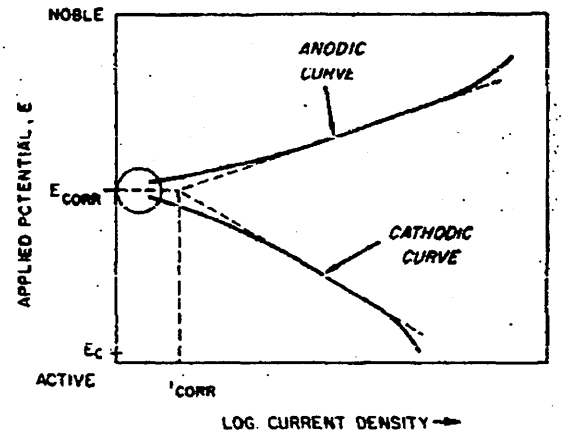

Figure **2.11**, Tafel extrapolation to determine E_{corr}/I_{corr} [111].

This third electrode can be made either anodic or cathodic to the specimen, depending upon the required correction. A computer controlled autostat is used to progressively polarise the specimen to potentials away from the steady state value E_{corr}. If this is done at a sufficiently low rate (~10mV/minute), then the specimen will stabilise at each increment before the potential and current are automatically recorded, to build up a polarisation diagram[111]. It can be seen that the region of the anodic and cathodic curves away from E_{corr} are linear, and may be extrapolated backwards to define the intersection E_{corr}/I_{corr} (Figure **2.11**). These linear regions are termed the Tafel regions, where the applied overpotential η obeys the Tafel equation:

$$\eta_A = \beta \log (I/I_0) \qquad (16)$$

Where the Tafel constant:

$$\beta = 2.3RT/\alpha z F \quad \text{and} \quad 0< \alpha <1 \qquad (17)$$

R, T, z and *F* have their usual meanings. At sufficiently high values of over potential the current density is limited by concentration polarisation when metal ions accumulate around the anode and are unable to diffuse away sufficiently rapidly.

2.7.2 Metals exhibiting passivity

Many metals and alloys are dependent upon the development of a surface film of some sort (passivity) for resistance to corrosion. Passivity is caused by formation of a thin,

protective hydrated oxide. A surface film that is the product of corrosion acts as a barrier to the anodic dissolution reaction, depending on the potential, or oxidising power of the solution. Stainless steel type 304 is passive in aerated but active in de-aerated salt water. These passive or protective films have the ability to protect the metal depending on the speed or ease with which they form when originally exposed to the environment, their resistance to mechanical damage or wear, and their rate of reforming when destroyed or damaged.

As shown in figure **2.12**[111], corrosion rates decrease above some critical potential E_p. Below E_p the alloys corrode at a relatively high rate. Examples are aluminium, lead, and stainless steels. Erosion corrosion results when these protective surfaces are damaged or worn and the metal and alloy are attacked at a rapid rate. Other soft metals such as copper are susceptible to erosion corrosion[110]. Hence, stainless steels are self-passivating in the presence of moisture and oxygen. The anodic/cathodic polarisation curve intersection shown in figure **2.13** demonstrates the relatively noble potentials exhibited by these alloys. The importance of self-passivation lies in the fact that if broken, the protective film is self-healing in a variety of environments[112].

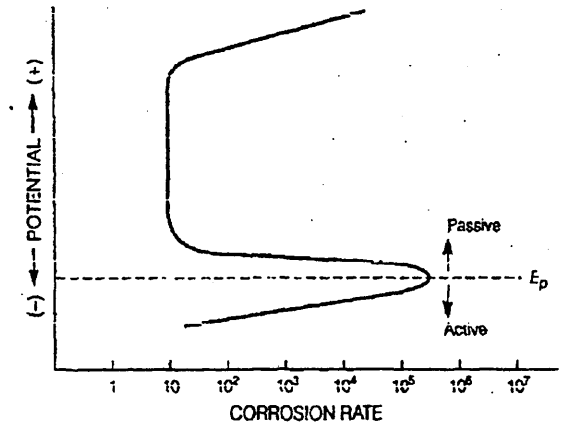

Figure **2.12**, Passivity at oxidizing potentials above E_p[111].

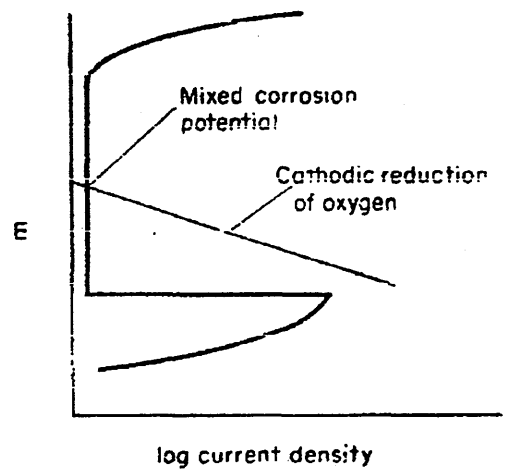

Figure **2.13**, Self passivation of stainless steel in aqueous oxygenated environments[112].

Kruger[14] cited the study of iron and Iron – Cr alloys made by Bohni which showed that if the film is a monolayer, the mechanism of breakdown involves the replacement of the adsorbed O_2 by an aggressive anion, such as a chloride ion. If the film is a phase oxide, breakdown requires that an aggressive anion must somehow traverse the thickness of the oxide film to the metal-oxide interface.

Ambrose et al[117] showed that chloride ions must penetrate the entire passive film on iron to the metal-oxide interface at a potential above a critical potential before breakdown can occur (figure **2.14**). There is an induction period for breakdown, which is the journey time of a chloride ion across the thickness of the passive film to the metal-oxide interface, no matter which mechanism is proposed. The effectiveness of the repassivation process according to Kruger[14] depends strongly on the limiting thickness of the regrown film; the smaller the limiting thickness, the more rapid the repassivation process, and the more resistant a given passive system is to breakdown.

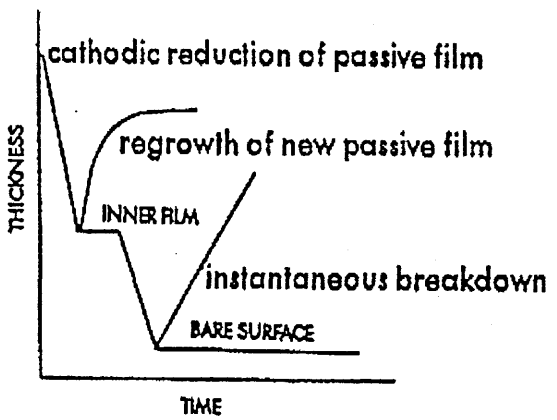

Figure **2.14**, Showing that when the outer portion of a passive film is cathodically reduced, leaving only the inner portion to prevent chloride ions from reaching a bare iron surface, a new film will form at anodic potentials. When the entire passive film is reduced, allowing chloride ions to interact with the iron surface, breakdown is instantaneous[117].

2.7.3 Electrochemistry of stainless steels

To obtain an understanding of the passivity of stainless steels by considering the potential-current density diagram, generally known as a polarisation curve, the specimen is first made to act as a cathode in the electrochemical cell containing the electrolyte. The cathodic potential-current density curve is measured over the potential range defined by E_{corr} and active potential E_c. In figure **2.15**, at E_{corr} the current density approaches zero, in theory intersecting the anodic and cathodic curves at point E_{corr} /i_{corr} should be linear[3].

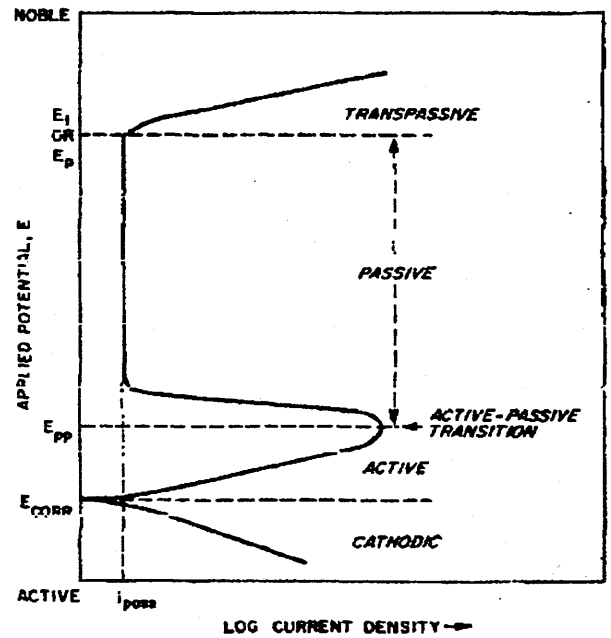

Figure **2.15**, A schematic polarisation curve for a stainless steel in a sulphuric acid solution[3].

Increasing the applied potential in the noble direction away from E_{corr} makes the specimen behave as an anode. The anodic current increases with increasing noble potential, giving rise to the measured anodic curve. Ultimately this current yields at a potential, called E_{pp} (the primary passivation potential) and the measured current ceases to increase with applied potential. The beginning of this decrease is known as the active-passive transition. Above this potential, the current drops to a very low value, i_{pass} (the passive current density) and remains at a low value over a wide range of potentials, this is called the passive potential range of stainless steel[3].

Corrosion rates in this range are very low. On continuing to increase applied potential in the noble direction, another potential is reached at which the measured current will again begin to increase. However, in chloride-containing solutions the current breaks at lower potentials (more active). This break is accompanied by the formation of corrosion pits on the surface of the specimen. Since pitting can perforate and destroy industrial equipment, this passivity range should not be exceeded and the operator of stainless steel industrial equipment should ensure that the material remains in the passive potential range during operations[3].

As this potential depends critically on the corrodent, such as in chloride free aqueous sulphuric acid solution, this potential represents the onset of the evolution of gaseous oxygen by the electrolysis of water. Some metal dissolution also takes place, and is known as E_p or E_t, at this potential representing the onset of the transpassive behaviour.

2.7.4 Characteristics of passive films

An oxide film survey on duplex and standard stainless steels was established in various solutions because of the necessity of knowing the characteristics of such parameters in the current research. Early work by Fontana et al[110] demonstrated an oxide film

thickness of 30 Å or less for various alloys. Frankenthal[130] stated that at low potentials in the passive region, the film measure is around 0.84 nm. Mitrovic et al[13] demonstrated that with a cathodically reduced Fe-26Cr alloy in pH 2.0 H_2SO_4 solution, the passive film surfaces appear to be composed of either a $(Fe,Cr)_2O_3$ type of oxide or an inner layer of Fe Cr_2O_4 and an outer layer of $(Fe,Cr)_2O_3$ depending on the anodising potential. The measured thickness of the anodic oxide films of Fe-26Cr alloy in a pH 2.0 H_2SO_4 solution, were ~17Å (+-5-10%). Similarly, Oltra et al[91] cited the finding of Pue[127] in the case of iron, the passive film consists of an inner layer of Fe_3O_4 and an outer layer of γ-Fe_2O_3 or only of a γ-Fe_2O_3 layer.

Poulson[115] pointed out that there are two general mechanisms of passivation that are postulated: (a) dissolution and subsequent precipitation, and (b) solid state reaction (oxide or adsorption) in parallel with metal dissolution. Castro et al[125] concluded that with iron in static solutions of LiCl no passivation occurs because of acidity build up, which is removed by using a rotating cylinder. Landolt[126] stated that a complete chemical characterisation of passive films in stainless steel alloys involves a knowledge of the elemental composition and of the binding state of the cationic and anionic species present as a function of depth and/or a knowledge of their spatial distribution.

Oranowska et al[128] studied the chemical breakdown of the thin thermal oxide films for stainless steel in aqueous environments containing chlorides and found that at low oxidation rates the sensitivity to pitting decreases for thicker layers; however, the trend was reversed in the case of fast oxidation rates. Meanwhile, Kruger[14] considered four properties of passive films:

Thickness: This is the property that determines how much of a passive film is needed to protect a metal surface from the process that leads to breakdown and the interaction of aggressive anions, e.g. chloride anions. Thickness can play an important role in the breakdown of passivity in at least three ways; (1) determining mechanisms of breakdown, (2) determining the induction period of breakdown, and (3) affecting the rate of repassivation.

Composition: Three instances in which breakdown alters the composition of the film are as follows: (1) breakdown changes the composition of the film (2) defects influence breakdown and (3) hydrogen involved in breakdown.

Foley et al[131] found that if the film was formed in the repassive or transpassive regions it was composed only of oxyhydroxides and even under conditions in which passivity conditions prevailed, oxyhydroxides were observed. This suggests that chloride ions caused the conversion of the spinel oxides to oxyhdroxides. Also film compositions involving hydrogen affect the breakdown process species (e.g. Cl^-).

Structure: This structure can affect the breakdown process by controlling the ability of damaging species to breach the passive layer. Vitreous structures appear to provide the most effective barriers.

Electronic properties: Electronic properties that are related to the ability of the passive layer to bond a damaging species tightly (e.g. those properties that determine the covalent character of a bond) affect the ease of breakdown.

3.0 EROSION-CORROSION

As the published data on the erosion-corrosion of duplex stainless steel (S31803) were scarce other type of stainless steel has been used to highlight the critical issues.

3.1 The history of erosion research

O ruin'd piece of nature! This great world shall so wear out to nought.
(Shakespeare: King Lear) [143]

In this section the reader will be taken through a historical review of the erosion-corrosion process. This was started by Tretheway et al[143] who defined erosion-corrosion as a poetic and self-explanatory name for a form of corrosion which results when a metal is attacked because of the relative motion between an electrolyte and a metal surface. Many examples of this form of corrosion can be attributed to mechanical effects, such as wear, abrasion and scouring. Similarly, Fontana et al[110] suggested that metal is removed from the surface as dissolved ions, or it forms solid corrosion products, which are mechanically swept from the metal surface.

A survey by Finnie[144] showed that the first fundamental studies of erosion were carried out in Germany in the 1930s. They found that both hard and soft steels, alloyed and unalloyed, suffered similar amounts of erosion damage when bombarded with a stream of quartz sand perpendicular to the surface. This contradicted the findings of recent erosion-corrosion research. Practical experiments had shown that ductile material carrying abrasive fluids lasted longer than soft ones. Finnie[145] reviewed the famous names of erosion research, such as Reynolds who wrote a paper on sand blasting in 1873. The first technical papers on erosive wear began to appear at the beginning of this century, and by 1946 Wahl and Harstein published the first systematic survey of erosion and listed 233 references. Attempts to understand the basic mechanisms involved in erosion started after the Second World War and have continued to the present day.

3.2 Mechanism of erosion-corrosion

Erosion-corrosion mechanism were studied by Bitter[150] and Evans[151]. They stated that erosion consists of two types of wear-deformation and cutting wear. When a solid particle strikes a surface, the impact on the ductile material, when the yield strength of the material is locally exceeded, causes plastic deformation in the vicinity of the impact. After multiple impacts, a plastically deformed surface layer may form near the eroded surface, and therefore, the yield strength of the material increases due to strain hardening. Upon further deformation, the yield strength will eventually become equal to its fracture strength and no further plastic deformation will occur. The material surface becomes brittle and its fragments may be removed by subsequent impacts.

Vyas[146] found that the conjoint action of erosion and corrosion involved a combination of mechanical and chemical modes of attack on a material. These are summerisd in some common criteria, such as: (a) *Surface scales*: The structure and morphology of surface scales, the kinetics of scale growth, and the mechanical properties of the scales have a large effect on the rate of erosion corrosion. (b) *Fluid mechanics*: The type of flow (laminar or turbulent) not only controls the mass and erosive species towards and

away from the metal surface, but, at high velocities, can generate surface shear stresses large enough to disrupt the protective scale, exposing bare metal to the aggressive environment. (c) *Particle impact events*: The impact of liquid drop, jet, cavity collapse or solid particles not only deforms the surface and leads to eventual material loss, but can easily crack and cause soft or brittle surface scale to break away. This results in accelerated corrosion at the local exposed areas. Equally, Fontana et al[110] demonstrated that erosion corrosion is characterised in appearance by grooves, gullies, waves, rounded holes and valleys, and usually exhibits a directional pattern. Figure **3.1**, shows the typical wavy appearance of an erosion-corrosion failure. This pump impeller was taken out of service after three weeks of operation. Figure **3.2**, is a sketch representing the erosion corrosion of a heat-exchanger tube handling water.

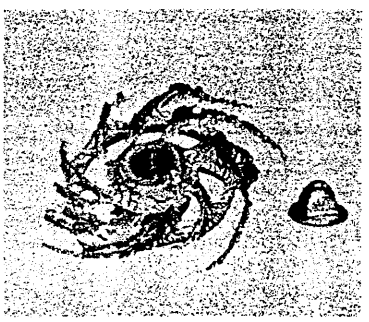

Figure **3.1**, Erosion corrosion of steel alloy pump impeller[110].

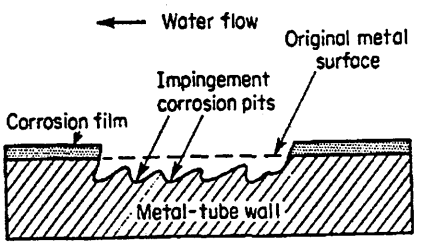

Figure **3.2**, Erosion corrosion of stainless steel condenser tube[110].

Lee[158] evaluated the relative erosion-corrosion behaviour of stainless steel types 304 and 316 in high velocity seawater and found out that velocity affects the performance of many materials. Modification of system design, applying coating and cathodic protection avoid velocity related corrosion problems. Similarly, Jones[111] considered the work of other researchers, and described them schematically. Figure **3.3** shows that turbulent eddies probably thin the protective film locally to account for downstream undercutting.

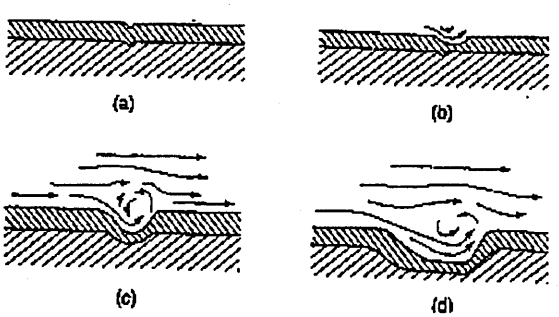

Figure **3.3**, Turbulence eddy mechanism for down stream undercutting of erosion corrosion pits[111].

Bjordal et al[18] carried out experiments on erosion-corrosion properties of duplex stainless steel UNS 31803 by comparing it with thermal spray coating in synthetic seawater containing 0.25% of silica sand. This showed that the wear rate increases as the flow velocity increases. The outcome of Neville et al's[19] study into the erosion

behaviour of SAF 2205 duplex stainless steel for marine pumping applications in 3.5 % NaCl solution demonstrated the complexity of erosion-corrosion in terms of material, environment and hydrodynamic influences. Kwok et al[21] was carried out a material ranking study on the cavitation of erosion of duplex stainless S31803 and super duplex stainless steels in a simulated marine environment (3.5% NaCl solution). This showed that in S31803 cavitation erosion resistance was higher than S31603.

3.3 Mechanical and chemical parameters affecting erosion-corrosion

3.3.1 Velocity of fluid flow

A literature review was undertaken which covered fluid flow velocity as one of the critical parameters in the evaluation of the current duplex stainless steel. Bjordal et al[18] exposed UNS 31803 duplex stainless steel to three different flow rate velocities in synthetic seawater. As shown in figure **3.4**, the material retains its passivity at all flow velocities, but the passive current density increases as the flow velocity increases. Neville et al[19] pointed out that under flowing conditions of 100 m/s in 3.5% NaCl, duplex stainless steel (SAF 2205) showed a positive shift in E_{corr} (by 80 mV) from a potential of + 400 mV, and promoted small reductions in passive potential ranges during anodic polarisation by about 10 mV. Similarly, Fontana[157] and Lee[158] concluded that stainless steel types 304 and 316 under excessive fluid motion (seawater solution) can cause mechanical removal of protective films by impingement of particles or bubbles carried by the electrolyte, by cavitation, or by a shear mechanism.

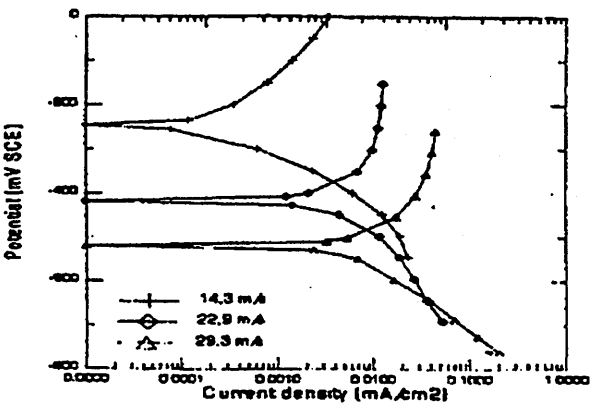

Figure **3.4**, Effect of rotational velocity on the polarisation curves of stainless steel[18].

Tretheway et al[143] reported that when fluid flows across a metal surface it can be imagined as a series of parallel layers, each moving at a different velocity. The lowest layer is adjacent to the metal surface where there are the greatest frictional forces and molecular collisions at surface irregularities, and layer velocity rises to a maximum at some distance into the bulk fluid. This effect is known as laminar flow. Efird[17] stated that when (UNS G10180) carbon steel in NaCl+sodium bicarbonate under CO_2 gas was used, an accurate definition of heat transfer (thermal), mass transfer (chemical) and momentum transfer (physical) characteristics as measured by τ_w is a requirement for describing fluid flow effects on corrosion for any system. However, a research paper by Poulson[115], indicated that at low velocities flow between metal and solution is laminar

and at high velocities it is turbulent. The transition occurs over a velocity range depending on the geometry, the viscosity of the liquid and the roughness of the surface. Nevertheless, the overall transport to the surface consists of bulk convection and turbulent convection which is an exchange of fluid between the boundary layer and the bulk.

Equally, Neville et al[152] reported that in instant ocean solution the effect of high velocity impingement on the corrosion resistance of SAF 2205 duplex stainless steel materials at ambient temperatures may be seen by; lower E_b, evidence of double breakdown on some materials during anodic scans with the first breakdown, E_b, in conjunction with the initiation of pits as shown in figure **3.5**, and more pits in the form of comets evident in static conditions.

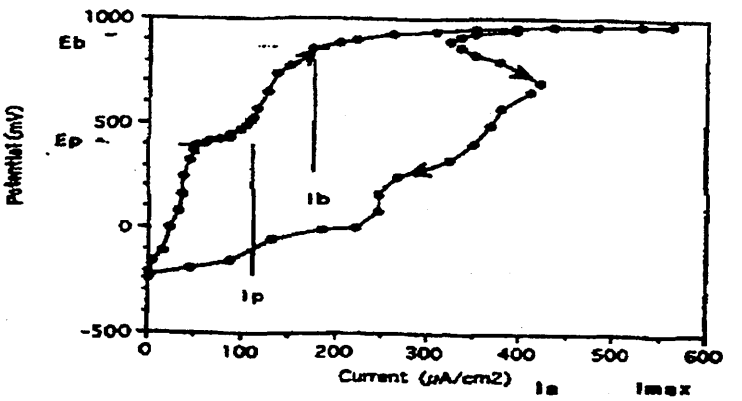

Figure **3.5**, The form of anodic polarisation under erosion conditions at increased temperature (SAF2205 at 30°C)[152].

3.3.2 Solid particle impingement

As the effect of fluid flow velocity with sand particles has a great relevancy to the current study of duplex stainless steel, a short review of the literature was carried out. Heymann[162] concluded that for most ductile alloys, liquid impingement erosion rates vary with about the 5th power of impact velocity, whereas solid particle erosion varies with about the 2.5th power. Liquid impingement erosion is greatest with normal (perpendicular) impacts, whereas solid particle erosion impacts some 60° to 70° away from the perpendicular; and the former exhibits a complicated time dependence, whereas the latter is linear.

Therefore, increases in velocity may increase attacks on steel by increasing the supply of oxygen, carbon dioxide, or hydrogen sulphide in contact with the metal surface, or velocity may increase diffusion or transfer of ions by reducing the thickness of the stagnant film at the surface. Umemura et al[161] demonstrated with 304 stainless steel in aqueous slurries of $NaOH/H_2SO_4$ solution (pH 4) that the active-passive transition potential shifted to more negative values as the particle velocity was increased. Conversely, Stack et al[160] showed that with mild steel in sodium carbonate and bicarbonate solution as illustrated in figure **3.6**, the active dissolution current only slightly increased in the presence of particles, probably due to an increase in turbulence in the slurry.

Neville et al[19] pointed out that drastic changes in the behaviour of the duplex stainless steel material are seen in the presence of sand particles in the impinging NaCl solution. Figure **3.7** shows that the free corrosion potential during liquid solid erosion was considerably more negative (active) than in static or liquid erosion conditions. High currents recorded immediately upon shifting the potential from E_{corr}, a transition to active corrosion in these particularly severe, liquid solid impingement conditions.

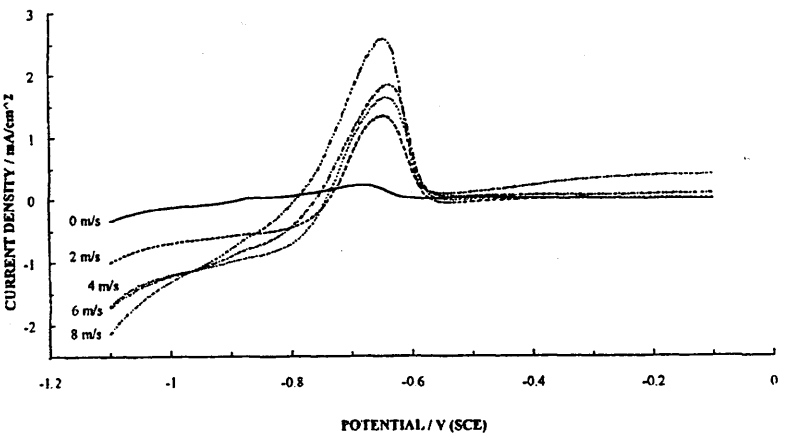

Figure **3.6**, Polarisation curves of mild steel at various fluid velocities in 0.5 M $NaHCO_3$ + 0.5 M Na_2CO_3 containing 300 g l^{-1} alumina (100 μm)[160].

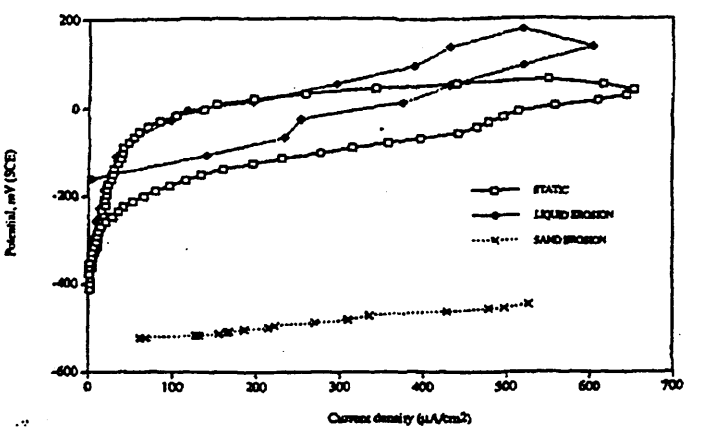

Figure **3.7**, Anodic polarisation on SAF 2205 in NaCl solution at 50 °C[19].

Figure. **3.8** (**a**), (**b**) showed that the effect of sand under cathodic protection (CP) was sufficiently erosive to mechanically remove the protective film from the stainless steel specimen held at + 50 mV from E_{corr} and render it active. Hence increases in current signified the depassivation process and a decrease in current indicates the cessation of slurry flows[19]. Tretheway[143] on the other hand, suggested that the flow may be sufficient to prevent deposition of silt or dirt, which might otherwise cause differential aeration cells in the crevices beneath.

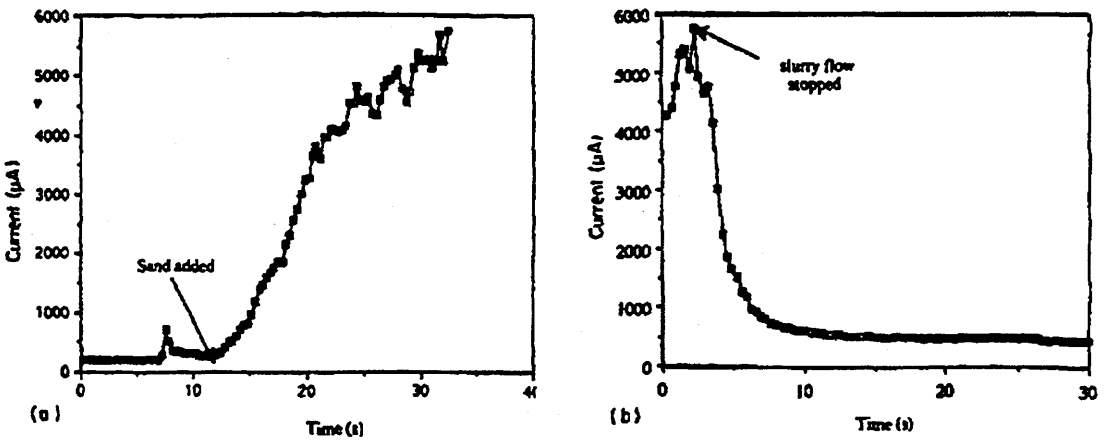

Figure **3.8** (a) Current progression on UNS S31603 as sand in the fluid stream impacts the surface, potential +50mV from E_{corr}. (b) Decrease in current on stopping the slurry flow on UNS S31603, potential + 50 mV from E_{corr}[19].

3.3.3 Hydrodynamic shear stress

A summary of the hydrodynamic characterisitic of water jet systems as applied in the current study is now given. As Dawson et al[22] reported, the adsorption of inhibitor films occurs only in regions of low surface shear stress for mild steel in aerated seawater, with the addition of a mine inhibitor. The effect of increasing fluid velocity is to lower the efficacy of the inhibitor. These conclusions support the concept of critical shear, the minimum force required for the removal of an inhibitor film from a metal surface. Research by Efird[164] showed that some specific alloys were susceptible to a critical surface shear stress in sea water where film breakdown begins and accelerated attack was initiated. When the critical shear stress was exceeded in a hydrodynamic system, the film produced by corrosion of a specific alloy degrades and was physically removed. The shear stress was greater than the binding force of the corrosion product film, this allowed localised corrosion and/ or accelerated general corrosion to occur.

According to Efird et al[17], when utilising carbon steel material in NaCl + sodium bicarbonate solution the wall shear stress was defined as a direct measure of the viscous energy loss within the turbulent boundary layer, and it is related to the intensity of turbulence in the fluid acting on the wall. It is not a force on the wall from the flowing fluid but rather a force within the flowing fluid at the wall.

Figure **3.9**[17, 22] shows the *water jet impingement wall* and the fluid flow shear stress regions established for a circular jet impinging on a flat plate. Region '**A**' shows the stagnation zone with a stagnation point at the centre, the flow is laminar near the plate, and the velocity component is changing from axial to radial, with a maximum velocity and minimum thickness at ~ $r/r_0 = 2$, which is the laminar- turbulent transition point. The stagnation zone is defined as a good mass transfer basis and poor on- wall shear stress basis, because the flow vector changes rapidly as radial distance increases. At Region '**B**' the turbulence rapidly increases with primary fluid flow vector parallel to the plate, and an increasing high wall shear stress existing. In region '**C**' with point $r/r_0 = 4$, the bulk flow rate and turbulence decay rapidly as the thickness of the wall jet increases momentum transfer away from the plate.

Region '**B**' mathematically characterised from published research demonstrated that wall shear stress is proportional to the velocity squared. Efird cited Giralt and Trass studies suggested that shear stress caused in the wall jet was calculated using jet radius from the following equation

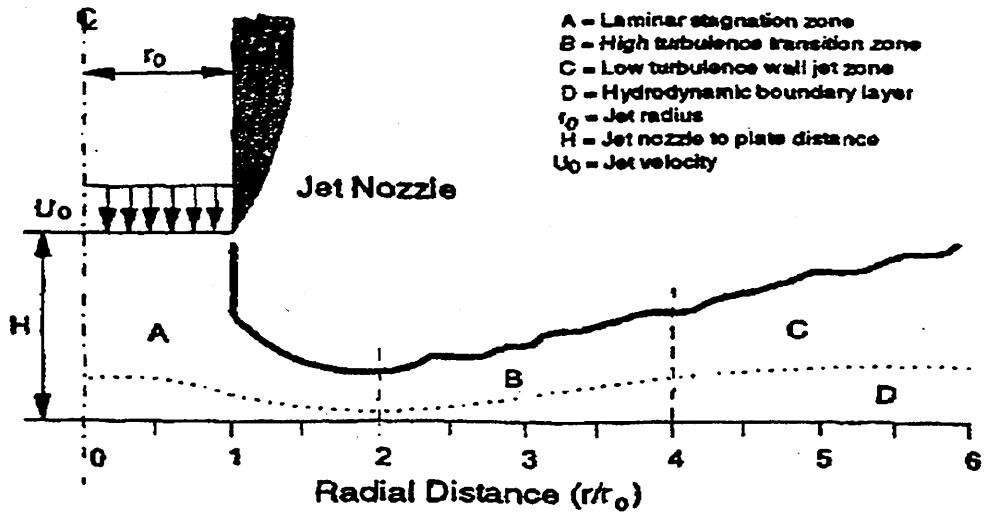

Figure **3.9**, Hydrodynamic characteristics of jet impingement on a flat plate showing the four characteristic flow regions[17, 22].

$$\tau_w = 0.179\,\rho\,U_0^2\,Re^{-0.182}\left(\frac{r}{r_0}\right)^{-2.0} \qquad (5)$$

Where

ρ : density (Kg/m^3)

U_0 : velocity of jet (m/sec)

Re : Reynold number at the orifice

r : radial distance from the centre of jet (m)

r_0 : radius of jet (m)

τ_w : wall shear stress (N/m^2)

ν : kinematic viscosity (m^2/sec)

The jet Reynolds number is defined as:

$$Re = \frac{2r_0U_0}{\nu} \qquad (6)$$

in Region '**C**' which is amenable to mathematical characterisation, because momentum transfer and fluid entrainment are in the opposite direction to the pipe flow.

3.3.4 System flow geometry

Changing the water jet impingment piping system diameter in the current study has a large effect on the erosion-corrosion process of duplex stainless steel material. This was reviewed by Postlethwaite et al.[168], who used a segmented test cell containing a sudden constriction, a sudden expansion, and a groove to produce disturbed flow conditions. Erosion rates for UNS S30400 stainless steel in seawater solution with silica sand were reduced by changes in the cell wall geometry that resulted from erosion further downstream because of the reduction in turbulence and particle dispersion. Neville et al[19] reported that even small changes in the geometry of a system can induce turbulence flows (vortices, eddies,etc) which will, in turn, cause hydrodynamic instabilities in the system.

3.3.5 Impact particle characteristics

3.3.5.1 Size

During SAF 2205 duplex material experimental evaluation a constant sand particle size range was chosen. Hence, the effect of particle size is the most puzzling aspect of erosion and abrasion of ductile materials, as the efficiency of erosive wear or abrasive wear decreases as particle size decreases below about 100 μm. Particles of about 10μm size are about 1/4 as effective as 100 μm particles[145]. Heymann[162] determined no obvious explanation for this phenomenon and a given total amount of liquid does less damage if divided into smaller drops, even though this implies a greater number of impacts on the surface. The erosion rate increases with tempering temperature for impacts at 100 m/s and a rough correlation with the yield strength and fracture strain is found. That is, erosion rate decreases with increasing yield strength and decreasing fracture strain.

3.3.5.2 Shape

Masden[171] found when testing 316 stainless steel with the addition of 0.06M Na_2SO_4 to the slurry, that recycling a sand slurry in a slurry pot tester led to reduced erosion rates and that this could not be attributed to a reduction in particle size. He concluded that 'micro-polishing' of the particles was responsible. In the mean time, in the current study the sand was not re-used for follow up experiments.

3.3.5.3 Surface finish

The sand particle used were semi-subangular in shape. Scanning electron microscopy was used on sand particles before and after sand slurry flow loop on UNS S30400 stainless steel. The difference became obvious at higher magnification (*2,000x*), the particles' rough edges were sheared during exposure. Hence particles with high micro-roughness eroded the metal at high rates by a cutting action of the micro-edge. For particles with a smooth surface, the erosion mechanism changed to a ploughing action in which individual particle impacts caused indentations and extrusions on the metal surface that were forged and broken off by successive impacts, resulting in much lower erosion rates [168]. Postlethwaite[23], in his classic analysis of erosion phenomena for carbon steel in a $K_2\ Cr_2O_7$ inhibitor, reported that surface roughness due to corrosion increases the local angle of impact of the slurry particles and hence greatly increases the erosion rate. Therefore, a *Cr* inhibitor-induced reduction in the corrosion rate also reduces erosion due to the resulting smoother surface.

3.3.5.4 Effect of particle concentration

Sand particle concentrations are considered to be one of the main parameters in the current experiment. As result, a literature survey was undertaken. Many authors[123, 171, 173, 174,] have reported that slurry erosion rates increase with increasing particle concentration. The decreased effect with increasing particle concentration is due to particle-particle interaction[123, 171]. Blatt et al[174] found that with ferrite austenitic steel (22% Cr, 5.3% Ni) in water contains which 3.8% NaCl, 0.44% $CaCl_2$, 0.07% $MgCl_2$ under 2 bar of CO_2 gas that erosion rates varied linearly with the particle concentration from 0 mass % to 0.5 mass % for fully developed pipe flow. Figure **3.10** shows the consequent results of three continuous 24 hour experiments with 2 vol %, 5 vol %, and 10 vol % sand on stainless steel type 304 (UNS S30400) in seawater solution. Erosion rates increase by a factor of about 2.5 within the concentration range of 2 vol % to 5 vol % and by only 20% within the range 5 vol % to 10 vol %, both in the constriction and at the maximum downstream of the reattachment in the expansion. The nonlinearity was attributed to particle-particle interference[168].

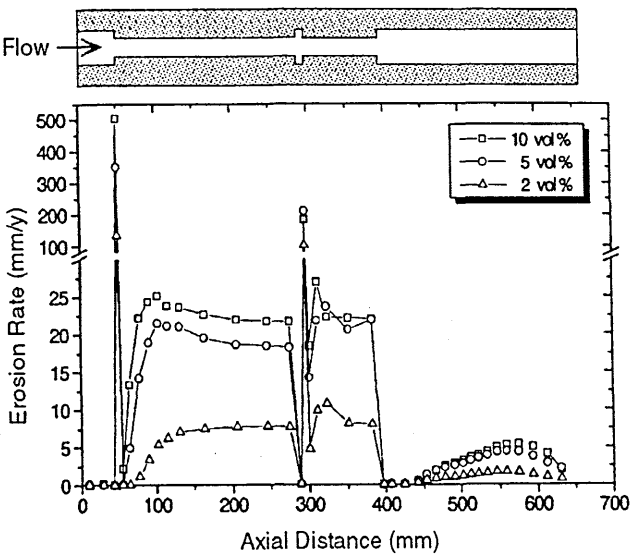

Figure **3.10**, Effect of sand concentration on erosion rates after a 24 hour run[168].

3.3.5.5 Geometry of crater

Sand craters have a great relevance to the erosion-corrosion modelling section of this current study. Therefore, an overview by Neville et al[19] is discussed. Figure **3.11** shows a macroscopical plan view of the wear scar produced on duplex stainless steel SAF 2205 in 3.5% NaCl solution with a clear mechanical removal of the material. In the central area where the jet nominally hits the specimen at 90° incidence, the appearance of the metal loss area is in the form of small indentations. Contrast this with the directional ploughing of the material and long, deep troughs found at the outer areas where the flow is in a radial direction.

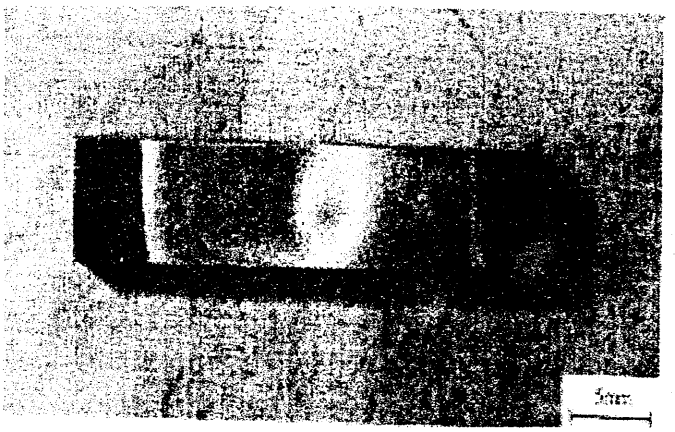

Figure **3.11**, Plan view of SAF after liquid solid erosion at 50°C in 3.5% NaCl. The lighter circle in centre of specimen represents depressed surface of wear shear region[19].

3.3.6 Angle of impact

A review was developed on the effect of different angle of impacts on erosion-corrosion rate. This is relevant to the 90° impingement angle of the nozzle in the water jet impingement system on the duplex stainless steel material. Finnie[145] suggested that at low grazing angles the particle strikes the surface, forms a crater and then leaves the surface (figure **3.12** curve 1). Different angles leave the material piled up at the sides or end of the crater. As velocity increases the particles dig deeper, the resultant force on the particle changes position and the rotation decreases, this leads to additional volume removal. At an angle of α=20° only 1/6 of the plates removed a chip without leaving material piled up on the eroded surface. Moving to higher angles, the particle comes to rest in the surface while cutting and material is piled up around and ahead of the particle.

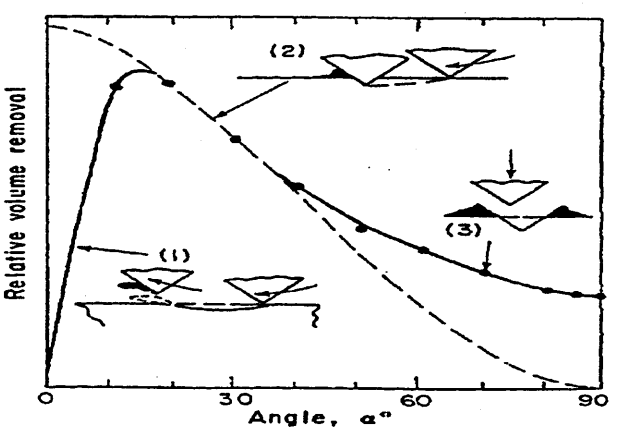

Figure **3.12**, Predicted variation of volume removal with angle curves 1 and 2 experimental values (curve 3 and data points) normalised to same value of maximum erosion[145].

This predicts a $\cos^2 \alpha$ curve 2 in figure **3.12**. At 90° the surface becomes roughened by many impacts so that subsequent particles strike the surface with a distribution of

impact angle[145]. Clark and Wong[176] found that the peak value of cutting wear for UNS 31803 in 3.5% NaCl solution correspond to impact angles between 20° and 25°. Chevallier et al[178] pointed out that the impact of particles on a surface of 38CD4 steel (pearlite-ferrite microstructure) can cause severe erosion damage, dependent upon the number of particles striking the surface, their velocity and their direction relative to the surface.

3.3.7 Effects of oxygen

Aeration parameter in the electrochemical measurements influences the results of cathodic and anodic reactions of duplex stainless steel material. Therefore, a summary of the recent research is discussed in this section. A mitigating factor for differential aeration cells was the replenishment of O_2. Stainless steel usually has improved corrosion resistance in electrolyte flowing above a given minimum velocity because the replenishment of oxygen maintains the protective oxide films[143]. Master[112] reported that if the cathodic curve in stainless steel in seawater solution is sufficiently polarised (shifted down and left) then the anodic/cathodic curve intersection which defines E_{corr} can drop into the high current potential region termed the active range (figure **3.13**). Cathodic polarisation can be caused by a decrease in reducible species such as oxygen.

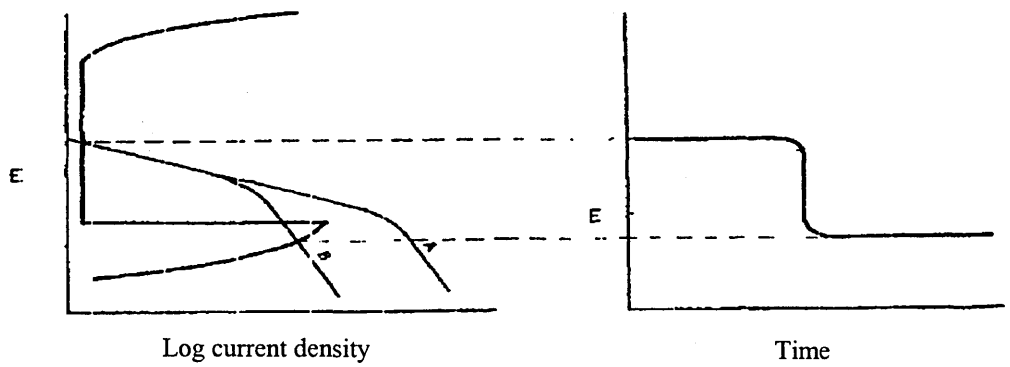

Figure **3.13**, Depassivation of stainless steel due to cathodic polarisation (A) Oxygenated. (B) De-oxygenated[112].

3.3.8 Effect of chloride

As a seawater electrolyte is being utilised in the investigation of SAF2205 duplex stainless steel, the effect of chloride ions and concentration was considered. Zhang et al[99] examined the acceleration of corrosive wear of duplex stainless steel by chloride in 69% H_3PO_4 solution; as the Cl^- content increases, the corrosion potential shifted to more negative values. The recovery of passive film may be retarded by Cl^- also increasing the density of defects in the wear subsurface. The development of dislocation and pitting is the initiation source of corrosive wear. Tretheway[143] suggested that a detrimental effect of increased flow rates was the replenishment of aggressive ions such as chloride.

Additionally Miura et al[38] stated that at high chloride contents above about 10%, in a sour gas environment the 22% Cr duplex stainless steels are particularly susceptible to cracking especially in the critical temperature range around 80°C. In the mean time Neville et al[20] demonstrated that the principal mode of corrosion attack on superduplex

stainless steel (UNS32760) in high chlorine concentrations was crevice corrosion. Figure **3.14** shows that at the lowest chlorine concentration, the potential attains a steady value of +600-650 mV (SCE). In contrast, an ennobled E_{corr} of 550 mV (SCE) was attained in seawater dosed with 400 ppm total chlorine, but after 30-35 hours it had fallen to a more active value. E_{corr} fluctuated, reaching positive values in excess of +500 mV (SCE) and active values of 0 mV (SCE). At total chlorine levels of 550-600 mV (SCE), the free corrosion potential, ennobling initially to +500 mV (SCE), maintained the value for only approximately 24 hours before a sharp fall in the potential was recorded[20].

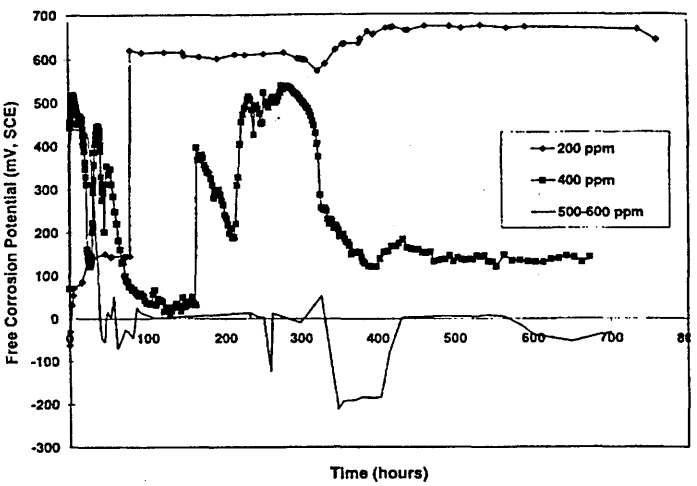

Figure **3.14**, Free corrosion potential (Ecorr) of pipe containing girth weld during one month's test in sea water containing 200 ppm, 400 ppm and 500 ppm to 600 ppm chlorine[20].

After one month's immersion in the 200 ppm solution, there was no evidence of any attack at the weld section. At the intermediate concentration (400 ppm), again no corrosion was detected but a small number of possible pitting initiation sites were seen. The highest concentration of 500-600 ppm induced significantly enhanced corrosion attack, not at the weld but at the artificial crevice, between the pipe and the flange. In addition, tests in hypochlorite containing seawater revealed that the attack was intergranular. Progressively increasing the concentration of hypochlorite had the effect of decreasing the breakdown potential. Interestingly, prolonged exposure had the effect of increasing the E_b value[20].

3.3.9 Synergistic effect

The synergistic effect review is essential to this study in order to identify the contribution of both mechanical erosion and elecrochemical corrosion processes on the erosion-corrosion process of duplex stainless steel. Erosion-corrosion is a synergistic process in that the metal lost in erosion-corrosion is greater than the sum of the metal lost when erosion and corrosion out separately. Pure erosion and corrosion rate and the corrosion rate under erosion must be measured carefully for accurate evaluation of synergitic effects in erosion corrosion. A study by Kosel[54] separates the synergistic regime between pure erosion and pure corrosion into two categories:

(1) Erosion enhanced corrosion (EEC), in which the impact damage zone is confined within a thick scale. The EEC causes increased metal thickness loss rates because erosion reduces the scale thickness and increases the corrosion rate, which is controlled by transport of metal or corrosive elements. Scale spallation can also be involved.
(2) Corrosion affected erosion (CAE), in which the damage zone includes a combination of both scale, metal and embedded erodent particle fragments. Although it appears to produce the highest loss rates, the mechanism is still not fully elucidated.

The sequence of increasing severity of corrosion relative to erosion is as follows: (1) erosion. (2) CAE, (3) EEC, and (4) corrosion. Rashel et al[37] described these categories, and figure **3.15** schematically illustrates these different regimes.

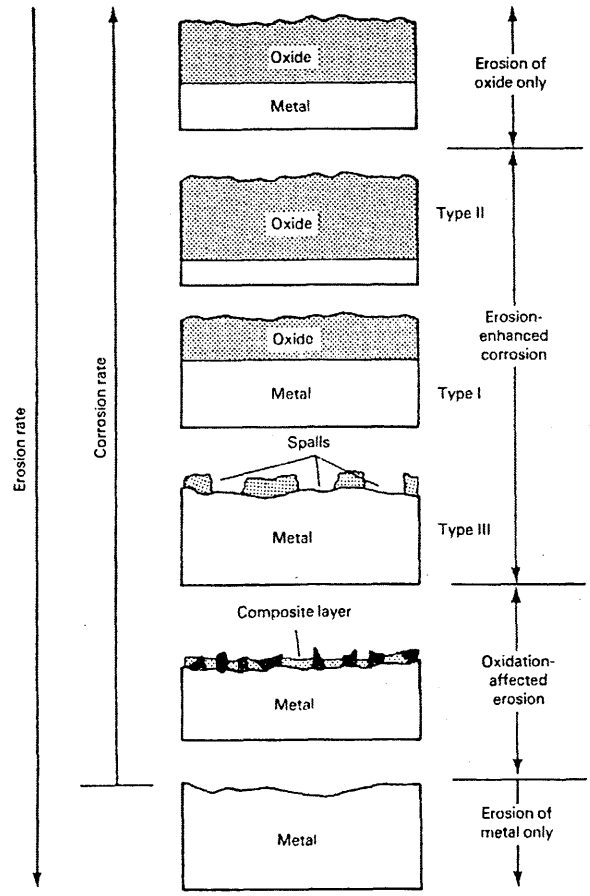

Figure **3.15** Erosion/corrosion interaction regimes shown in order of increasing severity of corrosion relative to erosion. Type I, II, and III regimes are subdivisions of EEC[37].

Pure erosion: occurs when the corrosion rate is negligible compared with the erosion rate, as in severe erosion conditions.

Corrosion affected erosion: a thin scale is developed, but the stress introduced by the particles is greater that the scale thickness, so that both scale and metal are deformed. The metal loss rate (the metal, scale and erodent particle fragments) is increased over pure erosion. Here the metal is repeatedly exposed to corrosion.

Erosion enhanced corrosion: this is broken down into three categories. The first two involve a steady thickness which is determined by erosion and corrsion rates, and the third involves spalling of the scale. During EEC, if a continous protective scale is maintained without spalling, scale is removed from the outer surface and depends on erosion conditions. However, if the specimen is exposed to simultaneous erosion-corrosion, scale builds up to a normal base thickness, while if it is peroxidised to a thickness larger than the base thickness and then erosion begins, this new thickness decreased until the base thickness is reached.

In Type I (EEC) the scale rate is essentially unaffected by the presence of erosion as postipulated by Chang et al[170] when Ni and Nb were investigated under erosion-oxidation condition. Type II (EEC) in this case the presence of erosion actually increases the scaling rate, as in low chromium steels in methane/air mixtures the scale thickness after E/C was about 50% greater than that for free corrosion[82]. Type III (EEC), is the erosion-induced spalling of the scale which enters as an additional scale loss mechanism, resulting in a very thin or absent scale and a high corrosion rate. Spalling was included in the EEC regime because it is a mechanism of discontinuous corrosion rate.

Pure corrosion: in this regime the ratio of corrosion to erosion rate is very high, resulting in pure corrosion. However, for a thick scale in the presence of erodent particles, its important to realize that unless the scale erosion is actually zero, there must always be a steady state scale thickness. Even though this thickness may be large, a constant rate of metal thickness loss would be expected with a constant scale thickness. Whereas for free corrosion the rate of metal thickness decreases continuously unless scale spalling occurs above a critical thickness.

Similarly, Stack et al[160] studied the synergistic effect of the erosion and corrosion of mild steel (BS6323) in sodium carbonate and bicarbonate solutions. They identified the transitions in erosion-corrosion regimes at room temperatures and found that corrosion rate was enhanced significantly by erosion, but the mechanism of the effect of erosion on corrosion depended upon applied potential.

Figure **3.16** indicates that at low potentials and low velocities in cathodic conditions, neither erosion nor corrosion occurs. At high velocities, plastic deformation takes place and therefore a transition to "pure" erosion occurs. As the applied potential is increased, and the dissolution of metal initiates, the transitions between the erosion-dissolution regimes are achieved by variation of particle velocity and applied potential. Increased velocity shifts the "erosion-dominated" regime to higher potentials because the corrosion as a function of increasing potential increases in this region. A similar phenomenon applies in the passive region, although the boundaries are less dependent on potential because the passive film thickness does not increase significantly with increasing potential in this case.

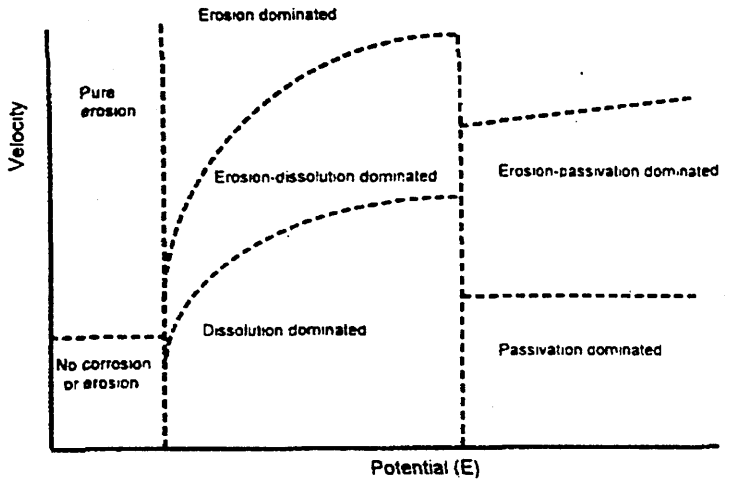

Figure **3.16**, Schematic diagram of an aqueous erosion-corrosion map for Fe in NaHCO3/$NaCO_3$ where the transitions between the erosion-corrosion regimes are given as a functions of velocity and potential[160].

Zhou et al[97] measured the total erosion-corrosion rate and the corrosion rate in the presence and absence of erosion for mild steel in sodium carbonate and bicarbonate buffer solution over a range of potentials and rotation velocities. The results show that corrosion rate increased with the introduction of erodent because of the effect of erosion on corrosion kinetics. The total erosion-corrosion rate under active dissolution and passsivation conditions was the sum of the pure erosion rate and the measured corrosion rate, suggesting that corrosion has no significant effect on the erosion process. However, in the active to passive transition regime, there were some synergistic effects attributed to erosion. In particular mechanical damage was enhanced by corrosion. Madsen[171] found that the amount of erosion was 63.4%, corrosion 1.2% and the synergism was 35.4% for 316 stainless steel in 0.06M Na_2SO_4 solution.

Zhiming et al's[65] results showed that cathodic protection could significantly decrease the erosion-corrosion rate of AISI 321 stainless steel in 10% H_2SO_4 +15% corundum sand. The more negative the cathodic potential, the greater the protection efficiency. Whereas, Burstein et al[77] found that the synergistic effect between erosion and corrosion for 316L stainless steel in 0.6M NaCl solution was enhanced more by oblique angle of impact of 40° and 50°, whilst the erosion corrosion rate is higher than the erosion rate alone at all tested angles.

3.3.10 Influence of temperature

Changes in temperature are reviwed. These have a direct effect on the erosion-corrosion process of the experimental duplex stainless steel. This was studied by Neville et al[152] who demonstrated that in a temperature range of 18-60°C for the electrochemical polarisation of SAF2205 duplex stainless steel alloy under static sea water conditions, loss of passivation was caused by:

- The lower resistance of duplex stainless steel due to a lower breakdown potential.
- Reduction in passive range of the material.

- Depolarisation of the oxygen reduction cathodic reaction. This indicates higher corrosion propagation and enhanced pit propagation.
- Changes in the relative corrosion performance of the material.

As temperature increases under impingement conditions the effects were illustrated by[152]:

- Pitting attack initiated at a relatively negative potential, E_p.
  From comparison between impingement conditions and static water:
- Pit depths were lower at the same temperature signifying retarded localised corrosion propagation.
- Repassivation occurred at a more positive potential than in static conditions after reversal of the anodic scan.
- At high temperature and high velocity the duplex stainless steel loses resistance to passivity breakdown as the temperature exceeds 40°C.

Bardal et al[138] showed that in natural seawater the formation of a biofilm on the surface of S31803 has an influence on the local corrosion initiation tendency and propagation rate at temperatures up to 30°C-40°C. Carranza et al[42] found that the passive film formed on alloy 800 (20.5% Cr, 32.5% Ni) in 0.1 M NaCl solution became more porous, and hence less protective, with increasing temperature (150°C). Under anodic behaviour the passive zone showed an increase in current density with an increase in temperature due to the nucleation of pits on the metallic surface. At low temperatures reduction of oxygen predominates whereas at high temperatures reduction of hydrogen ions coupled with higher anodic current density determines a mixed potential. This is equilibrium potential for hydrogen evolution. However, at 150°C, the loss of film protectiveness is more pronounced in chloride solutions.

Kim et al[169] confirmed that the erosion rates for AISI 403 stainless steel at normal incidence were 1.89, 3.2, and 3.59 mg/g for 390, 520, and 610°C tempering treatment conditions, respectively. A study by Angelini et al[31] illustrated that the highest weight loss was found with AISI 304 specimens immersed in bidistilled water in room temperature; a decrease in mass of 2.2 $\mu g/cm^2$ after the first year of immersion.

On the other hand, the study on heat exchangers (mild steel in sodium carbonate and bicarbonate buffer solution) by Stack[30, 160] concluded that at room temperature erosion was dominant. As the temperature increased, the oxidation rate increased and started to influence the erosion process. The increase in weight loss with increasing temperature was attributed to loss of oxide in addition to the underlying metal. This marked the transition to erosion-corrosion–dominated behaviour. At the critical temperature the overall weight loss started to decrease with increasing temperature. This identified the transition to the corrosion-dominated regime. A similar phenomenon has been observed by Matsumura et al[172] when testing the austenitic stainless steels AISI 304 and 316 for the resistance of the passive film at elevated temperature in aqueous slurries.

According to Kim et al[59], the passive current density increased ~ 100 times, and the passive potential region became narrower as temperature increased from 25°C to 75°C on duplex stainless steel SAF 2507 in 3.5% NaCl solution. No pitting was observed from any of the specimens tested at 25°C. However, all specimens tested at 75°C

showed indications of severe pitting corrosion. Cristofaro et al[50] tested super duplex stainless steel in a boric-borate buffer solution with and without chloride additions at different temperature and found that temperature increases improve the stability of passive films and a thicker chromium-bound water depleted film is produced when the in the range of 23°C to 60°C.

3.4 Erosion corrosion rate measurements

Stack et al[160] used electrochemical techniques to measure erosion-corrosion events. The steady state current density i_E during erosion can be approximated by the following expression:

$$i_E = \alpha \int_0^{\frac{1}{\alpha}} i(t)dt \qquad (9)$$

Where α is the fraction of bare surface area exposed by erosion per second, and $i(t)$ is the current density transient due to repassivation of the bare area. Clearly,

$$\alpha = fa \qquad (10)$$

Where f is the number of impacts per unit area per second, and a is the mean area of bare metal produced by an impact.

At low particle concentrations, f can be measured directly by counting current spikes, and the distribution of values of (a) follows from the height distribution of these spikes. Elastic collisions will be common at low velocities, and will normally give no current transient. The distribution of (a) values was due to the distribution velocity component of the particles normal to the electrode surface in the turbulent flow, and also to the variable geometry of the impact.

If particle size increases, the frequency with which a given particle hits the surface is reduced, but the kinetic energy of its more energetic impacts is increased. This analysis may be modified at low particle velocities, where the main effect is plastic indentation rather than metal removal.

Kim et al[169] reviewed the work of other researchers on tempered AISI 403 stainless steel and pointed out that the erosion rate of these steels tends to increase with an increase in tensile strength, whilst Finnie et al[137] found that the erosion rate of ductile materials is independent of either the impact or fracture toughness. Eventually, Boese et al[136] determined surface removal rates from the mass loss at free corrosion for X5CrNi (25% Cr, 6% Ni) in sodium suphate solution and at polarisation in the passive region in tribocorrosive processes. As mentioned by Lindsley et al[121], for heat treated iron-carbon alloy (0.2 to 0.4 wt %) the erosion rate is dependent on the depth of deformation and the increase in surface hardness. It was found that erosion resistance increased as the microstructural features decreased in size, with the microstructural variables being carbide spacing and ferrite grain size. These variables control dislocation motion in the ferrite and, in turn, affect the plastic deformation and erosion resistance of the spheroidised alloys.

The rates of active corrosion were calculated for duplex stainless steel SAF 2205 in 3.5% NaCl solution by evaluating the corrosion current, I_{corr} of actively corroding specimens by the well known Tafel extrapolation technique on potential vs. log current plots. The corrosion rates can be calculated via Faraday's Law from the I_{corr} data[19]. It is well known that in stainless steels materials, the current density of 1 $\mu A/cm^2$ developed during polarisation measurement is equivalent to 0.01 mm/year of the corroded material[111].

4.0 REVIEW OF EROSION-CORROSION TECHNIQUES

This section reviews various erosion corrosion experimental techniques with a focus on the water jet impingement nozzles and cell designs, which enhances the knowledge geometry of the cell and nozzle in the current project.

4.1 Water jet impingement systems

Esteban et al[163] confirmed that the advantages of water jet impingement systems are:

(1) The fluid flow is well characterised. The hydrodynamic shear for the impinging jet system in the stagnation region is a linear function of radial position, and can be measured through a sensitive electrochemical technique.

(2) Mass transfer to the disc is uniform. Limiting the electrode size to within the stagnation region prevents the establishment of differential oxygenation cells and aids in the interpretation of experimental results.

(3) The electrode is stationary and allows use of in-situ determination of film thickness by ellipsometry.

The jet impingement test can reliably and repeatedly simulate high turbulence conditions at high temperature and pressure for gas, liquid, and multiphase turbulent systems, and is most amenable to the use of electrochemical methods. It requires relatively small volumes of test fluids and is easily controlled. Limitations are the difficulty in accurately machining and assembling the test samples, the relatively small sample size and the inability to measure weight loss accurately[17, 105]. This was because the specimen was cold moulded, and the weight of the mould epoxy, even if it is dried, could absorb some water which alters the finite measured weight loss. In addition, specimen removal from the electrolyte could lead to the removal of a fragile poor adhesion oxide film, which affects weight loss measurement accuracy.

As reported by Shreir[153], the method most commonly used for testing condenser materials is the BNFRA May jet impingement test. Small sections of tube, abraded to a standard finish, are immersed in seawater and subjected to an underwater jet of seawater containing air bubbles. Poulson[115] suggested that it is possible to examine corrosion under highly turbulent conditions, allowing a variety of nozzle and specimen types to be used as shown in figure **4.1**. The three nozzles illustrated include the conventional jet which produces a wide range of mass transfer rates across a specimen, a similar jet with a larger diameter producing relatively constant mass transfer across a small specimen under laminar conditions and finally a specimen under conditions of equal mass transfer with laminar or turbulent conditions.

Efird et al[17] showed that in the jet impingement apparatus (Figure **4.2**) the test cell was non-metallic with a machined centre hole. The auxiliary electrode was fixed to the end of the jet cylinder before the centre hole was drilled. The test sample is made of two thick concentric rings, separated by a nonmetallic spacer, and held in position by a probe with threaded back section to allow for adjusting the distance between the

working electrode and the jet. The working electrodes were centred at $r/r_o = 3$, and $r/r_o = 5$.

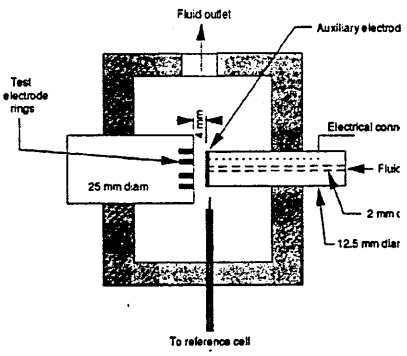

Figure **4.2**, Schematic diagram of the jet impingement test cell[17].

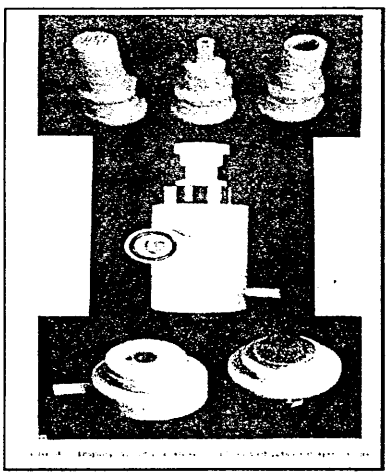

Figure **4.1**, Variety of nozzle types for water jet impingements[115].

Campbell[80] pointed out that in evaluating condenser tube materials, the test apparatus should accommodate all materials as in the manufactured condition. The general arrangement of the apparatus is shown in figure **4.3**.

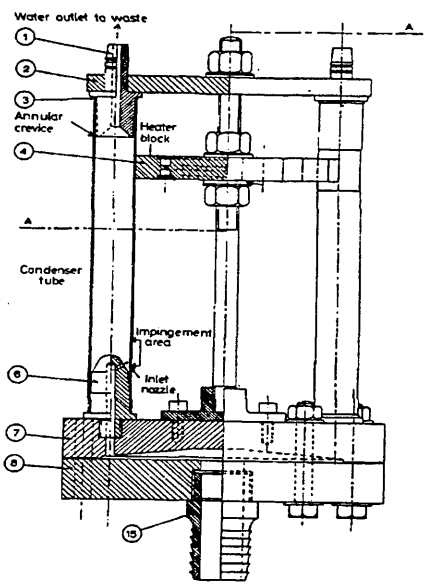

Figure **4.3**, Campbell test apparatus for determining the various forms of attack that the condenser tube materials are subjected to during service[80].

It accommodates 10 vertical condenser tubes spaced equally around a circle. Water enters the bottom of each tube through an inlet nozzle (Part No. 6) which fits inside the tube. The nozzle has a hole set at 45° to the vertical, through which the water emerges and impinges on the wall of the tube. The water then rises up through the tube and leaves through an outlet nozzle (Part No.1). The 10 inlet nozzles are fed with water

through a distributor (Part Nos. 7, 8 and 15) of the design used in the May jet impingement apparatus. The top part is fine machined externally to fit a semicircular notch in a brass heater (Part No.4), the tubes being held in contact with the block by a circumferential clip to ensure efficient and equal heat transfer between the block and each tube. Recent studies by Efird et al[17] and Liu et al[105] correlated a single phase, aqueous, sweet corrosion of carbon steel in turbulent pipe flow with corrosion in jet impingement and rotating cylinder laboratory tests.

4.2 Pipe flow apparatus

A pipe flow test cell was made of a circular flow test section. A stabilising section was installed before and after the test section. All sections had the same internal diameter and were connected together using flanges and O-rings. The differential pressure measurement allowed the flow rate and wall shear stress to be determined. Ring electrodes were used to make electrochemical measurements, and the working electrode was accurately machined with a centre hole of the appropriate diameter, which was located between the auxiliary and reference electrodes as shown in figure **4.4**[17].

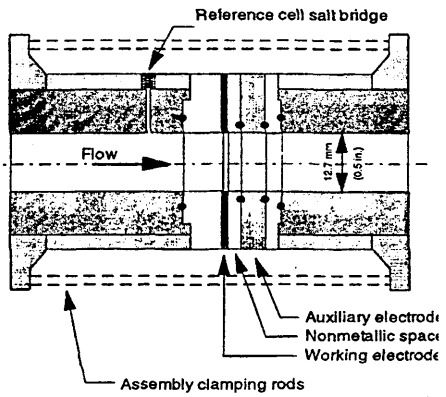

Figure **4.4**, Schematic diagram of the parallel flow (pipe) test cell, showing the electrode placement and locations of the reference salt bridge[17].

4.3 Rotating cylinder electrode

The Rotating Cylinder Electrode (RCE) test system was described by Efird et al[17], as compact, relatively inexpensive, and easily controlled. It provides stable and reproducible turbulent flow and requires relatively small volumes of test fluid. It creates three-dimensional boundary layer flow in a simple system, and is an ideal tool for the study of complex reaction systems, but cannot be used for high pressure or high temperature applications, or for gas and gas/liquid systems. It has relatively low turbulence limits.

Poulson[115] considered that the advantages of rotating systems are convenience based, i.e. they are small, cheap and easy to use. The advantages of flowing systems are the ability to test representative geometries and realistic materials, and the ability to maintain a constant environment, if this is desirable. Efird et al[17] showed that the rotating cylinder test cell produces rotational speeds of 0 rpm to 10000 rpm. The test

cell, shown in figure **4.5**, is made of polypropylene with threaded holes for the electrodes and a combined liquid/gas inlet and outlet, and thermowell. The test specimen was a cylinder of 12.7 mm by 7.5 mm in length, with baffles fitted at 60° in the lower surface of the cover to minimise vortex formation and axial flow[17].

For experiments under fixed environmental conditions (i.e. one electrode and constant O_2 concentration, temperature, and solution composition), the equation relating I_{lim} for a mass transfer controlled reaction to the electrode rotational rate (ω) was expressed as:

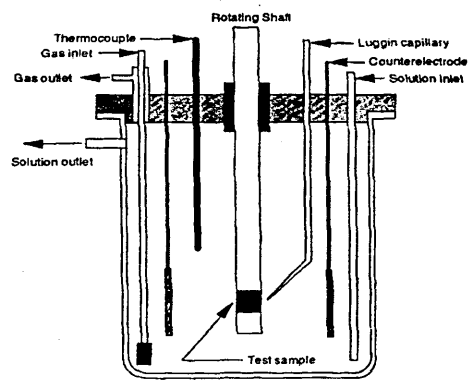

Figure **4.5**, Schematic diagram of the rotating cylinder test cell (baffle not shown)[17].

$$I_{lim} = K\,\omega^{0.7} \qquad (1)$$

Where K is a constant[17].

It has been shown by Liu et al[105] that pipe corrosion can be predicted using rotating disc disc data and the data produced using a theoretical model was in good agreement with experimental results. Bjordal et al[18] described an arrangement of RCE in which two cylinders were placed in a steel tank. One cylinder is fixed to the bottom of the tank; the other one is fixed to a rotor and rotates inside the stationary one. Between the cylinders there is a 4 mm gap. The inner wall of the outer cylinder is divided into 7 rings. The 5 rings in the middle are the test specimens; all the test specimens are electrically insulated from the others, and connected to an electrical contact. A saturated calomel electrode was connected to a tube placed in the tank beneath the rotating cylinder.

Eventually, Zhou et al[97] suggested a modified RCE system arrangement (figure **4.6**). The inner cylinder was constructed of nylon mounted onto a type 304 stainless steel shaft 9 cm long and 3.8 cm in diameter. The sample was mounted in the middle section of the inner cylinder; electrical connection was made via a spring connected to the rotating shaft. Both ends of the inner cylinder were extended sufficiently to avoid any end effects. A PTFE washer was used to prevent any crevice corrosion of the specimen. The outer cylinder inner diameter was 6 cm and it was 16 cm long, giving a capacity of 200 ml.

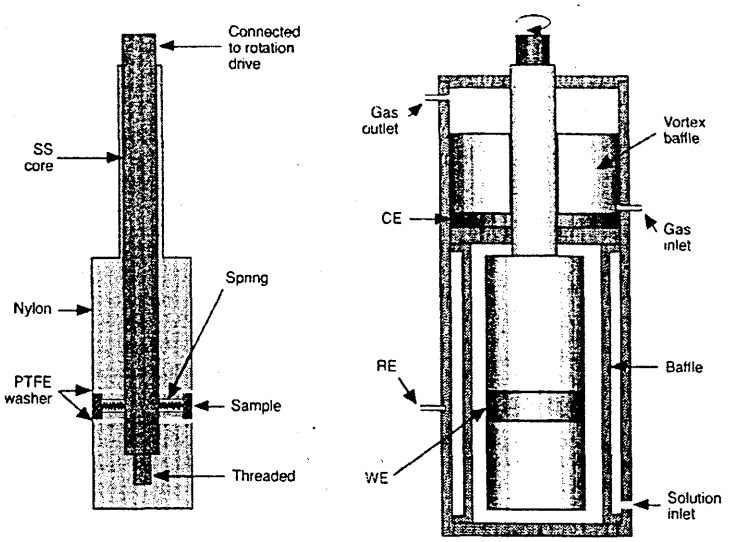

Figure **4.6**, Schematic of the RCE apparatus (RE, reference electrode)[97].

The cell was divided into two compartments, the top section was 6 cm long, and the bottom section was 10 cm long. A cover was mounted between the two sections and immersed in solution to prevent erodent particles flowing to the top, and bubbles to the bottom. Four baffles, 90° to each other, were mounted on the cover to minimise vortex formation. Six baffles were mounted symmetrically in the annular gap between the outer and inner cylinders to increase turbulence of the flow and impact angle of particles. A platinum counter electrode and SCE were placed in a side arm outside the outer cylinder.

In the rotating disc system described by Fontana et al[110], the specimens were hung in the tank for comparison between low velocity and the high velocity to which the disc is subjected. The liquid or slurry in the 150 litre glass lined tank is recirculated and pumped directly into the face of the rotating disc system. The discrepancy between Chin et al[72] and Estaban et al[163] in cell method design is that a disc electrode that is large enough to extend into the region where stagnation flow theory does not apply still has a significant portion of the disc in the stagnation flow region. In contrast, a ring electrode can be constructed to lie wholly inside or outside the stagnation region. The ring electrode measurements are therefore more sensitive to changes in the flow pattern.

It has been suggested by Gardner el al[69] that employing the ring disc electrode as a sectioned disc electrode, i.e. maintaining the same potential at the ring and disc electrodes, will cause current distribution on the disc electrode to be more uniform. This facilitates interpretation of the erosion-corrosion data.

Poulson[115] illustrated the precautions that must be taken when measuring limiting current density (LCD): (a) operating at a flow rate where there is a limiting current, (b) choosing an electrolyte having an excess of (+) and (-) ions so that reacting species do not migrate in the electric field, (c) choosing potential at which only the reaction of interest is occurring, (d) positioning the electrodes so that the current distribution is as

even as possible and neither affects the flow, and (e) if local mass transfer coefficients are to be obtained, the small electrodes must be surrounded by large active electrodes.

4.4 ASTM Standard for erosion corrosion of stainless steels.

Prior to starting the experiments some standard practices were reviewed such as NACE standard TM0270-72[57] which describes a procedure for conducting controlled velocity laboratory corrosion tests, also ASTM standard practices G31-72 and G73-93[69] (reapproved 1985). The G31-72 standard describes accepted procedures for and factors that influence laboratory immersion corrosion tests and the latter concern tests in which solid specimens are eroded or otherwise damaged by repeated discrete impacts of liquid drops or jets. The objective of this test is to determine the resistance to erosion or other damage, or investigate the damage mechanisms and the effect of test variables. This gave guidance in setting up a test, and specifies test and analysis procedures and reporting requirements that can be followed even with variety of materials, test facilities, and test conditions.

The G73-93[69] standard practice consists of two impingement tests: distributed and repetitive impact tests. The latter test produces erosion more rapidly at equal impact velocities. Liquid impingement tests are usually conducted by attaching specimens to a circular path rotating disc or arm. They repeatedly pass through and impact against liquid sprays or jets, at a velocity range in the 50 m/s to 1000 m/s, with jet diameters ranged from around 0.1 mm to about 5 mm. Data analysis uses cumulative erosion-time curves, which are characterised by the incubation time and the erosion rate.

5.0 PASSIVE FILM OPTICAL MEASUREMENTS

The evaluation of duplex stainless steel in seawater solution led to the following survey of passive film characteristics with particular attention to the effect of light on film thickness measurement.

5.1 Research review of passive film thickness measurements

A number of researchers [48, 66-67, 139-142, 148, 149, 155, 159, 179] have investigated the use of interference colours and other methods to determine the thickness of films that form on a metal surface. King et al[67] mentioned that thin films play an important role in many branches of science and technology and accurate measurement of their thickness is frequently required. He divided the measurement methods into two groups: firstly, those where the film can be prepared with a sharply defined edge, the step height at this edge then being measured; secondly, these methods was applicable to films covering the entire substrate surface. Film thickness was determined by the effect of the film on the reflection or transmission of a light beam.

Evans[155] cited Tammann work which considered that when light strikes the surface of a metal (D) covered with an oxide film (F), it is partly reflected by the air-oxide interference and partly from the metal oxide interface. Figure **5.1(case a)** shows that two light waves reflected from the two surfaces tend to reinforce one another, i.e. constructive interference. However, usually certain wavelengths are extinguished from the emergent light (FG), since the troughs of the light waves reflected from one interface will coincide with the crests of the waves reflected from the other, as shown in figure **5.1(case b)**. The wavelength of the light extinguished depends on the thickness of the film and its refractive index. The reflected light has the complementary colour to that of the extinguished wavelength.

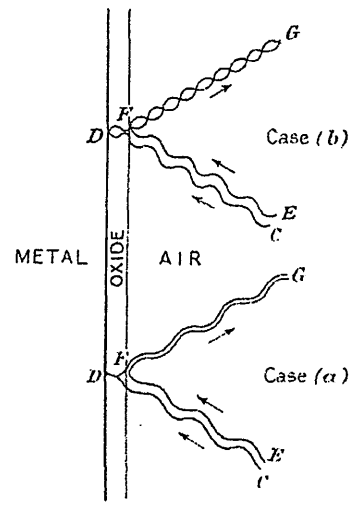

Figure **5.1(case a, b)** Light interference with oxide film(Tammann cited by Evans[155]).

Ansell et. al[46] showed that the film on stainless steel was composed principally of iron, chromium and oxygen and the species present in the film were invariant with thickness. However, according to Constable[66] there were a number of secondary factors which produced modification in the colour sequences. These are the dispersion of the metallic oxides, their specific absorption, and the variation in the intensity of the light absorbed by the metallic reflector at the back of the film with the wavelength of the incident light.

Meanwhile Kubaschewski was cited by Evan[159]and pointed out that when white light falls on the film, a certain interference of wavelengths can occur depending on the film thickness. As a result, the light reaching the eye was coloured if the wavelengths subject to interference were within the visible region of the spectrum. The width of the interference band varies with the absorbing power of the film and reflectivity of the surface, a higher absorbing power and lower reflectivity giving a broader band. A perfectly transparent film on a perfectly reflecting surface gives a band of zero width and no interference colours are seen. Variation in width of the interference band affects the colour seen by the eye. The absence from white light of a narrow band of wavelengths of one colour does not much affect the colour of the light, whereas the absence of a wider band of the same average wavelength will produce a pronounced colour.

As the thickness of the film increases, the first interference band enters the blue-violet range of the spectrum and the complementary yellow colour is produced. This changes to red and then blue as the thickness of the film increases, until the band reaches the infra-red region of the spectrum as shown in figure **5.2**, the colours produced being given in Table **5.1**[159] Whilst the film is still too thin for the first interference band to enter the visible region of the spectrum, no interference tints are produced.

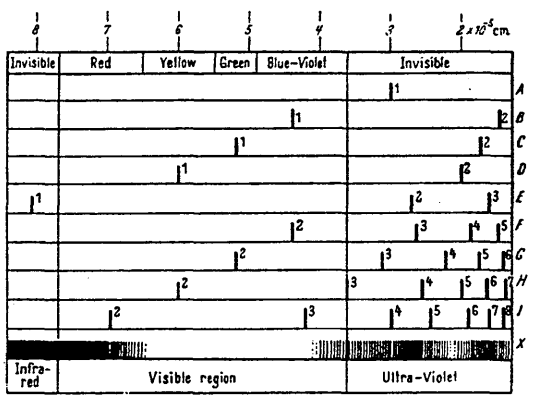

Figure **5.2** Production of interference tints.
(Kubaschewski cited by Evans[159]

Constable[66] cited Kundt's values for blue and red light which have been used to evaluate the constants in Cauchy's formula, giving the results for the variation in refractive index with wave length, λ, (in nanometers).

For iron oxide ($n Fe_2O_3 + m FeO$)

$$\mu = 1.35 + 18.8 \times 10^4 / \lambda^2 \qquad (1)$$

	Colours produced by Air Films between Glass ('Newton's Rings')		*Colours produced by Films on Metals*		
Order	*Reflected Light*	*Transmitted Light*	*Oxide on Lead or Nickel; Iodide on Silver; Hydroxide on Aluminium*	*Oxide on Iron*	*Oxide or Sulphide on Copper*
'Invisible Range'	*Colourless (black)*	*Colourless (white)*	*Colour of metal unchanged*		
First order	*Blue Faint green Yellow Red*	*Yellow Red-mauve Blue Green*	*Yellow-brown Rose-mauve Blue Silvery or Greenish*	*Yellow-brown Mauve Blue Silver grey*	*Brown Rose-mauve Blue Brilliant Silver*
Second order	*Blue Green Yellow Red*	*Yellow Red Blue Green*	*Yellow-brown Red Blue Green*	*— Pinkish blue Blue Greenish blue*	*Yellow-brown Red Blue Green*
Third order	*Blue Green Yellow Red*	*Yellow Red Greyish blue Green*	*Yellow Red Trace of Lavender blue Green*	*— Bluish grey (with trace of pink) Bluish grey (specific colour) ,,*	*Brown Red Trace of Lavender blue Green*
Fourth order	*— Green Red*	*Dull yellow Red Green*	*— Red Green*	*Bluish grey (specific colour) ,, ,,*	*— Dirty red Dirty green*
Fifth order	*Greenish*	*Red*	*Faint red passing into specific colour of film substance*	*Bluish grey (specific colour)*	*Grey (sometimes trace of red)*

Table **5.1**, Colours of air films between glass and colours of film on metals[15].

Evans et al[151, 179] determined actual film thickness by an optical method and assumed the apparent refractive index to be 2.2 for the film on stainless steel. As the refractive index has been found for iron by Kendt which was cited by Constanble[66], it may be reasonable to use these values to calculate the thickness of the oxide film for the more complicated second order colours found with iron. Seo and Sato[142] found that the thickness of an anodic oxide film on an Fe-Ni alloy increases linearly with anodic potential in the passive region. There was also an oxide film in the active and transpassive regions, where the film thickness was greater than that in the passive regions. The results were explained in terms of a combination of factors such as preferential dissolution of Fe component, preferential oxidation of Fe component, and preferential anodic dissolution of the Fe or Ni component.

Eventually, Constable[66] suggested that the interference between the rays reflected from the air-cupric oxide interface, and those returning after reflection at the copper oxide interface occur when:-

$$2t = (2n-1)\frac{\lambda}{2\mu} \qquad (2)$$

Where n = 1,2,3 (the value of n being limited by the general absorption in the film); and t = the thickness of the oxide film, λ the wavelength of maximum absorption in the spectrum of the reflected light and μ is the refractive index of the film for this wavelength. Thus $t = \lambda/4\mu$ for the first absorption band, $3\lambda/4\mu$ for the second, $5\lambda/4\mu$ for the third; there being maximum interference in the film for these thicknesses. For the waves to reinforce $2t = n\ \lambda/\mu$ where n = 1,2,3. Hence $t = \lambda/2\mu$ for the maximum reflection.

Other cases;
Sometimes, the reflection of the two rays, occurring at different types of surfaces, itself produces a relative phase change which is equivalent to a film thickness *C*. There is then maximum interference at thickness[159]

$$\lambda/4\mu\text{-}C,\ 3\lambda/4\mu\text{-}C,\ 5\lambda/4\mu\text{-}C,\ \text{etc} \qquad (3)$$

For a transparent oxide film attached to metal, it has been usual to assume that C = 0 and we may expect minimum reflection at $\lambda/4\mu$, $3\lambda/4\mu$, $5\lambda/4\mu$.

6.0 EXPERIMENTAL METHOD

6.1 Material

Two batches (**A** and **B**) of duplex stainless steel *SAF2205* were used in the experimental programme, but the majority of the experiments were carried out with batch **'A'**. Table **6.1** shows the chemical analyses of each batch.

Batch No	C	Si	Mn	Cr	Ni	Mo	P	S	N	Cu	Co
Batch A	0.02	0.49	1.5	21.9	5.4	3.1	0.025	0.003	0.18		
Batch B	0.028	0.22	1.34	23	5.15	2.92	0.027	0.017	0.1225	0.35	0.07

Table **6.1** Duplex stainless steel *SAF 2205* chemical composition

6.1.1 Metallographic Examination

Samples of the duplex stainless steel were mounted in epoxy resin, polished and etched for metallographic examination. The electrochemical etching technique made use of a Thompson 251-Autostat, specimen holder, saturated calomel reference electrode and a platinum counter electrode. The specimens were immersed in a 35 % potassium hydroxide (KOH) solution. A constant potential was held at –900 mV (SCE) for 5 minutes to reduce any surface oxide layer that might have been present and then the potential was gradually increased to 1000 mV and held there for approximately 3 seconds. After the etching procedure the specimen was cleaned with propanol and washed with running water and dried in air.

6.1.2 Microstructures

Micrographs of the etched specimens, taken using an Olympus Vanox-T metallurgical microscope with halogen illumination, are shown in Figures **6.1** (**a**), (**b**) and (**c**). Figure **6.1** (**a**), shows a general view of a duplex stainless steel specimen, etched in the 35 % KOH solution. It can be seen that a range of colours were produced on the surface such as light yellow in the centre, light pink, light green, and light orange due to the effects of the electrochemical etching at 1000 mV.

The longitudinal microstructure, illustrated in Figure **6.1** (**c**), shows equal proportions of elongated ferrite and austenite phases. The ferrite was the more deeply etched and exhibited a dark brown colour. In contrast, the austenite phase was a light yellowish colour. The transverse microstructure is shown in Figure **6.1** (**b**). The ferrite and austenite phases are indicated as dark and light coloured grains with a more equaixed shape. The grains were larger at the edge of the specimen.

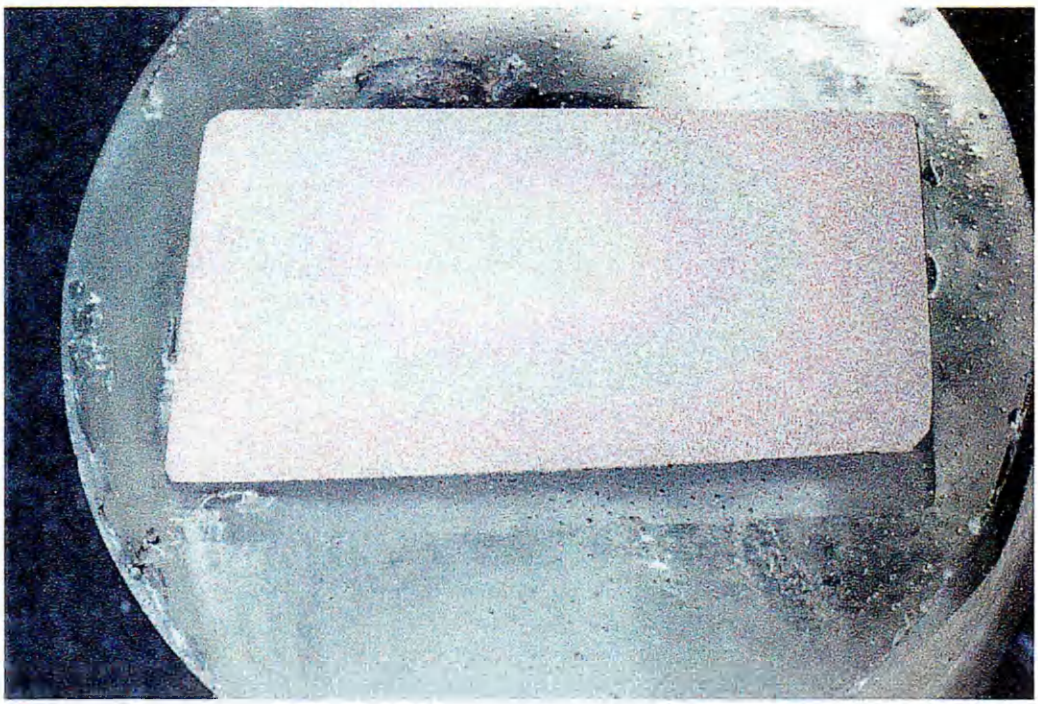

Fig **6.1** (**a**) Specimen of *SAF 2205* duplex stainless steel electrochemically etched in 35 % KOH

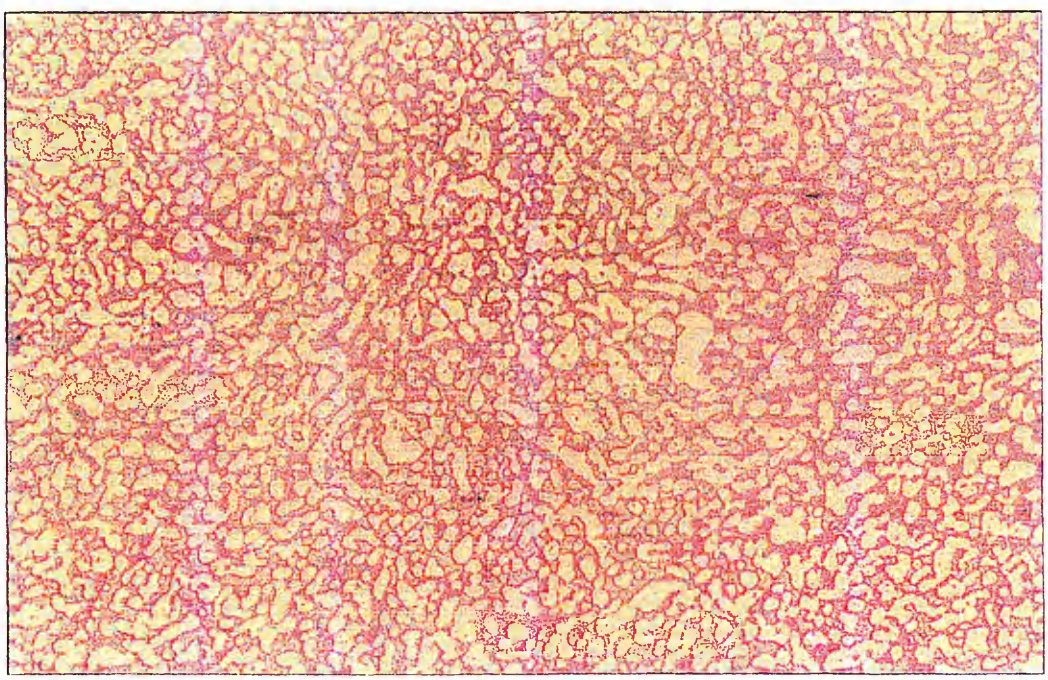

Figure **6.1** (**b**) Transverse microstructure of duplex stainless steel after potentiostatic etching in 35 % KOH solution. Mag x 100

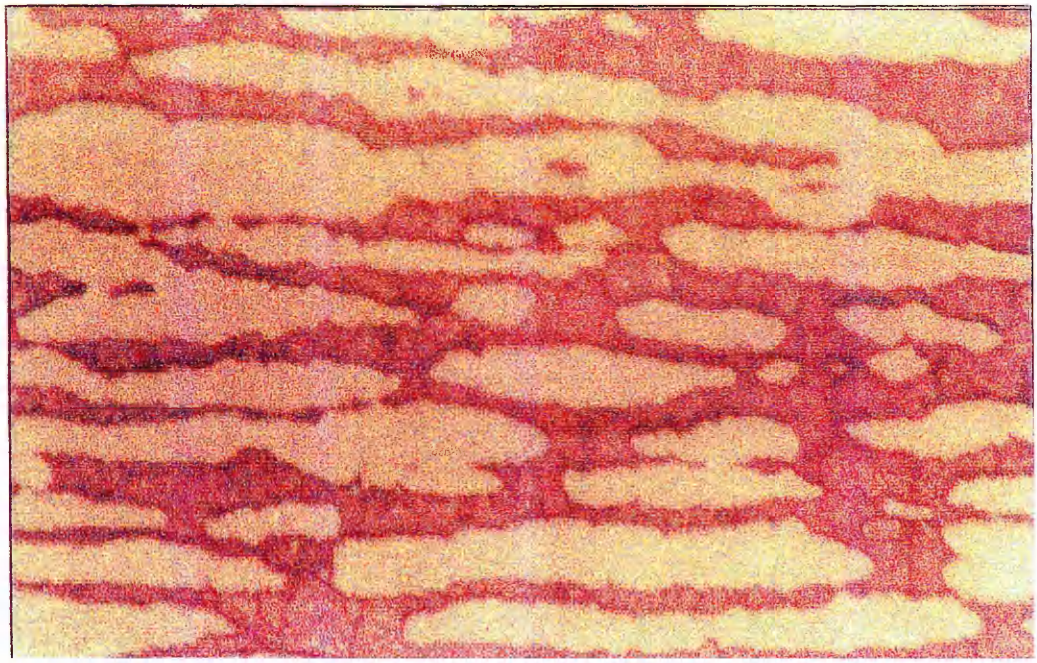

Figure **6.1(c)** Longitudinal microstructure of duplex stainless steel specimen after potentiostatic etching in KOH solution, Mag x 400

The appearance of the electrochemically etched specimen in the scanning electron microscope is seen in Figure **6.1 (d)**. The ferrite phase has been more deeply etched, leaving the austenite protruding from the surface.

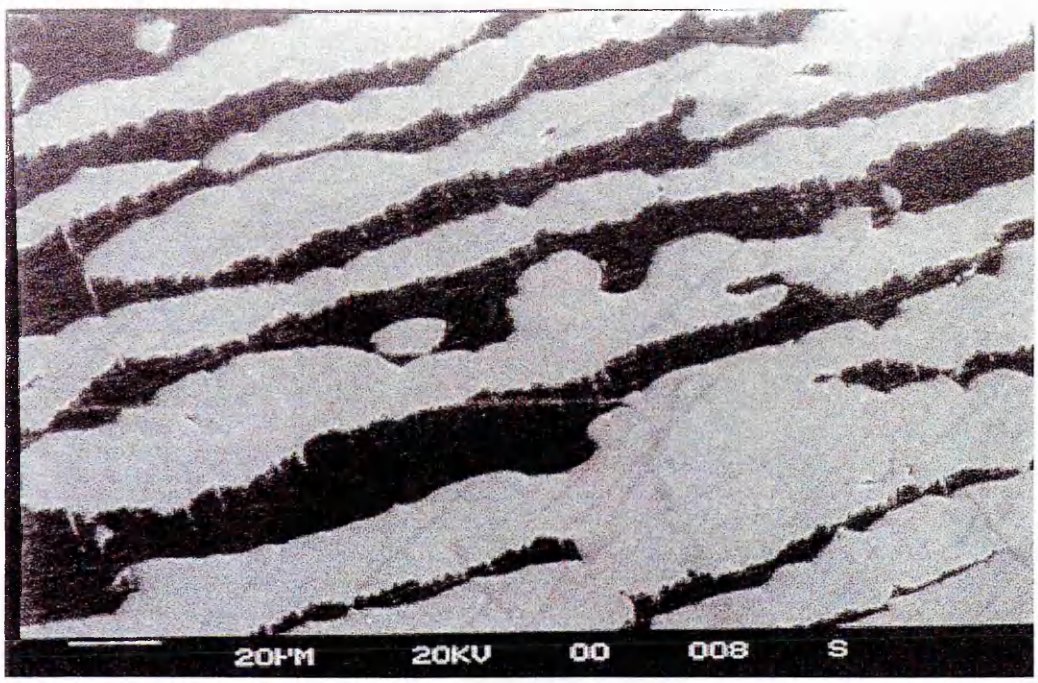

Figure **6.1 (d)** SEM micrograph of duplex stainless steel SAF2205 etched in KOH solution. Mag x 500

6.1.3 Phase compositions

As expected, the ferrite phase had a higher chromium content (24.1 %) and lower Ni content (5.1 %) than the average alloy composition as shown in Figure **6.2**. The austenite was richer in Ni (7.2 %) and had less chromium (21.8 %). The composition of each phase is summarised in table **6.2**. When comparing the chemical composition of duplex stainless steel SAF2205 in tables **6.1** with **6.2**, the difference in element percentages between the two tables is due to the electron beam in the scanning electron microscopy (SEM) equipment. This was applied and concentrated on a spot of ferrite or austenite within a small area of the specimen rather than on a large area. Table **6.1** demonstrates the analysis values for the whole area of the material (ferrite and austenite at different sites) and it would be consider as an average value for the ferrite and austenite phases when compared with table **6.2**.

On the other hand, elements such as Cu and Co were not found in table **6.1** and existed in table **6.2**. This is because the command was given to the SEM to registered them. This done by matching the foot print chart for every element contained in the equipment memory with the chemical analysis chart for the tested specimen.

Figure 6.2 Quantitive elemental analysis of batch 'A' duplex stainless steel *SAF2205* austenite and ferrite phases etched in 35 % of KOH solution

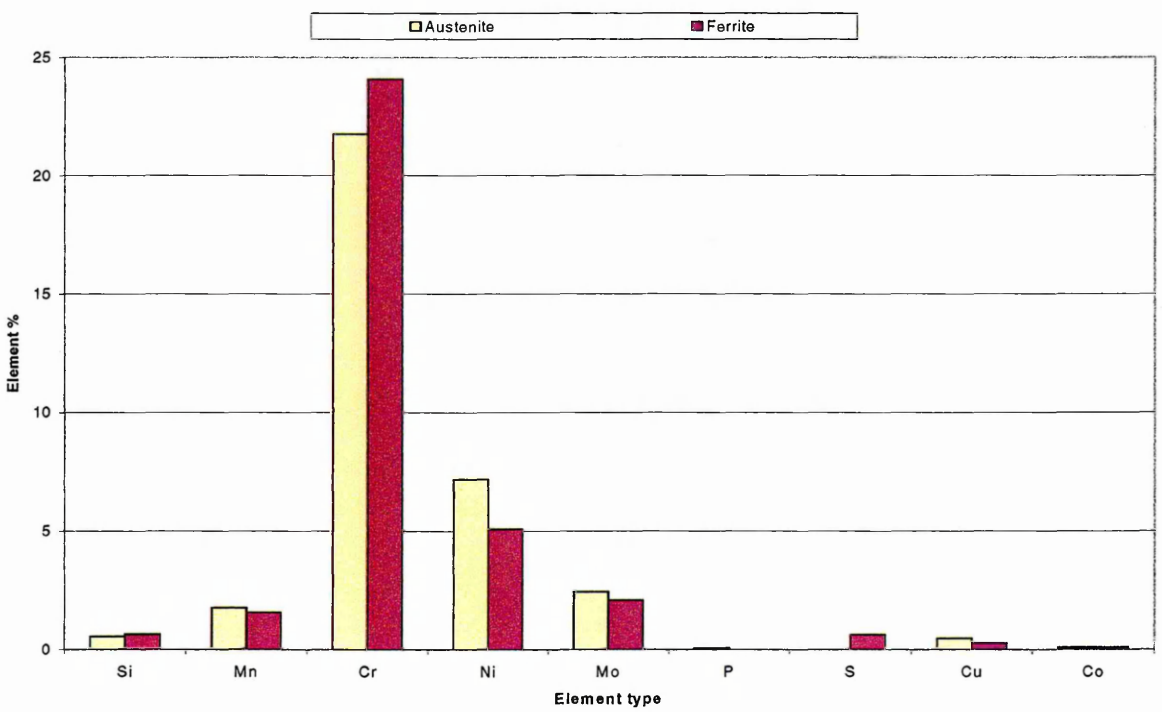

Element type	Weight % of austenite elements	Error (weight %) in austenite values	Weight % of Ferrite elements	Error (weight %) in ferrite values
Si	0.6	± 0.05	0.6	± 0.05
Mn	1.8	± 0.15	1.6	± 0.15
Cr	21.8	± 0.22	24.1	± 0.23
Ni	7.2	± 0.21	5.1	± 0.19
Mo	2.4	± 0.47	2.1	± 0.50
P	0.1	± 0.07	0	± 0.08
S	0	± 0.22	0.6	± 0.24
Cu	0.5	± 0.16	0.3	± 0.15
Co	0.1	± 0.18	0.1	± 0.18

Table **6.2** Quantitative elemental analysis of duplex stainless steel SAF 2205 (batch **A**) austenite and ferrite phases etched in 35 % of KOH solution

6.2 Closed loop jet impingement apparatus

The erosion corrosion impingement test rig, illustrated in figure **6.3** (**a**), consisted of a glass cell and impeller driven pump connected with 19 mm PVC tubing and pipe fittings. A regulator valve was used to control the flow and a heat exchanger, constructed from AISI 316 stainless steel, was included to control the heating caused by the high flow rates. The total capacity of the flow loop was approximately 3.0 litres. The glass cell had a capacity of 1.5 litres and contained the duplex stainless steel specimen suspended beneath the flow nozzle.

A combined electric heater and thermostat was used to maintain the temperature of the artificial seawater at 24 °C. The cell was fitted with a standard calomel electrode and a platinum electrode in order to carry out electrochemical measurements on the specimen. A thermometer and an air bubbler tube to aerate the electrolyte were installed in the cell. A pressure gauge and a manometer were used to record the back pressure in the loop and were calibrated to indicate the flow rate. Redox potential measurements on a platinum electrode were recorded to monitor the efficiency of the aeration of the seawater. An air-bleed valve could be opened to minimise air locks in the system. The water jet impingement system was later modified by adding a nozzle and a valve to make it easier to collect water samples containing sand particles. Figures **6.3** (**b**) and (**c**) show the modified water jet impingement system.

6.2.1 Pump specification

A rotary rubber impeller pump (make Arbo), with a discharge head of 0.7 bar and volume flow rate of 40 l/minute, was used to circulate the electrolyte solution through the system. The maximum flow velocity through the nozzle was measured to be 8.5 m/s.

6.2.2 Nozzle

The test specimen was fitted in a Perspex holder and held with a securing screw on the side and positioned opposite the fluid flow from a plastic nozzle of 5 mm diameter as shown in figure **6.4**. The distance between the specimen and the nozzle was 24 mm. According to Efird[164], the flow velocity is a function of the pressure and the orifice size. The operation of the flow loop was checked by measuring the volume flow rate at a specific header pressure. The various fluid flow velocities that were used in the different electrochemical tests were calculated from the water collected in 15 seconds.

In the light of the accuracy of the calculated volume fluid flow rates data and the inability to reproduce these data a standard deviation was carried out on all the fluid flow velocities. The calculated velocities were shown to be accurate within the range of 3% to 6% as shown in tables **6.3**, **6.5** of the Appendix. The standard deviation for the fluid velocities used in the erosion-corrosion experiments could be due to water splashed from the beaker whilst discharging from the nozzle, time lag during opening closing of the regulator valve or air bubble creation in the loop and discharging from the nozzle. Therefore, the maximum fluid flow velocity in meter per second can be read as 8.5 ± 0.53 (SD 6.0 %) while the minimum velocity read as 7.2 ± 0.41 (SD 6.0%). Similarly the maximum and minimum fluid flow rates in litre/minutes given as 10 ±0.64 and 9.0 ±0.49 respectively.

The following calculation shows the liquid volume flow rate in ms^{-1};
Average volume fluid flow rate (Q) = 2516 ml/15 Sec

$$Q = 2.516 \times 10^{-3}\ m^3/15\ Sec$$

Assuming that the liquid flow out of the nozzle in a cylindrical shape, then

Volume of cylinder of water/Second = (Area × Length of cylinder)/Second

Where, fluid flow velocity $= \frac{l}{t}$

$$\text{Area} = \frac{\pi \times d^2}{4} \Rightarrow \text{diameter of nozzle } (d) = 5 \text{ mm}$$

Then $$\frac{Volume}{Second} = \text{Area} \times \text{fluid flow velocity}$$

$$\frac{2.516\times10^{-3}}{15} = \frac{\pi\times5^2}{4} \times \text{Velocity}$$

Therefore, Fluid flow velocity $$= \frac{2.516\times10^{-3}\times4}{15\times\pi\times25\times10^{-6}}$$

$$= 8.5 \text{ m/s}$$

To convert fluid flow velocity to litre/minute;
In the appendix table **6.4** shows the average measured fluid flow rates were converted from millilitre to litre by dividing to 1000 and change from 15 seconds to minutes by multiplying to 4.

$$Q = 2516 \text{ ml/15 sec} \Rightarrow \frac{2516\times4}{1000} = 10 \text{ litre/minute}$$

6.2.3 Heat exchanger

The purpose of the heat exchanger was to prevent overheating of the artificial seawater due to the effect of the circulation and to keep the temperature as constant as possible. Initially, the heat exchanger was fabricated from 8 mm diameter 316 stainless steel tubing wound into a spiral, and inserted inside a Perspex tube (Figure **6.5**). Later the design was changed to straight tube as the first arrangement trapped some sand particles and restricted the fluid flow velocity.

6.2.4 Specimen design

The specimens consisted of three concentric rings machined from batch '**A**' duplex stainless steel. The rings were positioned in the stagnation, high turbulence and low turbulence regions of a flat surface erosion corrosion specimen as shown schematically in figure **6.6**. Each ring position was measured in millimetres from a flat specimen, which have been exposed to an erosion corrosion condition similar to figure **8.1** chapter **8.0**. The measured distances were converted to radial distances and the location of the rings were checked with a radial scale of the hydrodynamic characteristics of water jet impingement on a flat plate as shown in figure **3.11**. Equally, those reading corresponded with Hirooka[113] rings spacing.

An electrical connection was attached to each ring to enable electrochemical monitoring. This was done by inserting a wire into a drilled hole at the end of the specimen and soldering it. The rings had diameters of 5 mm, 13 mm and 23 mm and their corresponding areas were 0.196, 0.961 and 1.57 cm^2. Each ring was set in non conducting epoxy resin so that only one side was exposed to the seawater, as shown in figures **6.6** (**a**, **b**, and **c**). An additional specimen design, shown in Figure **6.6** (**d**), consisting of a cylinder 24 mm in diameter, was used specifically to study the optical properties of the passive film.

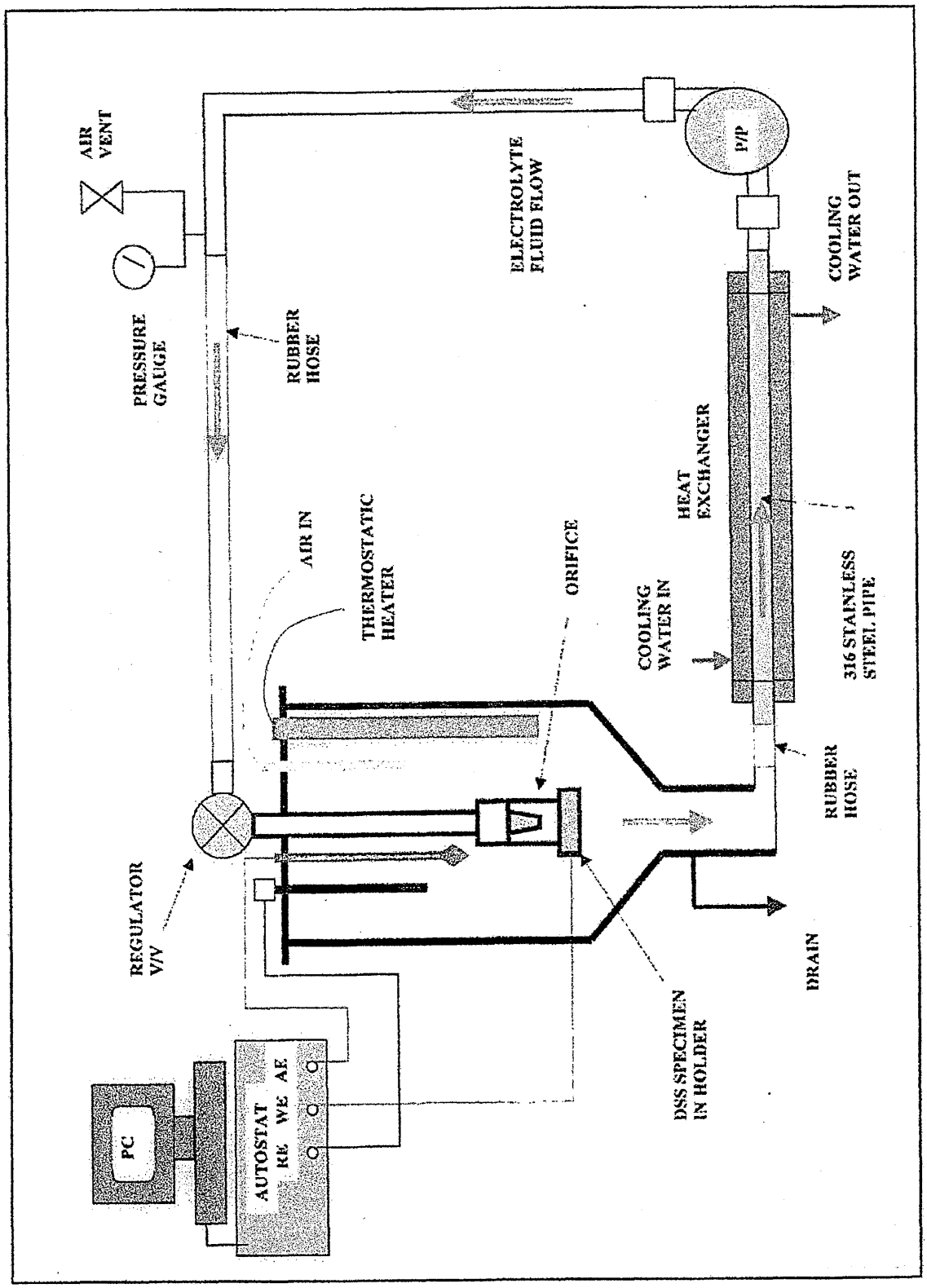

Figure **6.3** (a) Schematic diagram for the erosion corrosion water impingement test rig

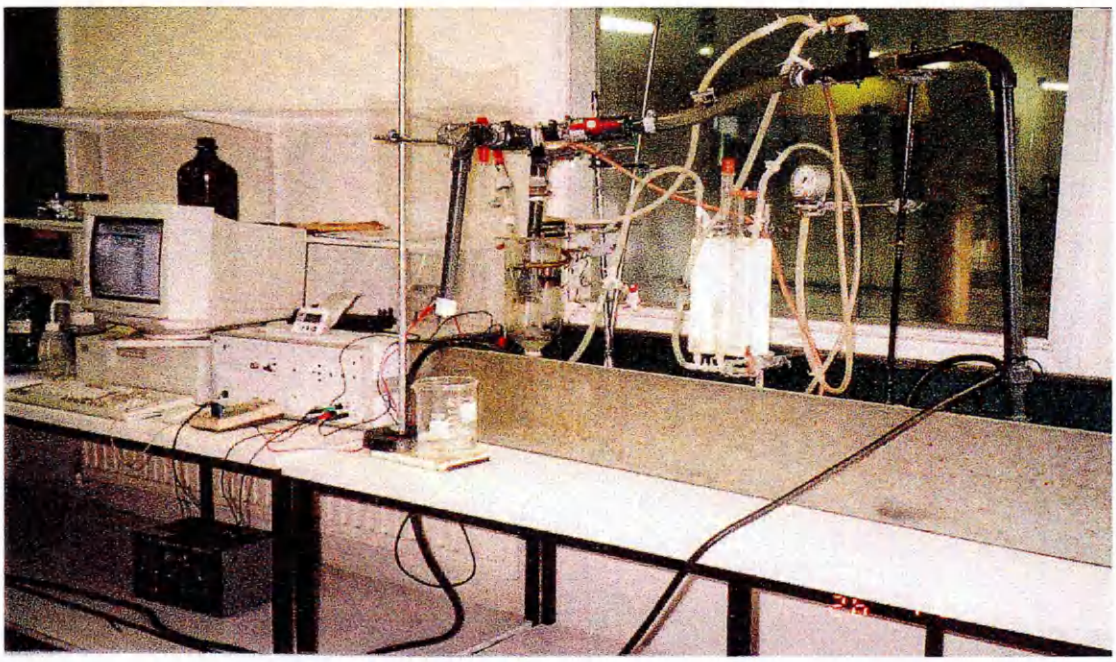

Fig **6.3** (**b**) The modified electrochemical water jet impingement test rig

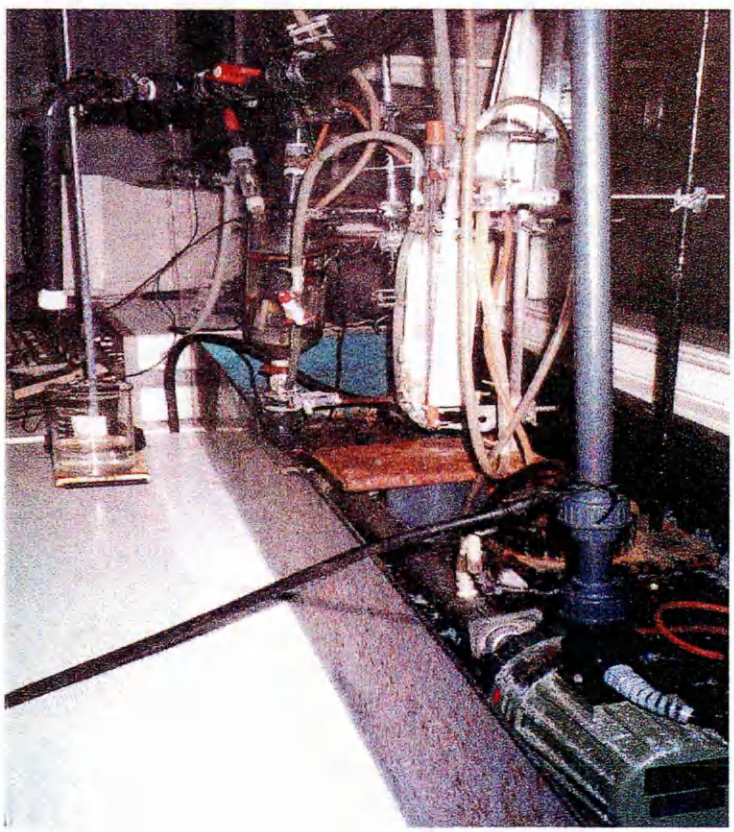

Figure **6.3** (**c**) Side view of the modified electrochemical test rig

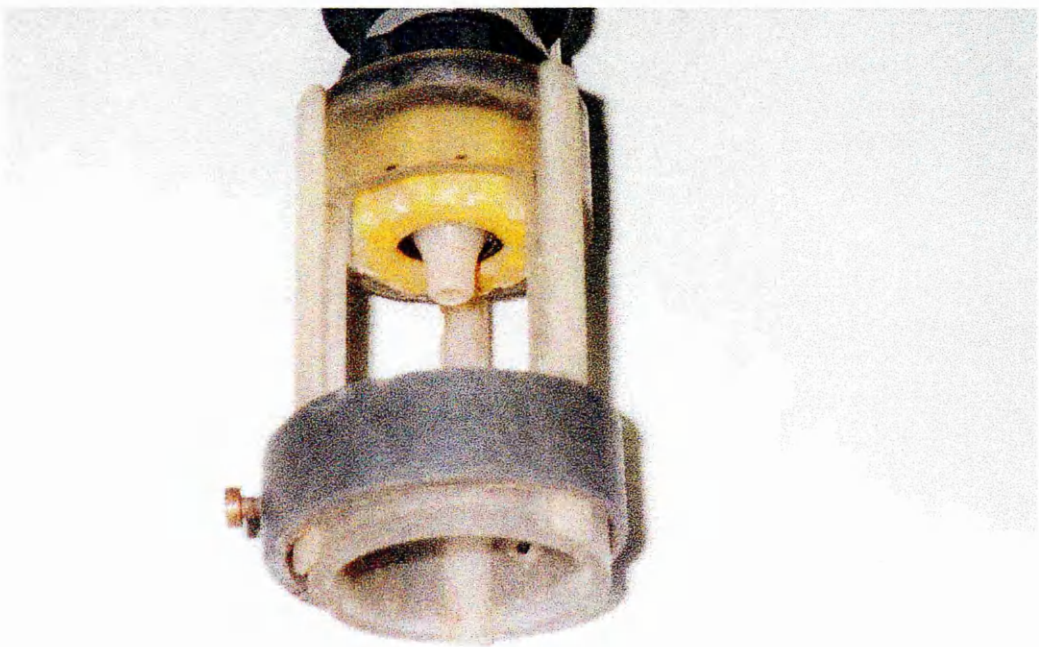

Figure **6.4** Specimen holder in the electrochemical erosion corrosion test rig

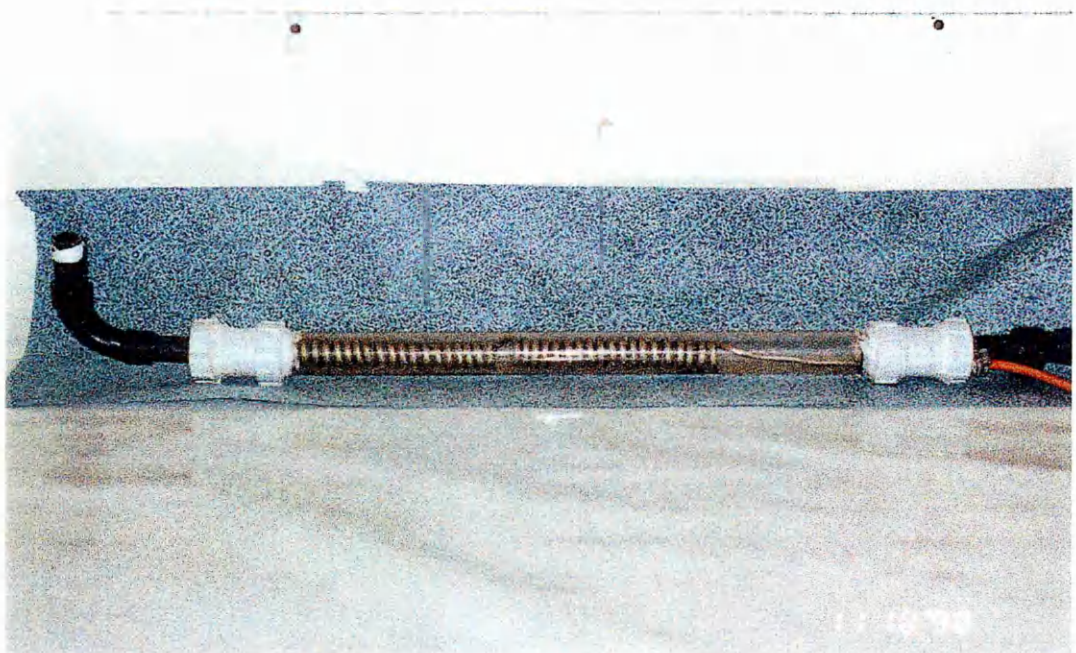

Figure **6.5** The fabricated spiral single flow heat exchanger contained in the impingement loop

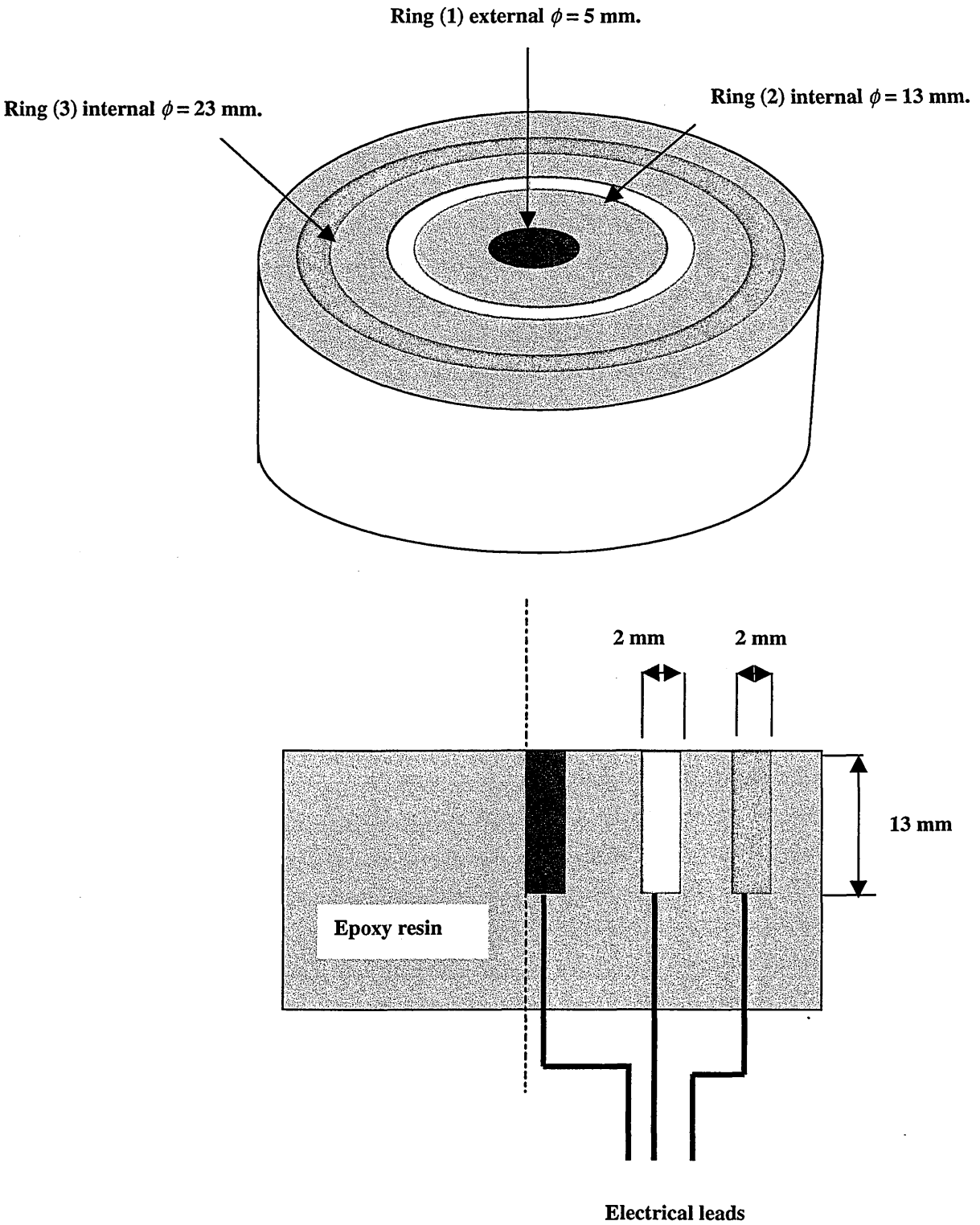

Figure **6.6** Duplex stainless steel erosion corrosion design

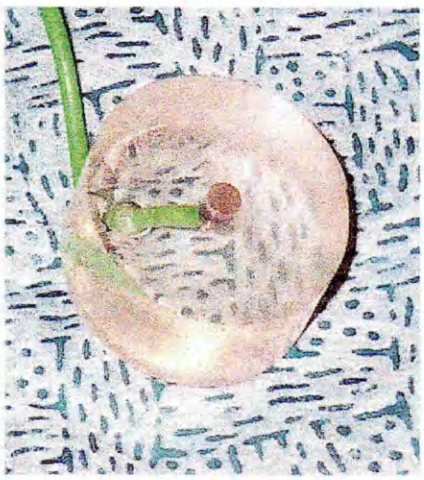

Figure **6.6** (**a**) Ring **1** specimen design

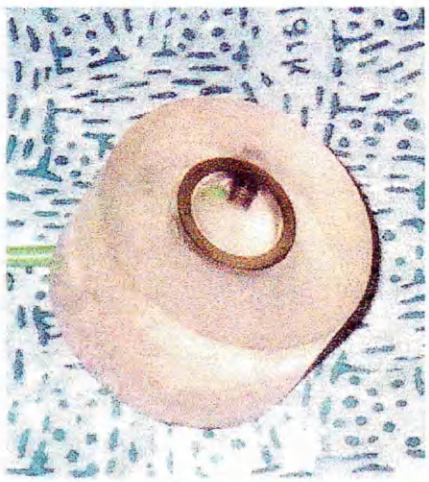

Figure **6.6** (**b**) Ring **2** specimen design

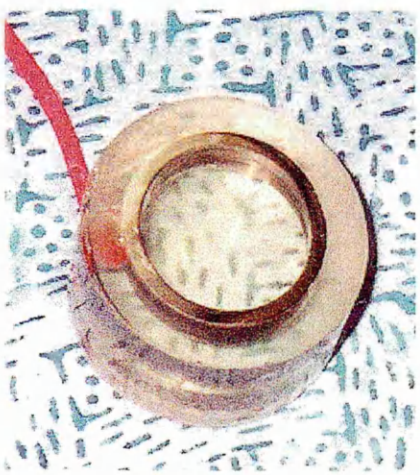

Figure **6.6** (**c**) Ring **3** specimen design

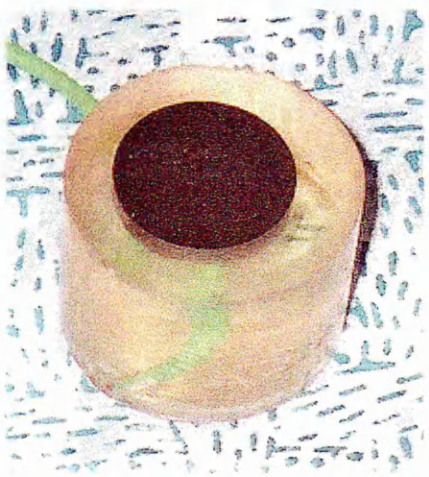

Figure **6.6** (**d**) Passive film optical properties specimen design

6.2.5 Surface preparation

The surface of each specimen was prepared according to the ASTM standard G1-81 for preparation, cleaning, and evaluating corrosion test specimens[69]. The duplex stainless steel was ground using 120, 220 and 1200 micron grit silicon carbide paper. The surface polishing was finished with diamond paste grades of 6 μm and 1 μm. Then the samples were washed with soap and water followed with an ultrasonic cleaning in propanol for 5 minutes. Finally, the specimens were rinsed with propanol and air-dried.

6.2.6 Sand particle characteristics

The following are the chemical and physical properties of the sand particles used in the electrochemical erosion experiments.

Geology:	Lower Green sand.
Production process:	Washing, Drying, Screening.
Typical colour:	Light cream.
Grain shape:	Low sphericity, Sub Angular to Sub Rounded.

Bulk density: Loose 1.32 grams/ml, compacted 1.50 grams/ml.

Chemical Analysis:

Material	Typical %
SiO_2	97.49
Al_2O_3	0.72
Fe_2O_3	0.53
CaO	0.02
MgO	0.02
Na_2O	<0.03
K_2O	0.43
LiO	0.35

Particle Size Distribution:

Particle size (microns)	Percentage by weight
106 - 180	2
180 - 250	26
250 – 300	55
300 – 355	8
355 – 425	4
425 – 500	2
> 500	3

Figure **6.7** shows the sand particles under scanning electron microscopy (SEM) at different magnifications. The shape of the sand particles was semi-spherical with irregular surface texture.

6.2.6.1 Weight of sand particles

The sand was weighed and sieved using a stack of sieves on a shaker. The sieves ranged in size from 500 μm to 106 μm mesh. The sand was sieved for 5 minutes and the sand particles that remained in each sieve were collected and their mass was weighed. Only sand particle category 250 μm to 300 μm was utilised in the erosion corrosion experiments because it has the highest sand particle size percentage by weight of 55% than other sand categories in 300 grams quantity of sieved sand. This category would produce a more effective erosion corrosion-current density during impact on the specimen than the smaller size sand categories. Therefore, a clearer correlation with current densities produced at flowing condition only at low fluid flow velocities, equally sand particle deposition would be less in the loop than the larger size categories.

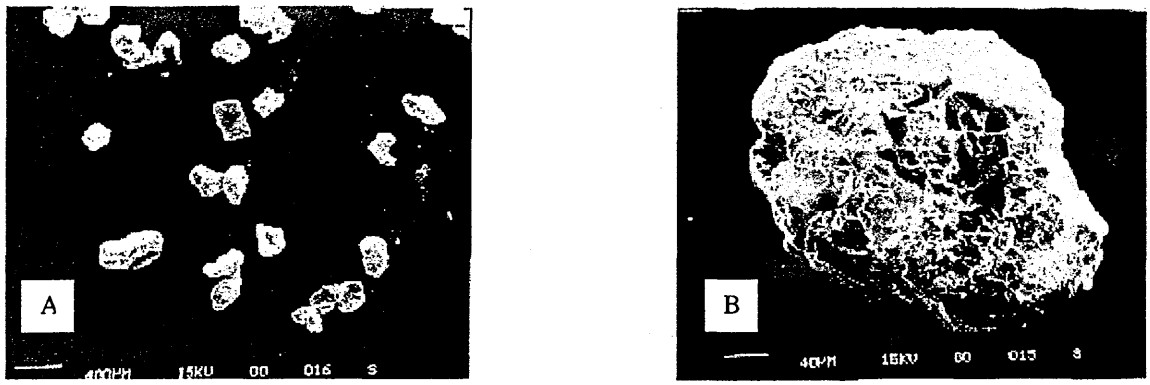

Figure **6.7** Appearance of the 275 μm sand particle under scanning electron microscopy (SEM). A = x 25 and B = x 250

6.2.6.2 Sand particles suspended in the flow

It was found that when the sand was added to the flow loop most of the sand was suspended in the flowing seawater, but some settled out in the pipe work. It was essential, therefore, to measure the proportion that was suspended in order to be able to calculate the rate of particle impacts.

The following method was used. The suspended sand was collected by redirecting the flow using the second nozzle. During this experiment the water in the system was topped up continuously to maintain a constant level. Samples of the seawater, containing suspended sand were taken after 10, 30, 50, 120, 180 and 240 seconds. After each sample the settled sand that remained in the loop was collected by flushing the system with four times the original quantity of water in the system.

Each sample of sand was filtered using 120 mm grade (1) filter paper. The papers were left for one hour inside an oven to dry and then weighed. The mass of sand on each filter was obtained by subtracting the weight of a new oven dried filter from the dried sand filter. By finding the mass of the suspended sand, the number of sand particles impacting the surface for each sand concentration at each fluid flow velocity was calculated.

6.3 Electrochemical testing

6.3.1 Potentiodynamic polarisation scans

Potentiodynamic polarisation measurements were carried out to provide information on the characteristics of the passive film on the *SAF 2205* duplex stainless steel. A Sycopel Scientific computer controlled potentiostat was programmed to change the specimen potential relative to a saturated calomel electrode (SCE). The scans ranged from – 600 mV to +1300 mV from the initial rest potential of the specimen, at a scan rate of 10 mV/minute. The time duration of each potentiodynamic scan was approximately 180 minutes.

At the completion of the potentiodynamic measurements, graphs of potential *vs* current density were produced. The current density in the passive range and the pitting potential were noted from the graphs for each experimental condition.

The electrochemical measurements were carried out under static conditions and also with fluid flow at a range of velocities both with and without the addition of sand particle impingement.

6.3.2 Electrochemical open circuit measurements

These experiments were designed to study depassivation of the duplex stainless steel and observe how the breakdown of passivity would result in either a noble or active shift in the corrosion potential. This was detected electrochemically by recording the duplex stainless steel surface potential.

Open circuit measurements were carried out on the duplex stainless steel ring specimens under a fluid flow velocity of 8.5 m/s. The specimens were left for one hour at – 600 mV from the initial rest potential to reduce any oxide films on the surface of the material. Then open circuit measurements were performed for six hours under static conditions or fluid flow with and without sand impingement.

6.3.3 Electrochemical current density measurements

The aim was to measure the current density in the passive range at fixed potential to confirm the values recorded in the potentiodynamic scans under the same flow conditions.

The working electrodes were held potentiostatically for one hour at – 600 mV from the rest potential under fluid flow velocity of 8.5 m/s, to reduce the passive film. Then the electrochemistry programme was changed to record current *vs* time at a constant potential under fluid flow with and without sand impacts. The time duration of the experiment was 90 minutes.

6.3.4 Passive film studies at fixed potential

6.3.4.1 Effect of various fluid flow velocities

The purpose of this investigation was to record the passive film optical properties as a measure of film thickness and to relate them to the potentiodynamic scans and the erosion- corrosion behaviour of the duplex stainless steel.

A series of duplex stainless steel *SAF 2205* specimens (Figure **6.6(d)**) were tested in the flow loop at different fluid velocities of 8.5, 7.9, 7.8, 7.5 and 7.2 m/s. The specimens were left for one hour under fluid flow conditions in the water impingement system to stabilise material rest potential, the temperature and aeration level of the artificial seawater.

The 251 Sycopel autostat was switched onto manual mode and the material was manually polarised starting at – 600 mV from the initial rest potential. Gradually the potential was stepped up with a scan rate of 10 mV/minute to the desired anodic potential of 400, 700 or 900 mV (SCE). The specimen was left for six hours at the noble

potential to develop a coloured oxide film and the current density was monitored during the experiment.

6.3.4.2 Effect of various fluid flow with and without sand addition

Three grams of 275 μm sand particles were added to the flow loop to evaluate the effect of particle impacts on the thickness of the coloured oxide film. In some cases the sand particles were added at the start of the experiment before polarising the specimen to – 600 mV from the initial rest potential and then left at the noble potential for 6 hours to develop the coloured oxide fringes. In other experiments, the oxide film was first developed in flowing conditions without sand particles as described in **6.3.4.1.** The sand was then added and the effect of particle impacts over a period of 10- 60 minutes was observed.

7.0 ELECTROCHEMICAL RESULTS

7.1 Crevice corrosion treatment of duplex stainless steel

The results obtained from the electrochemical experiments on batch **A** duplex stainless steel showed a considerable amount of scatter near the rest potential of the duplex stainless steel, which was attributed to crevice corrosion. Therefore a number of attempts to avoid crevice corrosion were carried out as follows:

1. Bee's Wax and Amber Resin were mixed to a ratio of 3:1, by weighing both substances, melting the wax first in a beaker then adding the resin to it, while continuously stirring the mixture. Wax was applied all over the specimen before a test was carried out but the plot obtained still exhibited scatter.

2. Immersion of the sample for five hours in nitric acid solution HNO_3 then polishing it to initiate the actual passive layer of the stainless steel surface and passivate the interface between the resin and the stainless steel. The result was not successful however.

3. Lacomit varnish was applied on the edges after cold moulding. The plot in figure **7.1** shows scatter and external noise but an obvious pitting potential at ~420 mV and break down in passivity at ~ 920 mV (SCE).

4. A black enamel paint was applied to the edges of the specimen using a brush. The result was good but the enamel paint had a tendency to affect the electrochemistry of the solution and the hydrodynamic flow pattern.

5. The specimen was coated with long curing Araldite, cold moulded resin polished, a thin layer of long curing Araldite was applied again on the surface and finally polished for the scan. The measurement shows a clear plot with two-passivity break down plateaux at 400 mV and at 900 mV as illustrated in figure **7.2.**

6. The duplex stainless steel specimen was coated with gold palladium and then coated with long curing Araldite and cold resin moulded. The results obtained for the passivity potentials breakdown in figure **7.3** were good. Finally, satisfactory results were obtained when a gold palladium coating was used with cold resin moulding.

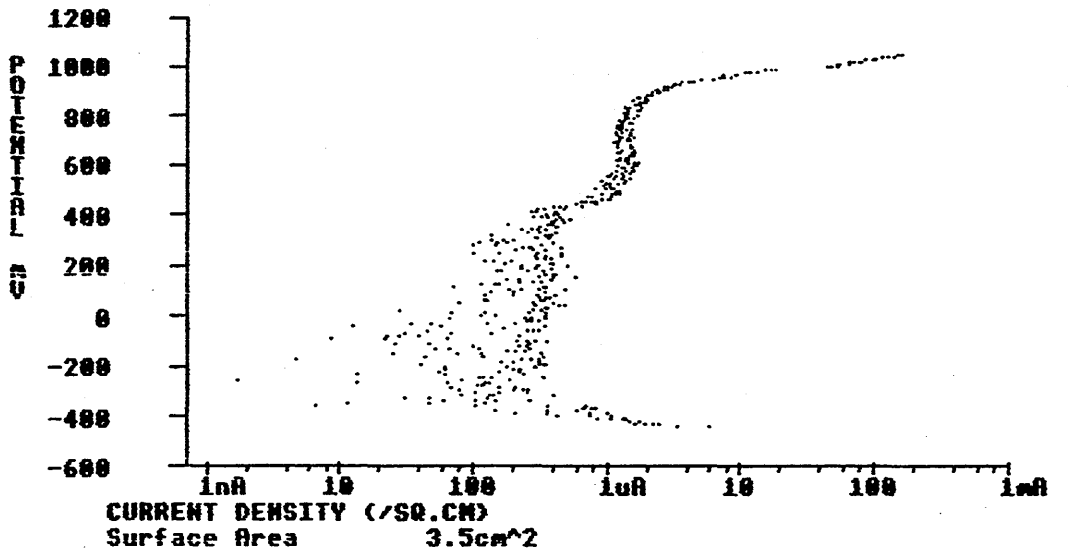

Figure **7.1** Duplex stainless steel (batch A) at fluid velocity of 8.5 m/s with lacomit lacquer, E_r = -247 mV, T = 24 C, E_{redox} = 89 mV, area = 3.5 cm^2

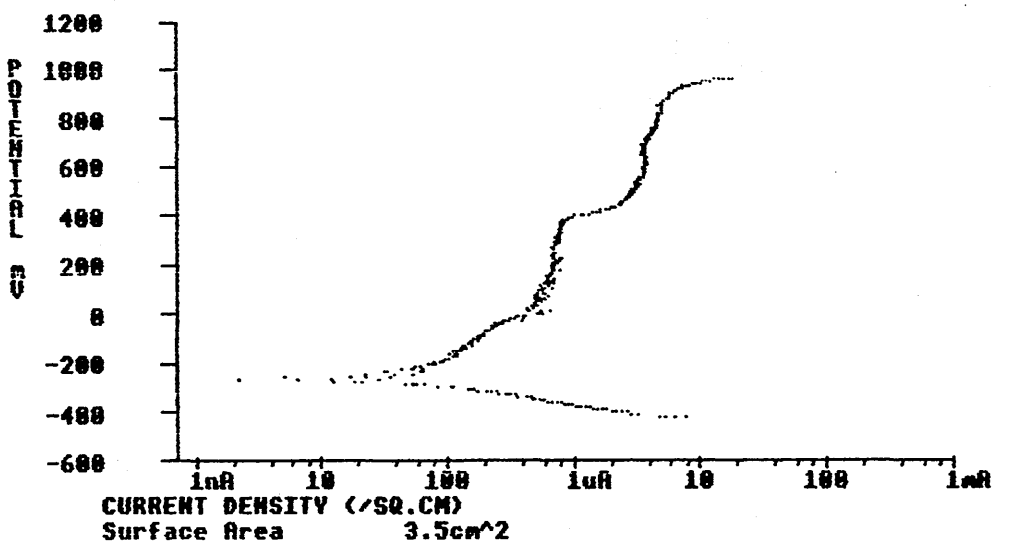

Figure **7.2** Duplex stainless steel (batch A) at fluid velocity of 8.5 m/s, E_r = -226.7 mV, E_{redox} = 21.5 mV, area = 3.5 cm^2

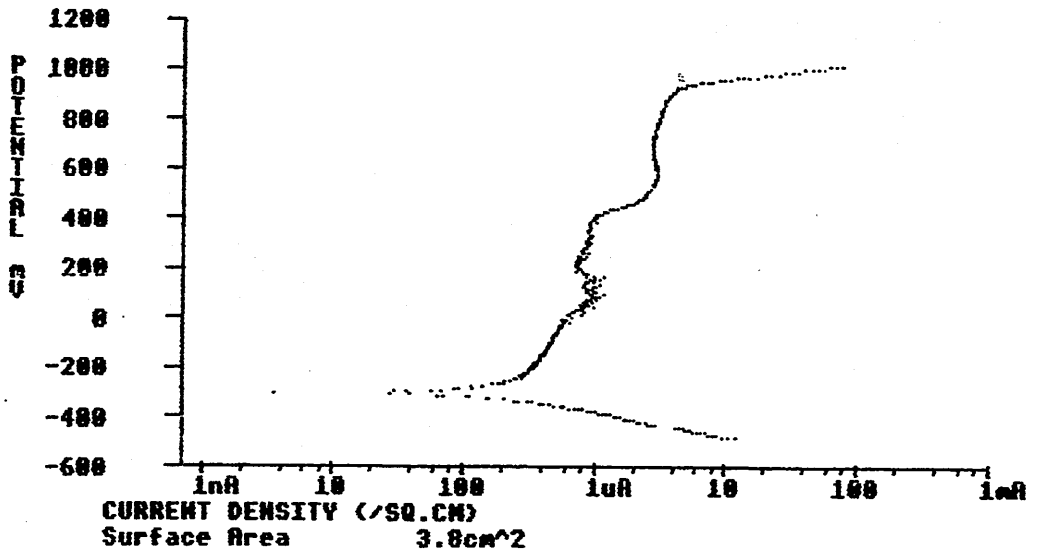

Figure 7.3 Duplex stainless steel (batch A) at fluid velocity of 8.5 m/s, E_r = -286 .1 mV, E_{redox} = 21.7 mV, area = 3.8 cm^2

7.2 Typical potentiodynamic measurements of duplex stainless steel in seawater

Potentiodynamic polarisation scans are particularly useful for evaluating erosion corrosion in seawater. In practice, the potential (mV) was plotted against the current density ($\mu A/cm^2$). The electrochemical scans started from the cathodic (active) potential then increased gradually up towards the noble potentials. Low currents were recorded until the pitting potential E_p, was reached. E_p represents the potential at which the current I_p starts to rise for a small increase in potential. This indicates that the passive film was breaking down and pit initiation sites were developing.

Further up in the positive potential, a significant sudden rise in current occurred over a small shift in potential, showing that the final breakdown potential E_b had been reached with a loss of passive film. The current corresponding to the breakdown potential was denoted I_b, the breakdown current.

7.2.1 Under static and fluid flow conditions

RING 1

Ring 1 (batch A) represents the stagnation region in the water jet impingement system on a flat plate as shown in figure **7.4**. In the active region, crevice corrosion was indicated by scatters in the current near the open circuit potential. As the potential increased anodically, a sudden increase in the current density was observed from 1.5 $\mu A/cm^2$ at 400 mV to 2 $\mu A/cm^2$ at 500 mV potentials. This was due to the first breakdown of the ferrite in the dual microstructure at a potential of 400 mV. Beyond 900 mV, austenite phase dissolution took place, where the current density increased drastically.

When the fluid flowing condition was introduced, the cathodic reaction curve was minimally affected but a shift in the open circuit potential to the negative direction was

observed, which was caused by the passive region being shifted to a higher current density. This was due to more oxygen diffusing to the surface of the specimen.

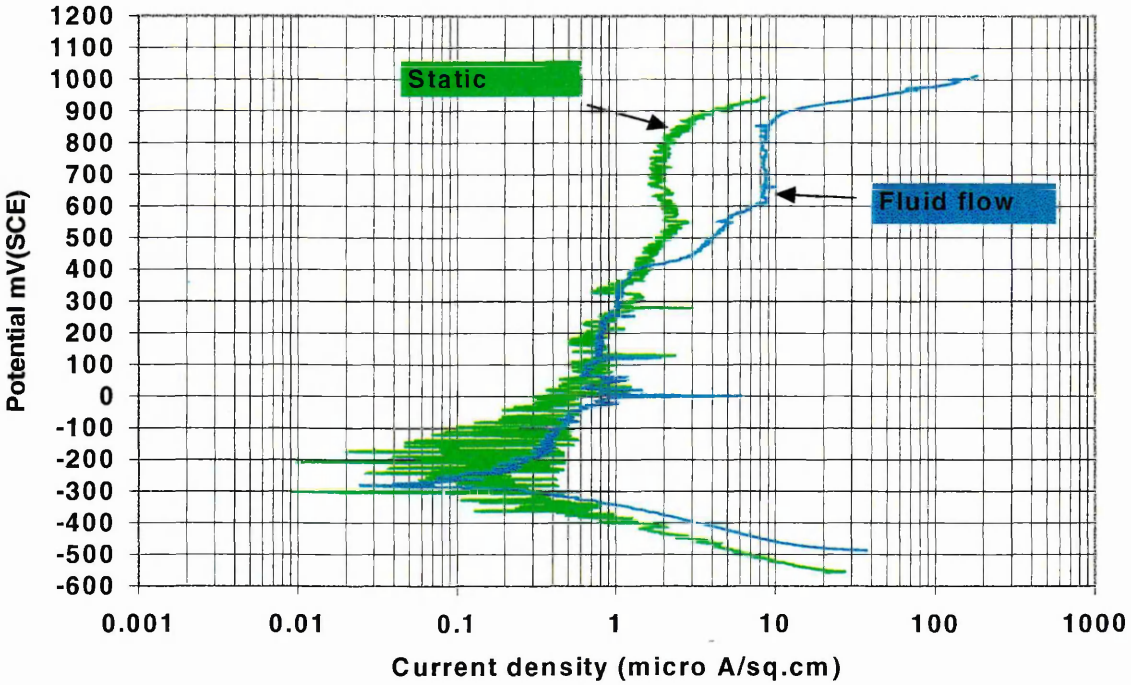

Figure **7.4** Potentiodynamic scan for ***ring 1*** (batch **A**) at static and fluid flow velocity of 8.5 m/s, area = 0.196 cm^2, $E_{rstatic}$ = -356.8 mV, E_{rflow} = -285.5 mV

RING 2

The ring represents the high flow turbulence region on a flat specimen as shown in figure **7.5**. Under static conditions the initial rest potential of the specimen was more of a negative value than the one at flowing conditions. This resulted from using different specimens of the same batch **A**. Consequently, this led to shift in the passive range under static to a higher current density value than the flowing condition. Ultimately, the first breakdown potential of 400 mV (SCE) on the duplex stainless steel (batch **A**) was unclear and the plot only showed the second breakdown at 900 mV, which read a passive current density value of 4 $\mu A/cm^2$. Under flowing conditions, the cathodic reaction was unchanged while the anodic reaction was promoted due to the high shear stress exhibited in this region of the flow and the oxygen transport in the electrolyte. A clear pitting of the ferrite phase at 400 mV (SCE) with current density value of 1$\mu A/cm^2$, this was followed by an increase in current density up to 8 $\mu A/cm^2$ in the delta ferrite pitting range, then a breakdown of the austenite phase at 895 mV.

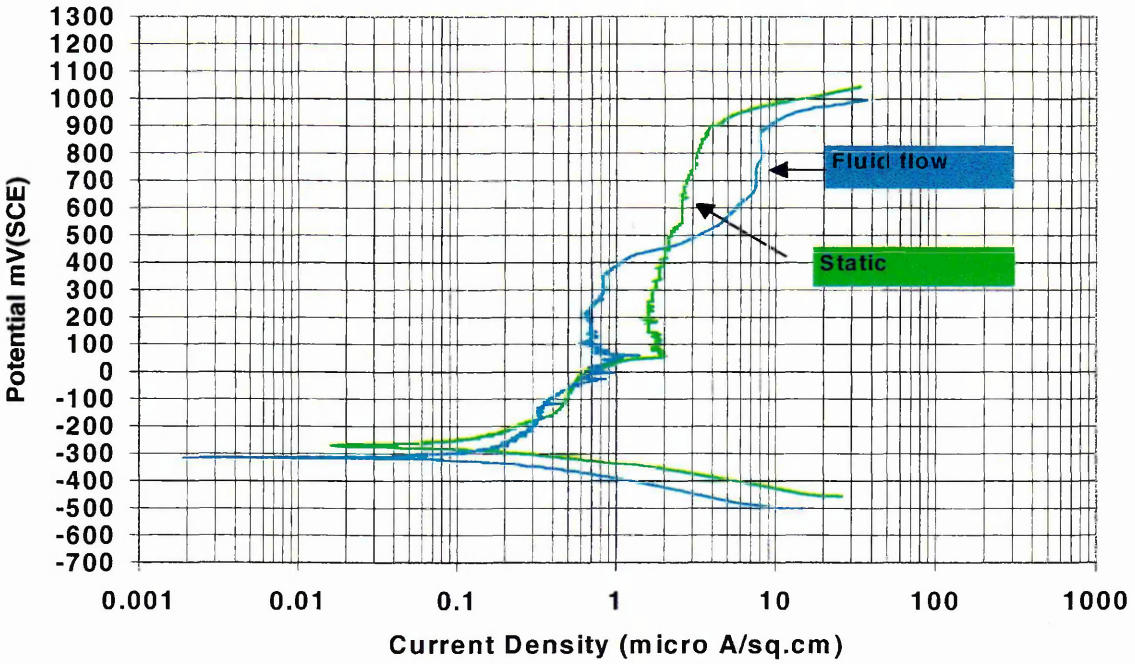

Figure **7.5** Potentiodynamic scan for ***ring 2*** duplex stainless steel (batch **A**) at static and fluid flow velocity of 8.5 m/s, $E_{rstatic}$ = -256 mV, E_{rflow} = -302 mV, area = 0.96 cm^2.

RING 3

Represents the hydrodynamic low turbulence region on a flat specimen. Figure **7.6** shows the electrochemical behaviour of duplex stainless steel (batch **A**) at static and 8.5 m/s fluid flow velocity. The cathodic curve showed a decrease in current density as the potential reached the metal rest potential.

As the potential increased in the noble direction at static condition, breakdown of the ferrite phase in the microstructure occurred at a potential of 380 mV. This was accompanied by a sudden increase in the current density from 1.8 $\mu A/cm^2$ to 3 $\mu A/cm^2$. As the scan progressed, the current density remained constant at a value of 3 $\mu A/cm^2$. At 840 mV a second breakdown of the duplex stainless steel occurred by a sudden increase in current density, due to the dissolution of the austenite phase in the microstructure.

Under flowing conditions, more oxygen diffused to the surface increasing the cathodic reaction. This caused a small shift in the cathodic curve and resulted in a positive shift to the rest potential. The scatter seen in the plot developed due to crevice corrosion development at the metal/resin interface.

With the introduction of flow, the delta ferrite pitting region was shifted to the right to a higher current density value of 7 $\mu A/cm^2$. Eventually, the anodic curves in both conditions nearly met at a potential of 910 mV. At this potential, the anodic reaction on the surface was not affected by the flow conditions.

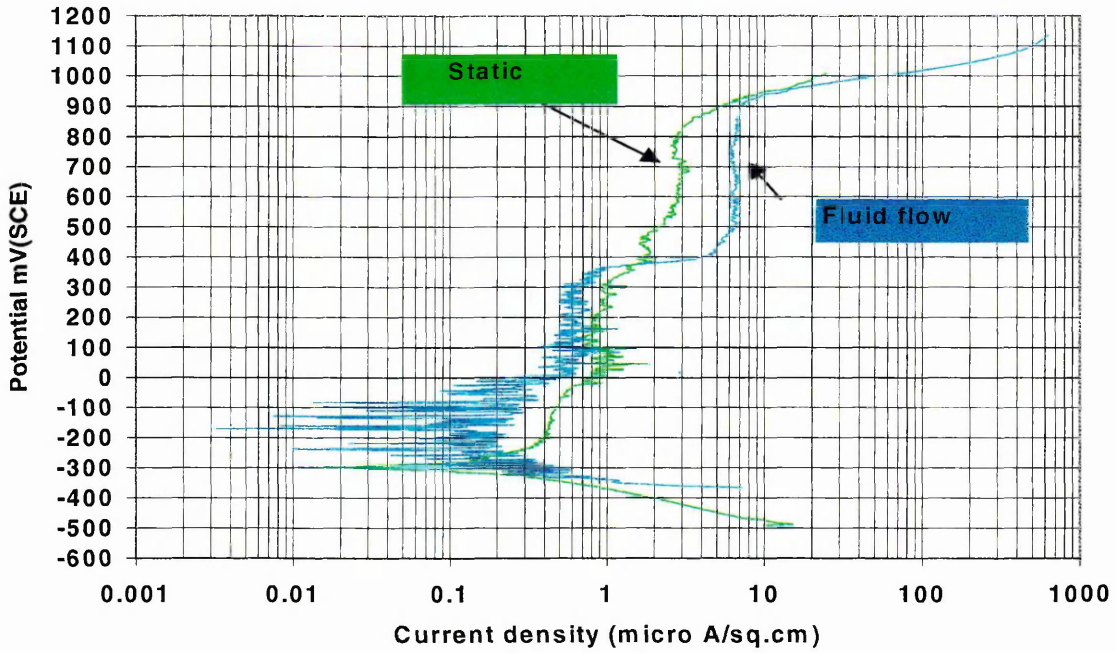

Figure **7.6** Potentiodynamic scan of ***ring 3*** duplex stainless steel (batch **A**) at static and fluid flow velocity of 8.5 m/s, area =1.57 cm^2, $E_{rstatic}$ = -290.1 mV, E_{rflow} = -164.3 mV

7.2.2 At various fluid flow velocities with sand additions

7.2.2.1 Fluid velocity of 8.5 m/s

RING 1

The polarisation behaviour of ***ring 1*** (batch **A**) at ***8.5 m/s*** is illustrated in figure **7.7**. As the sand concentration increased, the open circuit potentials shifted to more negative potential values. The reason was that the I_{pass} increased and so the intersection with the cathodic curve moved to more negative potentials, thus the cathodic curve was unchanged.

The passive film underwent multiple rupture and repassivation events under these conditions, which resulted in a clear double breakdown in the anodic potential at 400 mV and 900 mV. This led to an increase in current density values at 500 mV in the ferrite pitting potential range from 3.9 $\mu A/cm^2$ in the flowing condition to 7.6 $\mu A/cm^2$ at 1 gram of sand, 9.8 $\mu A/cm^2$ at 2 grams of sand and 10.3 $\mu A/cm^2$ at 3 grams of sand concentrations. Similarly, at 0 mV potential a clear shift was observed in current density from 1.6 $\mu A/cm^2$ to 2.1 $\mu A/cm^2$, 5.5 $\mu A/cm^2$ and 6.6 $\mu A/cm^2$ respectively for 1, 2 and 3 grams sand addition. Whilst in the transpassive region the anodic curves changed with the changes which occured in the open circuit potentials due the intersection of the anodic and cathodic curves.

The electrochemical behaviour on ***rings 2*** and ***3*** were very similar. However, the greatest effect of erodent particles was on ring 1 as it represents the stagnation area on a flat plate, which is situated directly under the nozzle. Therefore ***ring 1*** was used as the main focus of the current investigation.

Various fluid flow velocities were chosen to evaluate the erosion-corrosion of the duplex stainless steel. The maximum velocity was 8.5 m/s, as explained above, and the minimum was 7.2 m/s.

Figure 7.7 Potentiodynamic scans for ring 1 (batch A) duplex stainless steel SAF 2205 under fluid flow velocity of 8.5 m/s, with 1, 2, and 3 grams of sand. Erflow = -282.5 mV, Er1g = -371.2 mV, Er2g = -380.7 mV, Er3g = -446.8 mV

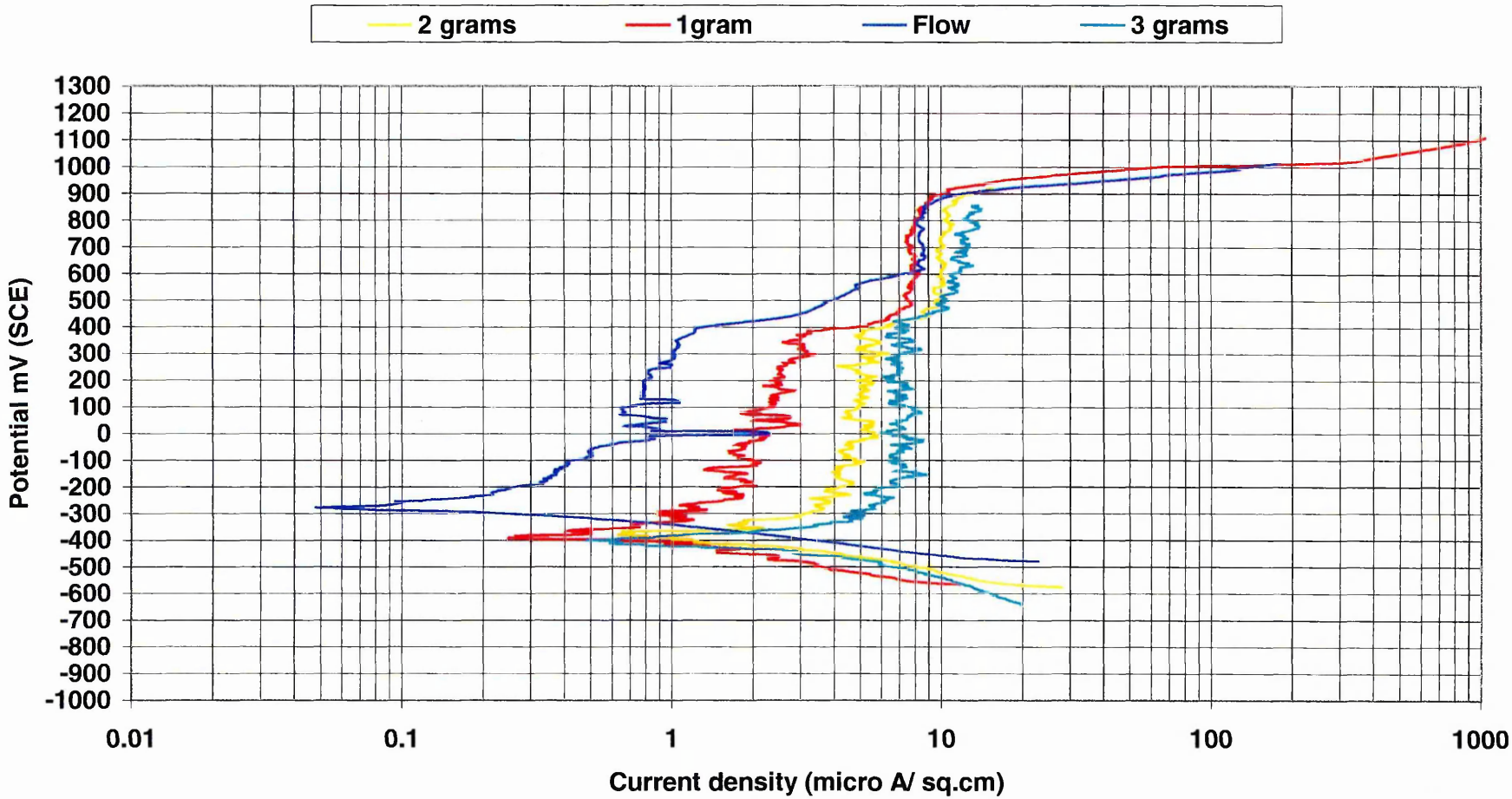

RING 3

Figure **7.8** shows the electrochemical behaviour of ***ring 3*** duplex stainless steel (batch **A**) at fluid flow velocity of ***8.5*** m/s with additions of 1, 2 and 3 grams of sand. The polarisation curves matched each other in all the polarisation regions.

In the active regions of the duplex stainless steel, similar cathodic curves existing at each different sand concentration were developed. As the potential increased anodically, pitting and crevice corrosion showed themselves as scatter in the range from –250 mV to 350 mV.

At 400 mV a sudden increase in current density from a value of 0.9 $\mu A/cm^2$ to 9 $\mu A/cm^2$ resulted from a clear breakdown of the delta ferrite phase. In the delta ferrite pitting region of the alloy, a simultaneous recovery of the passive film occurred in the range of 500 mV up to 880 mV with a constant dissolution rate of the ferrite phase and a uniform low constant current density. At 900 mV at the transpassive, a complete dissolution of both phases took place. In general, the electrochemical behaviour of ring 3, which represents the low turbulence region on a flat plate, showed little effect of sand impacts on the passive film.

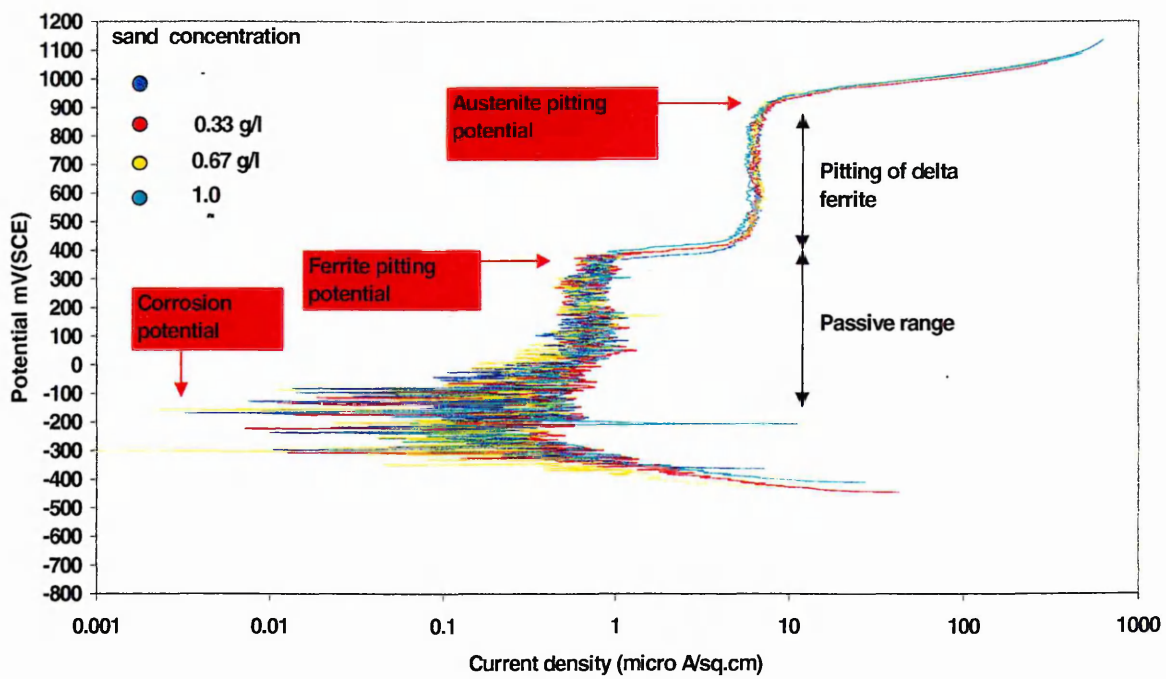

Figure **7.8** Potentiodynamic scans for ***ring 3*** duplex stainless steel (batch **A**) at fluid flow velocity of 8.5 m/s with 1, 2 and 3 grams of sand

7.2.2.2 Fluid velocity of 7.9 m/s

Ring 1 duplex stainless steel specimen (batch **A**) was exposed to a fluid velocity of ***7.9 m/s***, as shown in figure **7.9**, with various sand concentrations. As the sand particles increase, the rate of damage to the passive film increases, resulting in the production of more current density.

By comparing the potentiodynamic scans for duplex stainless steel at 7.9 m/s velocity with 8.5 m/s, the results revealed a similar double breakdown of the microstructure phases and a clear shift in current density. The scan at 7.9 m/s shows some scatter at 4 grams of sand. This could be related to crevice corrosion attack at the metal resin interface and a depassivation / repassivation process of the surface oxide film.

From the potentiodynamic scans, the active regions indicated a clear shift in the open circuit potentials to more negative potentials. This led to a negative shift in the anodic reaction curves of 1, 2 and 3 grams of sand when compared to the anodic curve under flowing conditions. But if the scan proceeded further to a higher cathodic potential, the cathodic reaction matched up together. Only at 4 grams sand concentration was the cathodic curve of less negative value. This was due to changes in the aeration level.

At flowing condition, the passive current density was reading 5 $\mu A/cm^2$ at 600 mV anodic potential. With the increase in solid particle impingement, the passive film underwent multiple depassivation and repassivation events. This led to an increase in the current density at +500 mV to values from 3.4 $\mu A/cm^2$ to 4.2 $\mu A/cm^2$, 6.7 $\mu A/cm^2$, 9.5 $\mu A/cm^2$ and 8.5 $\mu A/cm^2$ respectively for flow only and 1, 2, 3 and 4 grams of sand concentrations. At 0 mV potential, the current density readings were 0.68 $\mu A/cm^2$, 0.85 $\mu A/cm^2$, 2.4 $\mu A/cm^2$, 5.1 $\mu A/cm^2$, 5.7 $\mu A/cm^2$ respectively.

In the transpassive region, both ferrite and austenite phase dissolution took place, the anodic reactions on the surface of the metal were shifted by the increase in erodent concentration. At 3 grams of sand, the anodic curve had a less positive value due to the less negative rest potential exhibited at this condition.

Figure 7.9 Potentiodynamic scan of ring 1 at fluid flow velocity of 7.9 m/s with 1, 2, 3 grams (batch A), and 4 grams of sand (batch B). Erflow = -218 mV, Er1g = - 216 mV, Er2g = - 314 mV, Er3g = - 390 mV, Er4g = -221 mV

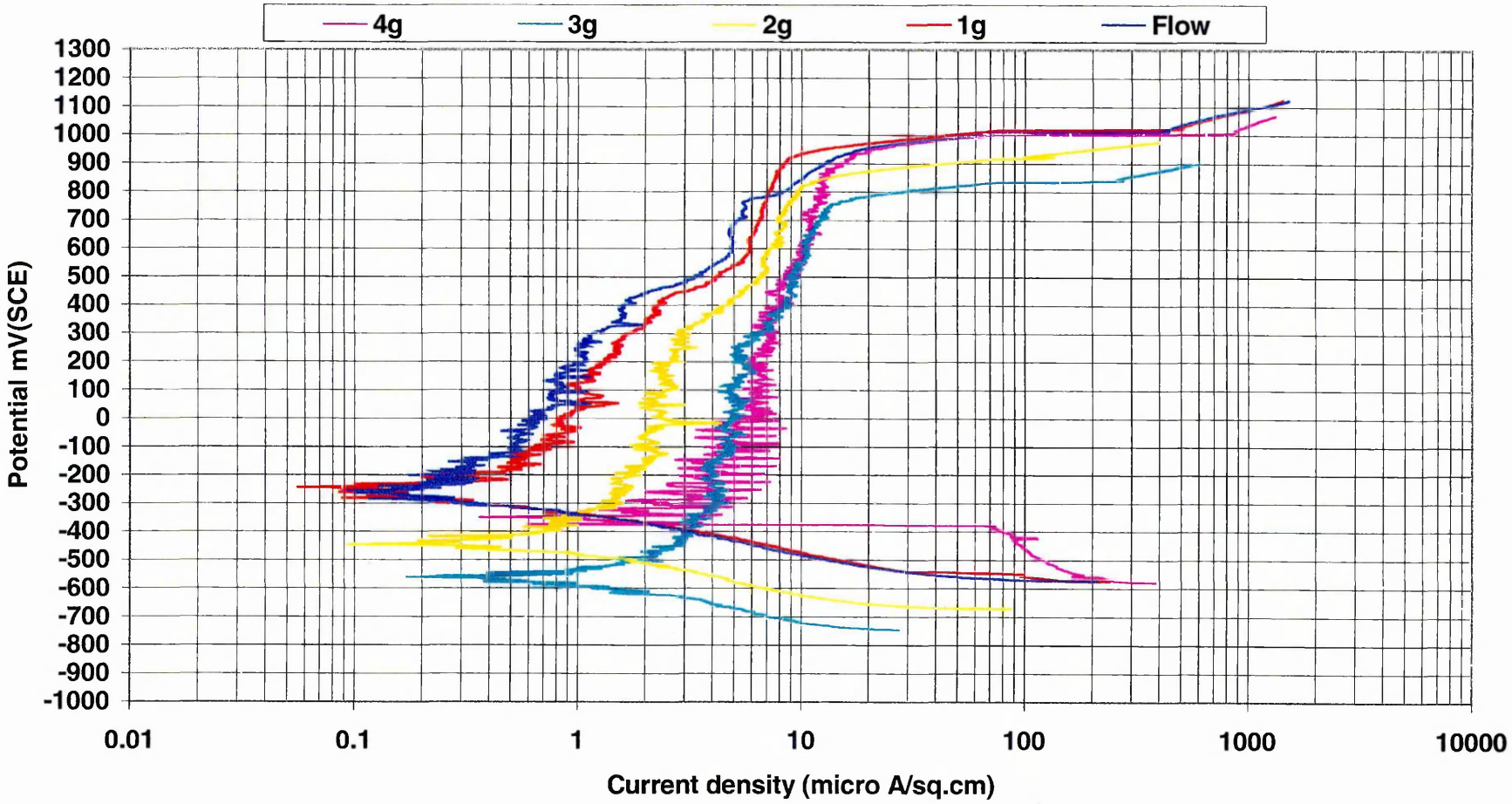

7.2.2.3 Fluid velocity of 7.8 m/s

At ***7.8 m/s*** fluid velocity, the dissolution behaviour of duplex stainless steel (batch **A**) was sensitive to sand concentration. A general reduction in the anodic curves was observed from the normal breakdown potential of 900 mV to 780 mV. This was related to the high negative rest potentials (E_r) especially at the open circuit potential prior to the potentiodynamic measurements and the enlargement of the cathodic areas exposed to the solution from the propagation of seawater at the metal/resin interfaces and uncovering the gold palladium coating. The minimum current density value under lowest fluid velocities at 500 mV and 0 mV were 2.8 $\mu A/cm^2$ and 0.49 $\mu A/cm^2$ while the maximum value readings at highest fluid velocities were 3.7 $\mu A/cm^2$ and 1.98 $\mu A/cm^2$ as shown in figure **7.10**.

The potentiodynamic scans at 7.8 m/s fluid velocity demonstrated a shift in current density but were not as clear as the sand content increased, owing to the reduction in the total area assembly of the polarisation scans. This was due to the repeated use of the same specimen, with the existence of crevice corrosion at metal/resin interface from previous scans, and the high negative rest potential at the starting condition. Eventually, when comparing 7.8 m/s fluid velocity scans with the scans at 7.9 m/s, in general the former velocity demonstrated less current density increase at various sand concentrations than the latter fluid velocity. This was due to the increase in the mean time between impacts of sand particles on the surface of the specimen.

7.2.2.4 Fluid velocity of 7.5 m/s and 7.2 m/s

As the fluid velocity decreased more to ***7.5 m/s*** and ***7.2 m/s***, a similar pattern of electrochemical behaviour with sand impingement resulted from the duplex stainless steel specimens. As indicated in figures **7.11-7.12**, the double breakdown of the oxide films were not so clear. Overall reduction in current density at the delta ferrite pitting ranges of 500 mV for both velocities were between 1 $\mu A/cm^2$ and 1.9 $\mu A/cm^2$. At 0 mV the current dissolution values were between 0.1 $\mu A/cm^2$ and 0.3 $\mu A/cm^2$. Evidence of scatter increased in the two velocity scans, owing to the repeated use of the same specimen for every scan, also to electrolyte seepage in the resin/metal interface which supports the promotion of crevice corrosion.

This reduction could be explained by a reduction in the number of transferred electrons between the bulk solution and the metal ions which led to a higher passivation domain in the plots. The negative shift in open circuit potentials changed the anodic curve positions to a higher current density while the cathodic curves stayed unaffected. Both polarisation scans were severely affected by the increase in the crevice corrosion initiation between the metal/resin interface.

Table **7.1** contains a summary of the potentiodynamic current densities for different fluid velocities and sand particle concentrations. Reduction in current density occurred as fluid flow velocity decreased with sand concentration and obvious initiation of crevice corrosion in every scan. Those current density developments resulted from the depassivation and repassivation processes which occurred to the surface of the duplex stainless steel specimens.

Figure 7.10 Potentiodynamic scan of ring 1 (batch A) under fluid flow velocity of 7.8 m/s with 1, 2, 3, and 4 grams of 277 micrometer of impinging sand particles. Erflow = -557 mV, Er1g = - 451 mV, Er2g = -605 mV, Er3g = -573 mV, Er4g = -596 mV

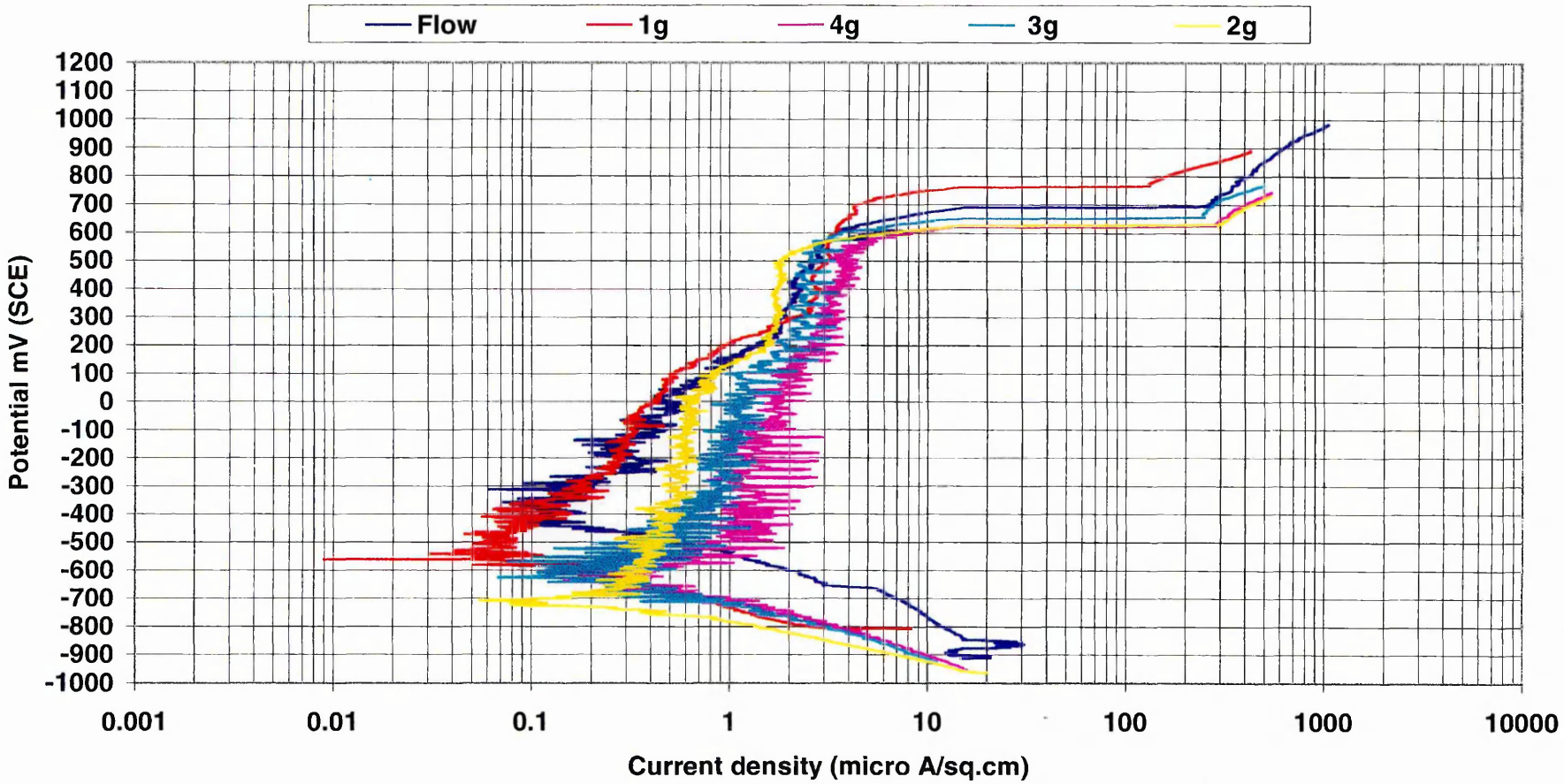

Figure 7.11 Potentiodynamic scan of ring 1 (batch A) at fluid flow velocity of 7.5 m/s with 1, 2, 3, 4 grams of sand. Erflow = -125 mV, Er1g = -173 mV, Er2g = -177 mV, Er3g = -173 mV, Er4g = -203 mV

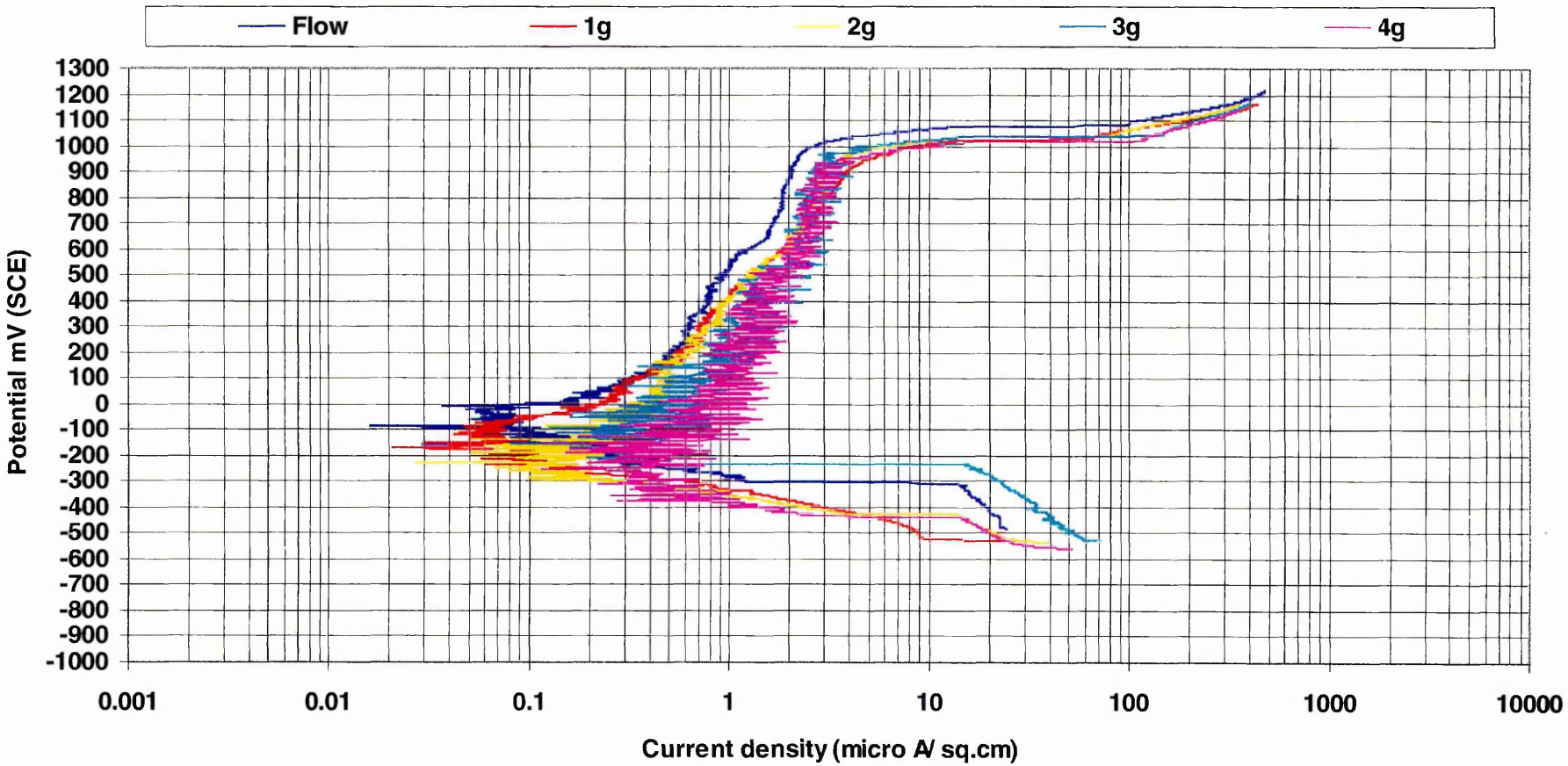

Figure 7.12 Potentiodynamic scan of ring 1 (batch A) at fluid flow velocity of 7.2 m/s with 1g, 2g, 3g, and 4g of sand. Erflow = -277 m, Er1g = -336 mV, Er2g = -291 mV, Er3g = -210 mV, Er4g = -223 mV

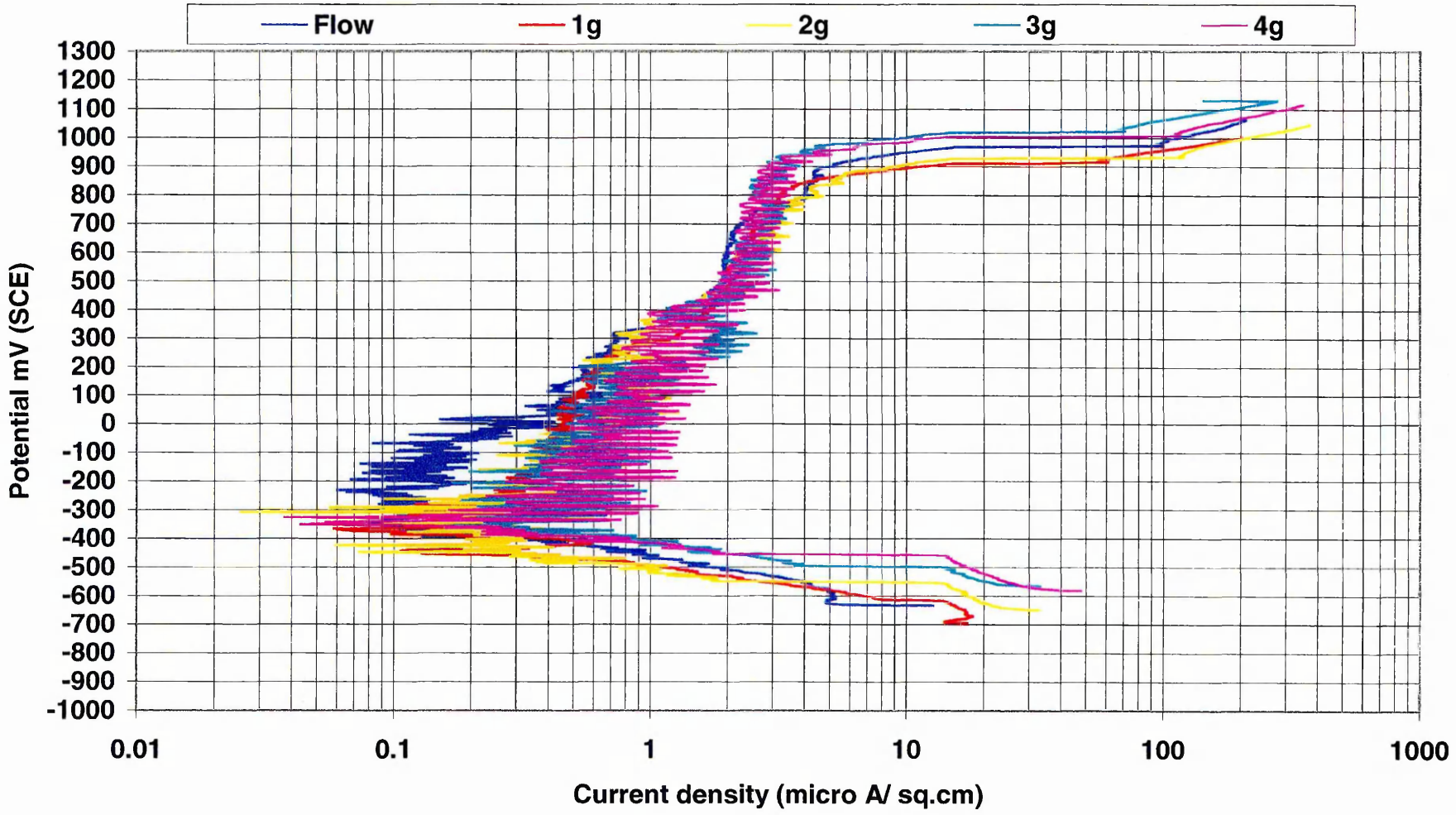

Table **7.1** Summary of average current densities measured from potentiodynamic scans for different fluid flow velocities and sand additions

Figure No.	Fluid flow velocity (ms^{-1})	potential (mV)	Current density at fluid flow state (μA /sq.cm)	Current density at 1 gram of sand (μA /sq.cm)	Current density at 2 grams of sand (μA /sq.cm)	Current density at 3 grams of sand (μA /sq.cm)	Current density at 4 grams of sand (μA /sq.cm)	Duplex stainless steel Batch
7.8	8.5	0	1.6 ± 0.68	2.1 ± 0.11	5.5 ± 0.21	6.6 ± 0.44		A
		500	3.9 ± 0.20	7.6 ± 0.16	9.8 ± 0.27	10.3 ± 0.29		
7.9	7.9	0	0.7 ± 0.04	0.9 ± 0.02	2.4 ± 0.12	5.1 ± 0.22	5.7 ± 0.32	A+B*
		500	3.4 ± 0.01	4.2 ± 0.07	6.7 ± 0.22	9.5 ± 0.25	8.5 ± 0.29	
7.10	7.8	0	0.5 ± 0.03	0.4 ±0.01	0.7 ± 0.05	1.1 ± 0.14	2.0 ± 0.25	A
		500	2.8 ± 0.03	3.2 ± 0.02	1.8 ± 0.02	2.9 ± 0.36	3.7 ± 0.47	
7.11	7.5	0	0.1 ± 0.03	0.2 ± 0.02	0.4 ± 0.04	0.6 ± 0.21	1.0 ± 0.16	A
		500	1.0 ± 0.03	1.3 ± 0.03	1.3 ± 0.03	1.7 ± 0.04	1.6 ± 0.21	
7.12	7.2	0	0.3 ± 0.05	0.5 ± 0.02	0.8 ± 0.07	0.6 ± 0.08	1.0 ± 0.16	A
		500	1.9 ± 0.02	2.1 ± 0.02	1.9 ± 0.03	2.2 ± 0.15	2.0 ± 0.14	

Notes:-

- (*) means the specimen was changed to batch **B** because of the unavailability of batch **A** material.
- The maximum average passive current density produced was 7.5 micro A/sq.cm for potential range between -200 mV (SCE) to 380 mV (SCE) at 3 grams sand concentrations under fluid flow velocity of 8.5 m/s.

7.2.3 Electrochemical open circuit measurements

Examination of the open circuit potentials gave qualitative information on the effect and the reactivity of duplex stainless steel with the seawater solution. Worsfold[165] mentioned in his open circuit measurement results, that the negative surges in potential were attributed to the anodic dissolution of the protective oxide film, while positive surges were attributed to cathodic reaction. Figure **7.13** shows the open circuit measurements of ***rings 1, 2*** and ***3*** at static, fluid flow velocity of 8.5 m/s with and without sand impingement.

The open circuit potential curve for both ***rings 1*** and ***2***, at the static condition stayed constant in the active region for nearly one hour at a maximum value of –50 mV. With the assistance of aeration, the residual oxygen level in the solution was constant which kept the passive film thickness stable. As the oxygen content in the solution started to decrease, after two hours the redox potential dropped to a negative value of –70 mV. This was due to the electrochemical reactions at various sites plus crevice and pitting corrosions initiation.

At ***ring 3*** a different pattern curve developed in static conditions, the result showing a positive shift in the redox potential towards the noble potentials direction combined with a gradual increase after two hours to a value of 30 mV. This positive potential was related to the stable oxide film at the surface of ring 3, which, owing to the large surface area of the specimen and the high ionic exchange between various anodic and cathodic sites, led to intacted passive film.

This negative trend in the open circuit potentials was related to the anodic dissolution at flaw and pit sites in the oxide films, while the positive shift in ring 3 was due to the cathodic reaction.

Under flowing conditions, all the ring redox potentials shifted in the noble direction. After two hours ***rings 2*** and ***3*** potential patterns were elevating to more noble potentials of 110 mV and 180 mV respectively. This was because more oxygen was adsorbed and absorbed to the surface.

While ***ring 1*** was located directly under the nozzle, the open circuit potential versus time graph resulted in fluctuation in the open circuit potential in the first hour, showing a value of 70 mV. This was due to the simultaneous repassivation and depassivation process of the oxide film. In the second hour the potential had a slow, gradual reduction to a value of 40 mV.

With 3 grams sand impingement, both ***rings 2*** and ***3*** potential behaviour curves were still in the positive potential values. ***Ring 2*** dropped in potential in the first few minutes then increased again and continued elevating to a value of 190 mV. The reason for this was the destruction made by the sand impingement and the flow shear stress to the oxide film was overcome by the simultaneous passivation effect of the duplex stainless steel.

Ring 3 exhibited a big drop in potential from 180 mV to 80 mV immediaely the sand was introduced to the flow. During the first 45 minutes the redox potential continued to

decrease to a minimum value of 50 mV, afterwards the potential recovered to a constant potential of 80 mV. These conditions were related to the same reasons as ring 2 under sand impingement.

At ***ring 1*** a negative constant potential was developed as seen in figure **7.13**, with severe fluctuation in potential between a value of –40 mV and –70 mV. These fluctuations were due to the passive film undergoing severe rupture and dissolution of its alloy compositions.

Figure 7.13 Rings 1, 2 and 3 (batch A) open circuit measurements held potentiostatically at -600 mV for 1 hour then scanned at open circuit for 6 hours under static, fluid flow velocity of 8.5 m/s with and with out sand addition

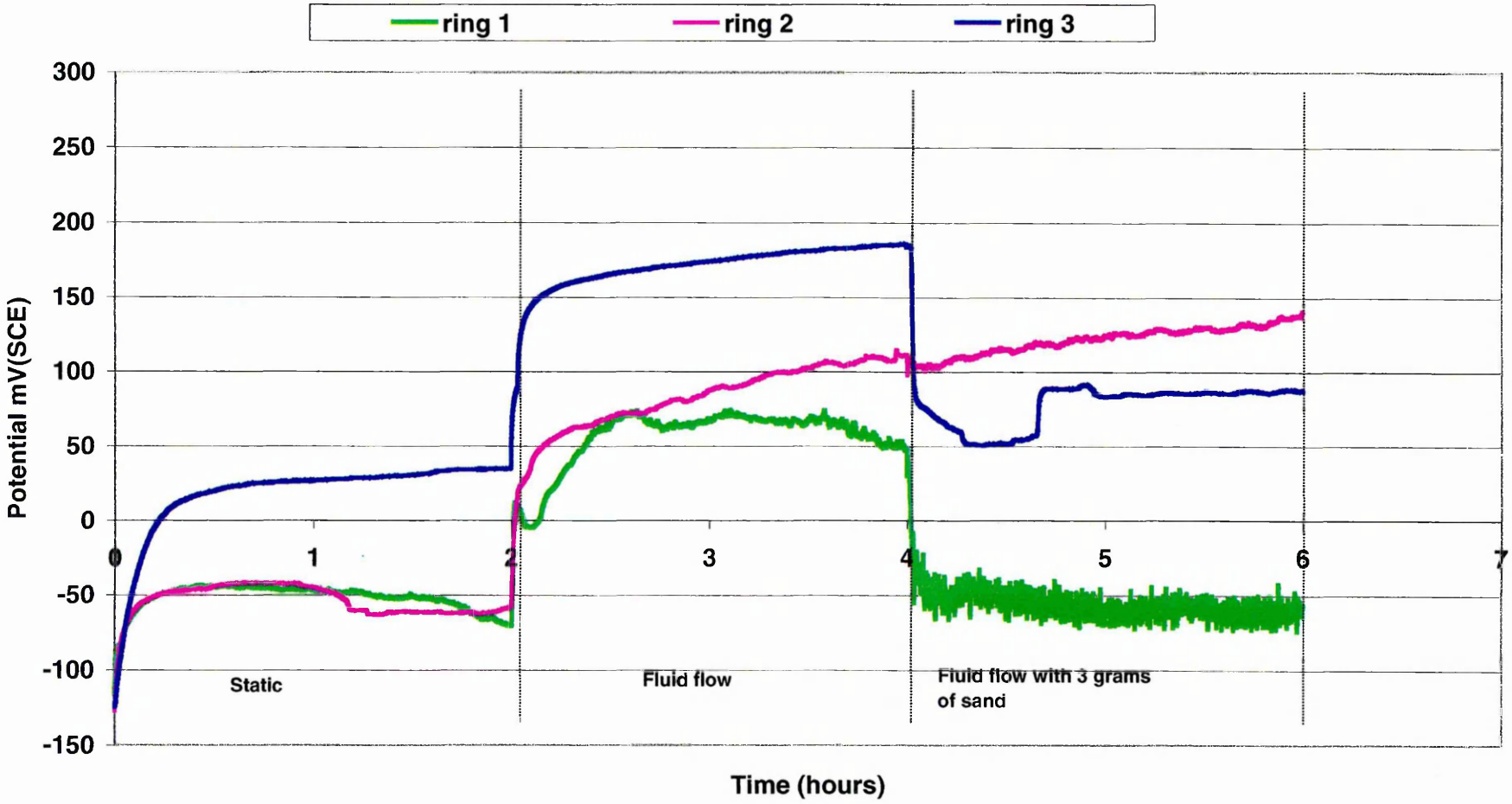

7.2.4 Electrochemical current density measurements

The current density in a potentiodynamic scan is the result of both anodic and cathodic reactions on the surface of the duplex stainless steel. To duplicate the behaviour of current densities in the potentiodynamic measurements, a potentiostatic experiment measuring the current versus time at fixed potentials was recorded for a duplex stainless steel specimen during immersion in a seawater solution.

According to the theoretical Evans diagram below:

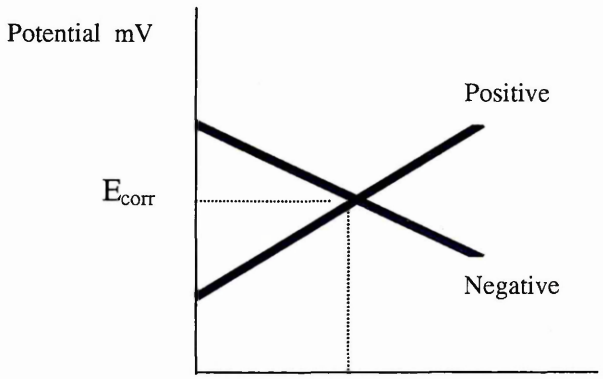

Figure **7.14** Shows theoretical Evans diagram

And Evans diagram shown experimentally:

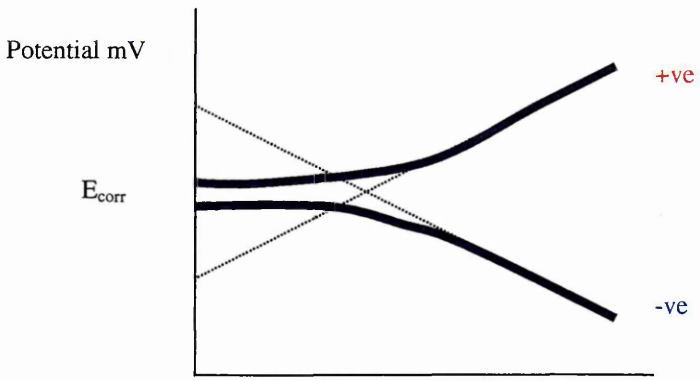

Figure **7.15** Shows experimental Evans diagram

The extension of both anodic and cathodic curves in Evans theoretical and experimental diagrams will intersect values of negative and positive in the potential axis. The resultant current density (i_{res}) value produced, which is equal to the difference in anodic and cathodic currents densities ($i_a - i_c$) that lay within those regions, is affected (see figure **7.16**). This leads to the holding potential having to be kept away from the effect of each anodic and cathodic extension (shaded areas), hence the resultant current density under fluid flow will indicate a positive sign current density. Eventually, the shaded area of the cathodic reaction effect increases in fluid flow with sand addition rather than fluid flow only as shown in figure **7.16**.

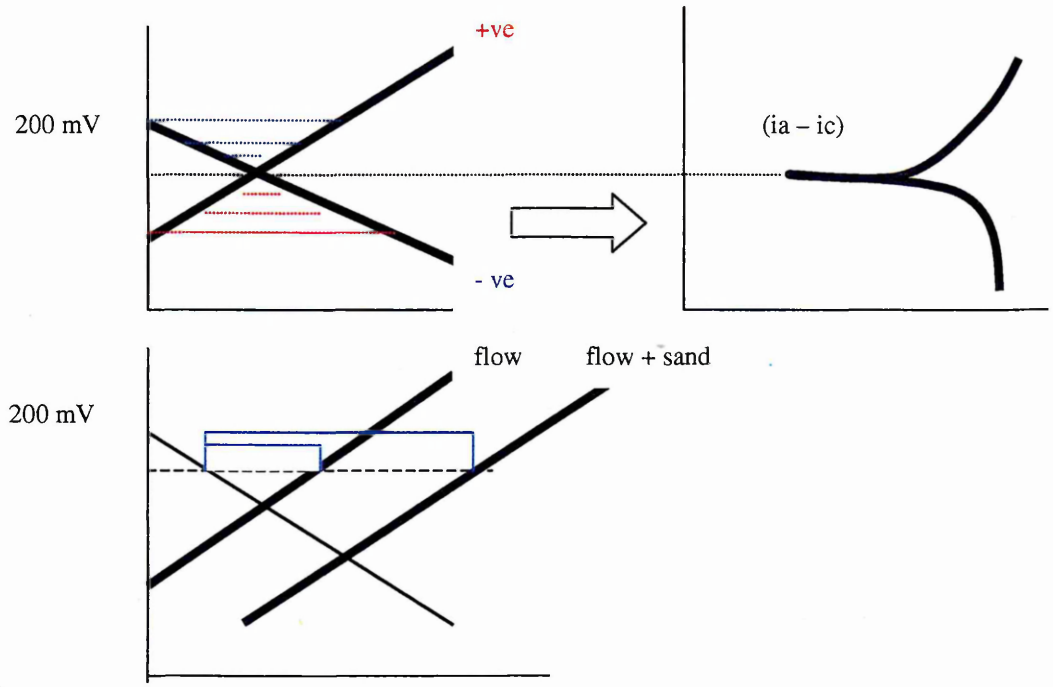

Figure **7.16** Illustrates the cathodic and anodic reaction shaded areas

For example in figure **7.7**, the potentiodynamic scan of ***ring 1*** at fluid flow velocity of 8.5 m/s. At 3 grams sand concentration, the extension curve of the cathodic potential values range between –650 and –500 mV (SCE) and tend to intersect the positive potentials between 200 mV (SCE) to 250 mV (SCE). This indicates that if a specimen is held at those positive potentials, then the resultant current density is going to be affected by the cathodic reaction blue region extension.

However, at any fixed potential above the range of 200 mV (SCE) to 250 mV (SCE), the resultant current density value produced will be of a positive sign and out of the effect of the blue region range. For example, figure **7.21** shows that at fixed potential of 300 mV (SCE), both current density values at fluid flow with and without sand addition are positive. While in figure **7.20** at a fixed potential of 100 mV (SCE), the current density produced after 30 minutes under flowing conditions is still a negative value. This indicates that the resultant current density value was not completely anodic because of the effect of the cathodic reaction.

Several attempts were carried out at different constant potentials such as –100, –200 and 100 mV (SCE) to raise the flowing condition current density values to the positive anodic side, but, unfortunately, all ended with negative current density values. Only at a potential of 300 mV was a positive current reading obtained.

7.2.4.1 At constant potential of –100 mV

The cathodic electrochemical scan as illustrated in figures **7.17** and **7.18** for ***rings 2*** and ***3***, shows that the potential held at –100 mV (SCE). The resultant current under fluid flow was in the negative value region. This means that the positive anodic current is still smaller than the cathodic current and the potential is in the area of cathodic effect.

7.2.4.2 At constant potential of –200 mV

The experiment procedure is the same as previous potential of –100 mV (SCE), but the potential was held at –200 mV (SCE), ***ring 1*** duplex stainless steel as indicated in figure **7.19**, under fluid flow condition. Unfortunately the current density values gradually started to creep toward the negative values. When the 3 grams of impinging sand was added, the passive current value developed did not correspond to the current density value for ***ring 1*** at the potentiodynamic scan (Figure **7.7**). This was due to the use of new specimens of the same batch, which have less crevice and pitting inclusions on the surface.

In the results strong random oscillations of current densities were found; a typical feature of all performed experiments. These oscillations according to Hakkarainen[84] were caused due to irregular distortions to the polarisation curves recorded in the computer memory as a set of momentary combinations of current and (uncorrected) potential values.

The findings indicated that these fluctuations in current density were related to depassivation and repassivation of the passive film, and also due to the current produced from the crevice and pitting corrosions exhibited on the surface of the specimen.

7.2.4.3 At constant potential of +100 mV

Despite the current developed under sand impingement for ***ring 1*** being of a positive value (7.4 μA/sq.cm) and similar to the value at the polarisation measurement in figure **7.7**, the resultant anodic current density produced at the flowing condition is still a negative sign, which is the effect of the cathodic extension region as shown in figure **7.20**.

7.2.4.4 At constant potential of +300 mV

This potential was chosen to be away from the effect of cathodic intersection. At the potentiodynamic scan of ***ring 1*** and at a potential of +300 mV, the current density under flowing condition was 1.2 $\mu A/cm^2$. This corresponded to the current versus time curve for ring 1 at flowing condition in figure **7.21**, the value of the passive current density being 1 $\mu A/cm^2$. With the sand addition in figure **7.21** a clear positive shift in current density readings reached up to 7.4 $\mu A/cm^2$ which was a duplicate value to the polarisation scan with sand.

Similar patterns of positive current density values were developed in ***rings 2*** and ***3*** as illustrated in figures **7.22** and **7.23,** both under fluid flowing conditions with and without sand additions. Hence the effects of sand impact were very little, with current density values for ring 2 equal to 1 $\mu A/cm^2$ and for ring 3 equal to 2 $\mu A/cm^2$.

7.3 Metal loss determination at 100 mV and 300 mV potentials

The duplex stainless steel was exposed to two different potentials of 100 and 300 mV (SCE). The potentiodynamic current density readings at each potential were converted to metal loss using Faraday's Law. (Note: a current density of 1 $\mu A/cm^2$ is equivalent to 0.01 mm/year weight loss of stainless steel due to corrosion process). Therefore, the corrosion rate of duplex stainless steel at each potential was determined by the metal loss measurements in mm/year as shown in figure **7.24.** Thus the eroded metal loss in

figure **7.24** measured values at potentials of 100 and 300 mV (SCE) which were in the range of 0.05 to 0.1mm/y.

By comparing the metal loss readings here, with the polarisation scan for ring 1 at 100 mV and 300 mV with 3 grams of sand at fluid velocity of 8.5 m/s (figure **7.7**), metal loss values of 0.08 mm/year and 0.09 mm/year were obtained. This clarified that the corrosion rate of metal was similar at different potentials.

Figure 7.17 Ring 2 (batch A) held potentiostatically at - 600 mV for 1 hour then held at constant potential of -100 mV for 90 minutes at fluid flow velocity of 8.5 m/s with sand addition

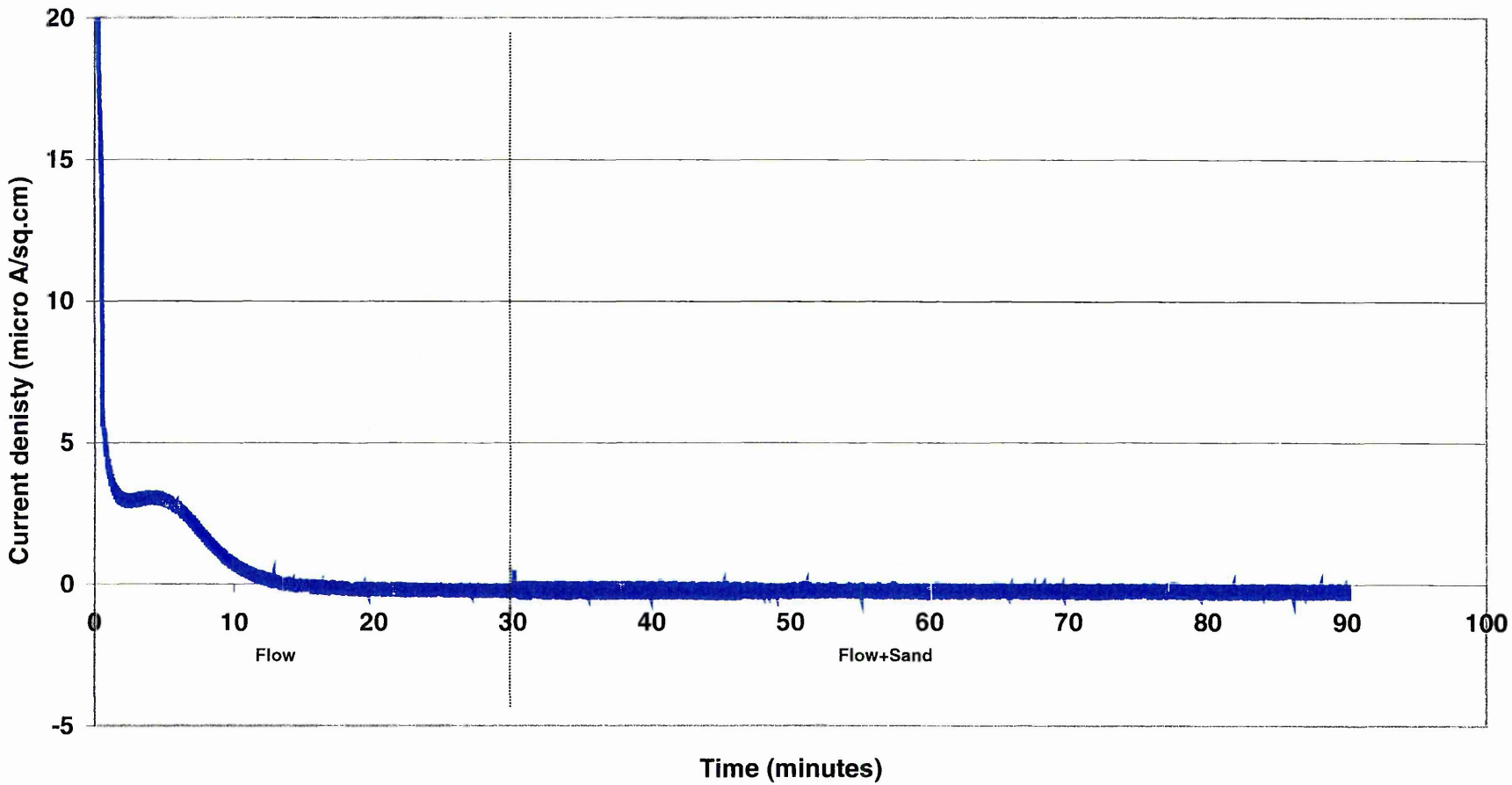

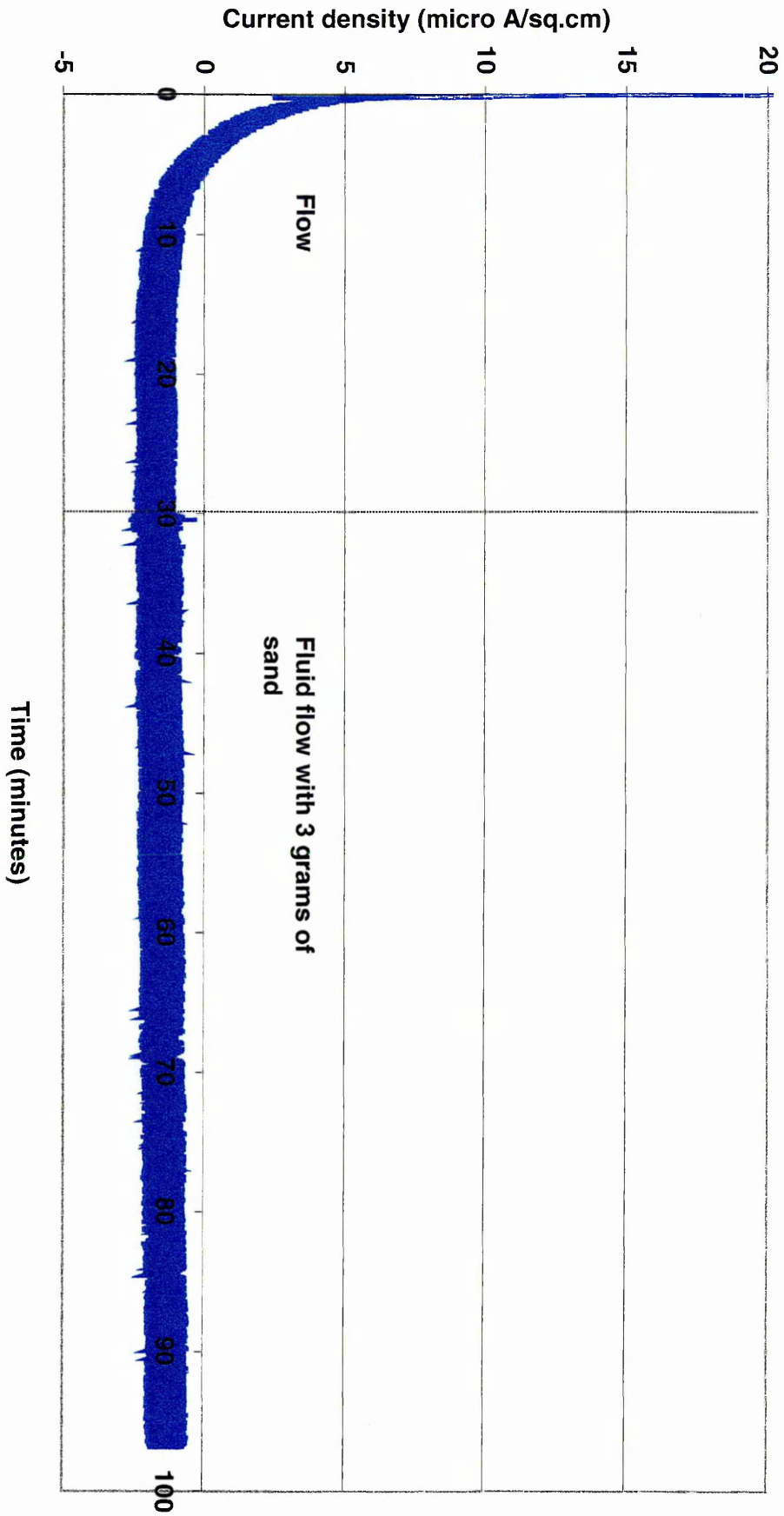

Figure 7.18 Ring 3 (batch A) held potentiostatically at - 600 mV for 1 hour then held at constant potential of-100 mV for 90 minutes at fluid flow velocity of 8.5 m/s with sand addition

Figure 7.19 Ring 1 (batch A) held potentiostatically at -600 mV for 1 hour then held at constant potential of -200 mV for 90 minutes at fluid flow velocity of 8.5 m/s with sand addition

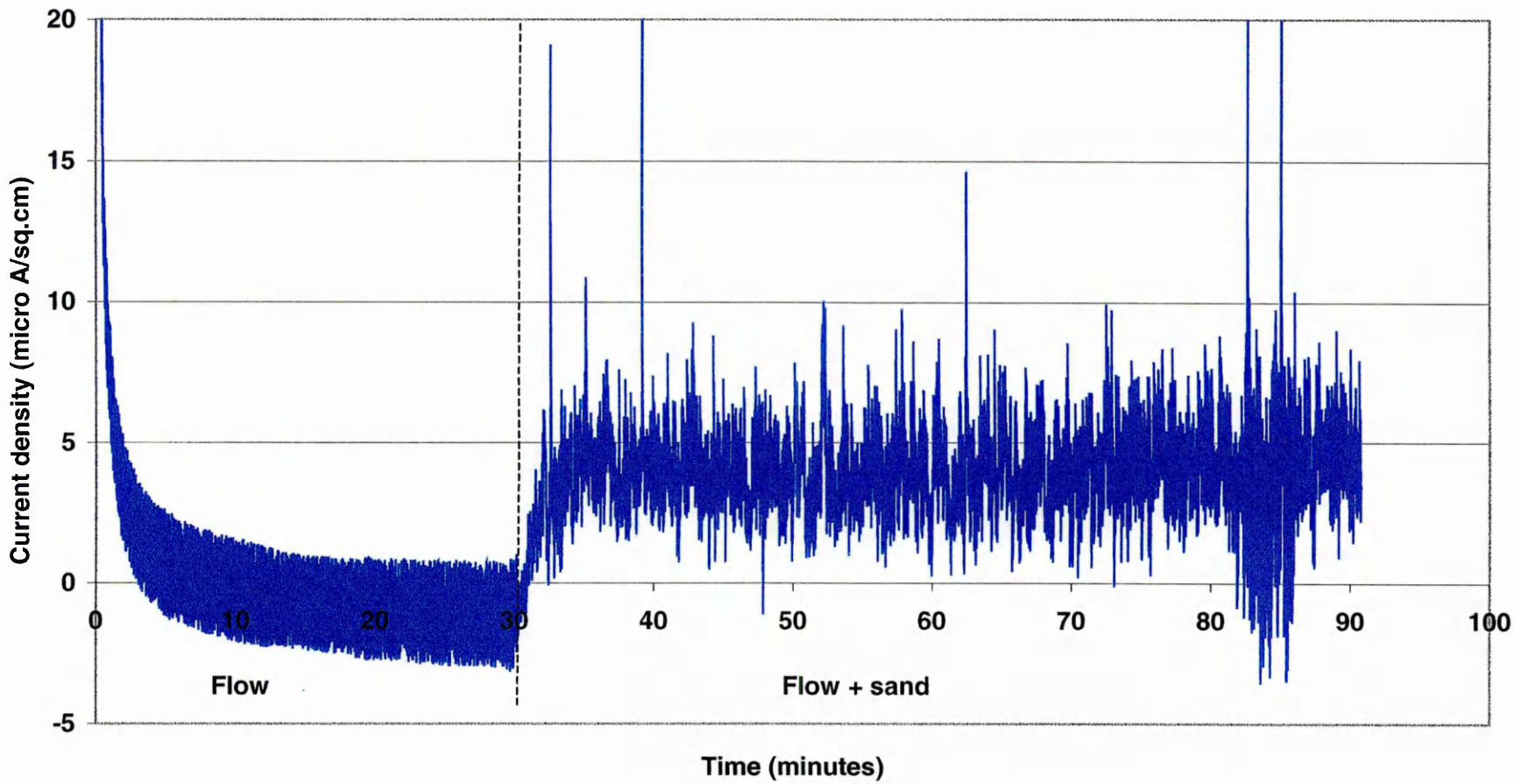

Figure 7.20 Ring 1 (batch A) held potentiodstaticlally at -600 mV for 1 hour then at constant potential of +100 mV(SCE) for 90 minutes under fluid flow velocity of 8.5 m/s with sand addition.

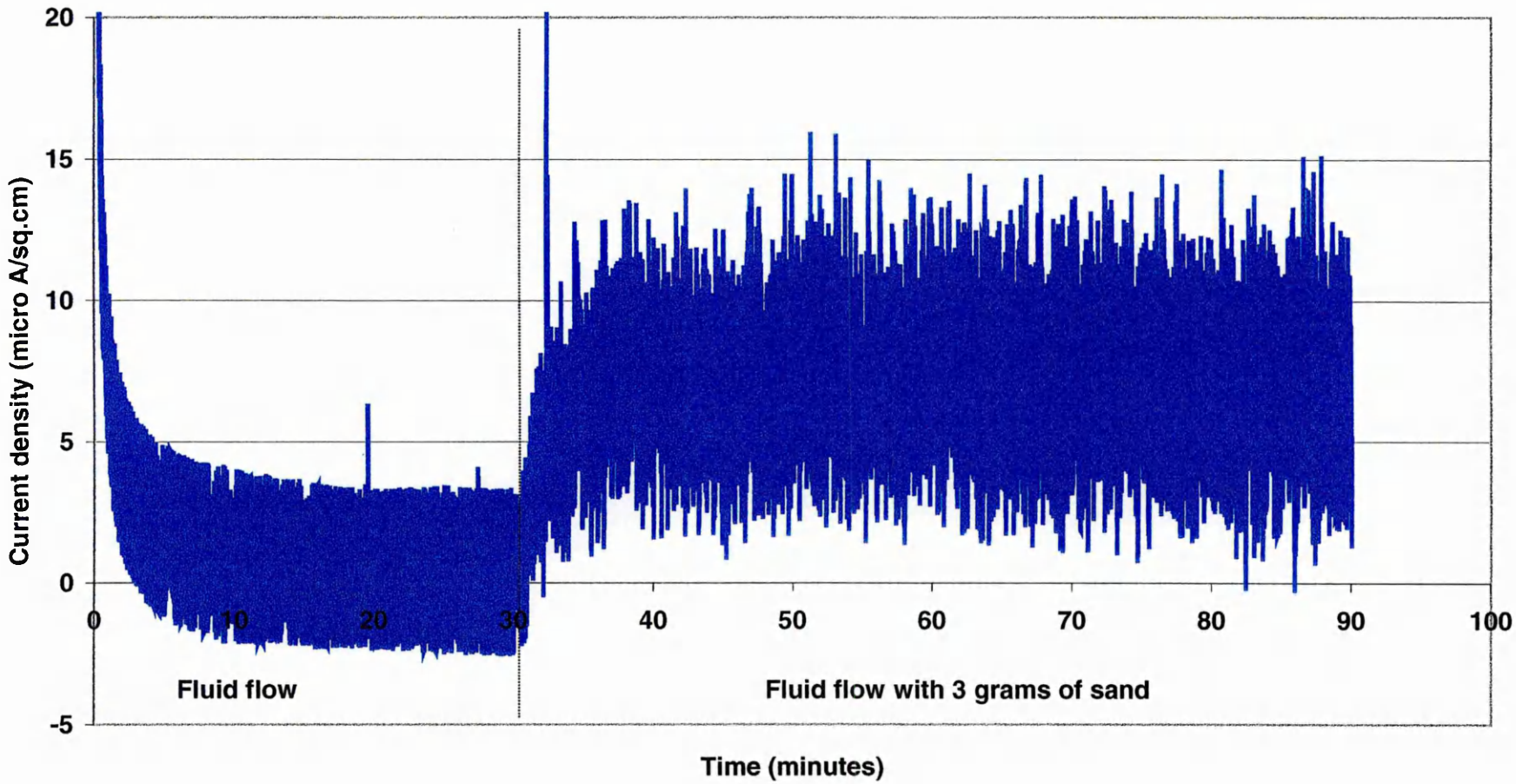

Figure 7.21 Ring 1 (batch A) duplex stainless steel held potentiostatically at -600 mV for 1 hour then at constant potential at + 300 mV (SCE) for 90 minutes at fluid flow velocity of 8.5 m/s with sand addition.

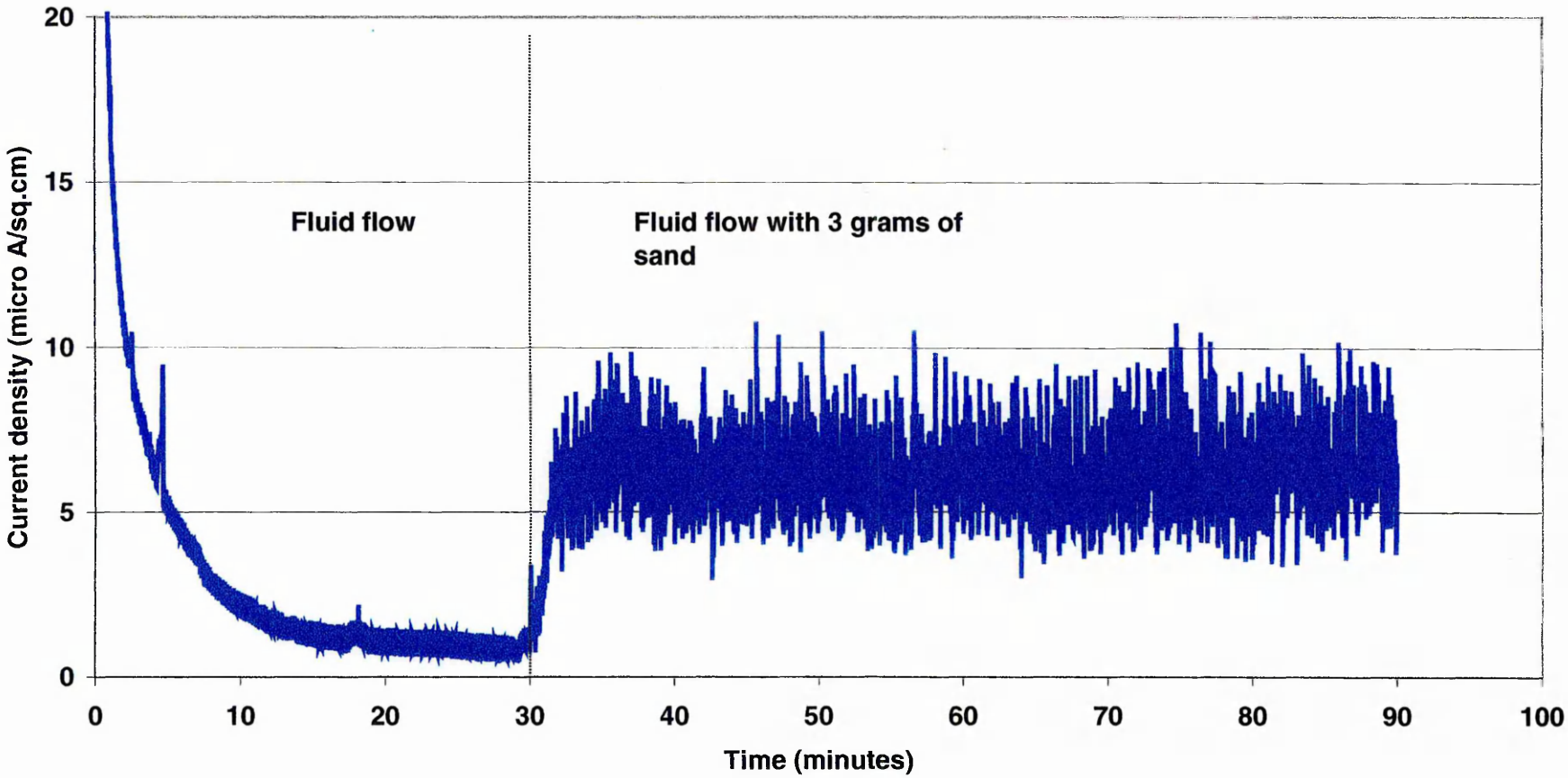

Figure 7.22 Ring 2 (batch A) held potentiostatically at - 600 mV for 1 hour then held at constant potential of + 300 mV (SCE) for 90 minutes at fluid flow velocity of 8.5 m/s with sand addition

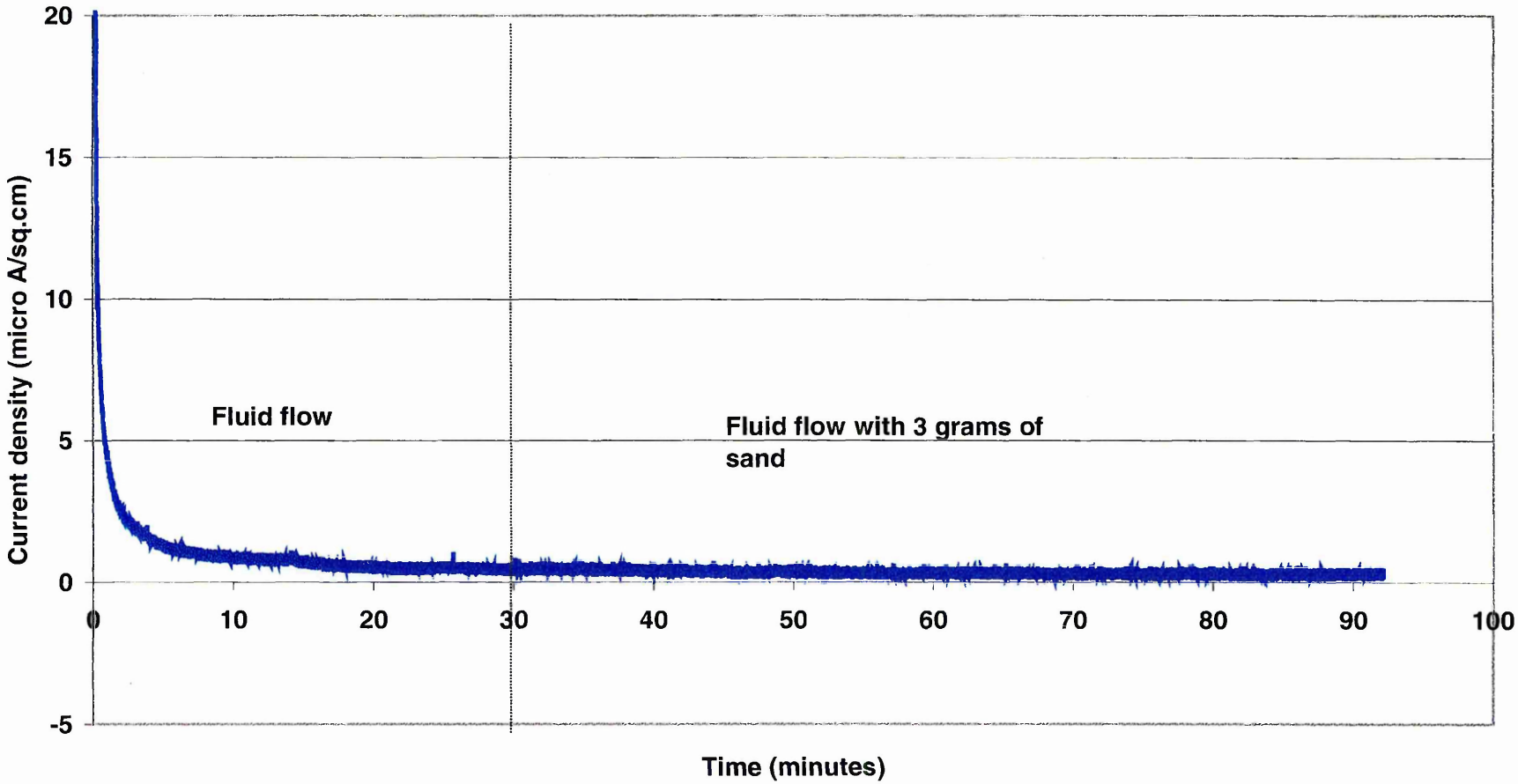

Figure 7.23 Ring 3 (batch A) held potentiostatically at - 600 mV for 1 hour then held at constant potential of + 300 mV (SCE) for 90 minutes at fluid flow velocity of 8.5 m/s with sand addition

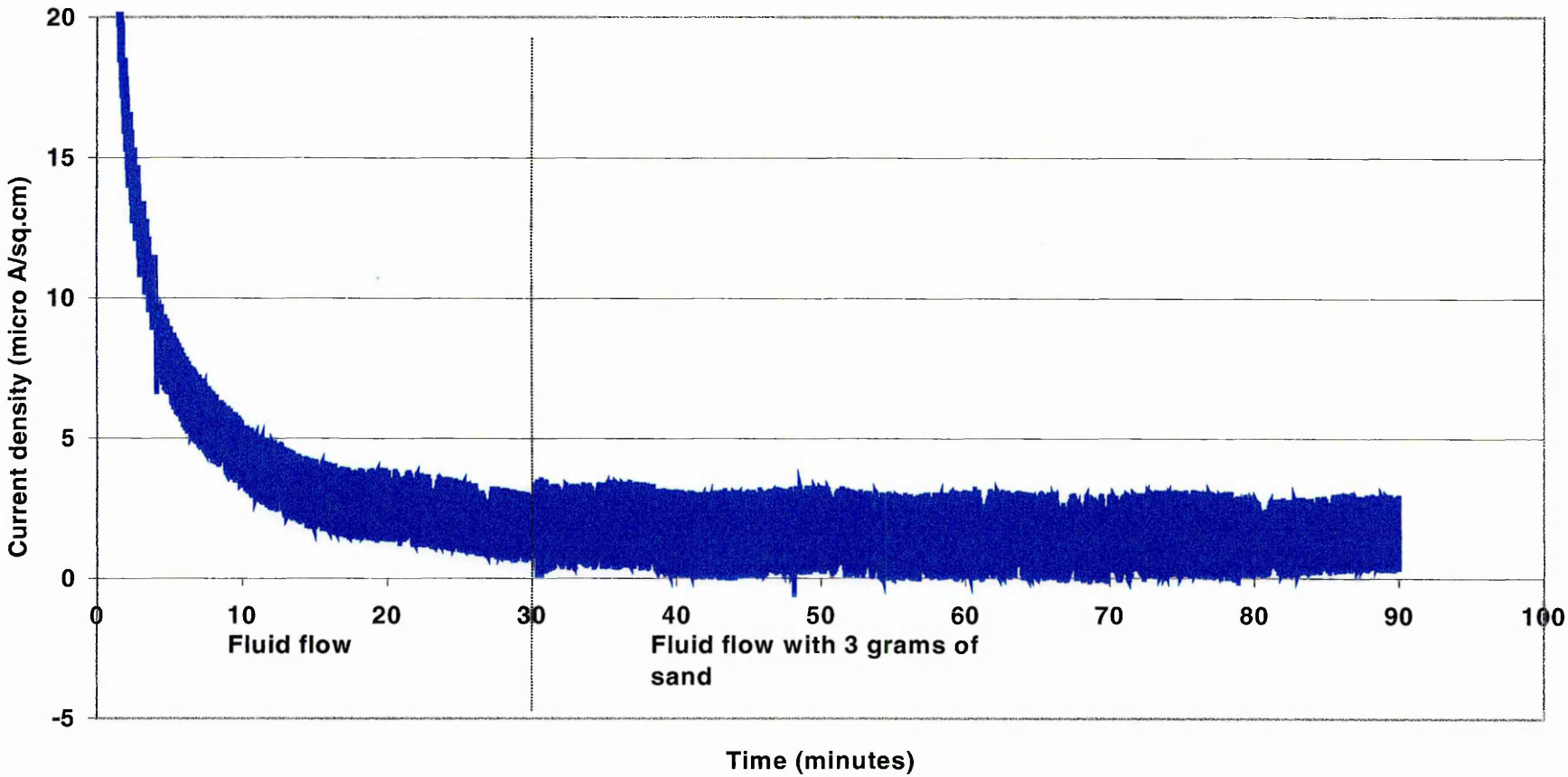

Figure 7.24 Ring 1 (batch A) duplex stainless steel metal loss held at constant potential of +300 mV (SCE) for 1 hour at fluid flow velocity of 8.5 m/s with sand addition.

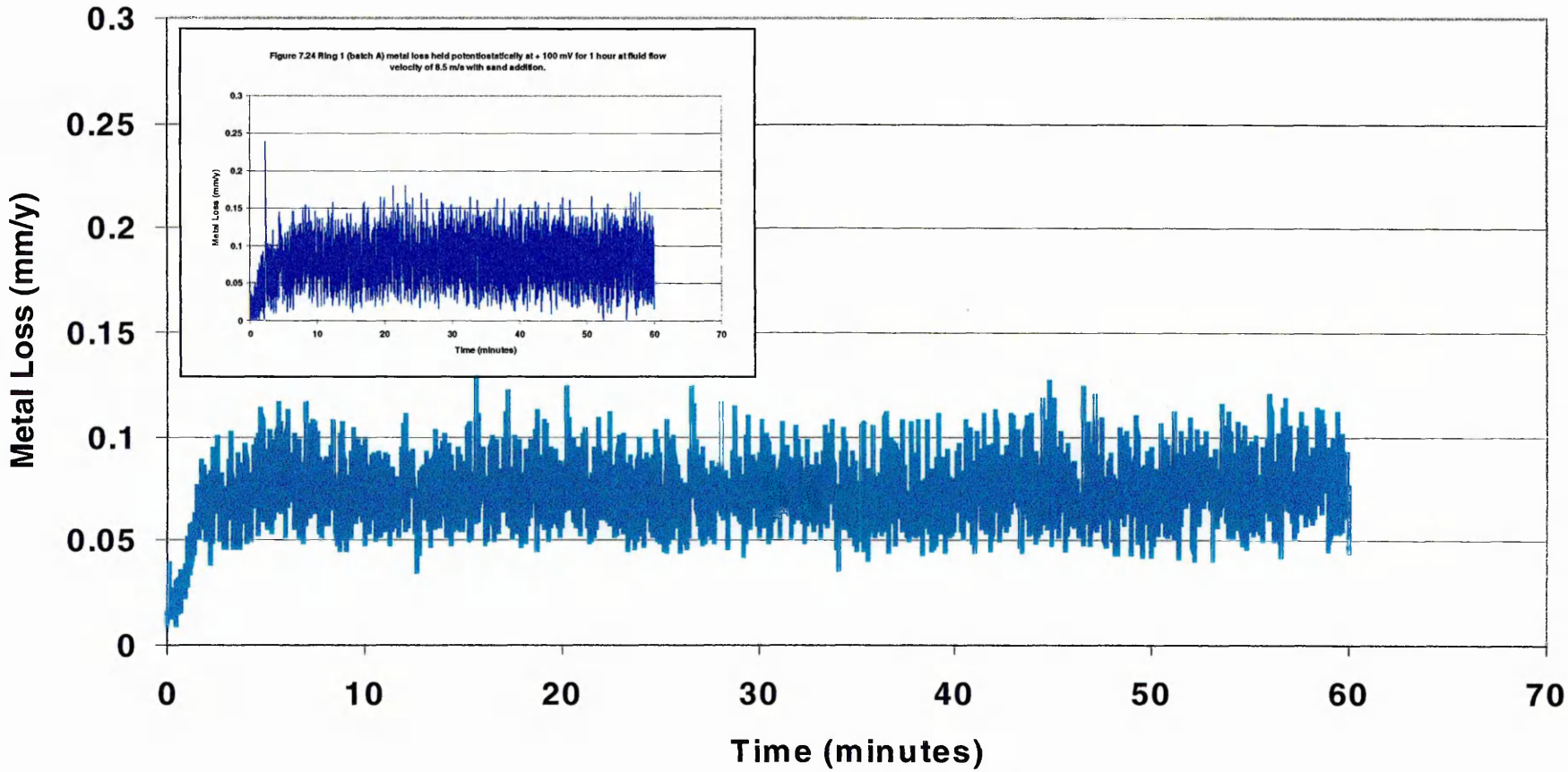

8.0 METALLOGRAPHY

8.1 Under flowing condition

Figure **8.1** shows the effect of the hydrodynamic fluid flow over the surface of the duplex stainless steel, paying particular attention to the three flow regions developed. Comets have been initiated from inclusions or pits on the surface in various sites, with a clear distinguished dark yellow film in the stagnation area, sky blue in the high turbulence area and dark yellow coloured film in the low turbulence area.

Figure **8.1** General view of duplex stainless steel (batch **A**) held at 900mV (SCE) to show the various regions of impingement and microstructure phases

Figure **8.2** points out that the elemental percentage found in different regions of the flow were very close to each other. As the Cr found at high levels in duplex stainless steel, the result shows that in the stagnation region the Cr percentage was 23.7%, at the high turbulence region it was 24% and at the low turbulence region 23.8%. Thus, the percentage of Ni was very similar in every region and reads as follow, 5.6% for the stagnation and low turbulence regions while the high turbulence region reads a value of 5.3%. For Mo element the percentages found were 2.6%, 3.4% and 2.8% respectively. When comparing with the KOH etched duplex stainless steel elemental analysis in figure **6.2**, no significant differences were seen in the elemental percentage, only a little reduction in the Ni and Mo elements with a minor increase in the Mn element. Elemental percentage standard deviation of figure **8.2** values were recorded from the scanning electron microscopy analysis as shown in table **8.1** in the Appendix.

Figure **8.2** Elemental analysis of duplex stainless steel (batch **A**) various impingement regions held at 900 mV (SCE) for 18 hours under fluid flow condition

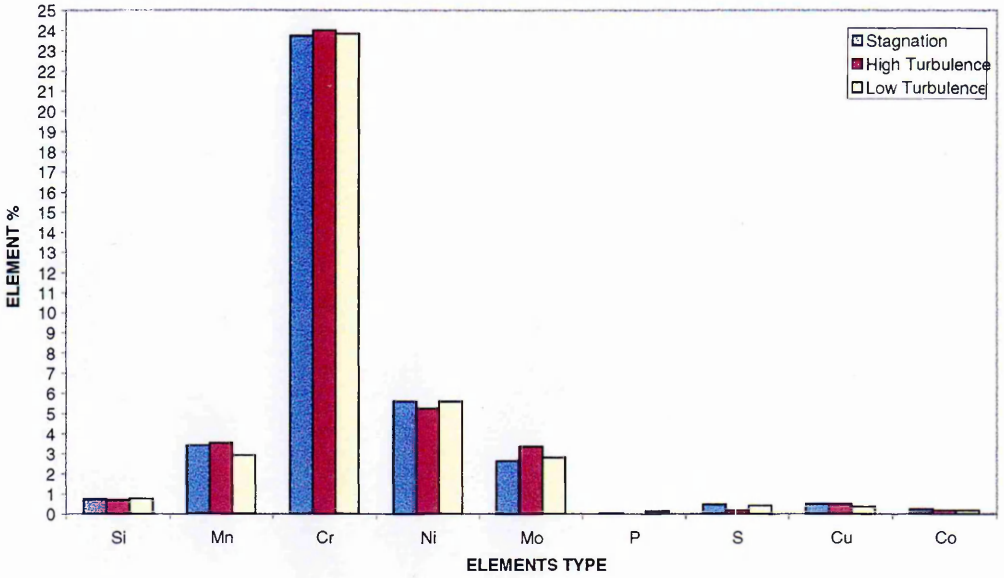

At 400 mV (SCE) the polarisation scans of duplex stainless steel indicates pitting of delta ferrite. Apparently, a long period of electrochemical etching was required to take place to see clearly both microstructure phases. Therefore, it was difficult to present a microscopic image of perfect resolution and sharpness for the microstructure phases at 400 mV in a short period of electrochemical scan. Eventually, the majority of images of the tested specimen under flowing conditions shows only a faint background of austenite and ferrite phases under the optical microscope.

To resolve such a condition, the polarisation scan was increased to 600 mV (SCE) and assuming the microstructure behaviour when holding the potential electrochemically at 400 mV (SCE) for a long period of time is similar to holding the specimen at constant potential of 600 mV (SCE) for 30 hours under fluid flow velocity of 8.5 m/s. Consequently, this increase in potential resulted in severe pitting of delta ferrite phase, occurring as indicated by figure **8.3**, dense black spots as shown while the austenite phase formation is specified as light coloured islands, those stayed protected in the delta ferrite pitting range.

Similarly, at 900 mV (SCE) in the transpassive region of the duplex stainless steel dissolution of both the austenite and ferrite microstructure under fluid flow velocity of 8.5 m/s occurred. In figure **8.4** the austenite light phase dominating the surface with preferential corrosion development at various sites, comet progress from pits mainly in the dark colour ferrite phase and other areas exhibit large pits initiation due to inclusion and defects in the material.

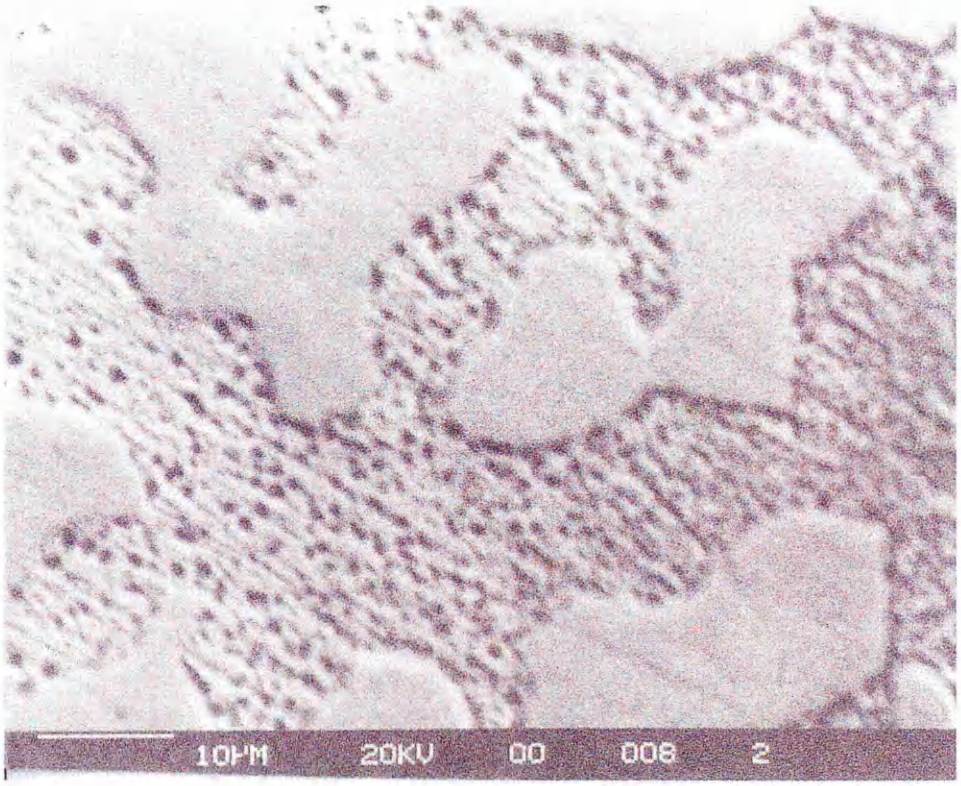

Figure **8.3** Scanning electron micrograph of ring 1 (batch **A**) held at 600 mV(SCE) for 30 hours at fluid flow velocity of 8.5 m/s, showing pitting of delta ferrite phase. Mag x 1500

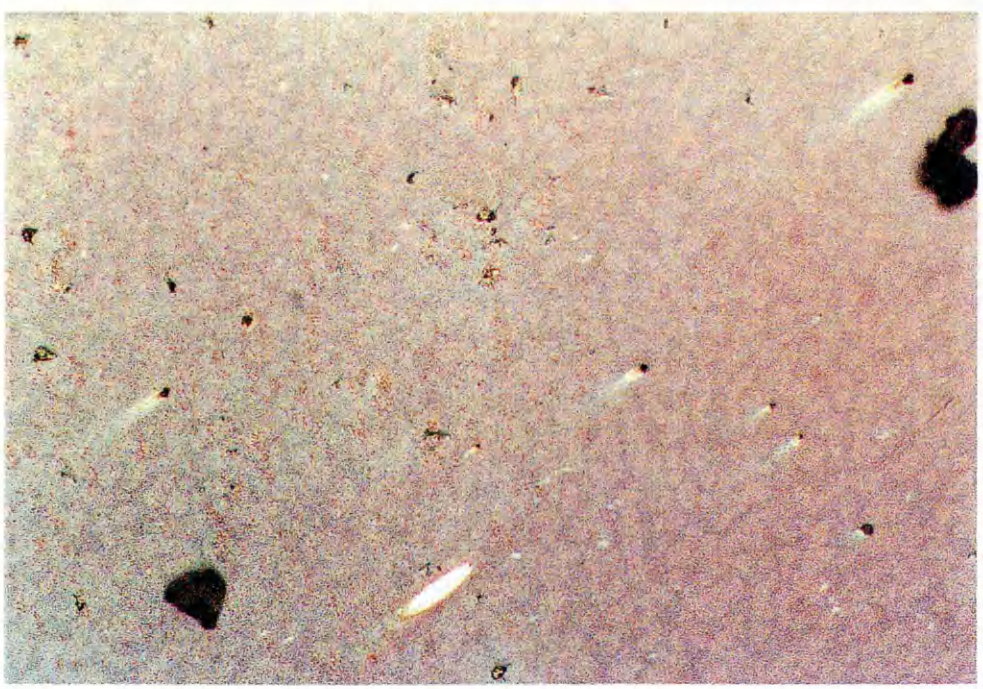

Figure **8.4** Shows the dissolution of the austenite and ferrite phases of duplex stainless steel (batch **A**) held at 900 mV for two hours under fluid flow velocity of 8.5 m/s. Mag x 500

8.2 Under flowing condition with sand addition

The optical microscopy shown in figures **8.5-8.7** illustrates the surface morphology of duplex stainless steel rings **1**, **2** and **3** after fluid flow with sand impingement. Crevice attack was found within the metal/resin interfaces, combined with visual dark brown colour corrosion products bleeding from the interfaces. At the surface of ring **1**, dense numbers of sand indentation were observed and crevice corrosion existed at the metal/resin interface. No sign of comets were seen on the surface.

At rings **2** and **3** the dense indentations were accompanied with some comets located at random inclusion sites. Most of these comets had tails with a range of colours. The inner diameter of ring **2** exhibited severe crevice corrosion conditions, which consequently led to the production of heavy corrosion products.

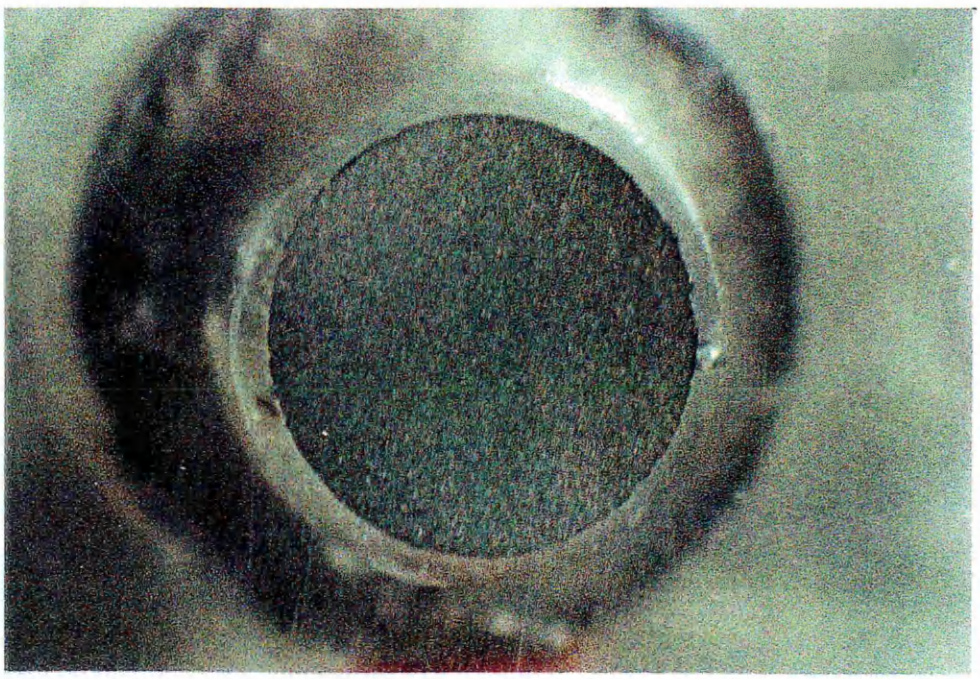

Figure **8.5** Surface morphology of ring 1 (batch **A**) after a potentiodynamic scan under fluid flow with sand addition. Mag x 125

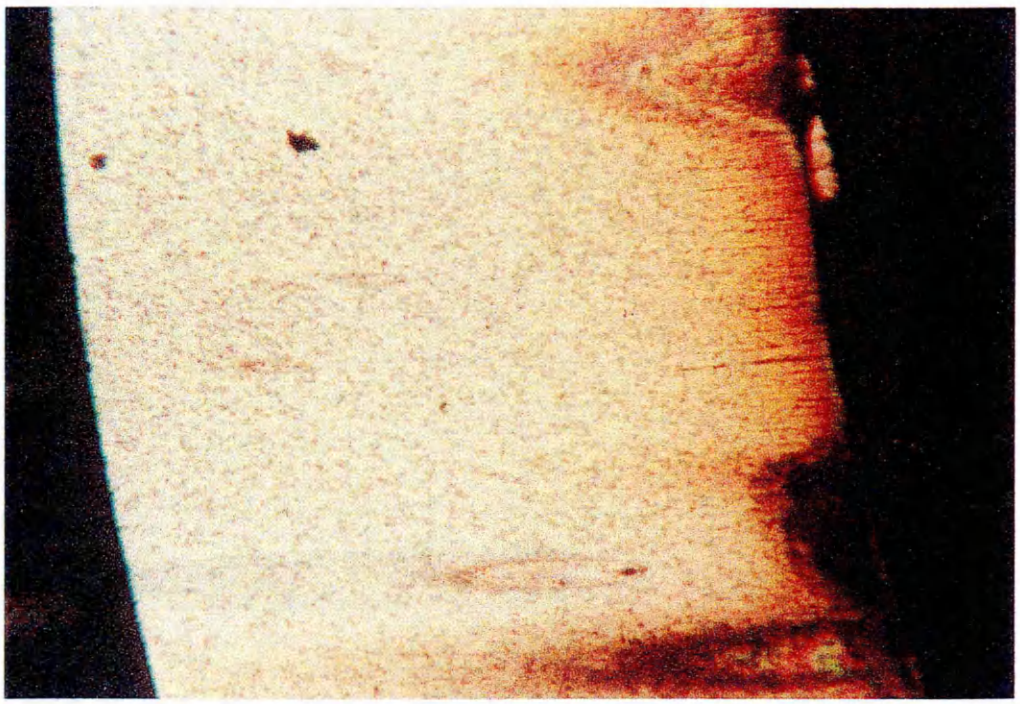

Figure **8.6** Surface morphology of ring 2 (batch **A**) after a potentiodynamic scan under fluid flow with sand addition. Mag x 100

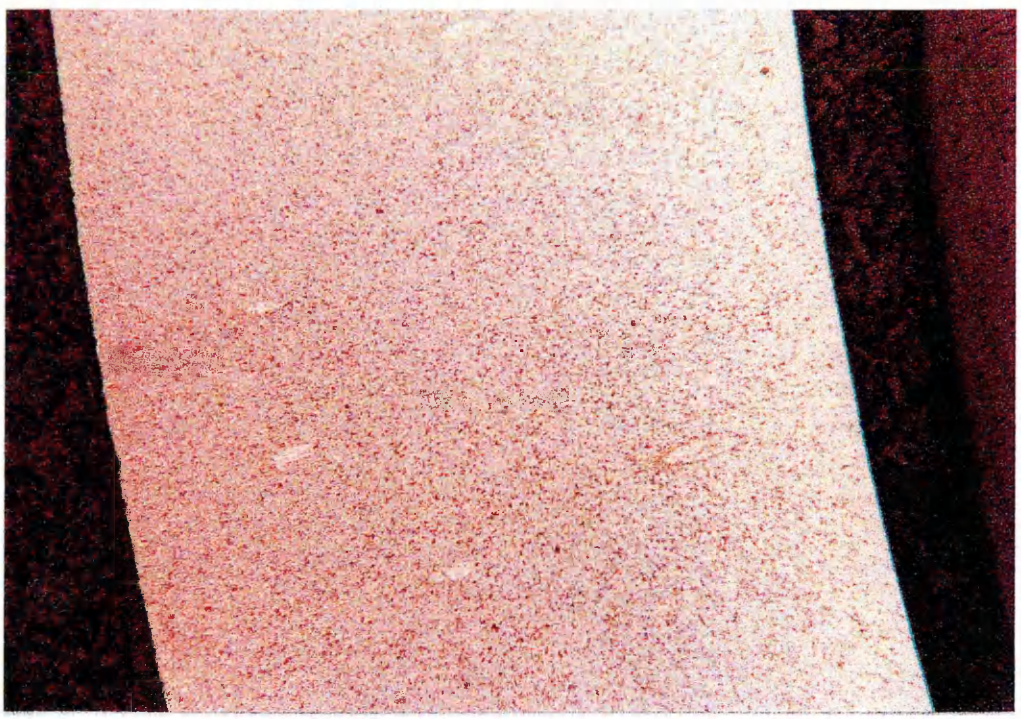

Figure **8.7** Surface morphology of ring 3 (batch **A**) after a potentiodynamic scan under fluid flow with sand addition. Mag x 250

9.0 PASSIVE FILM OPTICAL RESULTS

9.1 Passive film thickness in flowing seawater at fixed potential

Upon finishing the electrochemical experiment, film thickness was obtained from the coloured fringes on the sample surface. First the position of each fringe was measured in millimetres and then converted to a radial distance. The *Michel Levy Metrology* chart[86] (Figure **9.1**) was used to obtained the path difference for the first and second order coloured fringes ($\frac{\lambda}{2}, \frac{3\lambda}{2}$).

Allocation of colour fringes path difference order category in Michel Levy chart

After the specimen was left for six hours at a fixed anodic potential of 400 mV(SCE) to develop a coloured oxide film, the specimen was taken out of the electrochemical cell, washed with water, rinsed with propanol and air dried. The oxide film colours were recorded in various regions of the flow using second or third colour orders from the chart. It was assumed that the majority of the developed colour fringes lay in the second colour order category and in order to obtain accuracy, the specimen was returned to the loop and at optimum flow condition 3 grams of sand were added for 10 minutes only.

Eventually the specimen was taken out of the cell and the film colour fringes after sand erosion, were found to be eroded to a minimum thickness in the stagnation region. This resulted in shifting of colour fringes to the first order category of the chart, which supports the decision made on the second colour order.

To calculate the thickness of the film, t, the following formulae for the interference were applied;

For the first order colours $$t = \frac{\lambda}{4\mu} \qquad (1)$$

For the second order colours $$t = \frac{3\lambda}{4\mu} \qquad (2)$$

Where λ is the wavelength of the light undergoing interference and μ is the refractive index of the film at this wavelength.

Table (**9.1**) was used to obtain the complementary colour for each interference colour. For example, when the coloured fringe was yellow then the complementary colour was blue and it was this blue light that was eliminated by interference. The refractive index for the interfering wavelength was determined using the values in table **9.1**.

mean wavelength, (nm)	colour	complementry colour	Refractive index (μ)
417.5	Violet	Yellow-green	2.43
457.5	Blue	Yellow	2.25
485.0	Blue-green	Orange	2.15
495.0	Green-blue	Red	2.12
530.0	Green	Purple	2.02
570.0	Yellow-green	Violet	1.93
589.0	Yellow	Blue	1.89
577.5	Orange	Blue-green	1.9
700.0	Red	Green-blue	1.73

Table **9.1**. Refractive indices values for various film colours[12].

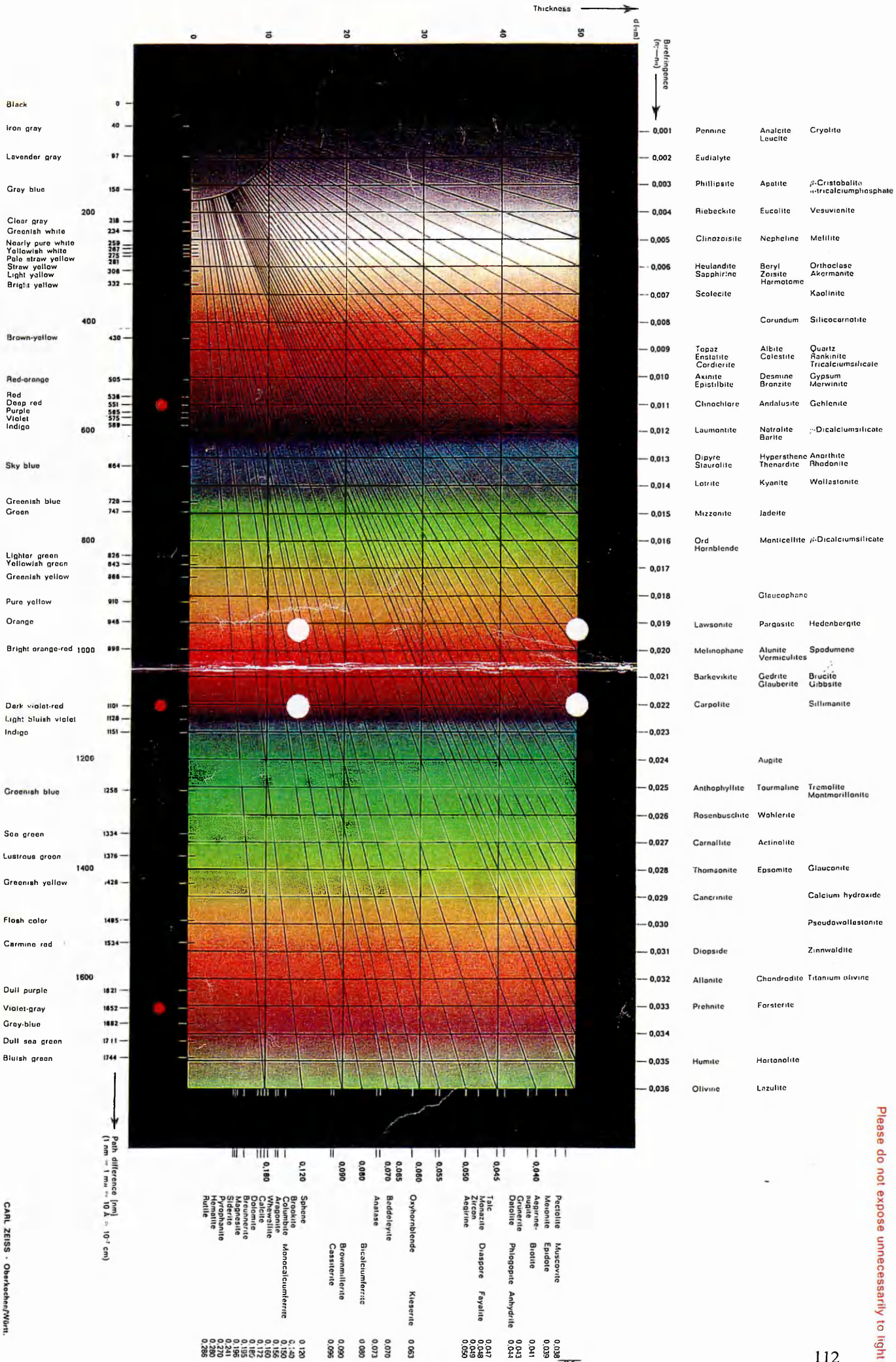

Figure **9.1**, *Michel Levy* metrological colour chart[86]

CARL ZEISS · Oberkochen/Württ.

9.1.1 At various fluid flow velocities

Figures **9.2-9.6** illustrate the thickness of the oxide films that developed under different fluid velocity and potentials. At **400** mV (SCE) constant potential and fluid flow velocity of 8.5 m/s the film thickness was 150 nm at the stagnation region. The colours were in the second order purple. As the velocity of the fluid decreased, a fluctuation in the film thickness occurred at the stagnation regions. The value decreased to 110 nm at 7.9 m/s to the first order brown yellow colour then increased again at both fluid velocity of 7.8 m/s and 7.5 m/s to second order indigo colour of 150 nm thickness. Finally, at a velocity of 7.2 m/s the oxide film thickness was 170 nm, which corresponded to green and green/yellow of the second order colours. High erosion rates were observed in this region due to the specimen location being directly under the nozzle.

In the high turbulence region, at a radial distance r/r_o = 2.5, the film thickness stayed constant at 70 nm from the maximum velocity of 8.5 m/s until a fluid velocity of 7.5 m/s. The film thickness corresponded to first order straw yellow and bright yellow colours. Only at 7.2 m/s did the oxide film thickness reach 90 nm with a bright yellow first order colour. The low film thickness in those regions was due to the high shear stresses of the fluid flow that existed in this area.

The low turbulence regions, at radial distance r/r_o= 5, indicated higher values of film thickness than the high turbulence regions. This was due to an increase in the fluid flow boundary layer. The film thickness at the maximum and the minimum fluid flow velocity was between 150 nm and 210 nm. The coloured fringes were all in the second order colours of purple and only the lowest velocity was greenish blue.

Visual observations showed that comets had developed all over the surfaces at different fluid velocities and crevice corrosion was evident in the metal/resin interface. A high variation in the brightness of the colours between one velocity and another was possibly related to the different samples used in each experiment.

At **700** mV (SCE) constant potential, the duplex stainless steel was in the passive potential range and both microstructural phases were stable. The film thickness in the stagnation region at 8.5 m/s was 150 nm (second order purple colour). A fluctuation in the film thickness occurred as the velocity declined to 7.2 m/s, which led to oxide film thicknesses of 75 nm, 160 nm, 75 nm and 170 nm respectively. These were related to first order colour of bright yellow for velocities of 7.9 m/s and 7.5 m/s, and second order indigo colour for velocities of 7.8 m/s and 7.2 m/s.

In the high turbulence region the majority of the film thicknesses were ranging from 33 nm to 80 nm, which followed the first order colour fringes of grey blue-bright yellow. In the low turbulence region the colour fringes were first order of light yellow and brown/yellow and also second order purple colour with oxide film thickness of 75 nm to 150 nm. The differences in film thickness were mainly due to small fluctuations in experimental parameters such as temperature of the solution or utilizing another duplex stainless steel specimen. Visual surface observation revealed both the initiation of pits and fully developed comets.

By increasing the potential to **900** mV (SCE) the film darkened in colour. This meant that the film was thickening as a result of dissolution of both ferrite and austenite phases and the production of corrosion deposits.

The oxide film thicknesses in the stagnation regions were between 170 nm and 70 nm, corresponding with colours of the second order sky blue-indigo and first order colours of light yellow-bright yellow. Only at 8.5 m/s did the thickness in the stagnation region increase drastically due to the longer immersion time of the experiment (18 hours compared with 6 hours for the other tests).

In the high shear stress region the film thickness varied between values of 30 nm, 50 nm, 50 nm, 150 nm and 30 nm. The coloured fringes were in the first order grey blue-bright yellow. Only at 7.5 m/s was the second order purple colour developed.

In the low turbulence zone at 8.5 m/s fluid velocity, the film thickness was 170 nm with sky blue second order colour. As the fluid velocity decreased, the following thicknesses were recorded: 70 nm at 7.9 m/s, 80 nm at 7.8 m/s, 170 nm at 7.5 m/s and 75 nm at 7.2 m/s. The colours were 1st order bright yellows for all the velocities except at a velocity of 7.5 m/s, when second order sky blue was developed.

Figure 9.2 Duplex stainless steel (batch A) held at 400, 700 and 900 mV (SCE) at fluid flow velocity of 8.5 m/s for 6 to 18 hours

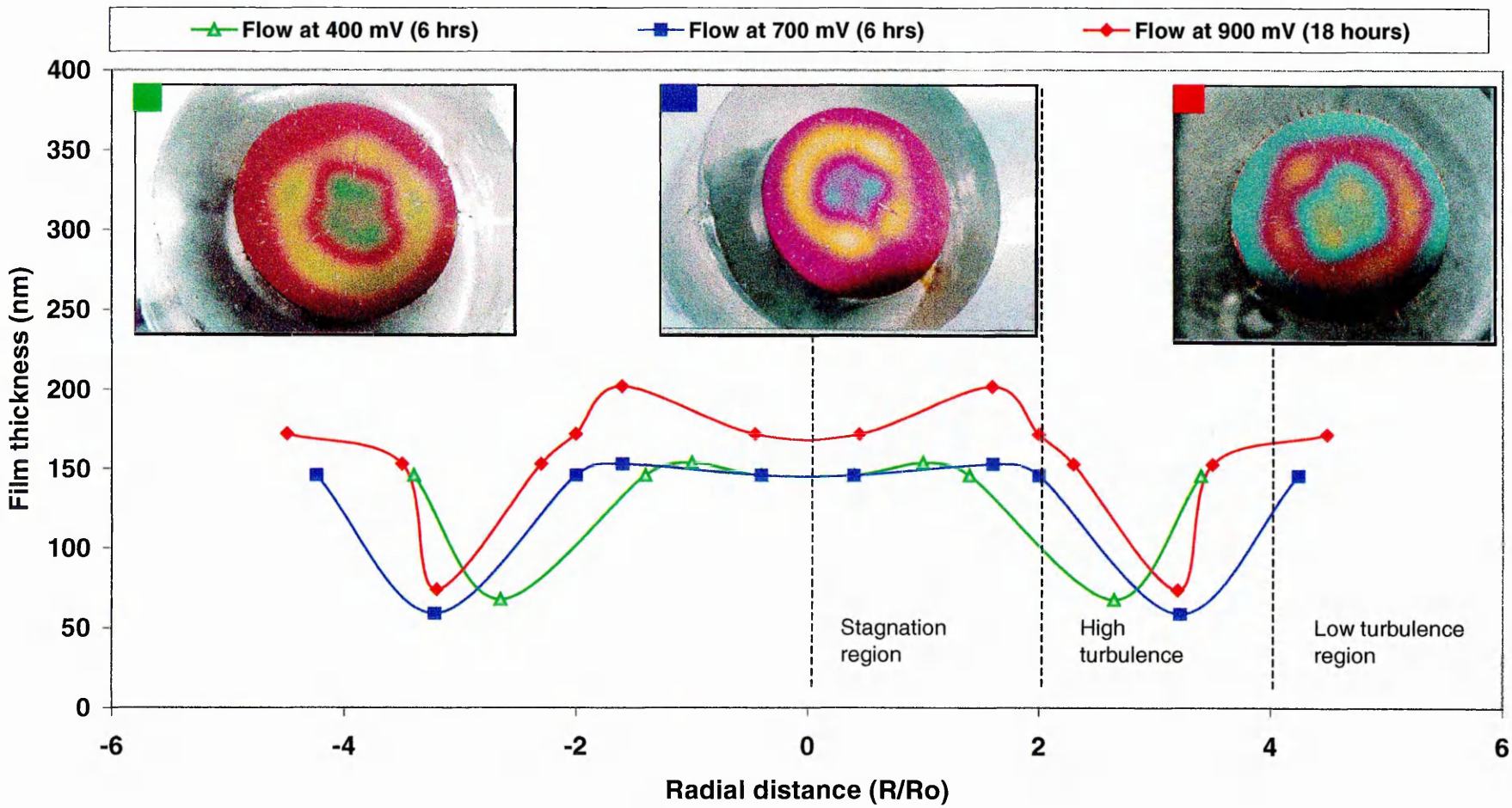

Figure 9.3 Duplex stainless steel (batch A) held at 400, 700 and 900 mV (SCE) at fluid flow velocity of 7.9 m/s for 6 hours

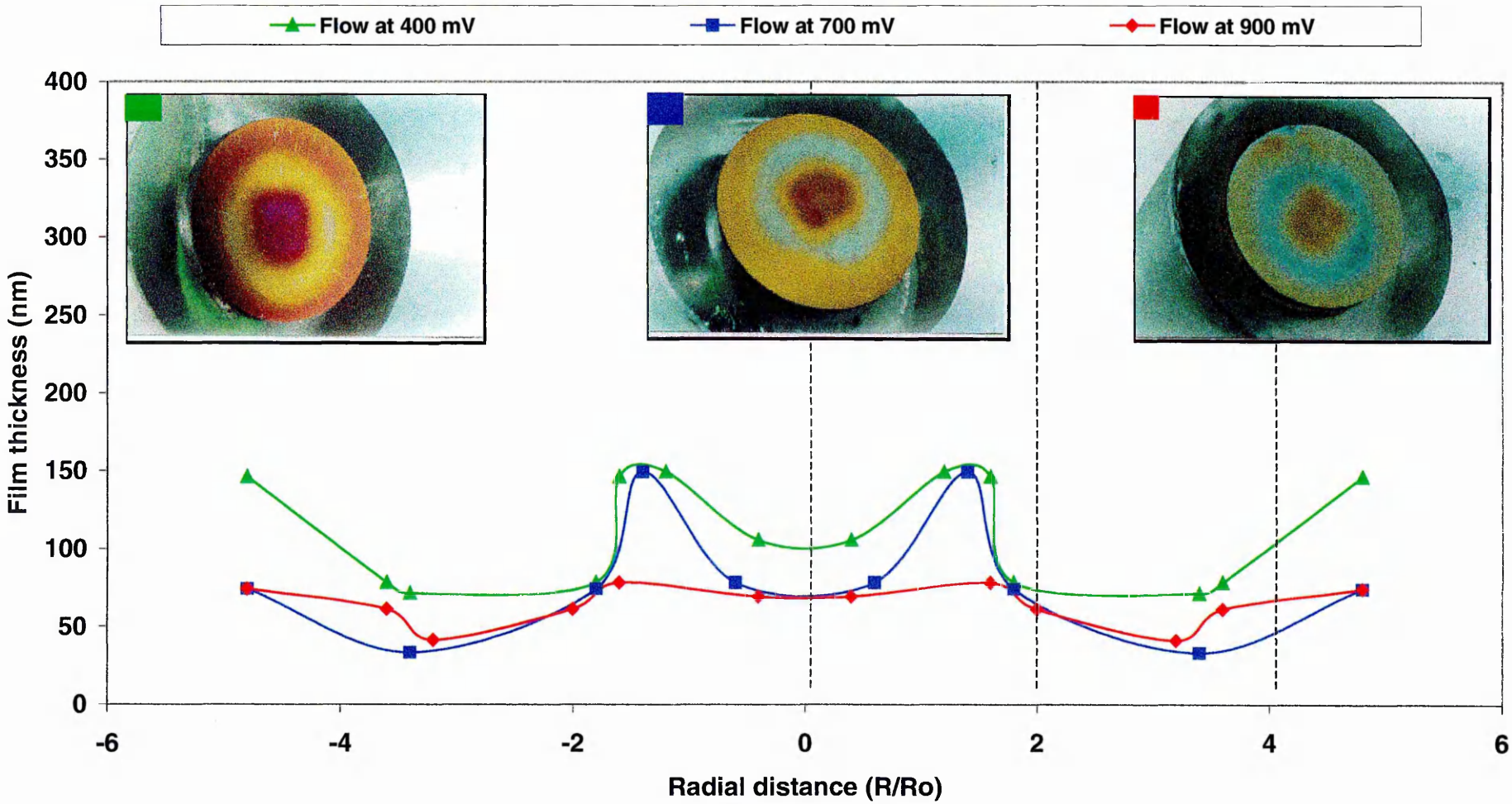

Figure 9.4 Duplex stainless steel (batch A) held at 400, 700 and 900 mV (SCE) at fluid flow velocity of 7.8 m/s for 6 hours

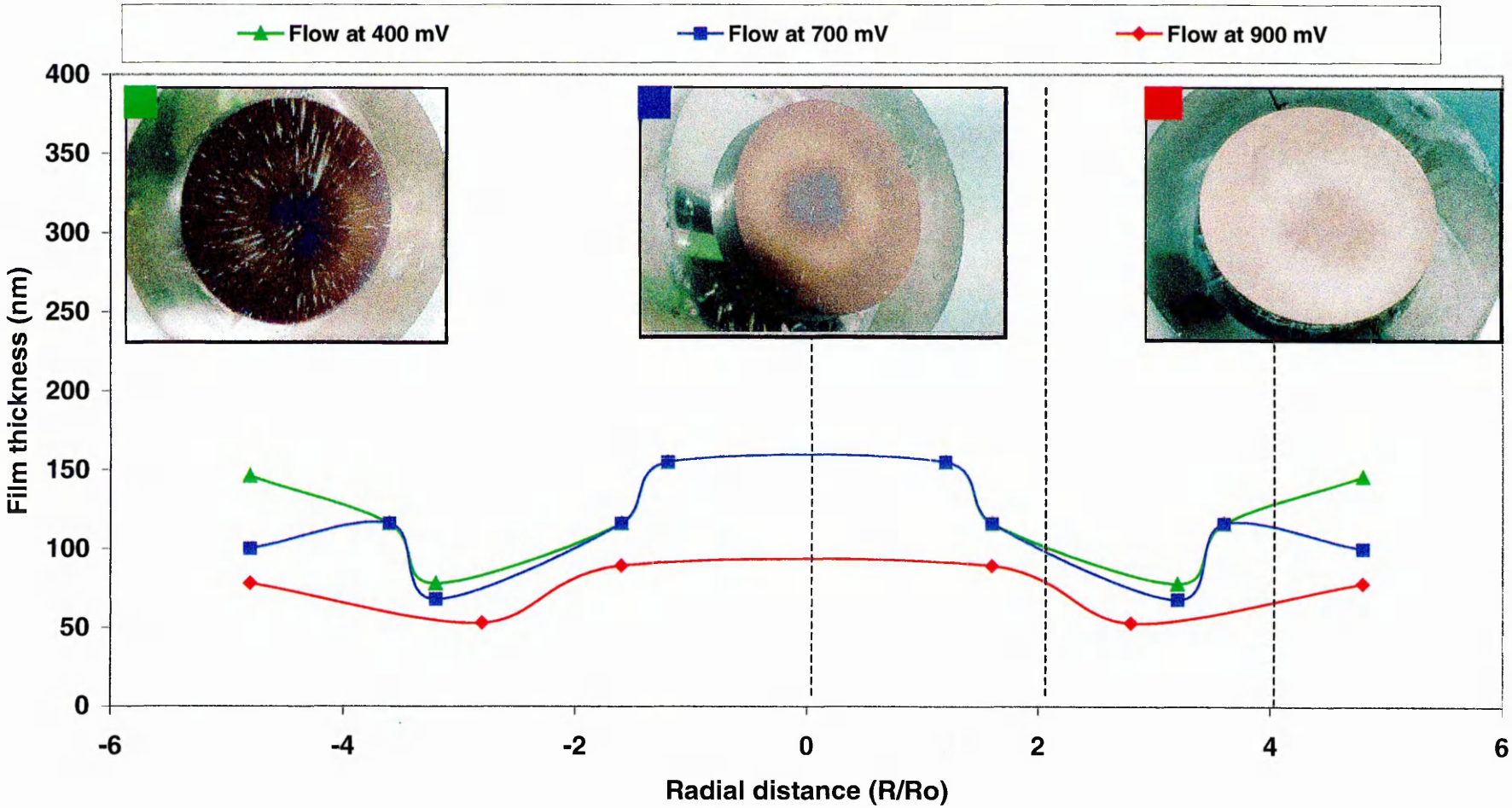

Figure 9.5 Duplex stainless steel (batch A) held at 400, 700 and 900 mV (SCE) at fluid flow velocity of 7.5 m/s for 6 hours

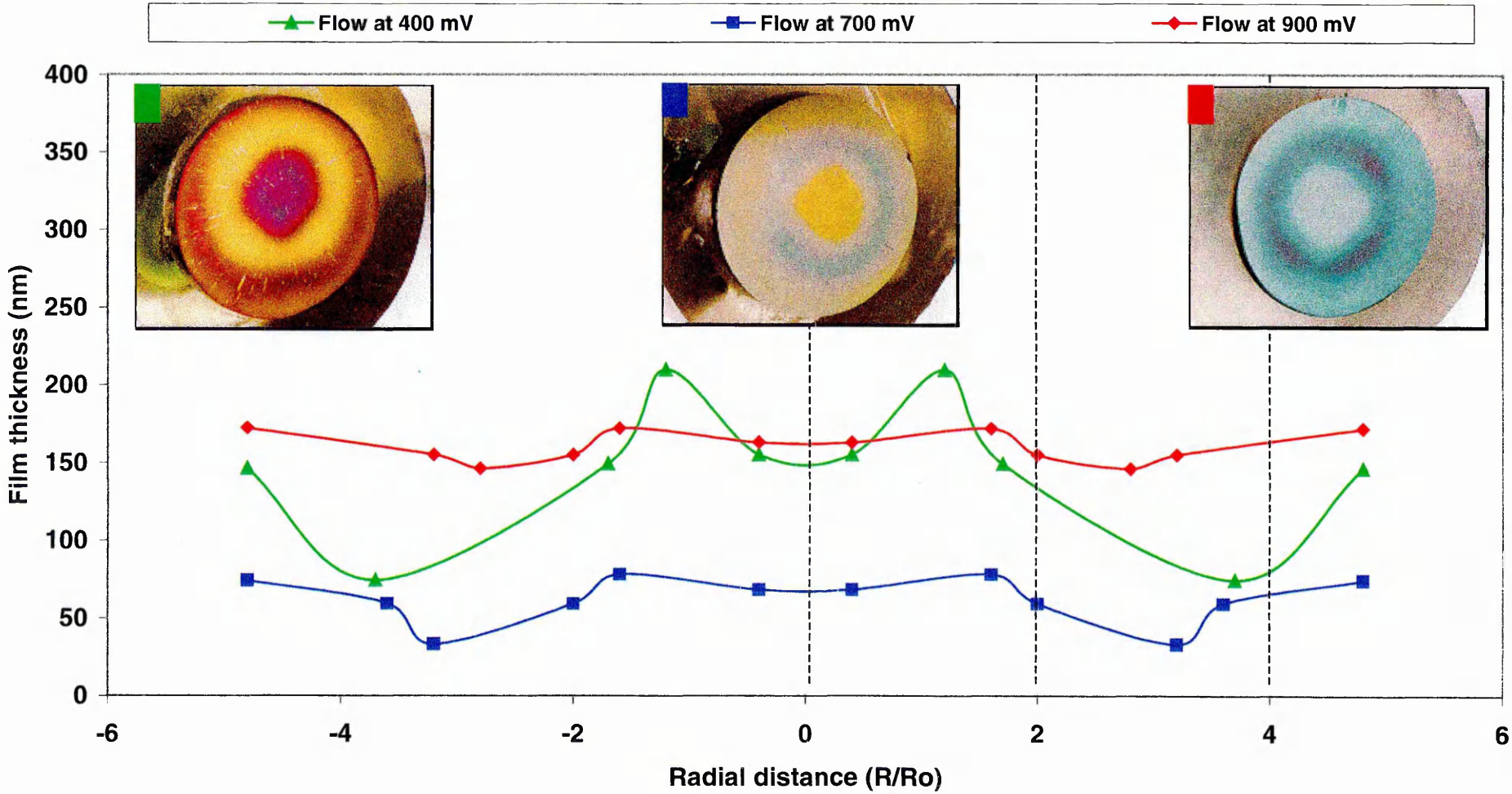

Figure 9.6 Duplex stainless steel (batch A) held at 400, 700 and 900 mV (SCE) at fluid flow velocity of 7.2 m/s for 6 hours

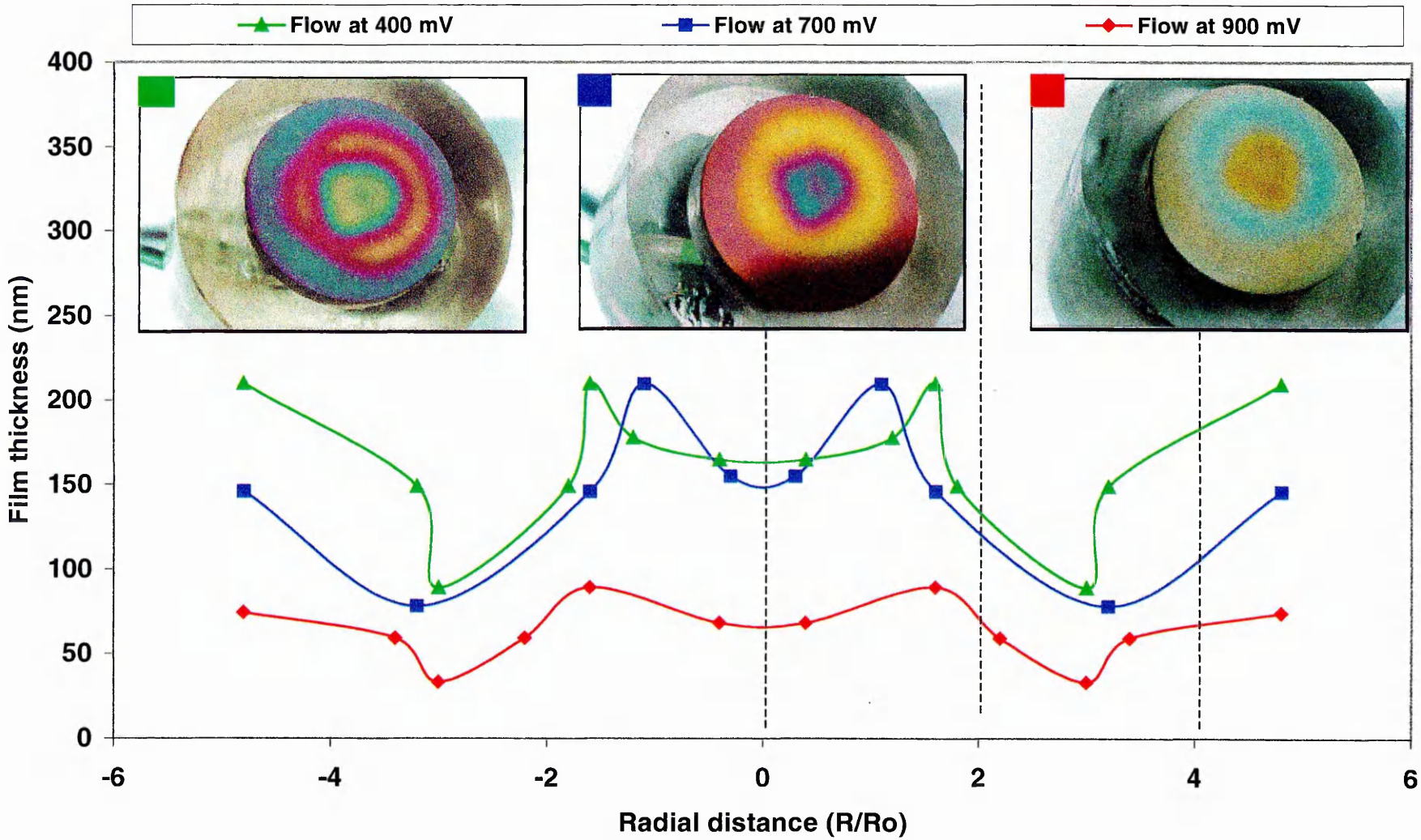

9.1.2 At various fluid flow velocities with sand addition

With the sand additions at fluid velocity of 8.5 m/s the colour fringes shifted to the first order colour. Large reductions in the passive film thickness were exhibited in all the stagnation regions at the different constant potentials with oxide film thicknesses around 33 nm (first order grey blue colour). At **400** mV (SCE) in the high turbulence region the second order violet colour (150 nm) was produced as shown in figure **9.7**. The increase in thickness and the strong adhesion of the film was possibly related to the fact that the austenite was still protected at this potential. In the low turbulence region the thickness that developed was second order greenish blue film of 215 nm.

At **700** mV (SCE) potential in the passive range and **900** mV (SCE) transpassive potential, the oxide films in both the stagnation and high turbulence regions developed thicknesses of 33 nm, which corresponded with grey blue first order colour. At **700** mV (SCE) anodic potential the low turbulence region exhibited first order bright yellow coloured film with 75 nm in thickness, while at **900** mV (SCE) in the low turbulence region the thickness was 120 nm, which corresponded on the Michel Levy chart between the red and brown first order colours.

It was noticed that with a longer time of immersion the outer regions tended to increase in film thickness. Visual inspection revealed that a few comets were developed on the specimen at **400** mV (SCE) but the other potentials did not exhibit any comets or pits, although they all shared the effect of roughness and indentation all over the surface and crevice corrosion at the edges.

Figure 9.7 Duplex stainless steel (batch A) held at 400, 700 and 900 mV (SCE) at fluid flow velocity of 8.5 m/s with 3 grams of sand for 6 to 18 hours

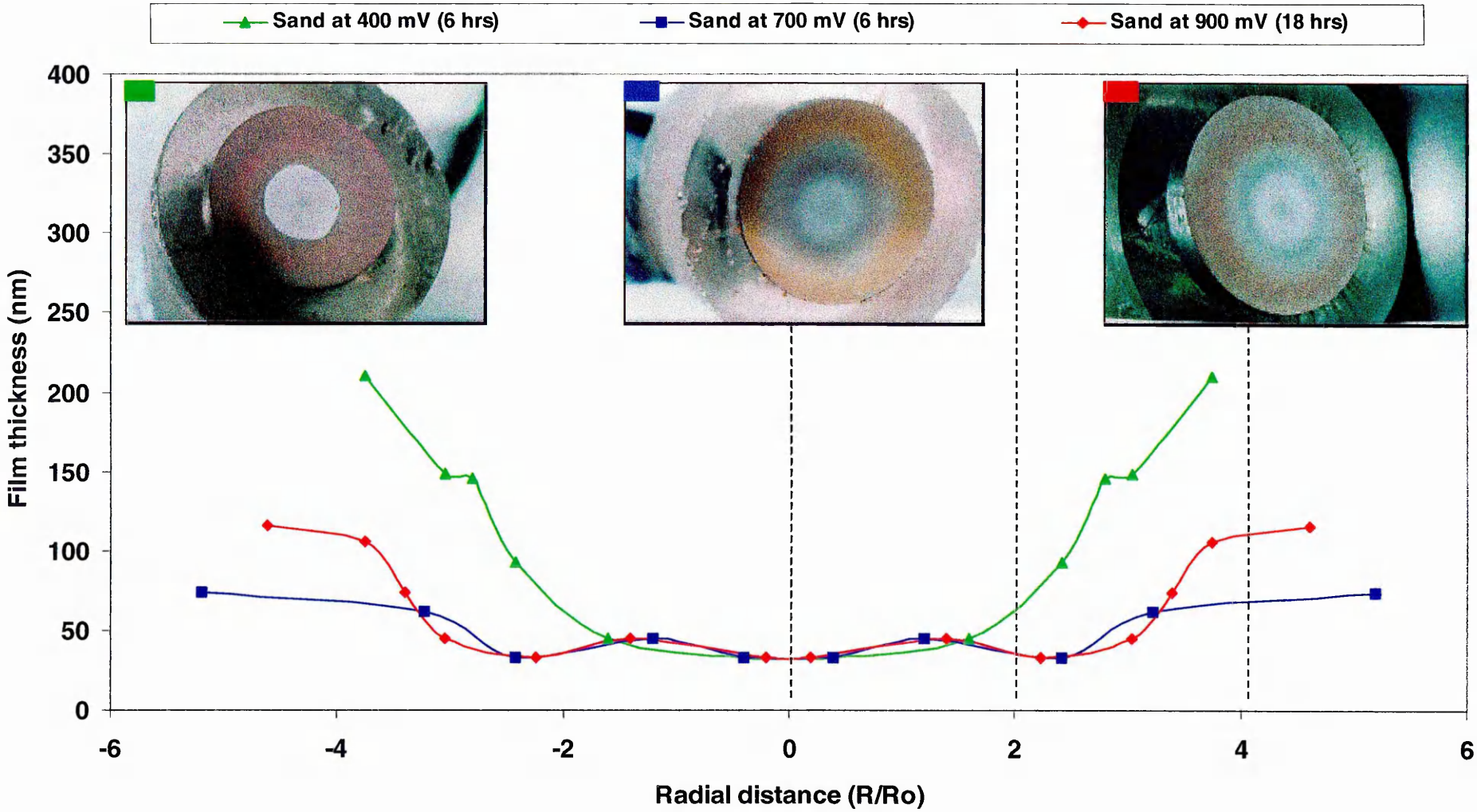

9.1.3 At various fluid flow velocities with sand addition for 1 hour

Passive film thickness profiles were measured across the surface of the specimens after 1 hour sand impingement as shown in figures **9.8-9.11**. When compared with the film thicknesses after 6 hours of sand impingement, the surfaces at one hour time duration showed similar thicknesses to the stagnation regions.

In the high turbulence region a variation in film thicknesses was evident. Those after 6 hours time duration (values of 150 nm at 400 mV (SCE), and 33 nm at 700 and 900 mV) (SCE) were reduced to values of 88 nm, 75 nm and 50 nm at 400 mV (SCE), 700 mV (SCE) and 900 mV (SCE) respectively. In the low turbulence regions the film thicknesses were reduced to 150 nm at 400 mV (SCE), 100 nm at 700 mV (SCE) and 80 nm at 900 mV (SCE), when compared with the 6 hours sand addition.

The surfaces showed evidence of pitting and general corrosion plus crevice corrosion at the metal/resin interface; some pits were developed into comets. Comets were observed on the coloured areas of the specimens at **400** mV (SCE) constant potential. By comparing all the graphs at 1 hour of sand addition, film thicknesses at the stagnation regions were between 20 nm and 33 nm. The developed films were first order colours ranging from lavender grey to grey blue.

In the high turbulence regions the thickness profiles of the passive films were readings of 78 nm, 89 nm, 74 nm and 100 nm and they were less affected by the sand impingement. The colours were first orders bright yellow and brown yellow.

At the low turbulence regions the erosion effects of the sand particles on the passive films were less than the previous regions due to the increase in the fluid flow hydrodynamic boundary layers. All the measured passive films were 2^{nd} order colours ranging from 149 nm (violet) to 211 nm (greenish blue).

The film thicknesses at **700** mV (SCE) passive potential followed a similar behaviour to the 400 mV (SCE) potential. The thickness of the passive films at the centre zones varied between 20 nm (first order lavender grey) and 33 nm (first order grey blue).

In the high turbulence zones, all the specimens at different velocities matched up together with film colours of first order bright yellow to brown yellow and thickness from 67 nm to 100 nm. Except for velocity of 7.5 m/s, the thickness was 33 nm for first order grey blue.

In the low turbulence zones both the 7.8 m/s and 7.2 m/s velocities gave similar thickness profiles, i.e. 148 nm (violet) and 155 nm (indigo). The remaining fluid velocities of 7.9 m/s and 7.5 m/s had similar thicknesses of 93 nm (brown yellow) first order colour and 78 nm (bright yellow) first order colour. Those variations in passive film were related to the different chemical compositions of different samples used and some variations in experimental parameters.

The film thicknesses at **900** mV (SCE) transpassive potential gave a consistently low film thickness within the stagnation regions, which varied between 20 nm (lavender grey) to 33 nm (grey blue). The continuous impacts produced significant damage in the

high turbulence zones of the orders of 48 nm at 7.9 m/s velocity, 61 nm at 7.8 m/s, 155 nm at 7.5 m/s and 100 nm at 7.2 m/s.

Similarities were observed in the passive film profiles in the low turbulence zones at various fluid velocities, except for a velocity of 7.5 m/s where the thickness was 181 nm (sky blue) second order colour.

Visual observation revealed high roughness on the surfaces of the specimens as a result of sand particle impingement. Comets were very clear at potentials of 400 and 700 mV (SCE) and there was evidence of crevice corrosion at the specimen's interfaces.

Figure 9.8 Duplex stainless steel (batch A) held at 400, 700 and 900 mV (SCE) at fluid flow velocity of 7.9 m/s for 6 hours then sand particles added for 1 hour

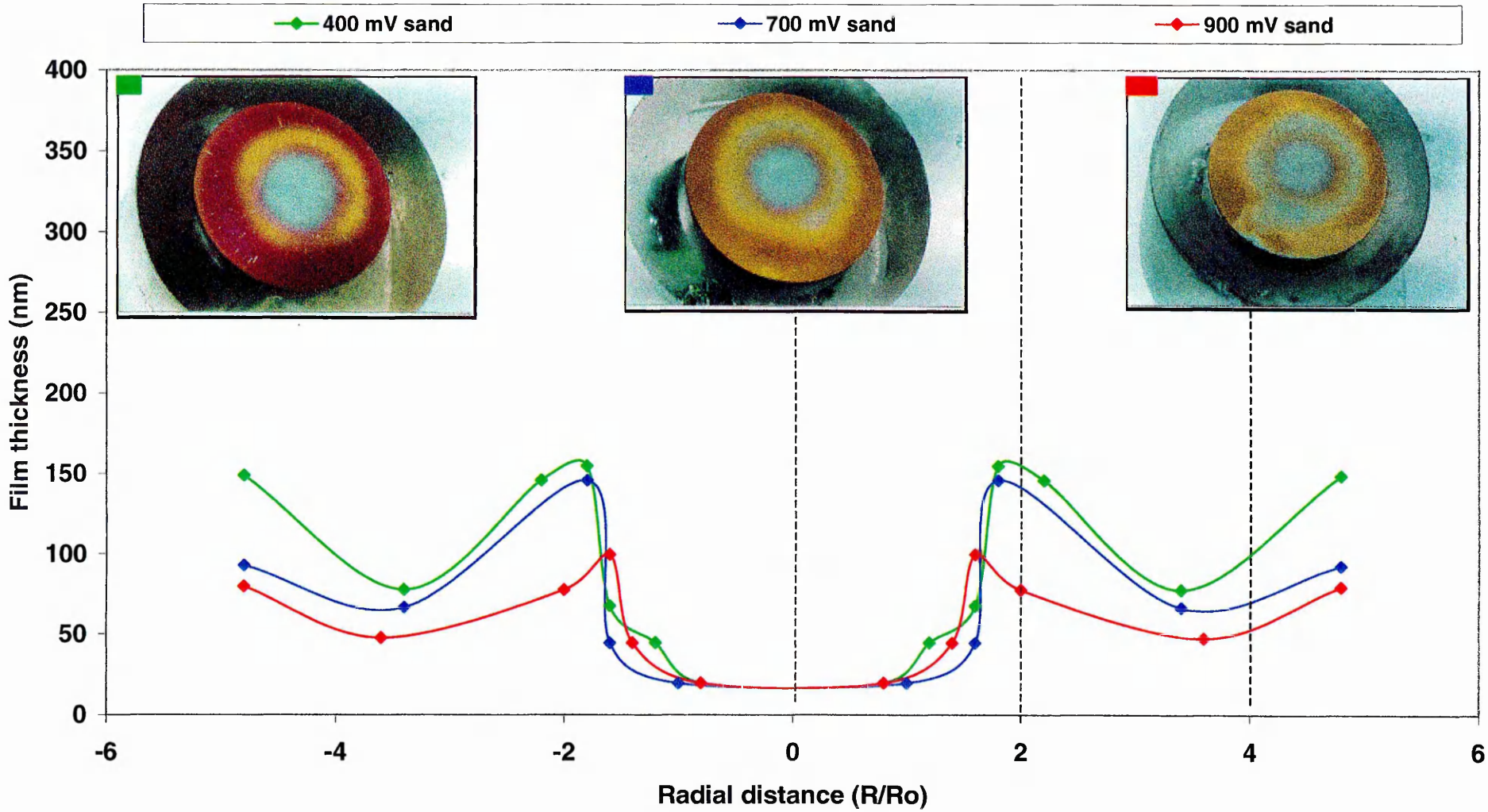

Figure 9.9 Duplex stainless steel (batch A) held at 400. 700 and 900 mV (SCE) at fluid flow velocity of 7.8 m/s for 6 hours then 3 grams of sand added for 1 hour

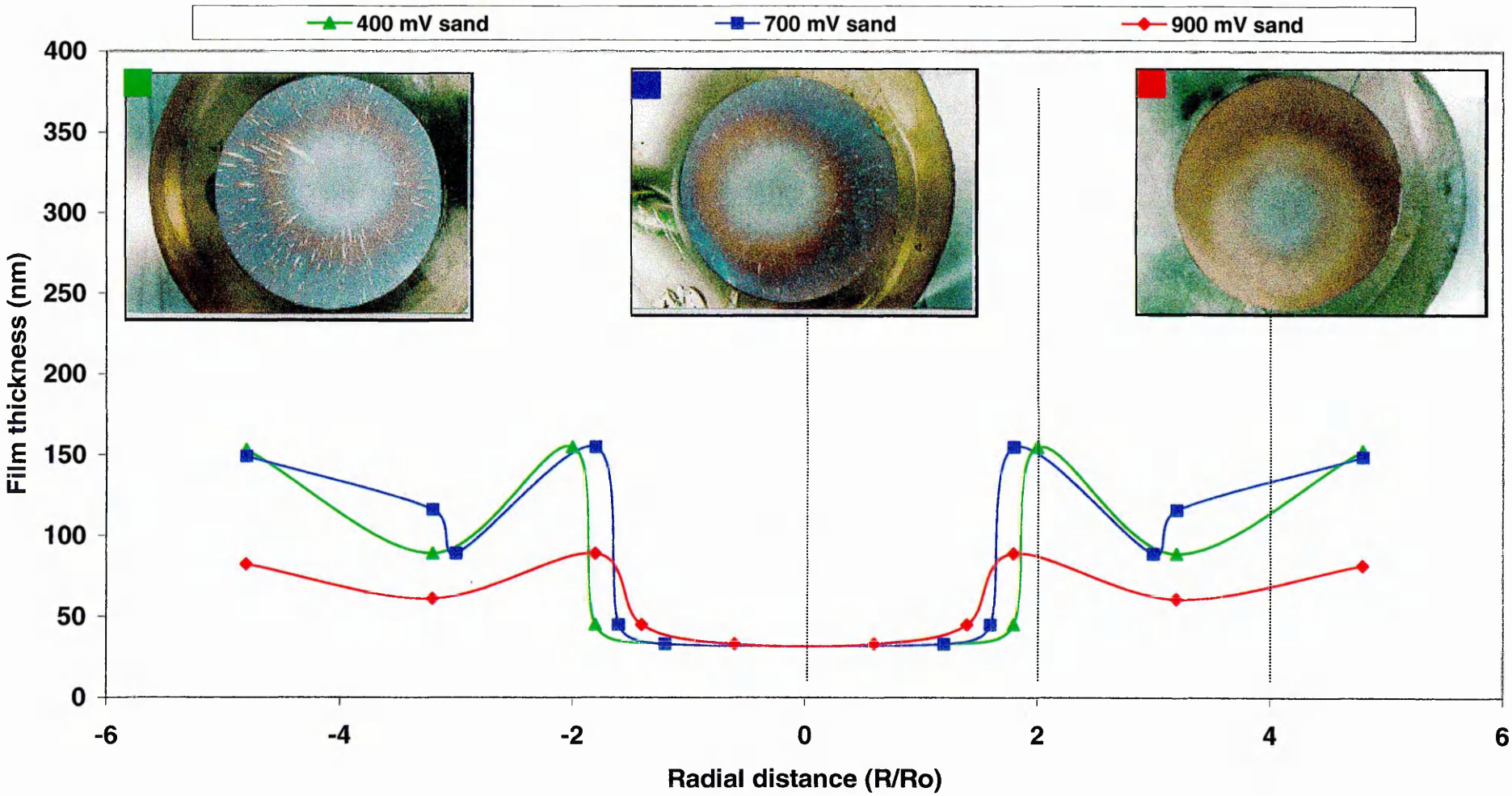

Figure 9.10 Duplex stainless steel (batch A) held at 400, 700 and 900 mV (SCE) at fluid flow velocity of 7.5 m/s for 6 hours then sand particles added for 1 hour

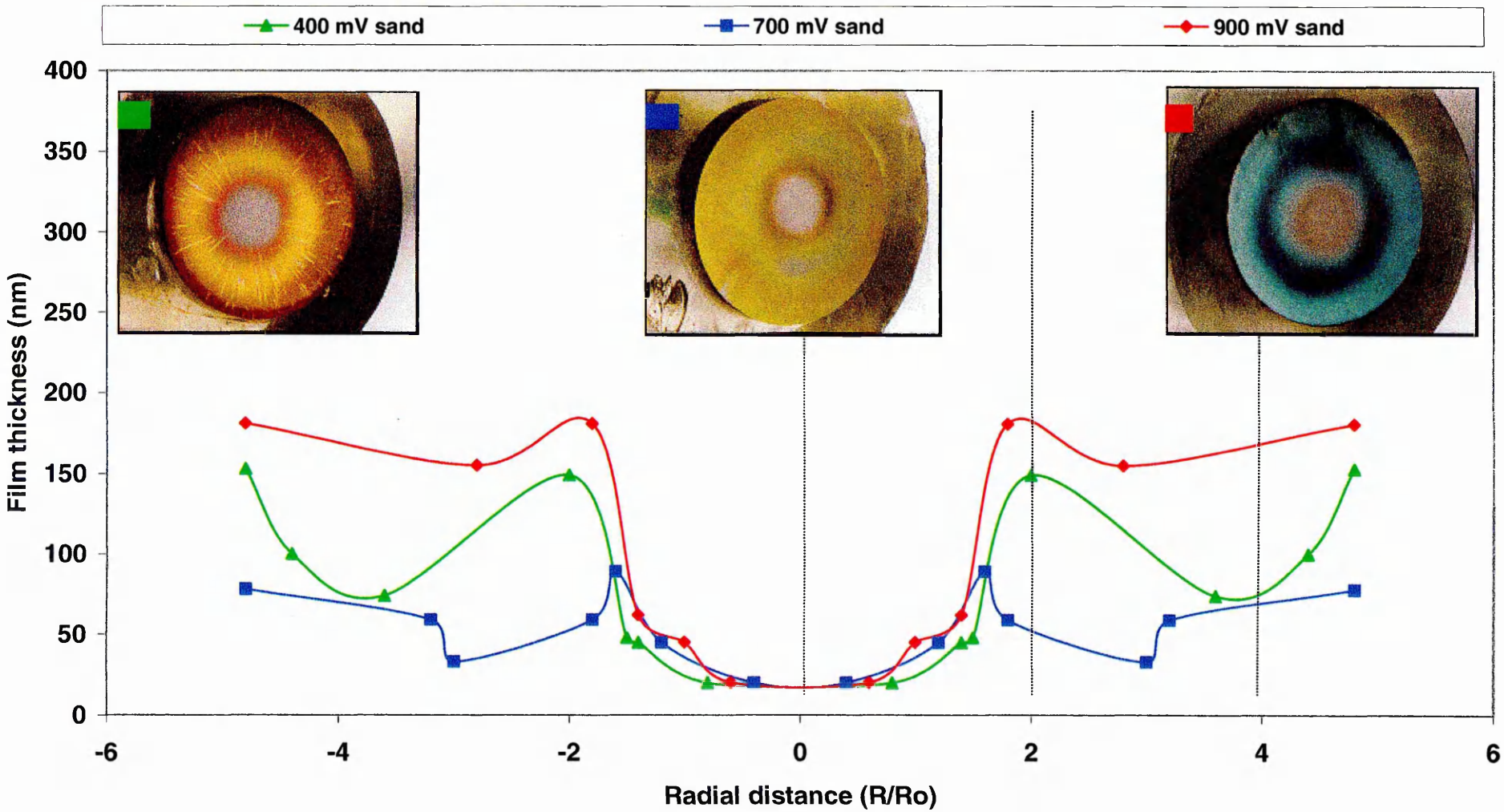

Figure 9.11 Duplex stainless steel (batch A) held at 400, 700 and 900 mV (SCE) under fluid flow velocity of 7.2 m/s for 6 hours then 3 grams of sand added for 1 hour

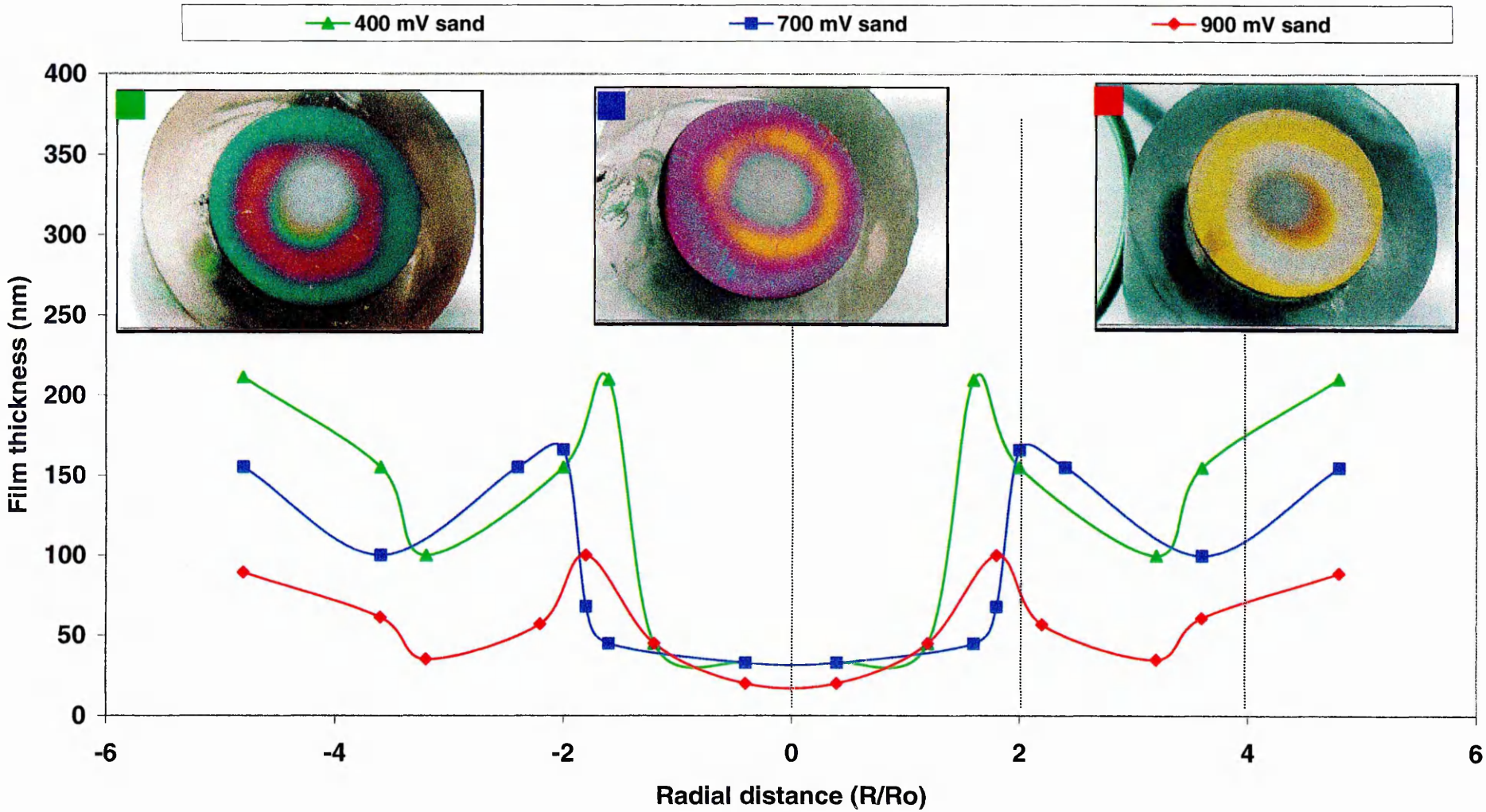

9.1.4 At various fluid flow velocities with sand additions for 10 minutes

Comparison between the 1 hour and 10 minutes sand impingement experiments revealed similar reductions in film thickness in the stagnation region (thicknesses of 33 nm (blue grey) colour). Areas outside the stagnation region also showed similarity in film thicknesses. The surface appearance in the centre with the radial flow was in the form of small indentations, while deep troughs were found at the outer areas where the flow was in a radial direction.

Under a constant potential of **400** mV (SCE), as shown in figures **9.12-9.16**, the patterns of damaged passive films produced by the water jet impingement were very similar. The remaining thickness of the passive films at the stagnation regions for 8.5 m/s velocity down to 7.2 m/s were between 33 nm and 44 nm. These corresponded to first order colours of grey blue through greenish white.

In the high turbulence regions the film thickness values were between 187 nm, and 74 nm. The film's colours were second order sky blue through to the first order bright yellow. In the low turbulence regions second order colours such as pure yellow, purple and greenish blue were developed, with film thicknesses of 200 nm, 146 nm and 210 nm respectively. Comets were only visible in coloured areas. These were related to the various sites of pits and surface inclusions.

At the passive potential of **700** mV (SCE), the passive film colouring of the stagnation areas changed to the first order colour range of clear grey to greenish white, with a distinctive appearance of the dark colours of the second order. The film thicknesses were between 33 nm and 48 nm respectively.

At the high turbulence areas the oxide films were ruptured by the impingement of the sand particles, resulting in the first order colours of grey blue, straw yellow, grey blue and bright yellow, which corresponded with film thicknesses of 39 nm, 68 nm, 33 nm and 78 nm.

In the low turbulence areas at **700** mV (SCE), thicker films were developed on the surface of the specimens and the areas were less affected by the sand particle impingements. The colours were first order bright yellow of 78 nm, brown yellow of 100 nm, bright yellow of 74 nm and second order purple of 146 nm at 7.2 m/s fluid velocity.

Localised corrosion such as pitting and crevice morphologies developed in the surface of the specimens during the colouring process.

Reductions in thickness of the passive film profiles occurred in the stagnation regions. This was related to the following colours and thicknesses: Grey blue at 33 nm through to straw yellow at 62 nm. Thicknesses of 187 nm, 45 nm, 53 nm, 146 nm and 33 nm were developed in the high shear stress regions, with second and first order colours such as sky blue, grey blue, nearly pure white, purple and grey blue respectively.

At the transpassive potential of **900** mV (SCE) the duplex stainless steel developed a thicker oxide film especially at the low turbulence regions with film thicknesses of 200

nm, 45 nm, 78 nm, 170 nm and 74 nm. A first order colour was produced on the surface. This was pure yellow, bright yellow, bright yellow, sky blue, and bright yellow. At the same time visual observation showed that the distribution of pits and inclusions increased, as well as crevice corrosion at the metal/resin interfaces.

Figure 9.12 Duplex stainless steel (batch A) held at 400 and 900 mV (SCE) at fluid flow velocity of 8.5 m/s for 6 hours then 3 grams of sand added for 10 minutes

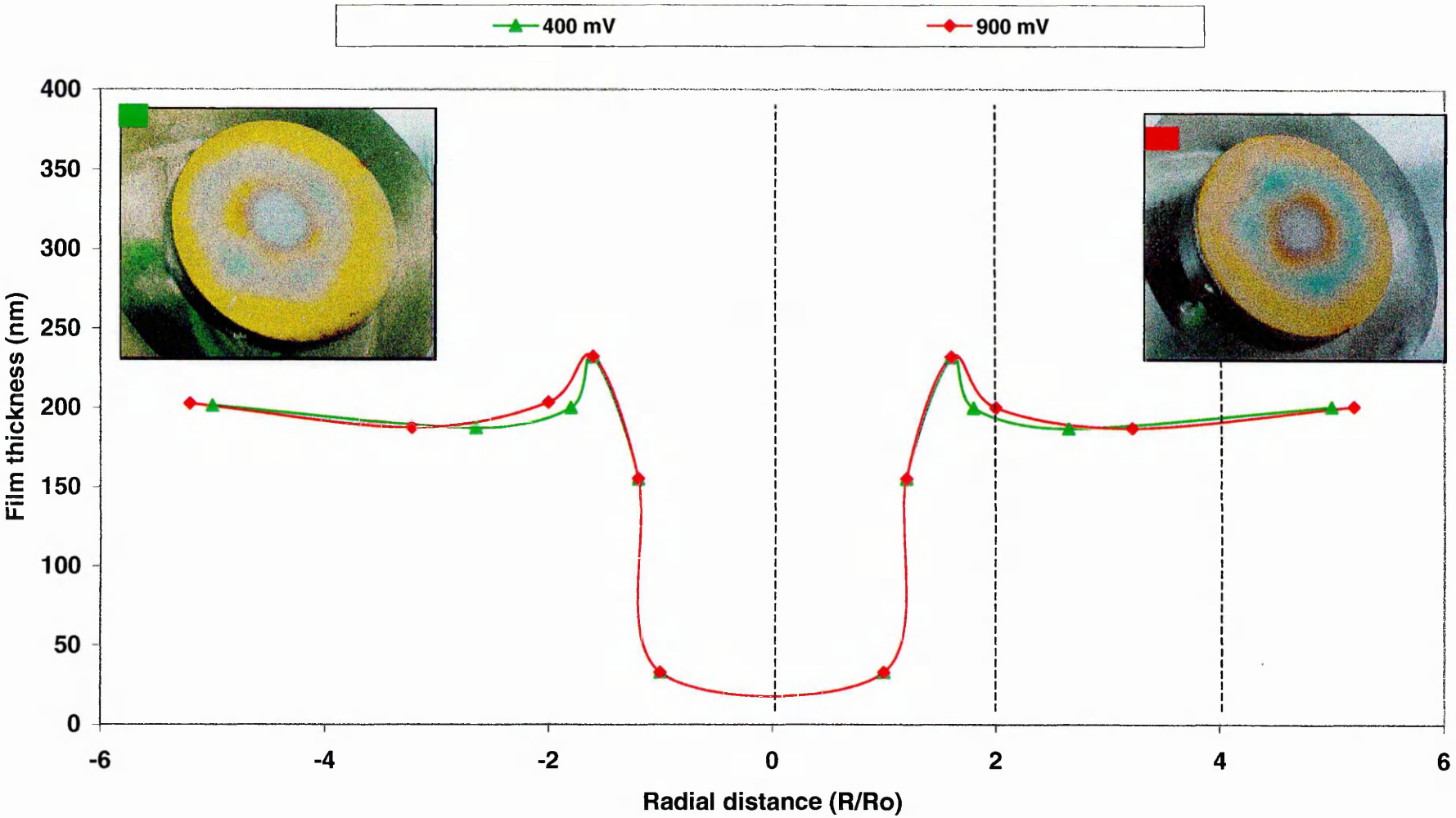

Figure 9.13 Duplex stainless steel (batch A) held at 400, 700 and 900 mV (SCE) at fluid flow velocity of 7.9 m/s for 6 hours then 3 grams of sand added for 10 minutes

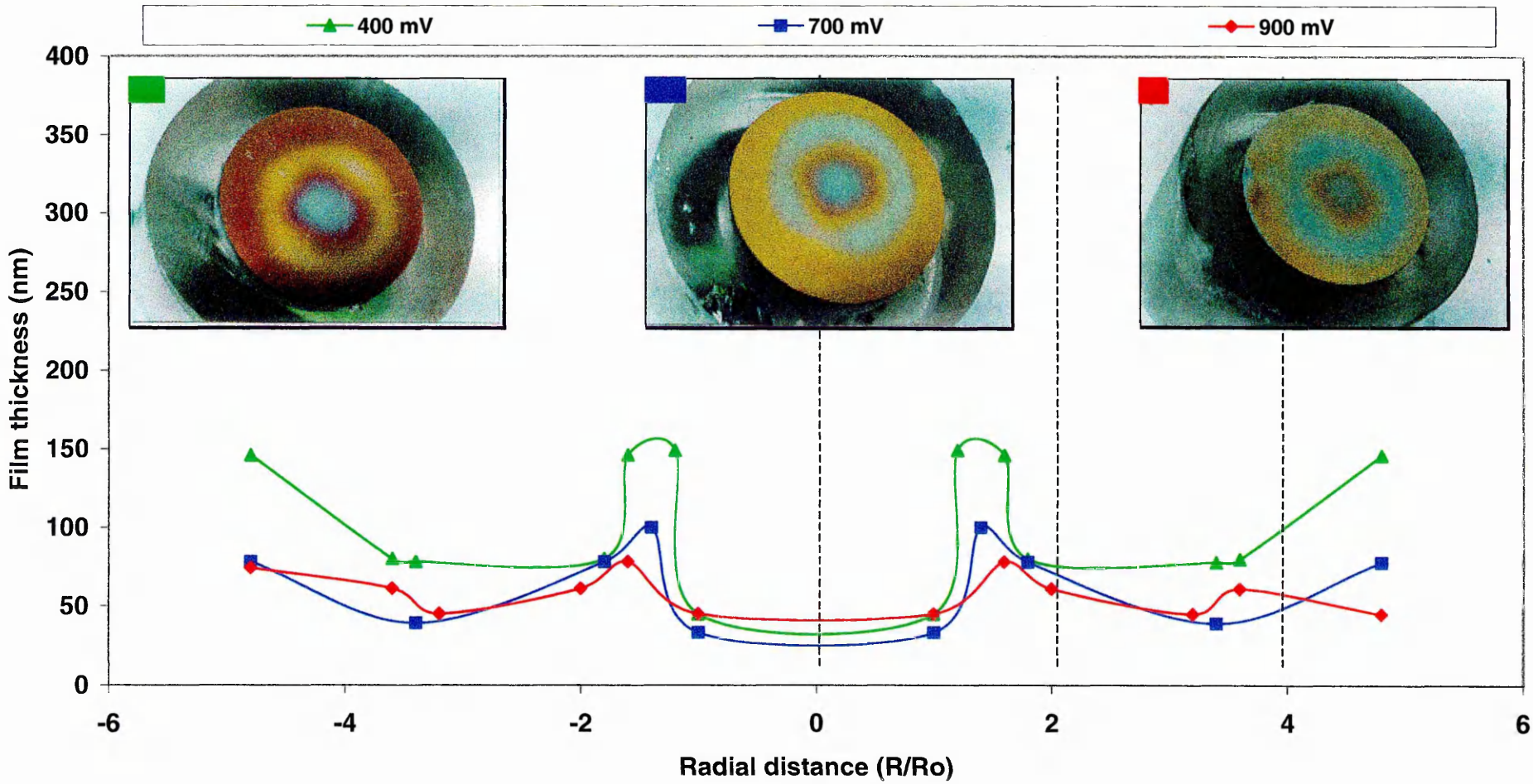

Figure 9.14 Duplex stainless steel (batch A) held at 400, 700 and 900 mV (SCE) at fluid flow velocity of 7.8 m/s for 6 hours then 3 grams of sand added for 10 minutes

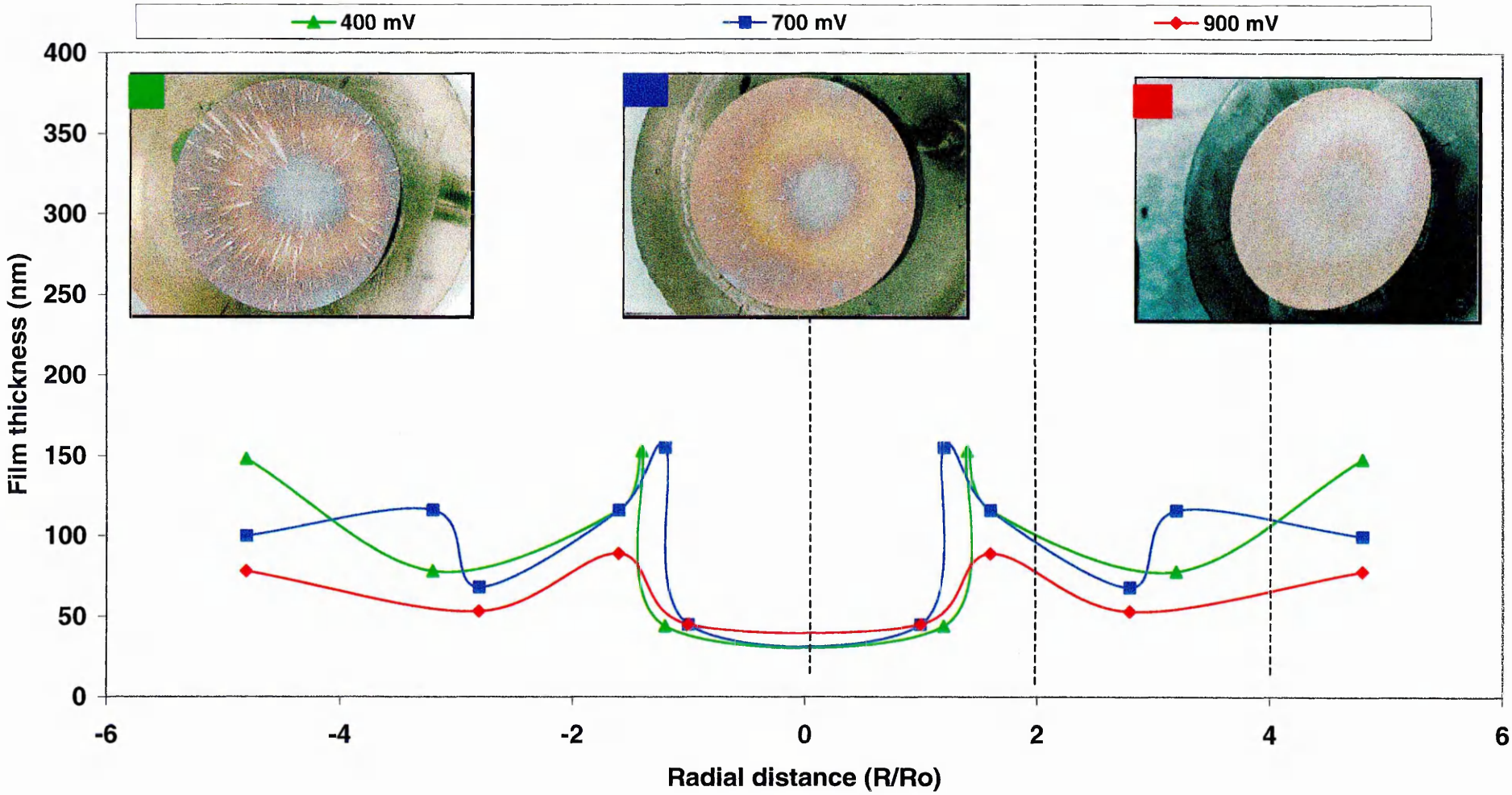

Figure 9.15 Duplex stainless steel (batch A) held at 400, 700 and 900 mV (SCE) at fluid flow velocity of 7.5 m/s for 6 hours then 3 grams of sand added for 10 minutes

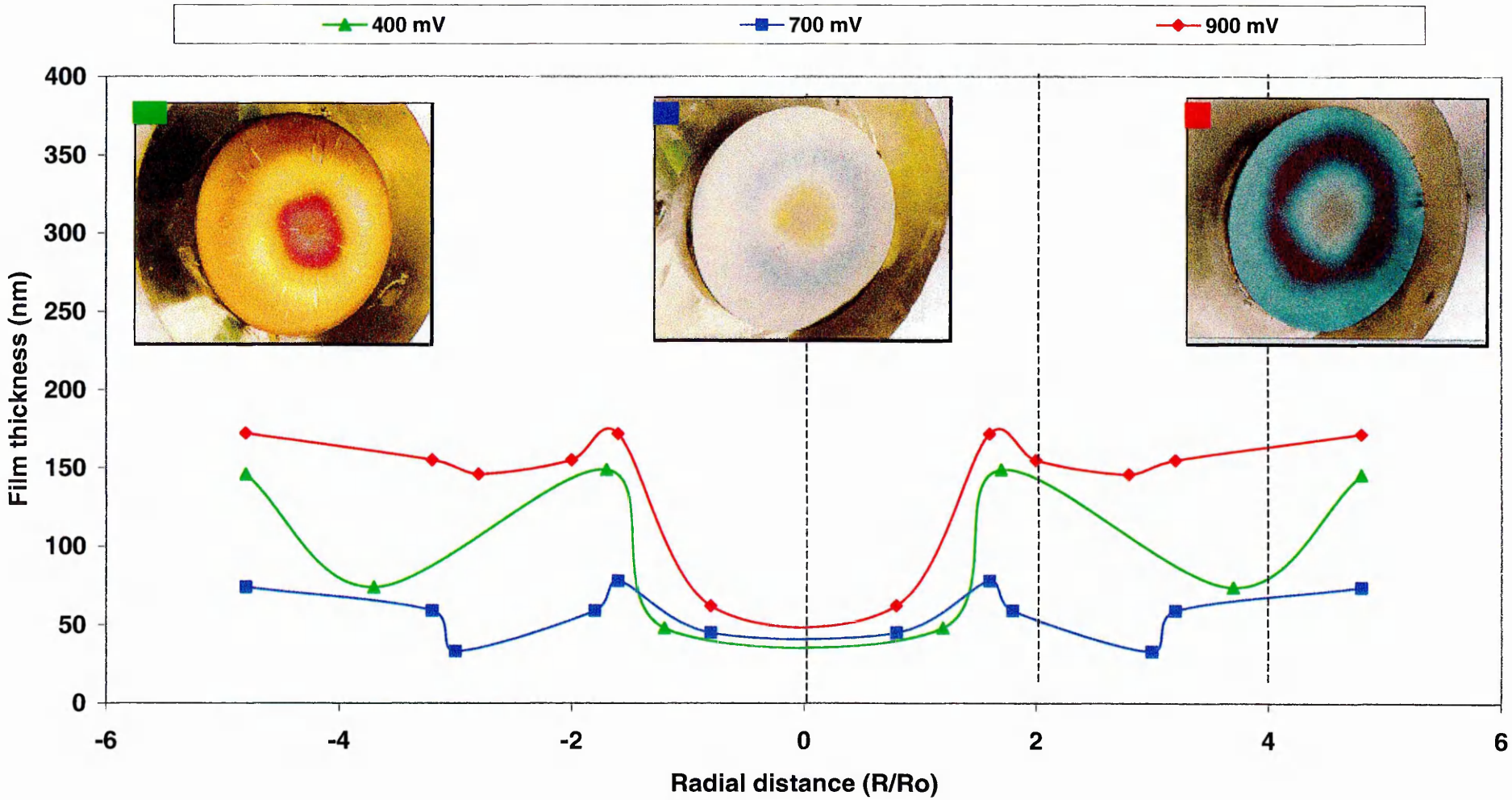

Figure 9.16 Duplex stainless steel (batch A) held at 400, 700 and 900 mV (SCE) at fluid flow velocity of 7.2 m/s for 6 hours then 3 grams of sand added for 10 minutes

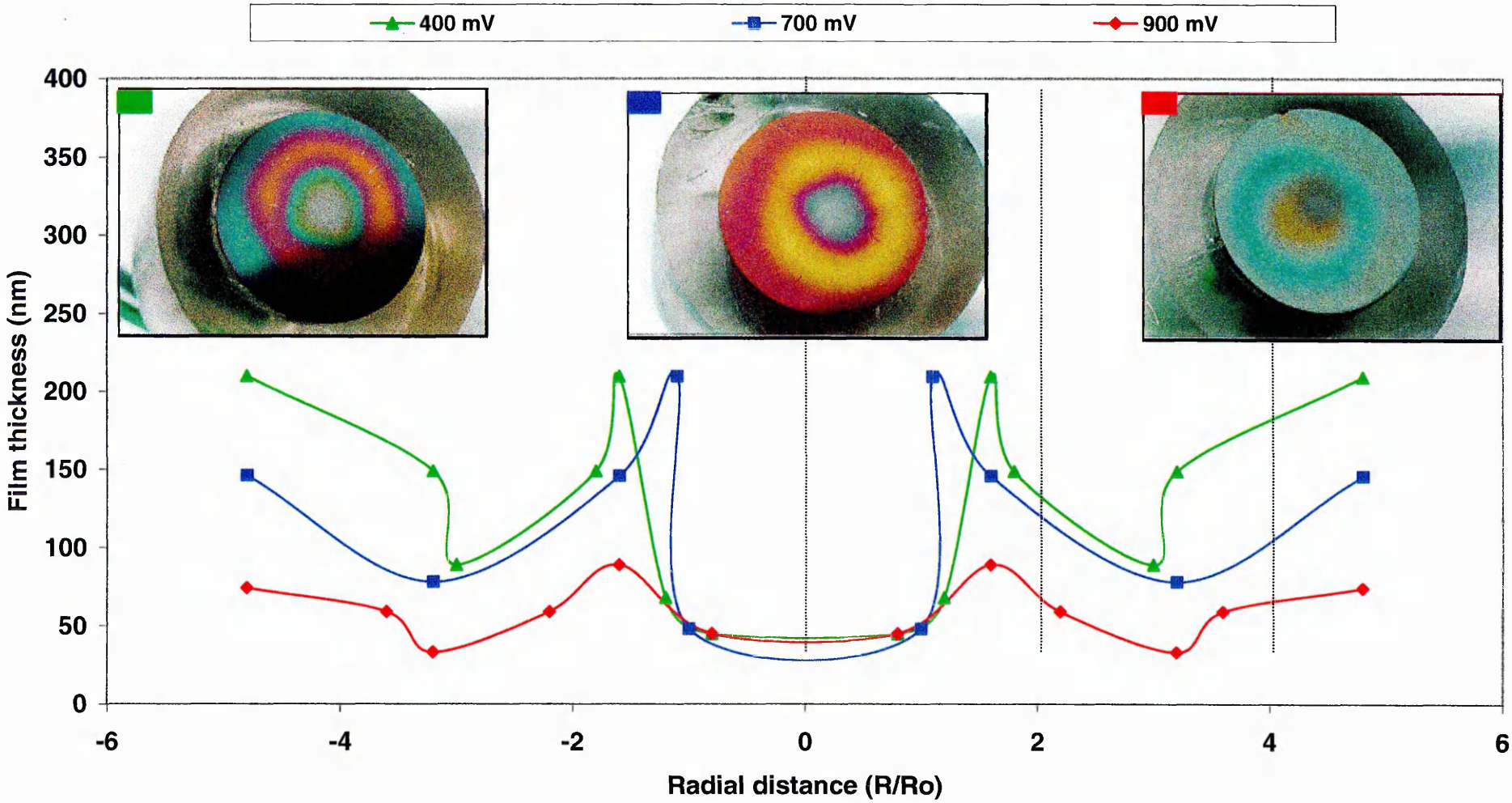

10.0 SAND IMPINGMENT RESULTS

Erosion-corrosion of duplex stainless steel consisted of two forms of mechanical and electrochemical damage occurring on the surface of the material. The investigation in this section is to measure the mass of suspended sand in order to be able to calculate the rate of particle impacts, which depassivate the surface of the material. This means that the form of damage occurring has been affected by the physical characteristic of the sand particles.

10.1 Sensitivity measurement

In the notion of data point's quality measurement, a sensitivity study of all measured data points was developed at different fluid velocities and sand concentration. By considering parameters such as the reproducibility value at the digital balance when measuring the mass of sand which was 0.1 mg, this produced an accuracy within ±0.0025%. Secondly, the minimum collection time in seconds that can be measured was one second on the digital stop watch, giving accuracy within ±10% at a time duration of 10 seconds as shown in figure **10.1** in the appendix. The results shows that a negligible effect of ±0.0025% in the vertical axis bandwidth which is the (N) number of particle impacts indicated by (N_{max} and N_{min}) while the time (T) in the second axis indicates a narrow bandwidth of ±10% indicated by (T_{max} and T_{min}).

Therfore, the ±10% bandwidth was considered to be the accuracy value for the measured mass of sand as indicated in figure **10.2** in the appendix. The number of particle gradients were considered at 4 grams and a velocity of 8.5 m/s. The stipulated trend line was passing through the majority of the data points bandwidth range, decreasing with the reduction in fluid velocity. Also an increase in the original value at 7.9 m/s over the 8.5 m/s could be a joint effect of random collection of heavy sand particles with the suspended ones and an error in collection time.

Another parameter which affects the value of the measured suspended mass of sand was the mass of sand that travels in batches in the water for some time, especially the larger diameter heavy particles. This could introduce error to the mass of suspended sand during the collection time and it is difficult to obtain a percentage value for this parameter at the moment. However, to validate the trend of the curves for every fluid flow velocity at various sand concentrations, graphical presentation of the fluid flow rate percentage versus number of particle impacts was shown in figure **10.3** in the appendix. The results describe the shape of the plots at 10 and 50 seconds time duration which have similar trend behaviour to those predicted in the sand impingement graphs.

10.2 Distribution of suspended sand at different fluid flow velocities

Initially, to predict the behaviour of sand particles in the loop with respect to time, some parameter values were determined like the time duration required for sand particles to flow once through the system.This was calculated as followed:

Area of the orifice $= \pi r^2$

$= \pi (2.5)^2$

$= 19.6 \text{ mm}^2$

$= 0.20\ cm^2$

Velocity fluid flow through the orifice $= 8.5$ m/s
$= 8500$ mm/second
$= 850$ cm/ second

In one second volume flow $= 850 \times 0.20$
$= 170\ cm^3$/ second

Volume of water in the loop system $= 3000\ cm^3$

Therefore, time for particles to flow around in the loop once

$$= \frac{3000}{170}$$

$= 18$ seconds

Other sand particle behaviour experimental parameters, such as number of particle impacts per second and the mean time between impact of each particle on the surface of the specimen, are discussed later in the chapter.

The mass of suspended sand comes from direct measurement of sand collected over a continuous period of 10 seconds, then the experiment stopped and the impingement system flushed, then a new experiment was commenced with a new time duration of sand collection. After the mass was obtained, their number of particles was determined and both were plotted against a time duration of 240 seconds. The behaviour of sand particle impacts at different sand concentrations and various fluid velocities are discussed below:

10.2.1 Mass of suspended sand at 4 grams sand particle concentration

During mass of suspended sand collection at fluid velocity of 8.5 m/s, more water was added to the system just to keep the level constant in the cell which considered the largest reservoir of water fitted in the impingement system. In figure **10.4** the mass of sand suspended in the cell (mass of sand impact on specimen) sharply increased up to the first 120 seconds which was indicated by nearly a straight line curve. As time duration increased the curve behaviour tended to be more of a horizontal line. The reason for this sharp increase was more sand coming out with the water, not enough time for the suspended sand to flow out from the nozzle, and with less dilution of sand occurred from the water addition to the system.

At high time duration, the mass of suspended sand in the system becomes more diluted by the addition of water. This resulted in more water coming out of the nozzle than sand. Keeping the large diameter sand particles deposited in the system and the lighter ones still suspended in solution, the mass of suspended sand drastically increased from 0.65 grams to 2.7 grams at the first 120 seconds then maintained a constant increase indicated at values between 2.7 grams and 3.2 grams.

At fluid velocity of 7.5 m/s, the behaviour of the mass of sand suspended at 240 seconds time duration retained a minimum value of 0.9 grams. The majority of the sand measurements plots showing fluid velocity of 7.8 m/s maximum values were higher than the values of 7.9 m/s velocity. This was due to the fact that at 7.8 m/s velocity was tested nearly two years ahead of 7.9 m/s when the pump impeller and the rest of the

system components were at their optimum condition with less time for erosion effect. Also at 7.2 m/s fluid velocity had overcome the 7.5 m/s one, which could be related to the fewer air bubbles developed during water addition which in turn could affect the flow stability in the system. This event tends to take a space in the flexible hose located prior to the nozzle.

The number of particle impacts on the surface of the duplex stainless steel specimen implies similar behaviour to the collected mass of sand, thus the particle numbers were calculated around 230,000 and 72,000 particles at fluid velocities of 8.5 and 7.2 m/s respectively as indicated in figure **10.5**. The difference in mass and number of particles between the maximum velocity of 8.5 m/s and the rest of the fluid velocities were as follows: at 7.9 m/s – 1.9 grams and 124,000 particles. At 7.8 m/s - 2.7 grams and 175,000, at 7.5 m/s - 0.8 grams and 65,000, finally at 7.2 m/s the difference was 1.1 gram and 72,000.

At 10 seconds time duration was considered the most essential timing in the sand measurement study, the curves at fluid velocities of 7.9 m/s and 8.5 m/ did not intersect the points.

This can be justified as scatter points which resulted from mixture of masses of suspended sand and batches of heavy sand, and consequently resulted in an unreal value of the mass of collected suspended sand. Apparently, the curves pass through the bandwidth ranges of the points, hence the curves are considered valid.

To justify the choice of 10 seconds time duration and the gradient location later on, the 10 seconds period was considered the best actual experimental data obtained, despite the fact that some of the points did not lay visually on the curves at different fluid velocity, but still the curves lay in their bandwidth range. The reason behind this choice was at different fluid velocities and sand concentrations at 10 seconds, the amount of water compared to mass of sand collected was small, meaning that a higher ratio of sand to water and a negligible dilution of sand particles occurred. Eventually, the a mount of water added to the system during a 10 second period was considered very small when compared with other water quantities added at time duration values of 30 seconds and higher. This resulted in water levels decreasing very slowly in the cell, because the collection time was so short. Therefore, the value at 10 seconds was indicated to be the most accurate real value of number of particle impacts and the best readings for measuring gradients.

As the collection time increased beyond 10 seconds, more water was added to the system to keep up with the pump discharge and maintain a constant water level at all times. With this water addition, as explained previously, the suspended sand becomes more diluted with water, meaning that the value of sand collected is not a stable value. With more water added the curve of the number of particle impacts tends to change from nearly vertical line behaviour to a more horizontal line.

10.2.2 Mass of suspended sand at 3 grams sand particle concentration

With the reduction in sand concentration, the number of particles and mass decreased as shown in figures **10.6** and **10.7**, and follows the same pattern of curves to the 8.5 m/s, but with less values of particle numbers and mass of sand.

At minimum fluid velocity of 7.2 m/s the readings were between 0.49 grams and 3,200 particles respectively. At the same time the maximum mass and number of particles impacted at a velocity of 8.5 m/s were 2.2 grams and 155,000 particles respectively. This indicated that with higher velocity, the number of particles and mass of sand curves tend to increase to higher values with nearly a straight-line relationship. Equally, the mass and number of particles at 7.5 m/s velocity is higher than the 7.2 m/s velocity at this sand concentration. A similar behaviour even detected at the number of sand particle impacts graphs.

10.2.3 Mass of suspended sand at 2 grams sand particle concentration

At 2 grams sand concentration, as shown in figures **10.8** and **10.9**, the mass of sand impacted range was between 0.3 and 1.4 grams while the number of particles impacted on the surface were between 26,000 and 98,000. Hence with decreased sand content the suspended sand and number of particles reduced. The mass and the number of particles impact curves at 7.8 m/s, still higher than the velocity of 7.9 m/s.

At 10 second time period both velocities at 7.8 m/s and 7.5 m/s curves were higher than the rest of the velocities. This could be related to the accuracy of the measured mass of sand, which could be due to the delay in the collection time or that a batch of heavy particles was mixed with the suspended ones.

10.2.4 Mass of suspended sand at 1 gram sand particle concentration

Figures **10.10** and **10.11**, show that the distribution of suspended mass of sand and the number of particles curves became closer to each other in value, but all the velocities are in order at this sand concentration. Only at 10 seconds the graphic curves order indicate a maximum value at 7.9 m/s, 7.8 m/s then at 7.2 m/s. The number of particles was reduced drastically to a maximum value of 43,000 and a minimum of 22,000. Comparing the sand measurement curves with the 2 grams sand concentration ones, this extrapolated that the ratio difference at each velocity of the 1 gram sand concentration in both cases of mass and particle number were lower in all the velocities.

10.3 Determination of the number of particle impacts in unit time

The mass of sand suspended in cell (mass of sand impact) was calculated from different sand concentrations. The value 275 μm was the most probable mean diameter of a sand particle, calculated from the sand range of 250 μm and 300 μm.

As the volume of sand particle (sphere) $= 4/3\ \pi r^3$ (1)
By substituting in equation (1) $= 4/3\ \pi\ (137.5)^3$
Changing the radius from μm^3 to cm^3 $= 4/3\ \pi\ (0.014)^3$
$= 1.1 \times 10^{-5}\ cm^3$

$\therefore$ Mass of one particle = volume of particle × sand particle density (2)
$= 1.1 \times 10^{-5} \times 1.3$

$$= 1.4 \times 10^{-5} \text{ grams}$$
$$= 1.4 \times 10^{-8} \text{ Kg}$$

Hence, the number of sand particles passing through the orifice can be derived from the mass of sand using the following equation.

$$N = \frac{M_S}{M_P} \qquad (3)$$

Where:

N = Number of particle impacts.
M_S = Mass of suspended particles (gram).
M_P = Mass of one particle (gram).

Using equation (3) set of graphs shown in sections **10.1.1** to **10.1.4** for the number of particle impacts was calculated from the mass of sand suspended measurements (M_S) at various fluid flow velocities. This revealed that both curves were nearly identical as shown in figures **10.4** and **10.5**. In order to avoid replication in graphs, the number of particle impacts graphs was shown as a small graph within the number of particle impacts curves.

Similarly, the number of particles impacts per second and the mean time between the impact of each particle on the surface of the specimen at 4 grams sand concentration and fluid flow velocity of 8.5 m/s were determined. As the maximum number of sand particles collected was 230,000 particles (figure **10.5**) then the number of particles impacted per second was calculated as followed:

$$= \frac{230{,}000}{18}$$
$$= 12{,}777 \text{ impacts/second}$$

Hence, time between impact of each particle randomly on the surface of the specimen

$$= \frac{18}{230{,}000}$$
$$= 7.8 \times 10^{-5} \text{ seconds}$$
$$= 780 \text{ millisecond}$$

Eventually, the aim was to be able to calculate the rate of particle impacts which rupture the surface of the material. The main interest from the mass of suspended sand distribution plot was to calculate the number of sand particle impact as a function of time, which is the gradient of the first 10 second period at 8.5 m/s fluid flow velocity.

10.4 Number of sand particle gradients in unit time

The number of sand particle gradients in unit time was determined using the equation

$$\text{Gradient} = \frac{N}{t(\text{seconds})}$$

Figures **10.5-10.10** show the number of sand particles impact gradients for the first 10 seconds at different fluid flow velocities and sand concentrations, which were indicated by coloured rectangular boxes on the top of the graphs. The gradients were determined only at 10 seconds time duration, because, as stated previously, at this time period is the most accurate condition of the steady state of the impingement system and the time when water addition was minimal. All the calculated gradients were illustrated in figure **10.12**, showing the number of particle impacts gradients versus mass of sand at different concentrations. The highest number of particles impacts gradient at the maximum fluid velocity of 8.5 m/s was 3800 at 4 grams and the lowest was 1000 at 1 gram, in spite of an increase in gradient of 7.9 over 8.5 m/s at 4 grams. This was related to the sensitivity of the measured data point as explained in section **10.1** (figure **10.2** appendix).

With the decrease in velocity, the number of particle impacts gradients were reduced. This reduction was accompanied with some variations in gradients values. As mentioned previously these were due to the accuracy of the measured data and the accompanied error effects of collection of heavy deposited sand particles with the suspended sand, timing and air bubbles trapped in the system during the addition of make up water to the system.

However, gradients at 30 and 50 seconds were not selected because their suspended mass of sand was more diluted, which means that the impingement system actual fluid flow behaviour was affected or disturbed, resulting in developing a non steady state condition in the system and the measured masses of sand being prone to change.

Figure 10.4 Disribution of the suspended sand for 4 grams sand concentration at various fluid flow velocities

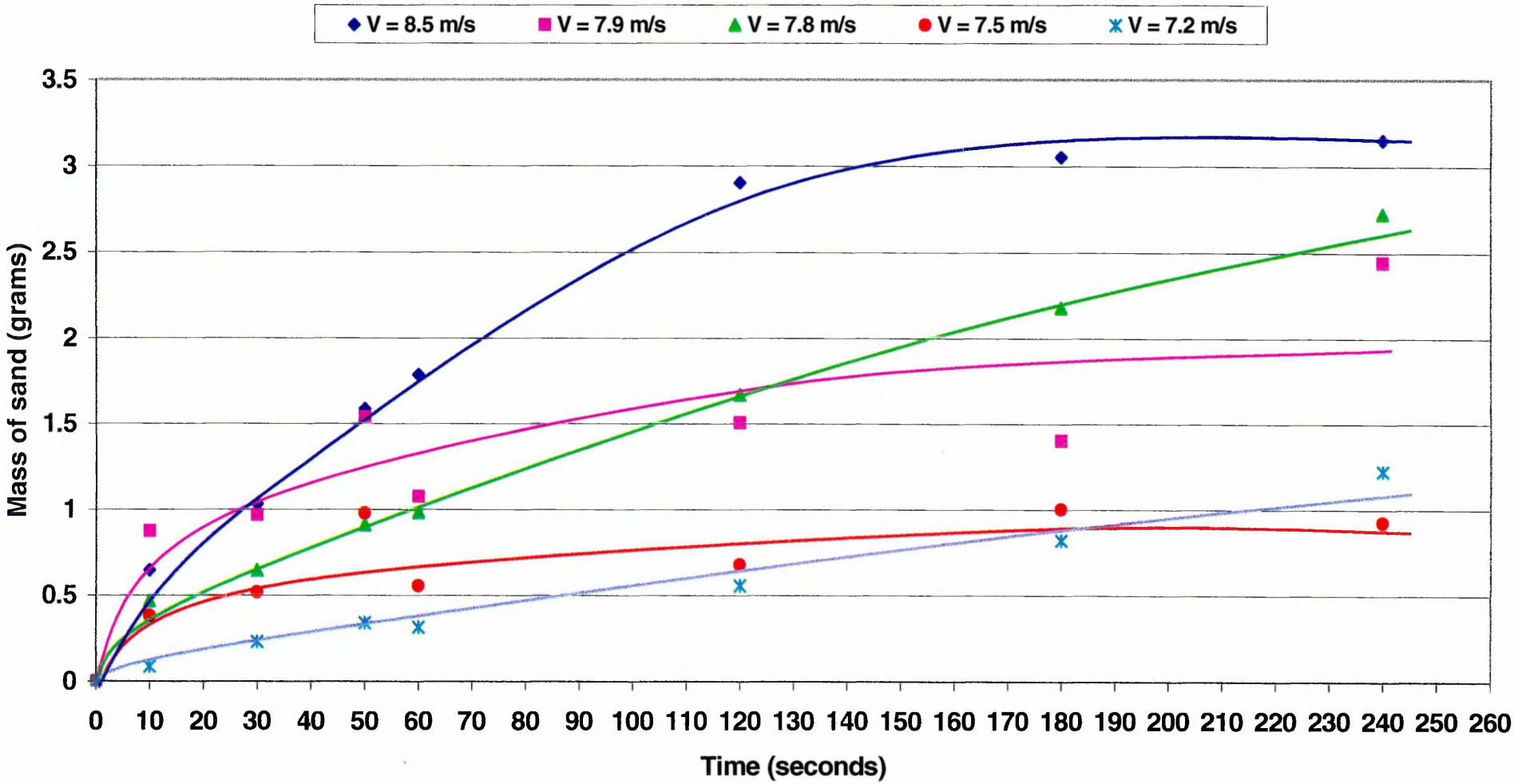

38000/ 10 = 3800

39000/ 10 = 3900

26000/ 10 = 2600

29000/ 10 = 2900

9000 / 10 = 900

Figure 10.5 Number of particle impacts for 4 grams sand concentration at various fluid flow velocities with gradeints values at 10 seconds collection time

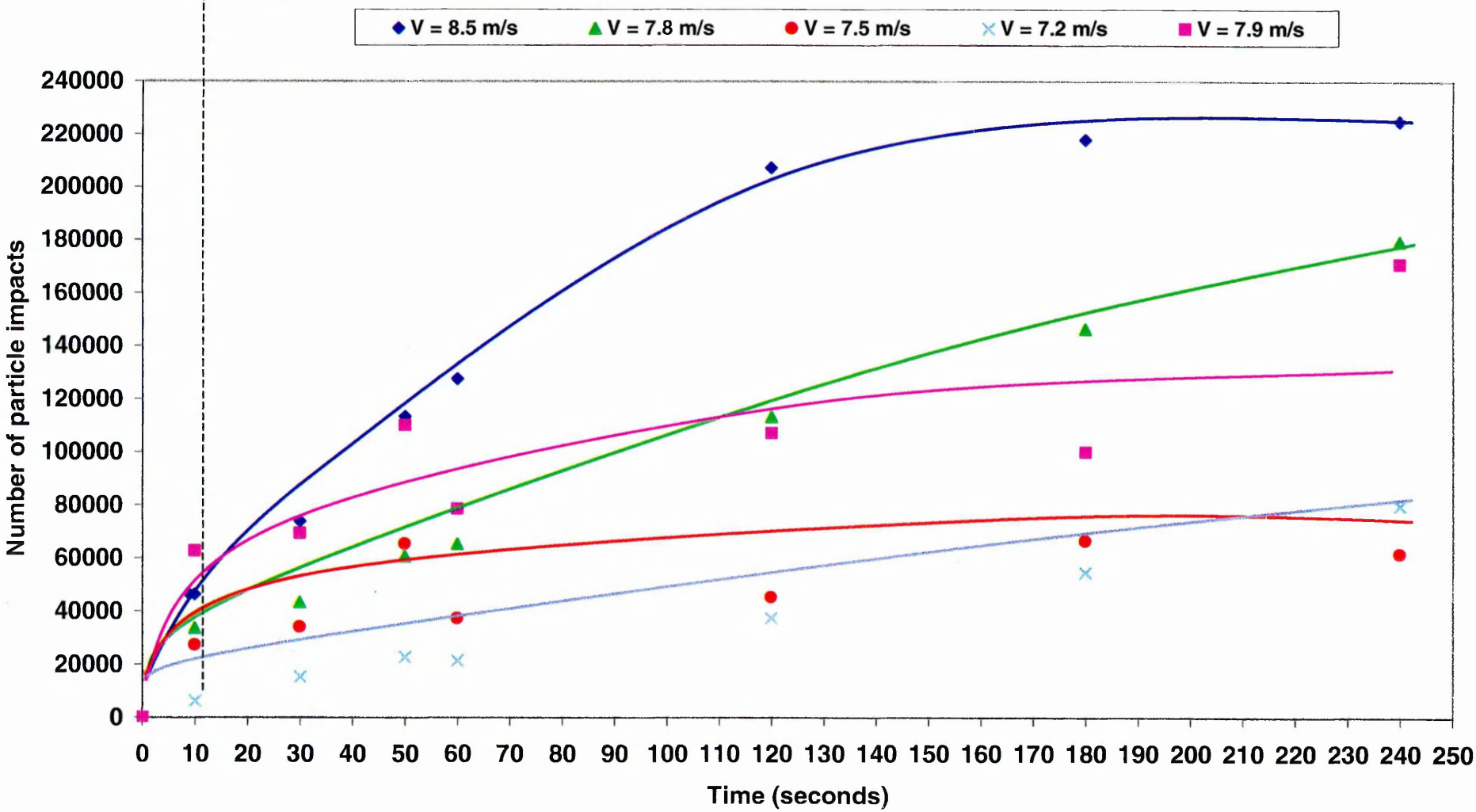

24000/ 10 = 2400

14000/ 10 = 1400

17000/ 10 = 1700

13000/ 10 = 1300

8000/ 10 = 800

Figure 10.6 Distrubution of the suspended sand for 3 grams sand concentration at various fluid flow velocities

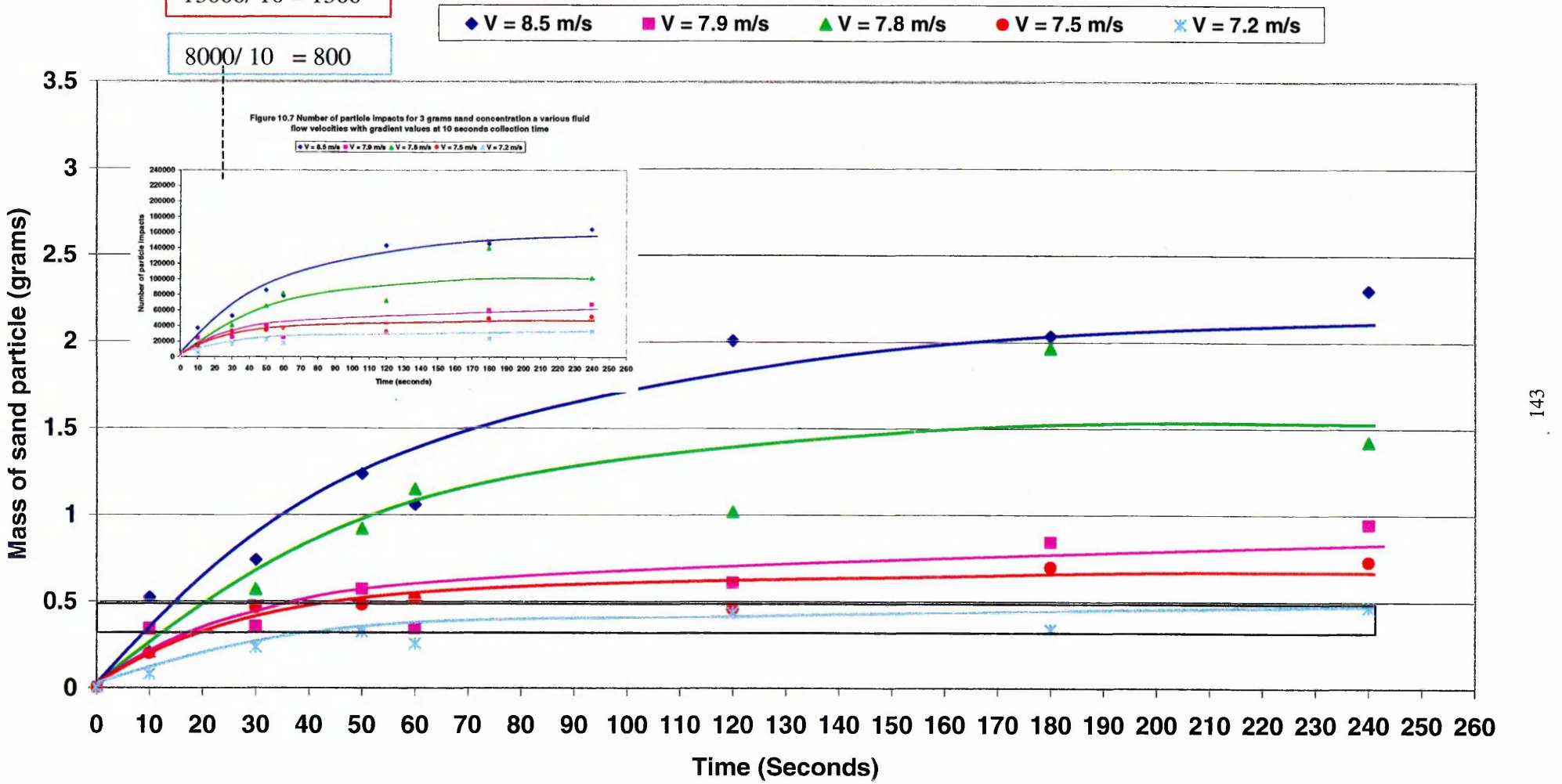

17000/ 10 = 1700

18000/ 10 = 1800

32000/ 10 = 3200

29000/ 10 = 2900

13000/10 = 1300

Figure 10.8 Distribution of the suspended sand for 2 grams of sand concentration at various fluid flow velcoities

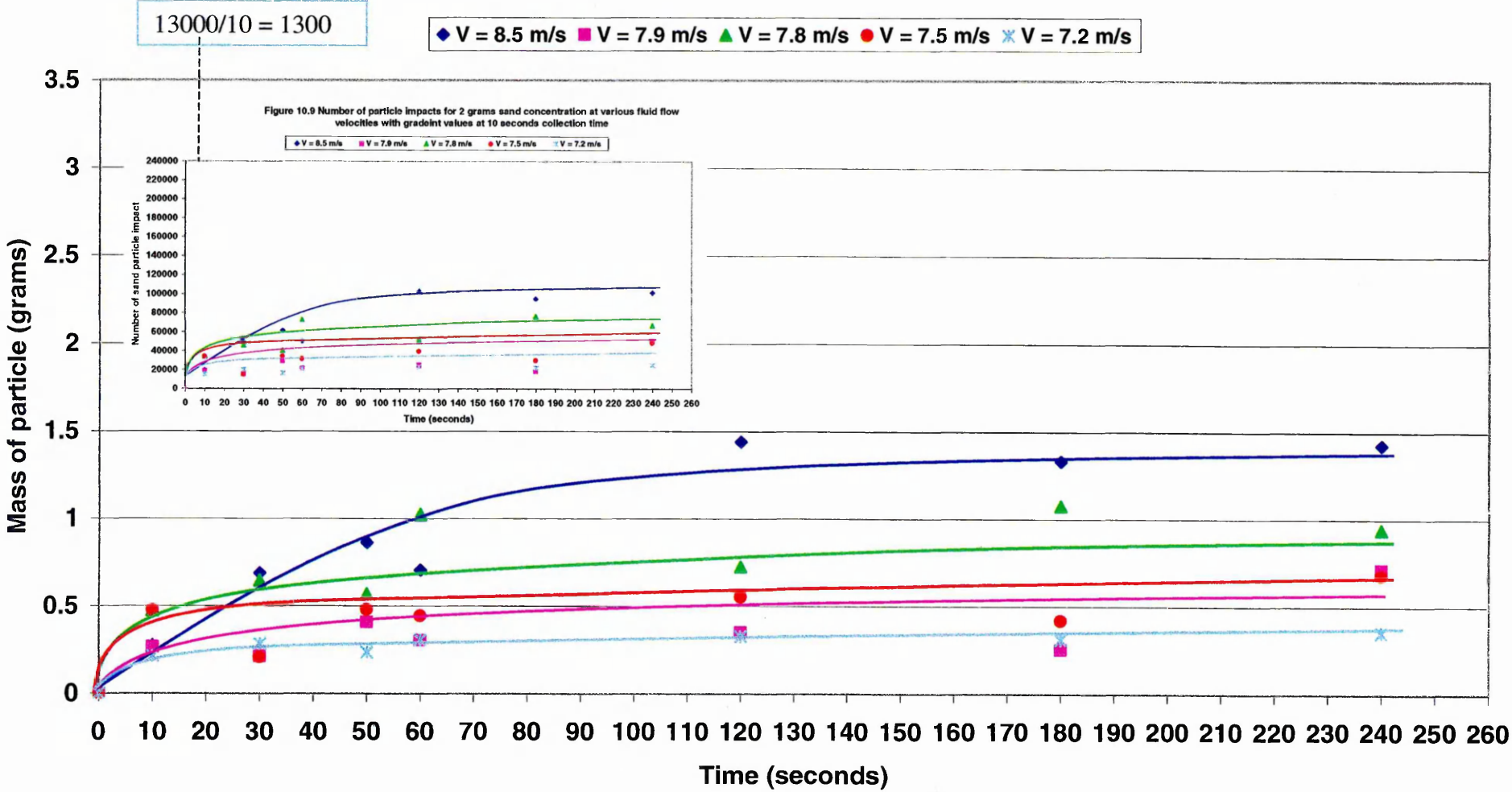

Figure 10.9 Number of particle impacts for 2 grams sand concentration at various fluid flow velocities with gradeint values at 10 seconds collection time

10000/ 10 = 1000

18000/ 10 = 1800

7000 / 10 = 700

13000/ 10 = 1300

11000/ 10 = 1100

Figure 10.10 Distribution of the suspended sand for 1 gram sand concentration at various fluid flow velocities

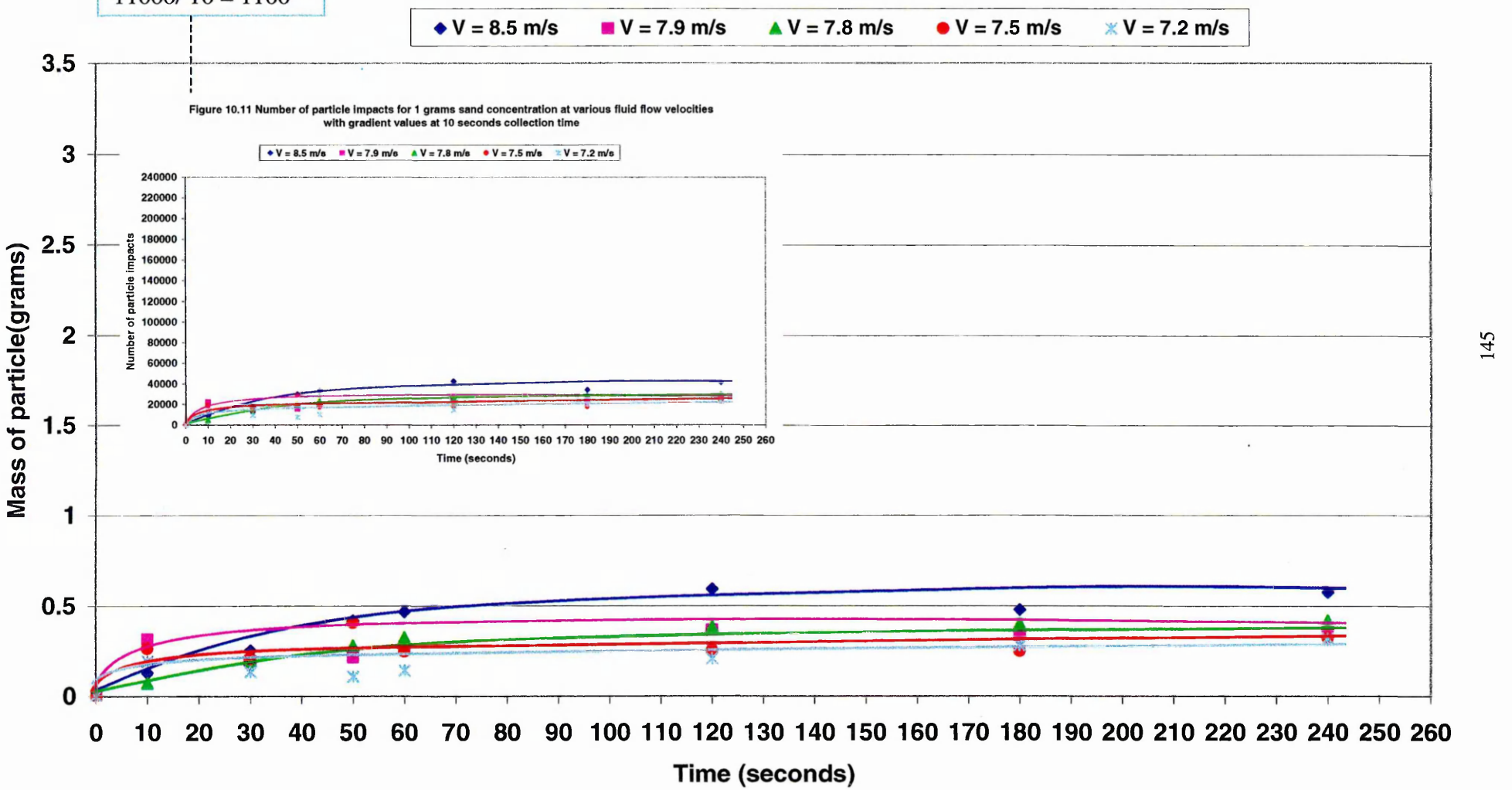

Figure 10.11 Number of particle impacts for 1 grams sand concentration at various fluid flow velocities with gradient values at 10 seconds collection time

Figure 10.12 Number of sand particle impacts gradient at 10 second time duration under different fluid flow velocity and sand concentrations

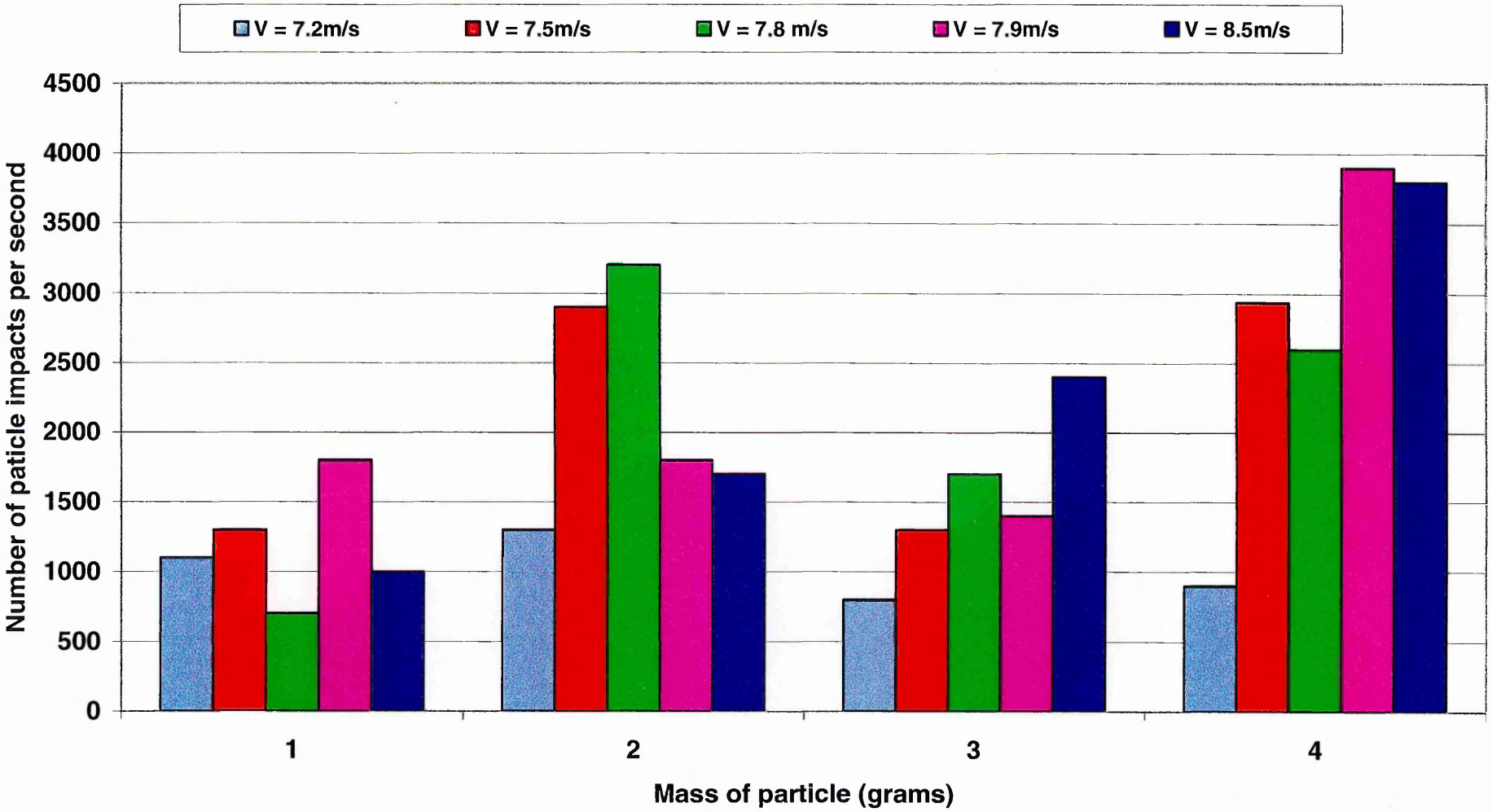

11.0 ELECTROCHEMICAL DISCUSSION

11.1 Potentiodynamic scans

11.1.1 At static and flowing condition

The experimental results presented previously showed that in the case of duplex stainless steel exposed to stagnant seawater (figure **7.4**), the corrosion process was controlled by the cathodic reaction, which was the reduction of dissolved oxygen. The flux of oxygen towards the metal surface was the main factor controlling the corrosion rate. At breakdown potential of 880 mV the current density was 3 $\mu A/cm^2$, this being attributed to the preferential dissolution of the austenite, while at lower breakdown potential of 380 mV, the current developed was 1.2 $\mu A/cm^2$ which corresponded to the pitting potential of the ferrite phase.

Acceleration of erosion corrosion under flowing conditions has been ascribed to either mechanical removal of the passive film by erosion from the metal surfaces, or to mass transfer effects, or both. During fluid flow conditions the anodic curve was promoted by liquid erosion while the cathodic reaction curve stayed unchanged. The intersection of both curves resulted in a polarisation diagram with a higher passive current density and more active rest potential as shown in figure **11.1**.

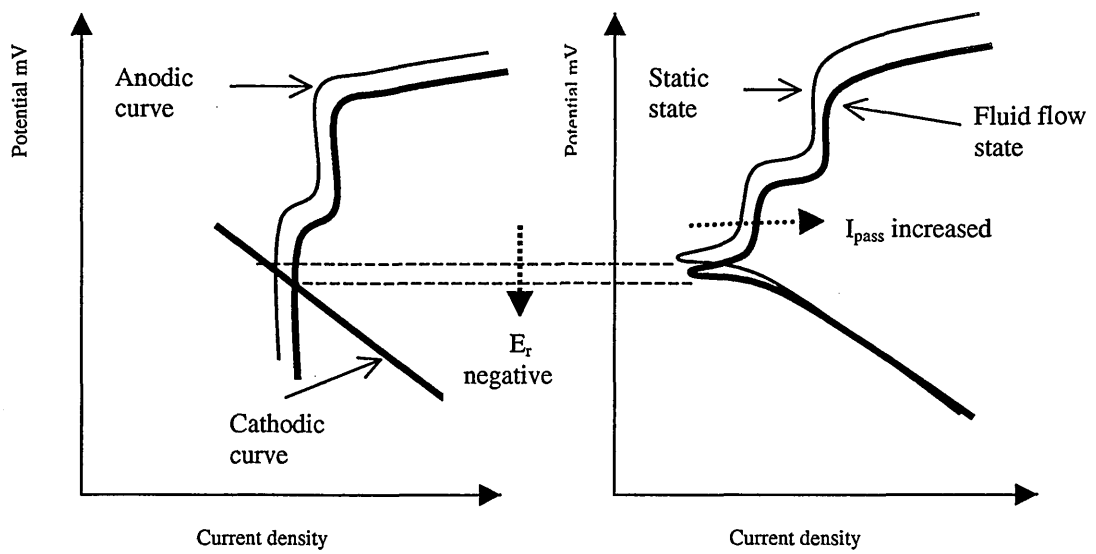

Figure **11.1**. A schematic diagram showing the effect of flow on the polarisation curve of ***ring 1*** duplex stainless steels

In the polarisation diagram of ***ring 2*** (Figure **7.5**) in the flowing condition, the current density at the delta ferrite pitting range increased to a value of 8 $\mu A/cm^2$ at 895 mV compared with the static current density of 4 $\mu A/cm^2$. As ***ring 2*** was situated in the high shear stress region a similar polarisation behaviour to ***ring 1*** was obtained with the same current density readings but with less signs of crevice corrosion exhibited in the active region of the diagram. With the higher current density the E_{corr} was slightly shifted to the negative direction.

With reference to the ***ring 3*** polarisation diagram (Figure **7.6**), the slight positive shift in cathodic reaction curve and the ennoblement of the open circuit potential (E_{corr}) was due mainly to different specimens of the same batch (**A**) being used for the static and fluid flow conditions. It follows similar behaviour to rings 1 and 2, and the pitting potential value recorded at flowing condition for ring 3 was 380 mV at 1 $\mu A/cm^2$ with a breakdown potential of 910 mV at 7 $\mu A/cm^2$.

An overall view of the three rings confirmed that the increase in the fluid flow shifted the anodic curve to a higher passive current density and the cathodic curve was unchanged. When comparing the current density of the three rings, very close values were recorded for the different regions. It was concluded that the fluid flow velocity at ***ring 2*** did not create enough shear stress on the surface to reduce completely the stability of the passive film, to produce a higher current density than ***rings 1*** and ***3***. Usually the region of high turbulence develops the highest current density at the hydrodynamic flat plate specimen, but in this instance the fluid flow was not sufficient to overcome the simultaneous repassivation effect of the passive film.

The current density developed at ***ring 1*** was mainly due to the mass transfer exhibited in this region, plus the pits and inclusion inherent in the surface. At ***ring 3***, as the fluid flow vectors changed from axial to radial flow and an increase in boundary layer exhibited within the low turbulence region, this resulted in less effect of the flow on the surface of the ring which then produced less value current density.

11.1.2 At fluid velocity of 8.5 m/s with sand additions

It is noted that the anodic passivation current density increases with an increase in percent solids, thus shifting the entire polarisation curve to the right. This is graphical evidence that the protective oxide layer that forms on the duplex stainless steel was continuously removed and simultaneously repassivated in the presence of sand and the rate of removal was dependent on the percent of sand concentration and the various fluid velocities.

Stack et al[160] confirmed the analysis of ***ring 1*** passive current densities as a function of velocity. In the presence of sand the anodic curve has been severely depolarised and therefore contributes to more active E_{corr} being recorded. Hence the cathodic reaction appears to be unaffected and under solid particle impingement the anodic reaction assumes the dominant role[19].

The anodic electrochemical reaction was enhanced by the solid impact effect, as shown in figure **11.2**. As the sand impact tends to rupture the passive film, a significantly higher current density was developed in the presence of 3 grams of sand at fluid flow velocity of 8.5 m/s, giving a current density of 6.6 $\mu A/cm^2$ at 0 mV. A normal double breakdown potential was observed for both the ferrite and austenite phases.

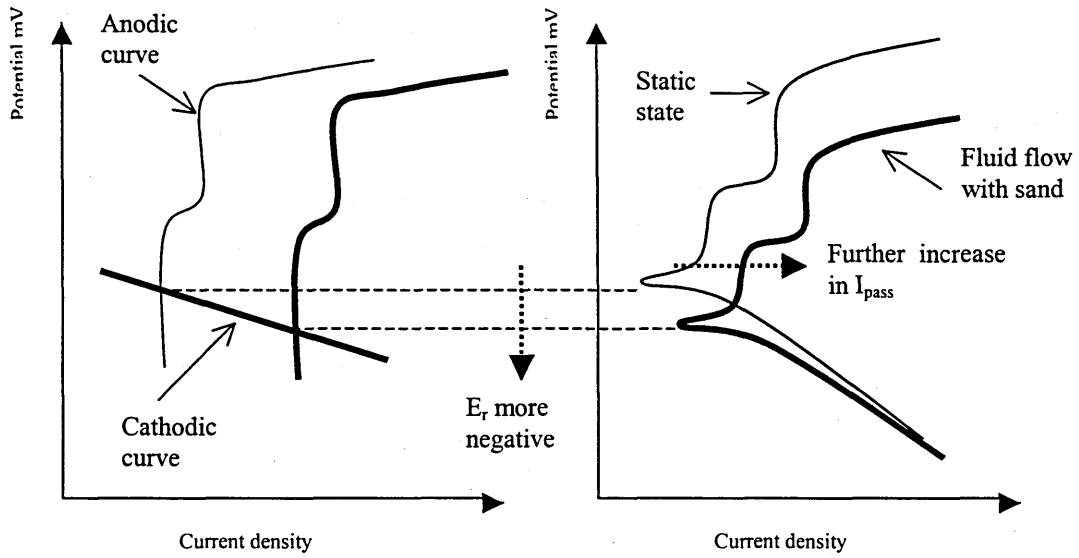

Figure **11.2** A schematic diagram showing the effect of flow with sand on the polarisation curve of ***ring 1*** duplex stainless steels

From figure **7.8** for ***ring 3*** show, no changes in the polarisation diagrams when sand impingement of various concentrations were added. This revealed that the low turbulence region of ring 3 positioned in the hydrodynamic fluid flow was not affected as much by the sand erosion. The electrochemical reaction mechanism follows a similar pattern to ring 1. The passive current density value was increased from 0.6 $\mu A/cm^2$ at flowing state to 0.8 $\mu A/cm^2$ at 3 grams of sand at 400 mV (SCE), while the austenite breakdown was recorded in the range of 7.5 $\mu A/cm^2$ to 8 $\mu A/cm^2$ at 900 mV (SCE).

In general the findings confirmed the active region of the duplex stainless steel mass loss was mainly due to erosion-corrosion. Evidence on the mechanical erosion process was indicated by the interference colour measurement. When the sand was added the oxide film in the stagnation region colour fringes shifted from second order to the first order colour category. Also a higher current density reading was detected from fluid flow only to fluid flow with sand particles.

At the same time, two electrochemical reaction processes were exhibited which produced current densities; firstly, rupturing the oxide film which rendered a bare metal surface condition and secondly, the simultaneous repassivation of the oxide film back to an equilibrium state, because both the ferrite and austenite phases were stable. Similarly, a very low current density was exhibited in this region, and this depended on the existence of crevice corrosion. However, in the active region of the duplex stainless steel a slight increase in current density was observed as the potential increased in the noble direction. Despite the high mass transfer exhibited in the stagnation region of the flow, the simultaneous repassivation and depassivation process of the oxide film was continuous.

In the austenite passive region (delta ferrite pitting region) the erosion tools were mechanical and electrochemical reactions (transition to erosion-passivation behaviour),

and confirmation of this is shown in figure **8.3**. Where it shows, the light austenite phase stayed protected and the dark ferrite phase pitted. The production of constant current density in this region under flowing condition was shifted to a higher constant current density which resulted from electrochemical reactions of ferrite dissolution and austenite repassivation, and sand particles mechanical erosion.

At the transpassive region above 900 mV (SCE) the high corrosion rate was due to the electrochemical reactions of bulk solution ions and the metal alloy dissolution. Corrosion-dissolution behaviour dominated at high velocity and high potential as indicated microscopically in figure **8.4**.

Preferential corrosion at austenite and corrosion product developed from comets, pits and metal dissolution. Equally, in the interference colour measurement, thickening of the film in the low turbulence region at 900 mV (SCE) due to corrosion products deposited from electrochemical reactions. Figure **7.7** demonstrated the difference in current density from a value of 9.3 μA/sq.cm at fluid flowing state to a reading of 10.4 μA/sq.cm under sand impingement condition. Clearly the sand particle mechanical erosion has little effect at this potential in the transpassive region when compared with the current density readings at a potential of 200 mV (SCE) in the active region.

11.1.3 At fluid velocity of 7.9 m/s to 7.2 m/s with sand additions

With the decrease in fluid velocity to 7.9 m/s, less passive current density developed at 0 mV (5.1μA/cm^2) due to less electrochemical reactions produced on the surface. A similar electrochemical behaviour to the velocity of 8.5 m/s was confirmed, by shifting the anodic reaction curves to a higher current density which in turn moves the E_{corrs} in the active direction potential as indicated in figure **11.2**.

According to Mingwi[2] the passive film formed on the surface of the specimen at separate anodic and cathodic reactions sites. Anodic dissolution at the base of the film and cathodic at the outer surface where film growth occurs, the concentration of ions decreases due to metal compound precipitation on the film surface. These ions can be replenished with the diffusion of ions (Fe^{+3}, Ni^{3+}, Cr^{3+}) dissolved at the stainless steel surface and the production of Cr^{3+} ion in the cathodic reaction.

The film begins to form, despite the fact that there is no visible evidence on the surface, the structure of the film having eluded definition because it is so thin and fragile. When the velocity and quantity of sand particles increases, the corrosion rate increases due to the removal of the chromium oxide film from the metal surface, but simultaneous repassivation occurs and tends to develop a thin film of first order colours with a thickness of 22 nm as indicated in the film thickness measurements using the Michel Levy chart.

With the frequent use of the same specimen, the cathodic area enlarged with the seepage of the electrolyte at the metal/resin interface, uncovering the gold palladium coating which was intended to be a cathodic site and probably the crevice corrosion would have been more severe without the coating. Scatter in the polarisation scan at 4 grams of sand could be related to the promotion of crevice corrosion.

As the fluid velocity decreased more to a minimum value of 7.2 m/s, a further reduction in passive current density occurred but with little difference between each fluid velocity. At the same time it was difficult to distinguish between the current density of the various sand concentration additions. The resultant mechanism of the electrochemical behaviour of the polarisation scans follows the same pattern of analysis as in figure **11.1**.

Despite the mechanism of attacks, it was apparent in the electrochemical curves of the duplex stainless steel that the oxide film was still adherent and fast-forming since the passivation persisted even at a maximum velocity of 8.5 m/s, even when sand concentration of 3 grams in the passive range of duplex stainless steel showed an average current density of 6.6 $\mu A/cm^2$ at 0 mV (SCE).

11.1.4 Microstructural analysis

The chemical analysis revealed an equal ratio of ferrite and austenite microstructural phases. Figures **8.5-8.7** represent the morphologies of coexistence of erosion corrosion on the surface of the duplex stainless steel specimens at different hydrodynamic regions. The surfaces showed dense and deep craters were formed on ***ring 1*** which was located directly under the nozzle, while ***rings 2*** and ***3*** suffered from comets and less dense craters all over their surfaces. This resulted later on in a considerable metal loss per year. Under the scanning electron microscopy a clear dissolution of the dark delta ferrite phase at 400 mV was revealed while the light austenite microstructure phase stayed protected. Then at the transpassive region of 900 mV, complete dissolution of both phases was recorded.

11.2 Open circuit potential

The value of the corrosion potential was a good indication of the electrochemical behaviour and the state of the duplex stainless steel specimen surface during sand impingement. At the highest velocity of 8.5 m/s with sand impingement, the potential became more negative indicating that the chemical reaction rate on the surface was increasing (Figure **11.3**).

The results showed that ***ring 1*** was severely affected by the erosion corrosion condition. Figure **7.13** describing the breakdown of passivity may be indicating an initial depassivation attack which would be shown by a sharp drop in potential on making the transition to the active state. The negative shift to a constant potential of -60 mV can be explained on the basis that, under such conditions, the breakdown of the oxide film was followed by a repaired condition. Hence, according to the polarisation scan in figure **7.7**, -60 mV potential was in the passive range of the duplex stainless steel with constant current density state. This certified the constant potential exhibited in figure **7.13** for ring 1.

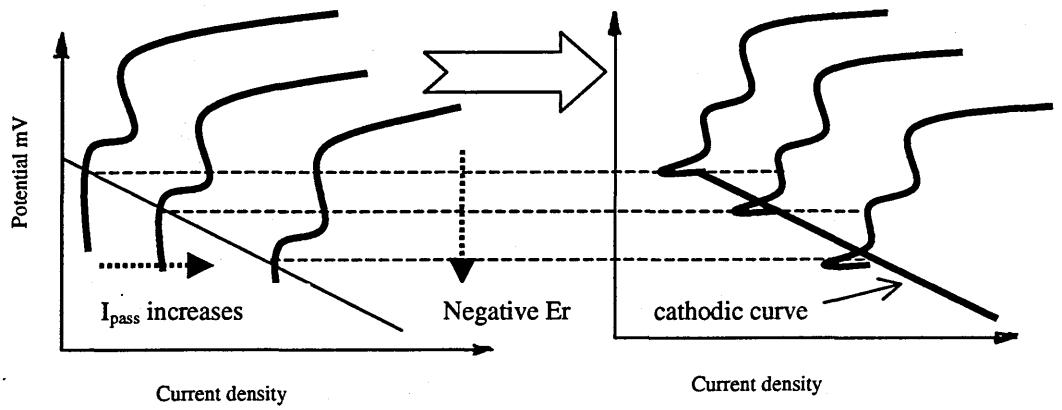

Figure **11.3** The effect of increase in sand impingement on the E_{corrs} of duplex stainless steel specimens

Rings 2 and ***3*** exhibited positive potentials under sand impingement which means that the surfaces were not as affected by the erosion corrosion condition due to the rings' position in the fluid flow and the repassivating rate of the oxide film being higher than the damage rate. The polarisation behaviour of ***ring 3*** in figure **7.8** shows that at 80 mV, the current density is still in the passive range of the material and holds a constant value which duplicates the constant potential in figure **7.13** in the last hour of the time duration. The same condition applied to ***ring 2***.

If the duplex stainless steel specimen was held at a fixed anodic passive potential, such as 100 mV (SCE) referring to figure **7.7**, the natural erosion corrosion processes would not be accurately simulated as if at the open circuit potential of duplex stainless steel.

Eventually, increasing the potential and holding it above 400 mV (SCE) or 900 mV (SCE) potentials were delta ferrite and austenite dissolution occurred respectively, the natural erosion-corrosion process of seawater entrained sand particles will not be truthfully replicated especially the accuracy of the pitting potential value. Closer the fixed potential to the free corrosion potential of the material such as at –200 mV (SCE) the erosion-corrosion process tends to be more natural.

11.3 Electrochemical current density

Under flowing condition at potential of –100 mV (SCE), –200 mV (SCE) and 100 mV (SCE), the current density values were partially mixed negative and positive values for all the rings. This was due to the effect of the cathodic reaction still existing. As these potentials were in the vicinity of the equilibrium potential of the alloy, the current developed was due to the electrochemical reactions from inclusion and pits already exhibited on the surface of the alloy and the flow of oxygen to the surface of the alloy. Only at 300 mV (SCE), was a positive current density obtained for all the rings unaffected by the cathodic curve reaction, as shown in figures **7.21-7.23.**

The severity of subsequent erosion-corrosion attack was quantified by the current density flowing from the anodic sites to the cathodic sites. Under sand particle impingement, the current density at the potential of –100 mV for ***rings 2*** and ***3*** stayed in

the negative region, suggesting that the alloy may have been repassivated. The corresponding potential behaviour in the polarisation scan for ring 3 (figure **7.8**) tends to confirm this with the active region potential being associated with this negative constant current.

While at 300 mV (SCE) potential for ***rings 3*** current density behaviour changed to positive values, different behaviour was observed of passive current density if compared with the polarisation scans. This could be related to different specimens being used from the same batch (**A**), resulting in less electrochemical reaction sites being developed in the polarisation scan, which reduced the current density value down to 0.8 $\mu A/cm^2$ instead of 2 to 3 $\mu A/cm^2$ as shown in figure **7.23**.

Similarly, it could be that the cathodic reaction effect existed at 300 mV (SCE) in figure **7.8**. Meanwhile in figure **7.23** the cathodic reaction effect diminished, as explained previously, which tended to make the current density of a positive value. For comparison '***ring 2*** current density with polarisation scan' was not possible due to the unavailability of a good polarisation scan with sand addition.

Ring 1 showed markedly different current/time behaviour at -200 mV(SCE) to the other rings when sand was added. In figure **7.19** the current density eventually increased to a value of 4.5 $\mu A/cm^2$ and stayed constant. This condition matched the 2 grams sand concentration current density developed in the polarisation scan (figure **7.7**) but not the 3 grams one. This increase in current density related to the potential was located in the active region of the alloy, where damage of the passive film had taken place due to sand particle impingement.

At 100 mV and 300 mV current density value of 7.5 $\mu A/cm^2$ to 7 $\mu A/cm^2$ was confirmed with the polarisation scan (figure **7.7**) due to the potentials' location in the passive range of the duplex stainless steel, which developed a constant positive current density. This can be interpreted by the simultaneous depassivation and repassivation effect of 3 grams of sand impingement on the passive film and at 300 mV no effect of cathodic reaction was observed on the anodic current values.

11.4 Metal Loss

The metal loss was calculated from the passive current density at various negative and positive potentials in seawater solution using Faraday's second law ($K_c = \frac{QM}{nFAT}$), which is explained in detail in the next modelling section. In the passive range of duplex stainless steel similar metal loss was observed at 100 mV (SCE) and 300 mV (SCE) constant potential, giving a value of 0.07 to 0.08 mm/year. This indicates that the duplex stainless steel has a good erosion corrosion resistance when immersed in a seawater environment.

12.0 PASSIVE FILM OPTICAL DISCUSSION

12.1 Quantitative measurement of passive film colour thickness

12.1.1 At fluid flow condition

When coloured film formed on the surface of the specimen the anodic and cathodic reactions occurred separately, the anodic dissolution proceeding at the base of the pores and the cathodic reaction at the outer film surface at the top of pores[11]. Figures **9.2- 9.6** showed the oxide film thickness profiles of the specimens anodically oxidized in a wide potential range from active to transpassive states for 6 to 18 hours. The reduction in the film thicknesses at the 400 mV (SCE) (δ pitting) potential were mainly due to both the ferrite in the duplex stainless steel being degraded while the austenite phase stayed stable and the second effect was the mechanical erosion due to fluid flow velocity on the surface of the specimen. Habazaki et. al[134] suggested that the thickness of the film formed in the active region decreases with molybdenum content of the alloy and gradually increases with polarisation potentials.

It is well known that the stagnation region exhibited high mass transfer and, with the flow of oxygen at the stagnation region, a thicker film was developed and the rate of growth was higher in some velocities than in other regions. This is because the film adhesion formed was stronger than the fluid velocity forces, also the mechanism of oxygen diffusion to the surface and the depassivation-repassivation of the oxide film was limiting the fluid velocity effect and tended to form a thicker oxide film.

In the high turbulence region, which retained a high shear stress, the consumed dissolved oxygen to develop the oxide film was overcome by the fluid shear forces. But with the usage of a maximum fluid velocity of 8.5 m/s, the simultaneous repassivation of the surface kept the oxide film growth at constant level. At the low turbulence region, approximately similar film thickness was retained to the stagnation region due to that region having the tendency to upgrade the oxide film growth due to the lesser hydrodynamic forces affecting the surface (thicker boundary layer). In general with the decrease in fluid velocity at different potentials, the oxide film increased in the stagnation and low turbulence regions, while the high turbulence region stayed unchanged.

At the passive potential of 700 mV (SCE) (austenite passive) where the delta ferrite dissolution was constant and the austenite phase is still protected, a stable film growth was developed in conjunction with the constant electrochemical current density produced. In the breakdown potential of 900 mV (SCE) (metal dissolution), electrochemical high current density was present due to the dissolution of the austenite phase, which produced high corrosion products, but with poor oxide film adhesion most of the oxide film thickness degraded with the flow. The erosion profile of the duplex stainless steel specimens in all regions at 700 and 900 mV (SCE) potentials showed some fluctuation but no definite changes occurred as the potential and fluid velocity increased.

As the velocity decreased a thicker oxide film was formed, hence film growth occurs due to the electrochemical reaction of the concentration of metal ions such as Fe^{3+}, Ni^{2+},

Cr^{3+} decreasing because of the precipitation of metal compounds on the film surface (corrosion products). Fluid velocity reduction has a maximum effect in the stagnation and high turbulence regions.

The film thicknesses at 400 mV (SCE) (δ pitting region) ranging between 150 nm to 170 nm and 70 nm to 90 nm respectively, at 700 mV (SCE) (austenite passive) the film thickness values were 150 nm to 170 nm and 33 nm to 80 nm respectively and at 900 mV (SCE) (metal dissolution), the film thickness between 70 nm to 170 nm in the stagnation region and varies between 30 nm to 150 nm respectively.

As Evans[151] suggested, the products of dissolution of metal diffuse through the porous network ultimately to form new film, with the products of the cathodic reduction of Cr^{6+} species at the outer surface of the film, i.e. a heavily hydrated, chromium-rich spinel oxide. While Mingwei[2] suggested that the variation of the surface concentrations of ions are responsible for the formation of a coloured film. Surface morphology observation revealed some preferential sites of corrosion and pit initiation; also comets were seen on the surface which developed from a corrosion of pits and inclusions.

12.1.2 At fluid flow condition with sand addition

The result of the sand addition with the flow for the duration of *6 hours* to *18 hours* since the specimen was left at –600 mV for one hour in the active region, shows accumulative impacts of sand particles led to a plastic deformation and fracture of the oxide film, as shown in figure **12.1**.

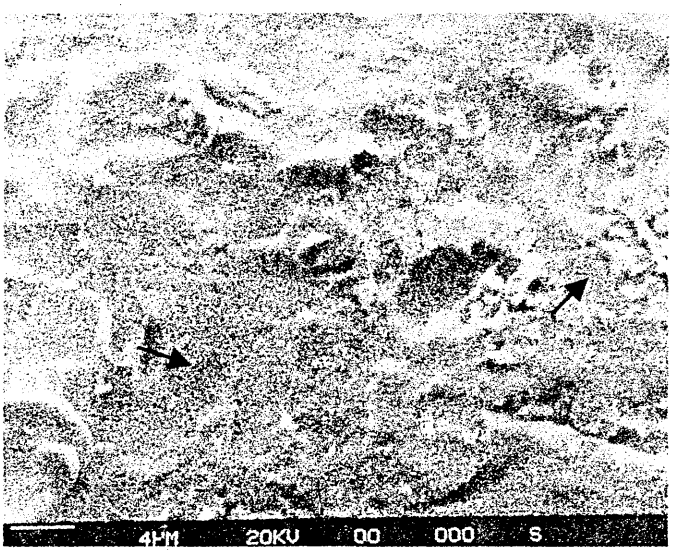

Figure **12.1** Scanning electron micrograph shows sand particle crater in the stagnation region at 400 mV (SCE) with plastic indentation having occurred to the metal surface and repassivation effect in other sites. Mag x 2500

In figure **9.7** the films thicknesses were drastically reduced in the stagnation regions at different potentials while the oxide film kept a gradual increase in thickness as the radial distance increased. Most of the film thickness colours were of the first order, especially in stagnation and high turbulence regions. The reasons for this were that both of these regions were affected severely by the hydrodynamic flow and the oxide film adhesion was overcome by the impact ploughing action of the sand particles. Despite this sand

erosion mechanism, a minimum oxide film thickness of unidentified colour still existed on the surface of the duplex stainless steel as indicated by the arrows in figure **12.1.** This was supported by the polarisation scan (figure **7.7**) with production of a constant current density in the austenite passive range of the duplex stainless steel. Eventually, in figure **9.7** a thicker film was detected at the 400 mV (SCE), especially in the high and low turbulence regions, than at the other two potentials.

However, at the 400 mV (SCE) potential which is the start of (δ) pitting and the austenite phase stayed protected, the mechanism behaviour can be classified as corrosion-passivation dominated, enhanced by erosion process.

This was supported by the potentiodynamic scan shown in figure **7.7** which demonstrates that at 400 mV (SCE) the corrosion reaction process had a log value of two order of magnitude on the current density axis under flowing condition and less than one order of magnitude for the mechanical erosion process due to sand addition. This means that the ratio of corrosion rate process was greater than the erosion rate process at this potential. At 700 mV (SCE) (austenite passive region) a similar mechanism of corrosion-passivation was dominated as the previous potential but with ratio of corrosion rate process to erosion rate of nearly three order of magnitude to one quarter order of magnitude respectively. Eventually at 900 mV (SCE) both microstructure dissolutions took place; dissolution behaviour was dominated with the ratio of corrosion rate to erosion rate reading values of higher order of magnitude than the 700 mV (SCE) potential.

Within ***one hour*** of sand addition and fluid velocity reduction from 7.9 m/s to 7.2 m/s as shown in figures **9.8-9.11**, at 400 mV (SCE), tiny changes in film thickness were observed in both stagnation and high turbulence regions while changes were relatively large in the low turbulence regions. Evidence of marked reduction in the oxide film due to solid impacts was found only in the stagnation regions in all the potentials to thicknesses between 22 nm to 33 nm. The sand impacts resulted in clear reduction of the dark colour oxide films limiting the repassivation effect occurring at different potentials.

Frankenthal[130] found that at low potentials in the passive region, the film measured was less than a unit cell for Fe_3O_4 or γFe_2O_3 (around 0.84nm). This film may be considered to be adsorbed oxygen. Above these potentials, he measured thicknesses greater than the unit cell for a phase oxide. In the high and low turbulence regions the oxide film colours stayed unchanged but thickened as the exposure time increased. Thicker and darker coloured oxide films were observed at 400 mV (SCE) in the high and low turbulence regions, due to the high electrochemical reactions of oxygen reduction leading to metal dissolution and precipitation. Those regions were not affected as much by the sand impingement and the film adhesion and repassivation overcame the fluid shear forces. This kept the oxide film intact.

At 700 mV (SCE) in the austenite passive range, reduction in the film thickness occurred in the stagnation regions. Due to sand particle impacts on the surface of the specimen, tiny changes in surface morphology were detected at different fluid velocities, with more participation of electrochemical reaction activities. At the high turbulence region a slight increase in thickness was detected with velocity reduction,

despite the flowing fluid shear forces exhibited in this region of the flow, while the low turbulence region showed no definite changes in film thickness. As the material was within the delta ferrite pitting range (austenite passive) the austenite microstructure remain stable while the ferrite phase was in a stable dissolution state. This led to film thicknesses at 700 mV (SCE) always being lower in thickness profile than at 400 mV (SCE) potential.

At the transpassive potential of 900 mV (SCE) a similar oxide thickness existed at the stagnation region to the previous potentials and thickness fluctuation as velocity decreases at both the high and low turbulence regions. According to Ansell et al[46], during transition from the austenite passive to the transpassive regions (900 mV) the composition and thickness of the surface film changes and this may occur at a certain potential and be marked by an increase in dissolution rate. As Mingwei[2] stated, the composition, surface morphology, film growth rate, and thickness of the layer are all affected.

The predominant feature of low particle velocity erosion-corrosion was the presence of an eroding scale layer on the surface of the metal rather than bare metal. At 900 mV a complete breakdown of the material occurred, corrosion process products are severed and precipitate at the anodic sites, especially seen as a dark film at the high and low turbulence regions, with a poor fragile film adhesion apparently resulting in an easily wiped off film with the current two-phase jet flow.

In general this led to the conclusion that, at various fluid velocities and fixed potentials, the constant impingement of the erodent particles initiated deformation patterns of a minimum thickness profile in the stagnation regions, whilst the high and low turbulence regions indicates an increase in film thickness.

In some cases, the oxide film often seen in the cell was removed from the substrate when taken out of the solution. There was evidence to suggest that the detachment may occur within the film adjacent to the metal, a possible fracture within the film. This may suggest that the long term reduction in film thickness is due to a failure of cohesion within the film rather than a failure in adhesion. According to Evans[179], chemical dissolution of the outer surface and within the outer regions of the film in the aggressive environment may also play an important role after prolonged exposure times.

Within ***10 minutes*** sand addition, follows similar behaviour as with the one hour time duration with most, but not all, film thickness being reduced, thus the reduction in the stagnation region of up to 1.5 radial distance while the 1 hour was covered up to 2 radial distance. Shalaby et al[78] confirmed that the rate of mass loss increases with exposure time.

As anticipated, at 400 mV (SCE) a combined mechanical effect of the erodent sand particles and an electrochemical reaction took place at the stagnation areas. This means that the dark oxide coloured films were removed down to minimum thickness, but as fluid velocity decreased the changes in thickness were minimal and no changes occurred in outer regions, which exhibited a good film adherence. The changes in colour orders from 2 to 1 were significantly obvious between the stagnation, high and low turbulence

areas. At 700 mV (SCE) mainly corrosion-passivation dominated this potential of the duplex stainless steel. No clear changes were seen in the centre region and there were tiny alterations in the high turbulence regions film thickness, while there was a large increase in erosion profile at the low turbulence regions. At 900 mV (SCE) no obvious changes in the oxide film were seen.

Comparison of the oxide film colour thickness curve for the stagnation region at various velocities was between 79 nm and 117 nm, at the high turbulence region the film thickness was between 79 nm and 175 nm and in the low turbulence region between 282.5 nm and 166 nm.

12.1.3 Combinations of various duplex stainless steel film thickness curves

Upon combining fluid flow curves with sand addition for 10 minutes and 1 hour at a maximum fluid velocity of 7.9 m/s, figures **12.2-12.4** were produced. A view of the oxide film thickness profiles shows that as the potential increases, more reduction occurred at different hydrodynamic regions.

This is owing to the 400 mV (SCE) potential being situated at the starting of the ferrite (δ) pitting region of the duplex stainless steel. The starting of delta ferrite pitting elements occurred, which means oxide film breakdown and simultaneous repassivation of the oxide film took place, as shown in the polarisation scan in figure **7.7**, by a constant current density range above the 400 mV (SCE) anodic potential. Microscopic evidence also can be seen in figure **12.1** with thick colour film in the stagnation region. This resulted in the ratio of corrosion to erosion rate increases if the 400 mV (SCE) potential is compared with higher potentials. Therefore, in general, the mechanism behaviour was dominated by corrosion-passivation when erosion enhances the corrosion rate.

From the observation of colour film thickness in the stagnation region, at 700 mV (SCE) in figure **12.2** showed that the oxide film has the same tendency behaviour as the 400 mV potential, but with less thickness values. This led to the conclusion that the ratio of corrosion to erosion rate decreases as potential was increased as stated by Stack et al[160] and the transition in the mechanism behaviour is identical to the previous potential, corrosion-passivation domain when erosion enhances the corrosion rate. This resulted in a constant austenite passive current density as shown in the polarisation scan in figure **7.7**. Metal dissolution in the ferrite phase is limited by pits initiation and development in preferential sites, whilst the austenite remains passive as indicated in figure **8.3**. Therefore, the ratio of corrosion to erosion rate is decreased compared with the previous potential and increased drastically when compared with the 900 mV (SCE).

At 900 mV (SCE) corrosion dominated behaviour was registered by a complete breakdown of both microstructure phases as seen in figure **8.5** and supported evidence showing a reduction in film thickness in all regions of the flow. The ratio of corrosion to erosion rate was increased when compared to the 400 and 700 mV (SCE). At this point there is a tendency for darker film as the immersion time increases.

Overall observations revealed that when comparing the three applied potential oxide films during sand addition, the transition from the active, passive to transpassive regions

changes the composition and film thickness[130]. In general a visible drastic reduction in the stagnation regions was seen with minor changes in film thicknesses in the outer regions. At potentials of 400, 700 and 900 mV (SCE), the film thickness at the stagnation regions dropped from 105 nm, and 75 nm to 65 nm with corresponding colours of brown yellow to light yellow. When sand was added for 10 minutes the film thicknesses were between 45 nm, 33 nm and 45 nm, while at one hour sand addition, the thicknesses were 22 nm in all the potentials, with first order colours of clear grey, grey blue to clear grey. Figure **12.8** shows little changes in film thickness beyond a radial distance of 2, with a larger reduction in the centre region.

A minimum velocity of 7.2 m/s is shown in figures **12.5**-**12.7**. Similar erosion profiles to velocity of 7.9 m/s are seen, but with higher oxide film thicknesses. This proves that the film thickness increases as the velocity reduces. In the stagnation regions the film thickness profiles were decreased from 165 nm at 400 mV, and 150 nm at 700 mV to 68 nm at 900 mV. At 10 minutes sand addition, the film thicknesses were 45 nm, 48 nm and 45 nm respectively and at one hour sand additions, the film reduced to 33 nm, 33 nm and 20 nm respectively. Figure **12.9** shows a combination of erosion curves under flow and sand addition, but with minimum velocity and higher oxide film thicknesses.

Figure 12.2 Duplex stainless steel (batch A) held at 400 mV (SCE) under fluid flow velocity of 7.9 m/s for 6 hours then 3 grams of sand added for 10 minutes and 1 hour

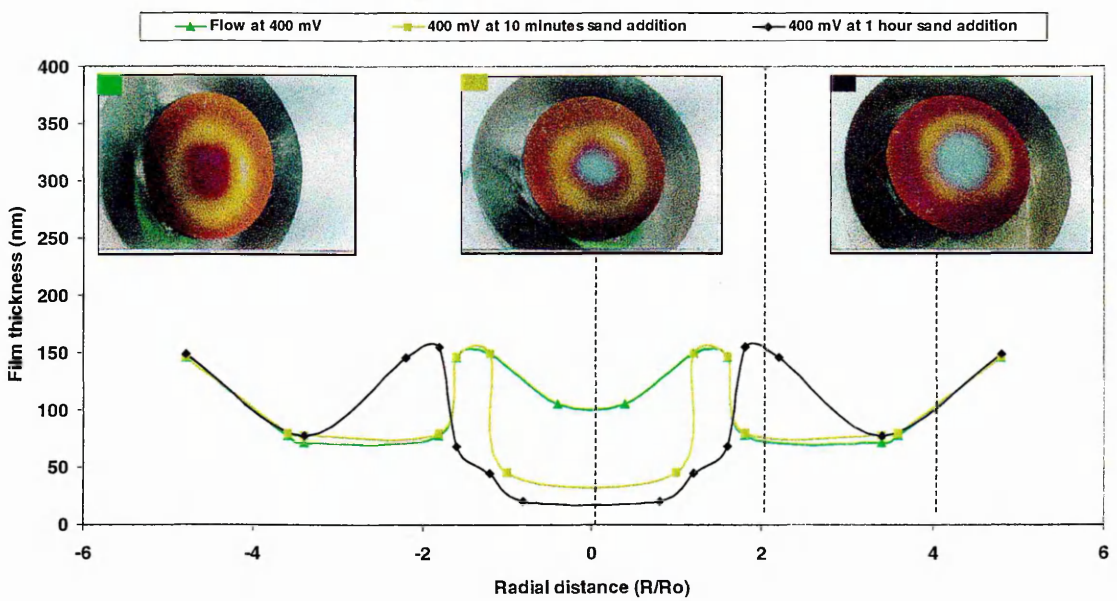

Figure 12.3 Duplex stainless steel (batch A) held at 700 mV (SCE) at fluid flow velocity of 7.9 m/s for 6 hours then sand particles added for 10 minutes and 1 hour

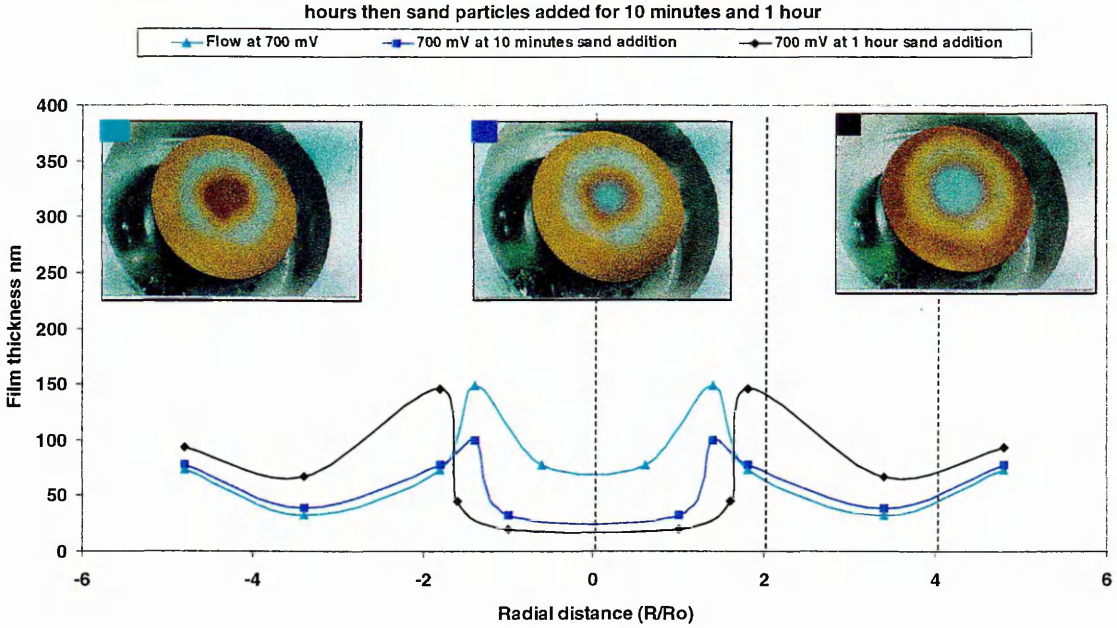

Figure 12.4 Duplex stainless steel (batch A) held at 900 mV (SCE) at fluid flow velocity of 7.9 m/s for 6 hours then 3 grams of sand added for 10 minutes and 1 hour

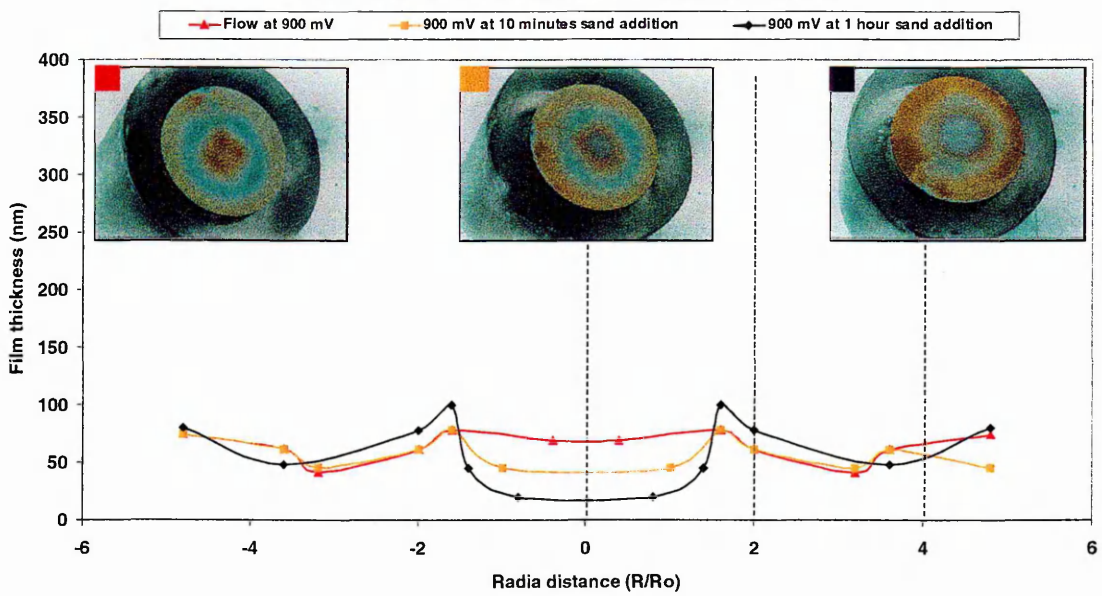

Figure 12.5 Duplex stainless steel (batch A) held at 400 mV (SCE) at fluid velocity of 7.2 m/s for 6 hours then 3 grams of sand added for 10 minutes and 1 hour

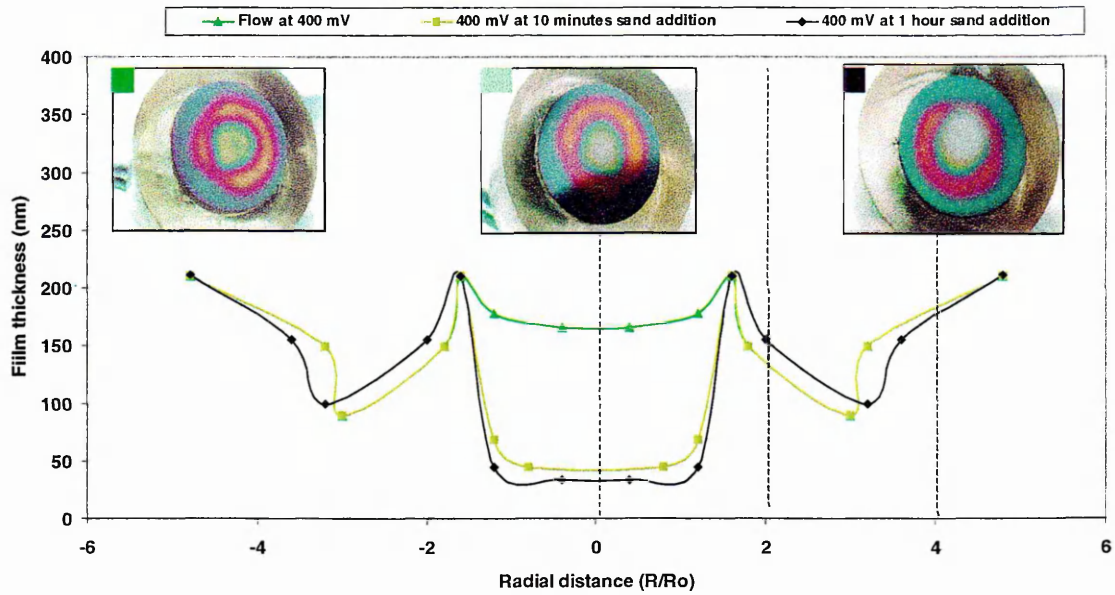

Figure 12.6 Duplex stainless steel held at 700 mV (SCE) at fluid velocity of 7.2 m/s for 6 hours then 3 grams of sand particles added for 10 minutes and 1 hour

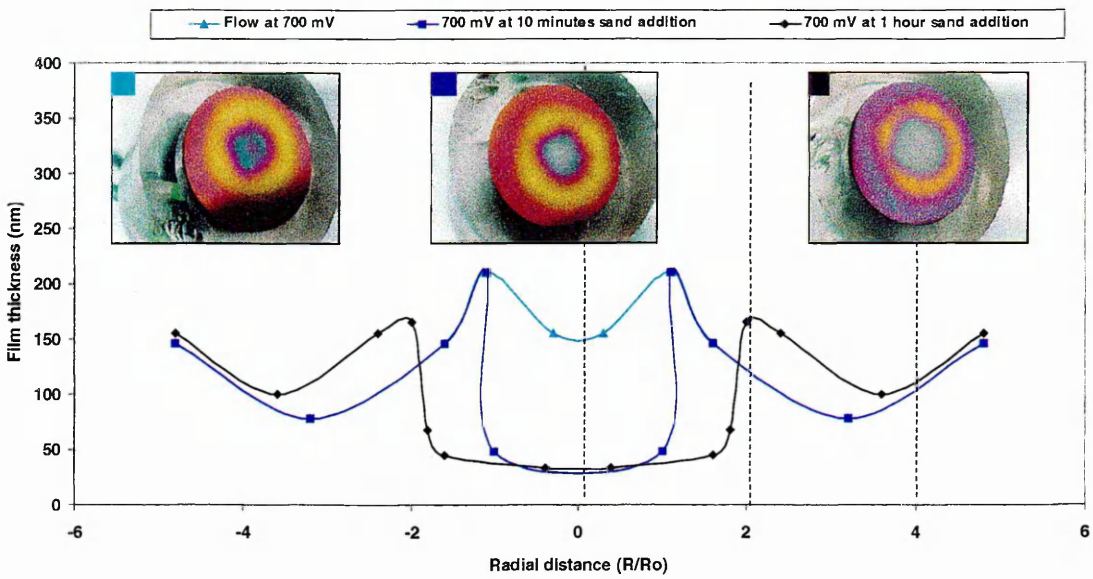

Figure 12.7 Duplex stainless steel (batch A) held at 900 mV (SCE) at fluid flow velocity of 7.2 m/s for 6 hours then 3 grams of sand added for 10 minutes and 1 hour

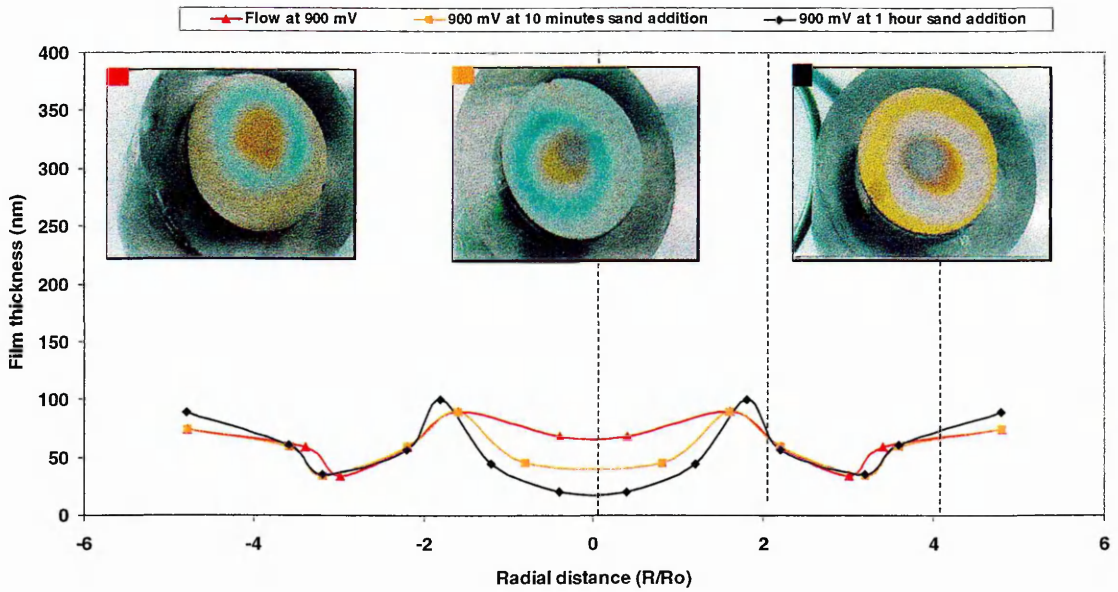

Figure 12.8 Duplex stainless steel (batch A) held at 400, 700 and 900 mV (SCE) at fluid flow velocity of 7.9 m/s for 6 hours with and without 3 grams of sand added for 1 hour

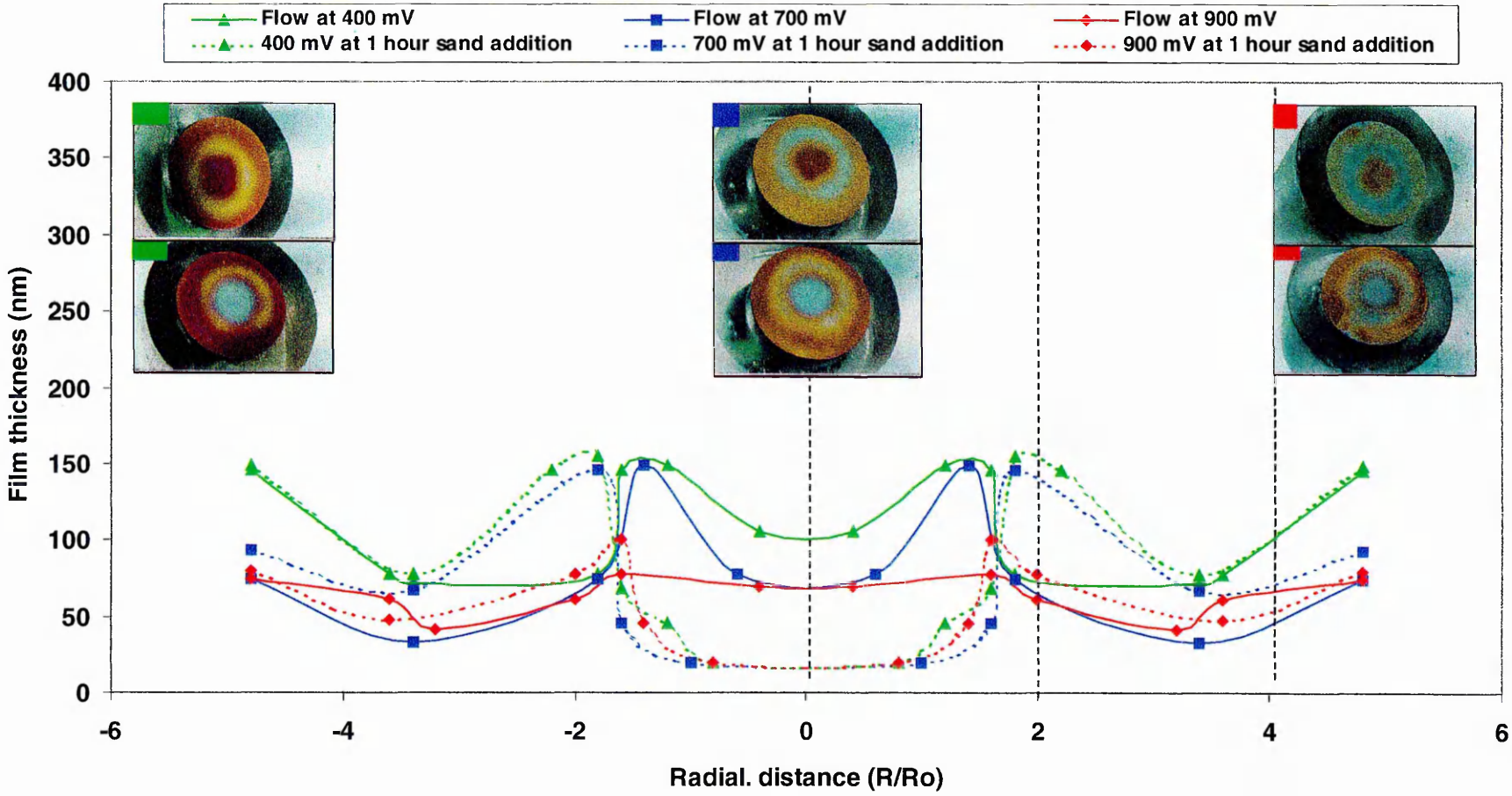

Figure 12.9 Duplex stainless steel (batch A) held at 400, 700 and 900 mV (SCE) at fluid flow velocity of 7.2 m/s for 6 hours with and with out 3 grams of sand particles added for 1 hour

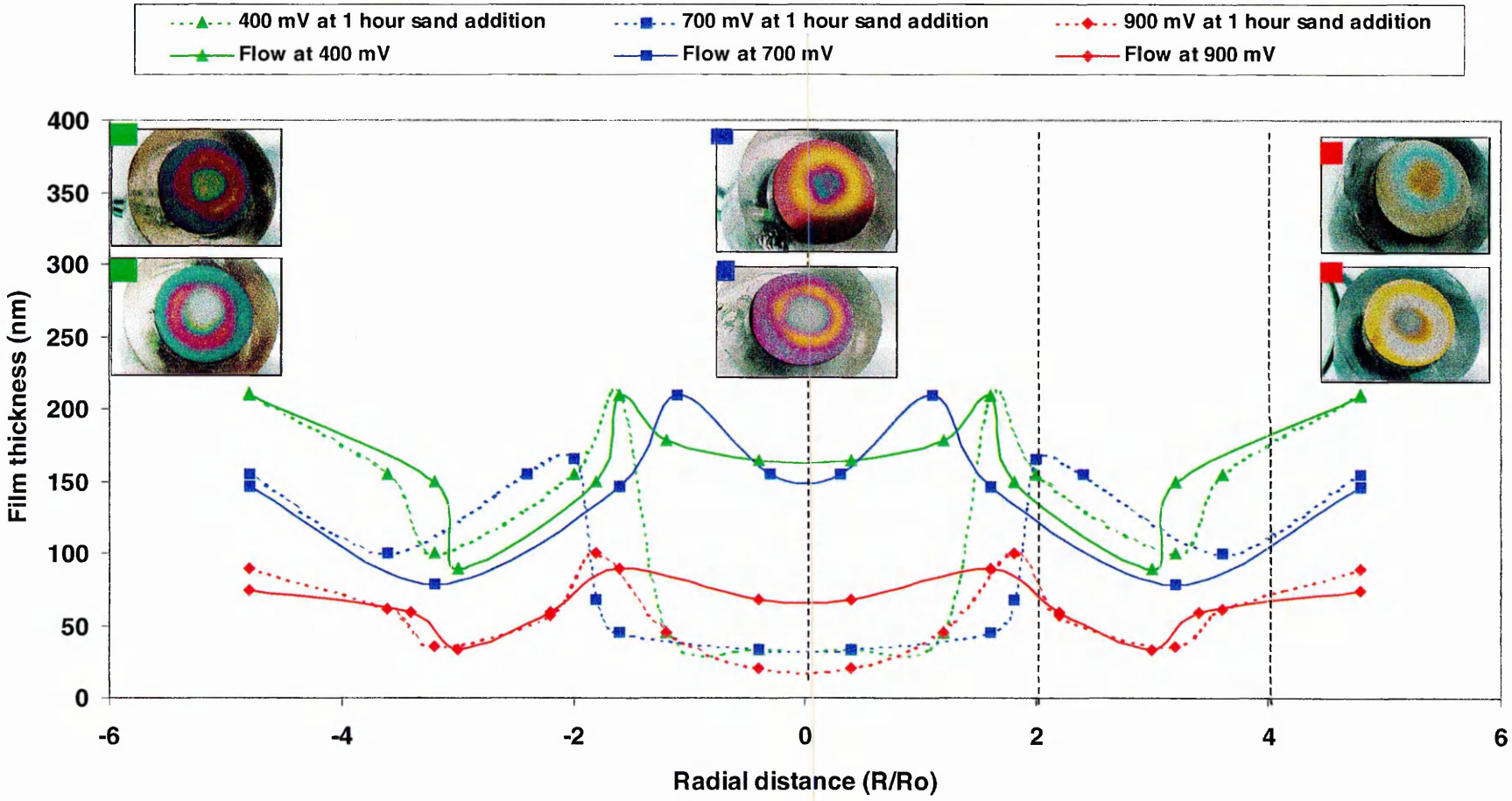

13.0 EROSION CORROSION MODELLING

Appropriate modelling was developed for the erosion-corrosion mechanism of duplex stainless steel with sand particle impacts, the erosion-corrosion process resulted in transient electrochemical reactions. The consequence of which may be the onset of localized corrosion or repassivation revealing a sequence of anodic current transients due to individual impacts[77]. To analyse the consequence of the mechanical damage in the current study, the impact of sand particles was considered as the main cause of damage on the specimen. Therefore, the form of damage should be affected by the properties of the sand.

As the sand particles were carried by the flowing liquid in the jet impingement system, analysis of the passive current densities as a function of fluid velocity can be seen in table **13.1** and in figure **13.1** which was derived from the passive current density at 0 mV (SCE) from the potentiodynamic scans (figures **7.7**, **7.9-7.12** chapter **7.0**).

The reason for selecting 0 mV (SCE) potential, because it is approximately the starting value of increase in current density in the duplex stainless steel at the passive range, when changing fluid flow velocity and the current densities can be read clearly in every potentiodynamic scan measurement. At fluid velocity of 8.5 m/s the passive current density of 4 grams sand concentration was not determined experimentally, which led to a missing data point of a maximum current density value on various graphs.

Table **13.1** Shows the electrochemical measurement average passive current density at 0 mV(SCE) potential under different sand concentrations and fluid flow velocities

Fluid flow velocity (m/s)	I_{pass} at 4 grams of sand	I_{pass} at 3 grams of sand	I_{pass} at 2 grams of sand	I_{pass} at 1 gram of sand
8.5	N/A	6.7	5.6	2.1
7.9	1.1	1.0	0.5	0.2
7.8	2.0	1.1	0.7	0.4
7.5	1.0	0.6	0.4	0.2
7.2	0.9	0.5	0.8	0.4

However, the graph in figure **13.1** indicate that the current densities were proportional to the increase of fluid velocity in the absence of sand particle erosion. In the presence of sand, as reported by Madsen[156], the passive current density increased significantly, indicating that erosion had a significant effect on the passivation. The corrosion rate was increased significantly by breakdown of the passive film from the impact of particles and the subsequent reformation of the film, with possibly some dissolution of metal on the bare surface. The corrosion rate, therefore, was dependent upon the exposed surface area, the film thickness, and the repassivation efficiency.

As the mass of particles impacting on the surface is proportional to fluid velocity, and considering that the passive current density value depends on the rate of particle erosion of the oxide layer during sand particles impact, eventually, some kinetic energy was released during sand particle impact and this kinetic energy is proportional to the mass of particles and fluid flow velocity squared.

released during sand particle impact and this kinetic energy is proportional to the mass of particles and fluid flow velocity squared.

The result, in figure **13.2**, shows the passive current density values increases with the fluid flow velocity cubed. A steep curve relationship was developed which revealed that the difference in the rate of particle suspended in each experiment was not even throughout the loop and the suspended sand particles increased as the fluid velocity increased. Equally, the passive current density at 4 grams was higher four and half time than at 1 gram of sand concentration, this due to the effect of fluid velocity. Consequently, an approach to another relationship was carried out between the total kinetic energy, which participated in the impact and the passive current density value under various fluid flow velocities.

13.1 Kinetic energy sand particles per second impacting the specimen

As the mass of suspended particles flowing from the orifice can be used to calculate the number of particles that impact on the specimen, this means that the sum of kinetic energy of particles, which take part in the depassivation process in unit time, can also be calculated as follows: -

The kinetic energy when one particle was concerned is given by

$$KE_P = \frac{1}{2} \times M_p \times V^2 \qquad (1)$$

Where:

KE_P : Kinetic energy of a particle
M_p : Mass of a particle

Considering the total kinetic energy of all particles and assuming that the particles had the same spherical shape of 275 μm diameter, which is the average size for the particles in the range of 250 μm to 300 μm, the sum of the kinetic energy of sand particle per second was determined using the following equation:

$$KE = \frac{N \times m_{av} \times V^2}{2} \qquad (2)$$

Where:

N : Number of sand particle impacts per second
m_{av} : Average mass of sand particle (grams)
V : Velocity of fluid flow (m/s)

A summary for the number of particle gradients at various fluid velocities is shown in table **13.2** from chapter **10**, to be used as a reference during kinetic energy calculations. The maximum sand concentration of 4 grams at 8.5 m/s fluid flow velocity was considered as the initial reference point of the kinetic energy calculation.

Table **13.2** Shows the sand particles gradients at 10 second mass of sand collection time at different sand concentrations and fluid flow velocities

fluid flow velocity (m/s)	Sand particles gradient at 4 grams	Sand particles gradient at 3 grams	Sand particles gradient at 2 grams	Sand particles gradient at 1 gram
8.5	3800	2400	1700	1000
7.9	3900	1400	1800	1800
7.8	2600	1700	3200	700
7.5	2900	1300	2900	1300
7.2	900	800	1300	1100

Table **13.3**, shows the mean the kinetic energy ($\frac{KE_2}{KE_{8.5m/s}}$) at every fluid velocity which was determined using as datum points the initial number of particle per second at 8.5 m/s fluid velocity and the calculated mass of sand particle of 1.4×10^{-8} Kg from chapter **10**. This means kinetic energy is a good indication for the effect of changing fluid velocity on the surface of the specimen. As the fluid velocity decreased to 7.9 m/s, the kinetic energy of the impacting particles recorded was 0.0018 J/sec. Hence, the reduction in kinetic energy was nearly 10%. At a velocity of 7.8 m/s, and despite little alteration in fluid velocity, the kinetic energy changed further to a value of 0.0011. This means that the kinetic energy reduced by nearly 45%. Therefore, changes in the kinetic energy between the fluid velocities were high which resulted in vigilant control to the narrow fluid velocity margin. Similarly, the reduction in kinetic energy per second was seen as the fluid velocity reduced from 8.5 m/s giving a value of 0.0020 J/sec to 0.0003 J/sec at 7.2 m/s.

Table **13.3** Show the kinetic energy of 4 grams of sand concentrations at different fluid flow velocities.

Velocity (m/s)	Suspended mass (gram)	Impacts/Sec	KE J/Sec Watts	$V_2^2 / V_{initial}^2$	$KE_2/KE_{initial}$
8.5	0.65	3800	0.0020	-	-
7.9	0.88	3900	0.0018	0.86	0.90
7.8	0.47	2600	0.0011	0.84	0.55
7.5	0.38	2900	0.0012	0.77	0.60
7.2	0.09	900	0.0003	0.71	0.15

As the erosion of the oxide film was caused by impacts of particles which resulted in transferring some energy to degrade the oxide film, therefore, the kinetic energy of the sand particles changed by altering their velocities.This led to a shift in average passive current density value. Eventually, a relationship to correlate sand particle kinetic energy at 0 mV (SCE) potential with passive current density was considered.

13.2 Kinetic energy and potentiodynamic passive current density at 0 mV

The passive film mechanical erosion was caused by the energy transfer from the impact of sand particles to the surface of the material. By relating the kinetic energy to the degradation, this reflected on the values of the average passive current density

produced. Figure **13.3** shows a straight-line behaviour of the potentiodynamic average passive current density and particle kinetic energy at different fluid velocities.

A large difference occurred in the average passive current density between fluid velocity of 8.5 m/s and the rest of the reduced fluid velocities was observed despite the vigilant control to the narrow fluid velocity margin through the diversion valve in the water jet impingement system.

Overlapping of the average passive current density of the kinetic energy at 7.2 m/s over rest of fluid velocities and 7.8 m/s over 7.9 m/s. This could be related to the uneven distribution of sand particles flowing throughout the loop and repassivation efficiency of the oxide film.

Figure 13.1 Shows duplex stainless steel average electrochemical current densities for ring 1 from a potential of 0 mV (SCE) under various fluid flow velocities with and without different sand concentrations

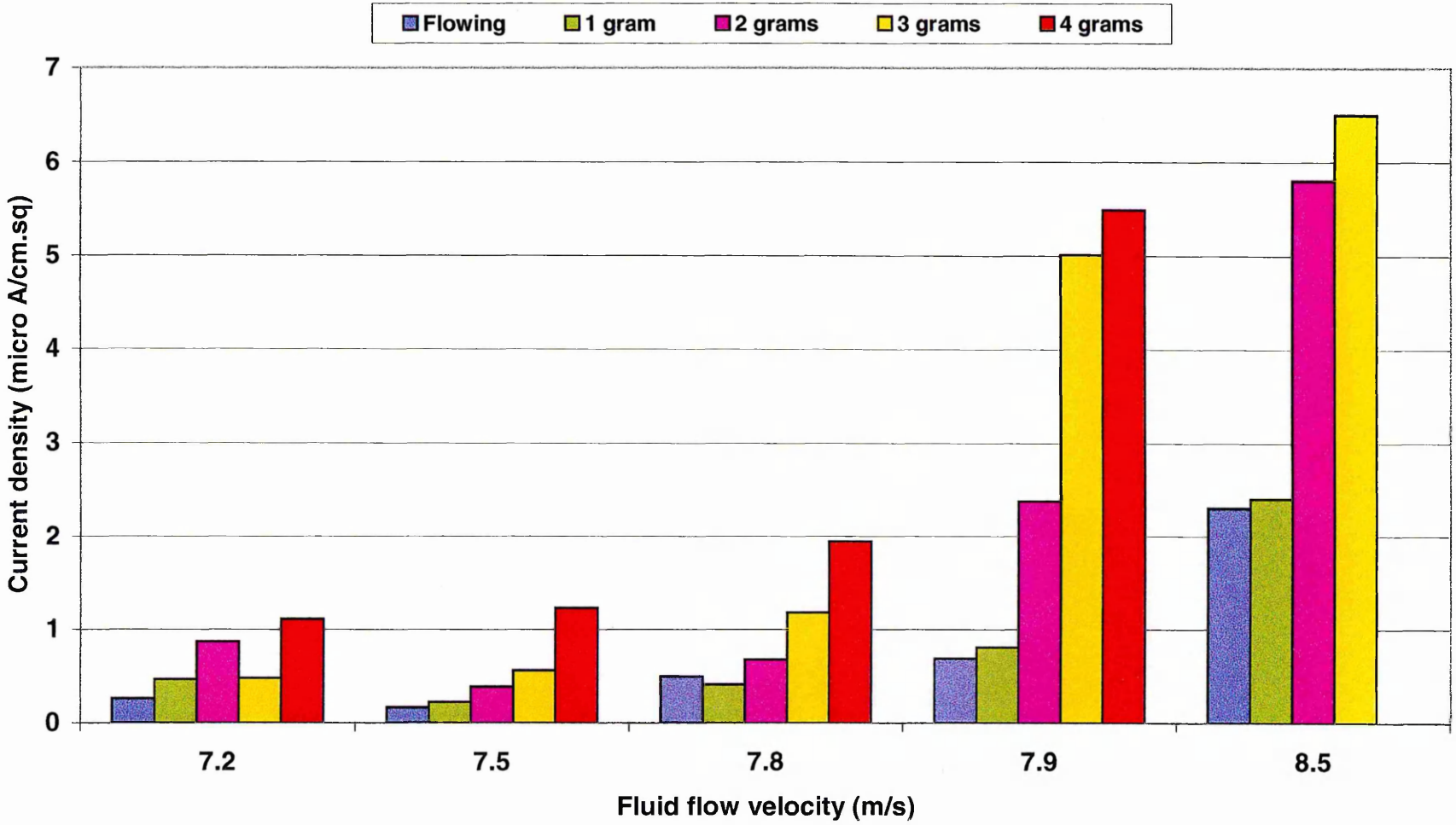

Figure 13.2 Shows the relationship between passive current density plotted against fluid flow velocity cubed at various sand concentrations

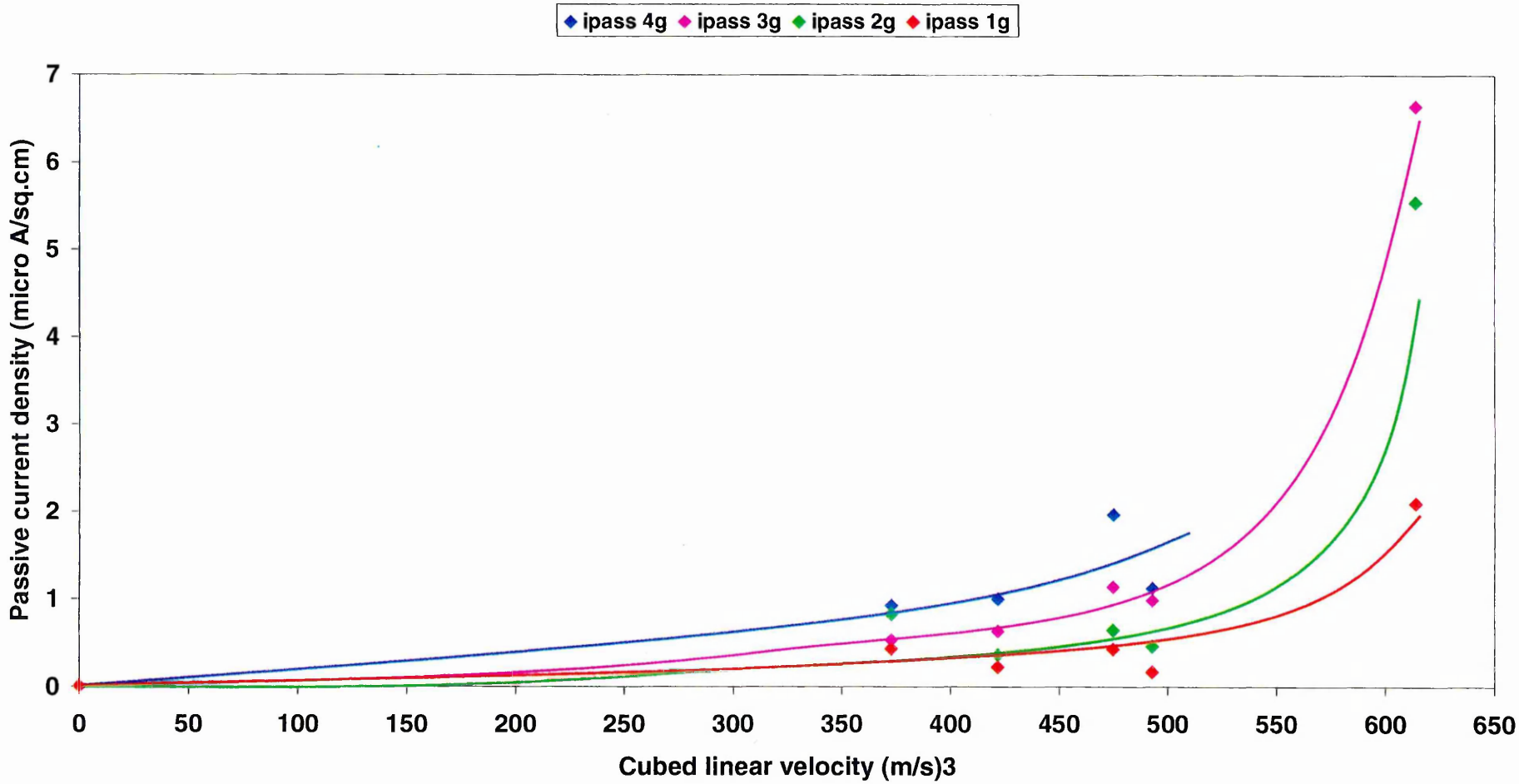

Figure 13.3 Shows the relationship between passive current density (Ipass) values at 0 mV potential and the particles kinetic energy

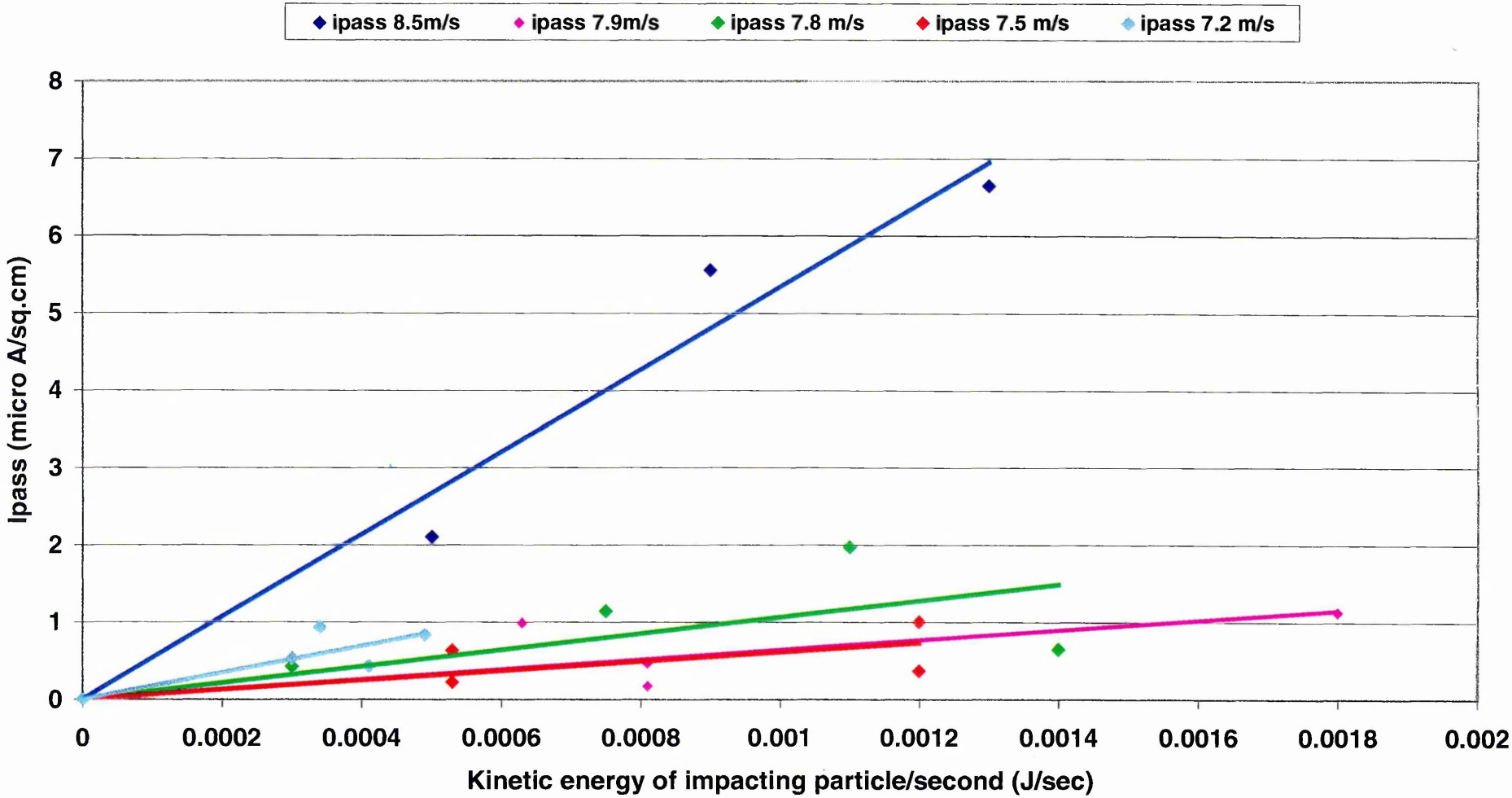

13.3 The relationship between mean time between particle impacts and the transient current developed

Various researchers studied the current-time transient due to passivation and depassivation in order to obtain a quantitative picture of the erosion corrosion process (Table **13.4**).

Table **13.4**. Shows the impact duration time in seconds.

Alloy	Impact period time duration in seconds	Electrolyte
304L	14 ms or 300 ms [129]	1.0 KOH, pH 14.
Fe	0.002 sec[109]	Borate buffer, 1.0 M Cl^-, pH 9.35
AISI 304 SS	Within 500 second scale[28]	Analytical grade reagents and deionized distilled water.
Fe-18Cr-1Mo	10-15 sec[11]	1.0 M NaCl
AISI 304 SS	(48 sec)[84]	10 M HCl
Stainless steels	(0.008 sec)[95]	0.5 M $NaClO_4$
AISI 302 SS	> 2 sec[166]	0.1 M NaCl
13.2.1.1 Alloy A2	(0.04 sec)[65]	Wet process phosphoric acid production (WPA)

Burstein et al[129] used the technique which involved the impact of a diamond stylus on to the surface of a rotating disc specimen and Galvele et al[11] used SiC point mounted on luggin capillary to scratch the surface. Their results of the current transient described the consequent effect upon film rupture under erosive conditions. Figure **13.4** shows that at point **A**, the current rises in the anodic direction and continues for the period of the stylus contact. The stylus falls away from the metal surface at point **B** after which the current decays with time. It is a direct measure of the corrosion, which occurs due to a single erosion event under the electrochemical being imposed on the metal.

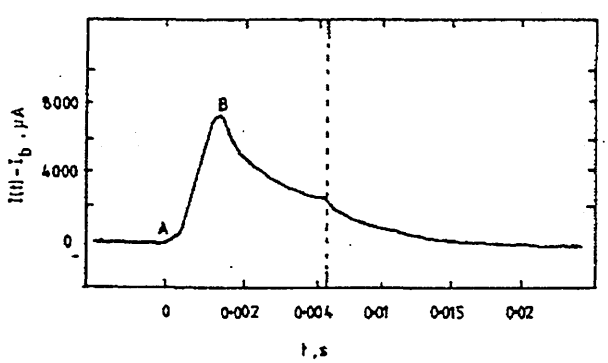

Figure **13.4** Current transient due to scratch on 304L stainless steel in 1.0 M KOH, pH 14 at E = - 605 mV(nhe). A: scratch commences. B: scratch complete[129].

13.4 Determining the time between impacts of sand particle

To determine the time interval of impact of particles on a single point on the surface of the duplex stainless steel, the number of particles (n) at 3 grams which hit the surface of a single point can be calculated using an existing formula from the Hirooka[113] model given as:

$$n = N \times \frac{a_{imp}}{A_s} \qquad (3)$$

Where:

A_s : Surface area of specimen equal to 0.2×10^{-4} m^2
a_{imp} : Impacted area
N : Total number of impacts

With reference to table **13.2**, the number of sand particles gradient value of 2400 at sand concentrations of 3 grams was considered in the calculation at fluid velocity of 8.5 m/s instead of 4 grams particles gradient of 3800 because no current density at 4 grams was determined experimentally at this fluid velocity. Thus, to find out the electric charge pass per impact, using the maximum average passive current density produced at this fluid velocity which was 7.5 μA/cm^2 (table **7.1** chapter **7**), and as the microscopic average size of the crater is equal to 11.8 μm, then the impacted area of a single particle can be calculated from:

$$a = \pi r^2 \qquad (4)$$

$$a = \pi \times (5.9 \times 10^{-6})^2$$

$$a = 1.0 \times 10^{-10} m^2$$

$$a = 1.0 \times 10^{-6} cm^2$$

$$n = 2400 \times \frac{1.0 \times 10^{-10}}{0.2 \times 10^{-4}} = 0.01 \text{ impact/second}$$

Therefore, the mean time between impacts in seconds is:

$$t = \frac{1}{n} = \frac{1}{0.01} = 100 \text{ seconds}$$

If the size of the crater was less than 11.8 μm then the number of particle impacts on a single point per second will be reduced, but the mean time between impacts of the sand particles on the surface of the specimen will increase and vice versa if the size of the particle crater was large. A similar criteria will apply if the number of particles gradient of a reduced fluid velocity was utilised, such as 7.8 m/s with a number of particles gradient of 2600, (reference table **13.2**) instead of the 8.5 m/s gradient value of 3800.

13.5 Relationship between the sand impact measurements, polarisation scans and the passive film thickness

Assumption, as fluid flow and sand particles remove passive film at the point of impact then film repassivates at this point of impact and passivation current flows. That is measured in the polarisation scan which is the sum of the charge passed in each repassivation. If there are more impacts then more charges are passed and this resulted in measuring a larger passivation current. Thus the reason behind thinner film with sand

particles was because passive film does not have time to grow to full thickness between impacts.

According to Faraday's second law, the corrosion rate was obtained directly from the current density using the given formula:

$$K_C = \frac{I_{PASS} \times t \times M}{F \times Z} \qquad (5)$$

Where F is Faraday's constant (96,500 coulombs/equivalent), Z the number of electrons transferred, M = atomic weight, and t the time. Where I_{PASS}, defined as current density, equals I/A. Current density rather than current is proportional to corrosion rate because the same current concentrated into a smaller surface area results in a larger corrosion rate. Corrosion rate is inversely proportional to area for the same dissolving current. Unit of penetration per unit time results from dividing the above equation by the density ρ of the duplex stainless steel.

As the maximum average passive current density produced = 7.5×10^{-6} (reference table **7.1** chapter **7**)
So in 1 second charge passed

$$Q = i \times t \qquad (6)$$
$$= 7.5 \times 10^{-6} \times 1$$
$$= 7.5 \times 10^{-6} \text{ coulomb cm}^{-2}$$

In 1 year charge passed
$$= 7.5 \times 10^{-6} \times 3600 \times 24 \times 365$$
$$= 236.5 \text{ coulomb cm}^{-2}$$

For *Fe*, 1 Faraday (96,500 coulomb) is charge passed to corrode

$$= \frac{55.9}{2}$$
$$= 27.95 \text{ grams of } Fe$$

Assuming alloy is 67.6% *Fe* $= 0.676 \times 27.95$
Amount of *Fe* corroded $= 18.9$

For *Cr* $= \frac{52}{3}$
$= 17$ grams of *Cr*

Assuming alloy is 21.7% *Cr* $= 0.217 \times 17$
Amount of *Cr* corroded $= 3.7$

For *Ni* $= \frac{58.7}{2}$
$= 29.4$ grams of *Ni*

Assuming alloy is 5.4% *Ni* $= 0.054 \times 29.4$
Amount of *Ni* corroded $= 1.6$

For *Mo* $= \frac{95.9}{2}$
$= 47.95$ grams of *Mo*

Assuming alloy is 3.0% *Mo* $= 0.03 \times 47.95$
Amount of *Mo* corroded $= 1.4$

Therefore, in 1 year mass corroded of the alloy at random points over the surface

$$\Delta m = \frac{7.5\times10^{-6}\times3600\times24\times365\times[(18.9)+(3.7)+(1.6)+(1.4)]}{96500}$$

$$= 0.06 \text{ g/cm}^2$$

Convert to depth of attack;

The volume of elements lost must be determined as $\rho = \frac{m}{V} \Rightarrow V = \frac{m}{\rho} \Rightarrow$ as ρ for stainless steel[111] 7.7 grams/cm^3. Hence, volume of duplex stainless steel corroded in 1 year/cm^2

$$= \frac{0.06}{7.7} = 0.008 \text{ cm/year}$$

Therefore, the corrosion rate in cm = 0.008 cm/year
$= 80$ µm/year

Assuming that an increase in I_{pass} is needed to maintain the passive film in conditions recorded using the colour method, i.e. this increase in I_{pass} corresponds to the sum of charge / time for 'N' impacts.

i.e. By knowing the fluid velocity and amount of sand suspended, so the impacts/second can be determined, which is equal to 2400 impacts/second for 3 grams of sand at 8.5 m/s (Table **13.2**). But current density is equal to charge passed/second, *i.e.* 1 Ampere = 1 coulomb / second.

To find the charge passed / impact;
Let consider the dissolution of 1 cm^2 of *Fe* in 8.5 m/s fluid velocity with 3 grams of sand. The mean current density produced was 7.5 µA/cm^2 (reference table **7.1** chapter **7**).

The mean current in *Ring No. 1* = current density × area
$= 7.5 \times 10^{-6} \times 0.2$
$= 1.5 \times 10^{-6}$ Ampere

Mean charge passed in one second is equal to 1.5×10^{-6} coulombs

Therefore, the mean charge passed per impact $= \frac{1.5\times10^{-6}}{2400} = 6\times10^{-10}$ coulombs

Accordingly, the mean charge passed in 1 second for a single point where there are 0.01 impacts/second (from section **13.4**)
$= 0.01 \times 6 \times 10^{-10}$
$= 6 \times 10^{-12}$ coulombs

The mean current passed in 1 second from a single point $= 6 \times 10^{-12}$ Amperes

Therefore, the current density that has flowed from the surface of duplex stainless steel of 0.2 cm^2 specimen was equal to 7.5 $\mu A/cm^2$ and for a single point impact area was 1.0 $\times 10^{-6}$ cm^2 and the absolute current was 6×10^{-12}. When compared with Burstein et al's[114] experiment result, the minimum recorded current density was approximately 0.9 mA/cm^2, since the scratch area of his specimen was 4.4×10^{-4} cm^2 which represents an absolute current of 0.4 μA and this was about the minimum current which could be accurately recorded. This revealed that Burstein et al[114] had considered a larger area of scratches while in our situation a small impact point area produced a finite current. Thus, the reason that a thinner film was developed when sand particles were introduced was because passive film did not have enough time to develop to full thickness between impacts.

Hirooka[113] considered that when the number of sand particles impacting on the surface per second (n) is small then the time between impacts increases, resulting in enough time to repassivate the damaged surface. As shown in figure **13.5** (**A**), the surface damage by the impact has already been repassivated sufficiently when the next impact happens. But when the value of (n) increases, the time allowed for one transient cycle becomes shorter, as illustrated in figure **13.5** (**B**). This means that current will not decay back to $I_{initial}$ and the next transient comes before the previous cycle end.

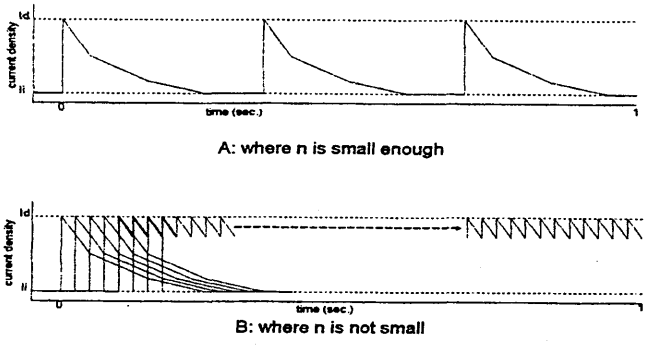

Figure **13.5** Shows schematic diagrams of passivation and depassivation cyclic processs due to particle impacts[113]

During the potentiodynamic measurements on the duplex stainless steel, the increase in sand concentration in the electrolyte, from 1 gram to 3 grams, led to the increase in the cycle of the number of sand particle impacts/second on the surface from one transient cycle to three cycles. This resulted in a significant increase in the current density values. But with the addition of 4 grams of sand and despite the cycle being increased to six transients, the current density did not change as much and stayed constant. Accordingly, I_i was defined as the initial current density developed on the passive surface of the specimen before sand impact and I_d was the passive current density under depassivation by sand impacts erosion conditions.

The mean time between impact on a single point on the surface of the duplex stainless steel was calculated for all the sand concentrations, giving values of 200 seconds, 111 seconds, 100 seconds, and 50 seconds, for 1, 2, 3 and 4 grams respectively. The depassivating current density time duration was recorded in seconds and such

measurement needed sensitive equipment to detect micro changes in current during impact. Therefore, it was a difficult decision to decide whether the duplex stainless steel result agreed with case **13.5 (A)** or **13.5 (B)**. This concluded that at sand concentration of 1 gram, only 1 complete wide transient current cycle was produced in the 300 seconds scale while the mean time between impacts was 200 seconds. At 2 grams of sand 2 cycles, at 3 grams of sand 3 cycles and finally at 4 grams of sand 6 narrow cycles were produced, as illustrated in figures **13.6 (A, B, C, D)**.

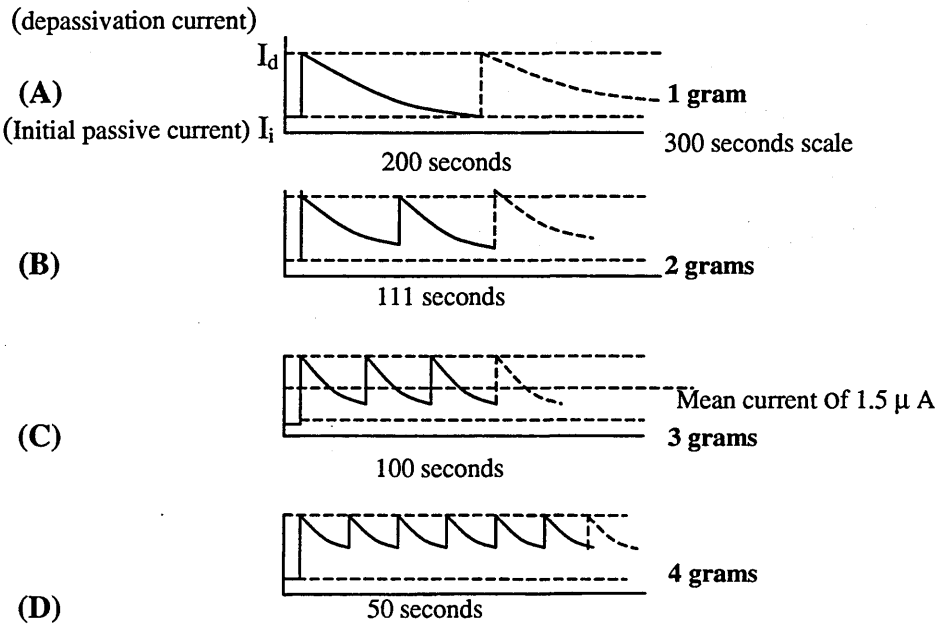

Figure **13.6 (A, B, C, D)**. Show the current transient at various sand concentrations.

This suggested that at 4 grams of sand the cycles became narrower which could means that the next impact current comes at a location closer to I_d rather than to $I_{initial}$ before the previous current transient returns to initial current, and could leave the surface partially depassivated. But if the sand concentration increased to 5 or 6 grams then the breakdown of one cycle and starting of the next one may occur closer and closer to I_d instead of $I_{initial}$ at which time the surface will be totally depassivated. Upon that a mean current of 1.5×10^{-6} amperes was produced and charge passed per impact taken into account to assist in compromising between the two conditions.

With the assistance of the supported evidence of an existence of passive range in the potentiodynamic scans and the thin colour fringe thickness of 33 nm, it was concluded that in the current study the depassivation process, when compared to the cases in figure **13.5 (A, B)**, was more similar to case **13.5 (A)** than case **13.5 (B)**.

But if an assumption was made to consider the case in figure **13.5 (B)**, the surface will be depassivated all the time (close to I_d). The number of sand particle impacts per second (n) must be considerably larger, plus the mean time between impact has to be in milliseconds rather than in seconds. Of course with the more sensitive current measurement such proof can be achieved.

13.6 Passive film thickness modelling

In the present experiments, if time between impacts is more like 100 seconds, then case **13.6 (A)** will apply. As all the charge passed goes towards film formation and growth, this permit to relate the film thickness at time t to the total charge density passed from the depassivated impact surface[129]. Thus:

$$x(t) = \frac{M}{ZF\rho} q(t) \qquad (7)$$

Where:

$x(t)$ = film thickness
q = Charge passed after 6 hours
M = Molecular weight of the film
ρ = Film density
Z = Oxidation number of the metal ions
F = Faraday's constant

Several studies have been performed by various researchers[2, 46, 91, 109, 114, 140, 142] on passive film thickening mechanism. The investigations show that the passive film chemical composition usually consists of CrO, FeO or Cr_2O_3, Fe_2O_3 oxides. Burstein et al[114] considered the values of $Z = 2$, $\rho = 5.7$ g cm^{-2} and $M = 70$ g mol^{-2}. These are compatible with ρ (FeO) = 5.7 g cm^{-3}, ρ (CrO) = 5.7 g cm^{-3} and M (FeO) = 72 g mol^{-1} and M (CrO) = 68 g cm^{-3}. In this connection it is fortunate that the densities of FeO, CrO and NiO were all of comparable value, as indeed are their molecular weights. Upon this the calculated value is for a film thickness with no dissolution as shown below:

$$x = \frac{7.5 \times 10^{-6} \times 21600 \times [70]}{2 \times 96500 \times 5.7}$$
$$= 1.0 \times 10^{-5} \text{ m}$$
$$= 10 \text{ μm}$$

This calculation shows a difference in value of passive film thickness when compared with the experimental film value of 33 nm. The experimental value of 33 nm would be for particles impacted on the surface, removing the film and damaging the substrate. A new film forms up to 33 nm in thickness, but it never reaches the thickness of 10 μm due to particle impacts. The calculated passive film value of 10 μm was for passive film thickness after 6 hours with no metal dissolution having occurred to the surface, and is thus for sites which have not been impacted by sand particles.

13.3 Erosion-corrosion synergism behaviour

Synergistic effects between erosion and corrosion have been cited frequently in erosion-corrosion studies[100, 125, 173]. The term "synergism" means the metal loss, caused by erosion and corrosion when the two processes act separately, is less than the sum of erosive and corrosive metal loss acting together. The synergistic effect represents the interaction between erosion and corrosion and their clarification is useful in understanding the erosion corrosion mechanism. Not only does the presence of erosion promote higher corrosion, but the corrosive attack on the specimen surface can aid the erosion process, allowing the metal to be removed more easily by corroding the metal.

This promotes the loss of larger pieces of material that might not have been removed as soon if it were not for the corrosion process.

However, synergism is not always well defined and in some cases[100, 174] the corrosion rate in the presence of erosion has not been measured. The synergism in these cases is the sum of the increments in erosion and corrosion rates affected by each other, and contributions of erosion and corrosion to the synergism cannot be separated.

The increase in current density with increasing fluid velocity, as seen in figure **13.1** from the potentiodynamic measurements (chapter **7.0**), in the presence of sand particles, indicated a transition from purely passive behaviour to a situation where erosion enhanced the average passive current on the surface. However, when the velocity was reduced from 8.5 m/s to 7.2 m/s, the average passive current density was reduced by five orders of magnitude, indicating that the film was continually being removed and reformed at these velocities under fluid flowing with sand particles. The results of negative corrosion potentials at high velocity in the potentiodynamic scans, indicated that the transition to passive behaviour changed as a function of an erosion parameter.

According to various research studies[11, 29, 97], to analyse precisely the synergistic effect and understand the mechanism between erosion and corrosion, it is important to provide an accurate erosion and corrosion rate baseline and to separate the contributions of erosion and corrosion to the total synergism. The data show that a synergism exists between the erosive and the corrosive components of erosion-corrosion, but because the electrochemical pure erosion rate was not determined, the synergism could not be calculated between erosion-corrosion. Therefore the synergy between pure corrosion and erosion in the presence of corrosion was calculated.

As Zhou and Stack[97] reported, the total erosion-corrosion rate ($K_{e\text{-}c}$) consisted of the summed contributions of the erosion and corrosion rates given as:

$$K_{e\text{-}c} = K_e + K_c \qquad (8)$$

Where;

K_c = Corrosion rate in the presence of erosion
K_e = Erosion rate in the presence of corrosion
$K_{e\text{-}c}$ = Total erosion-corrosion rate

The synergy equations[97] were modified to suit the current experimental condition. Therefore, by determining the total erosion-corrosion rate and the corrosion rate in the presence of erosion from the potentiodynamic scans, the erosion rate in the presence of corrosion (K_e) can be calculated using:

$$K_e = K_{e\text{-}c} - K_c \qquad (9)$$

OR

$$K_e = K_{e\text{-}c} - K_{co} - \Delta K_c \qquad (10)$$

Yue et al[29] related $K_{e\text{-}c}$ to the pure erosion and corrosion rates (K_{eo}) and (K_{co}) in the absence of corrosion and erosion respectively:

$$K_{e\text{-}c} = K_{eo} + K_{co} + \Delta K_{e\text{-}c} \qquad (11)$$

Due to the low fluid flow velocities used in the water impingement system, the pure erosion rate (K_{eo}) amount was finite and mixed with the corrosion process, and could not be determined using the current electrochemical measurements. Therefore, equation (11) is not valid for the current study and equation (8) or the following one (12) was implemented:

$$K_{e\text{-}c} = K_{co} + K_e + \Delta K_c \qquad (12)$$

$\Delta K_{e\text{-}c}$ is the synergistic effect from the interaction of erosion and corrosion [29, 97] and

$$\Delta K_{e\text{-}c} = \Delta K_e + \Delta K_c \qquad (13)$$

Where ΔK_e and ΔK_c are the synergistic effects related to erosion and corrosion enhancement, respectively:

$$\Delta K_e = K_e - K_{eo} \qquad (14)$$

$$\Delta K_c = K_c - K_{co} \qquad (15)$$

ΔK_e was not determined, because K_{eo} was not defined experimentally. Similarly, the synergistic effect related to corrosion, which is the only synergistic effect that can be calculated, using either equations (13) or

$$\Delta K_c = K_{e\text{-}c} - K_e - K_{co} \qquad (16)$$

The literature reveals that interactions between erosion and corrosion are subject to differences, between various workers, in ascribing measured parameters to the interactive terms variously discussed in the equations above. In the discussion over the next few pages, the following correlations are assumed:-

Measured current densities in static conditions = pure corrosion rate in absence of erosion (K_{co})

Measured current densities in flowing (zero solid) conditions = corrosion rate in presence of erosion (K_c)

Measured current densities in flowing conditions with solids = erosion rate in presence of corrosion (K_e)

The total erosion-corrosion rate was the sum of the corrosion rate in the presence of erosion and the erosion rate in the presence of corrosion in the active dissolution and passivation regions. Likewise, the sum of pure corrosion in the absence of erosion, erosion rate in the presence of corrosion and the synergistic effect related to the corrosion process, resulted in the total erosion-corrosion rate.

From the results of the electrochemical experiments there was extensive evidence of transitions between erosion-corrosion regimes. Figure **13.7** shows the corrosion rate in the presence of erosion (K_c), erosion rate in the presence of corrosion (K_e) and the total erosion-corrosion rate ($K_{e\text{-}c}$) at fluid flow velocity of 8.5 m/s as a function of potential. It also shows the base line of pure corrosion rate in the absence of erosion (K_{co}), and all those values were obtained from tables **13.5** and **13.6**.

Figure 13.7 Erosion, Corrosion and Erosion-corrosion rates of duplex stainless steel SAF 2205 at fluid velocity of 8.5 m/s as a function of potential

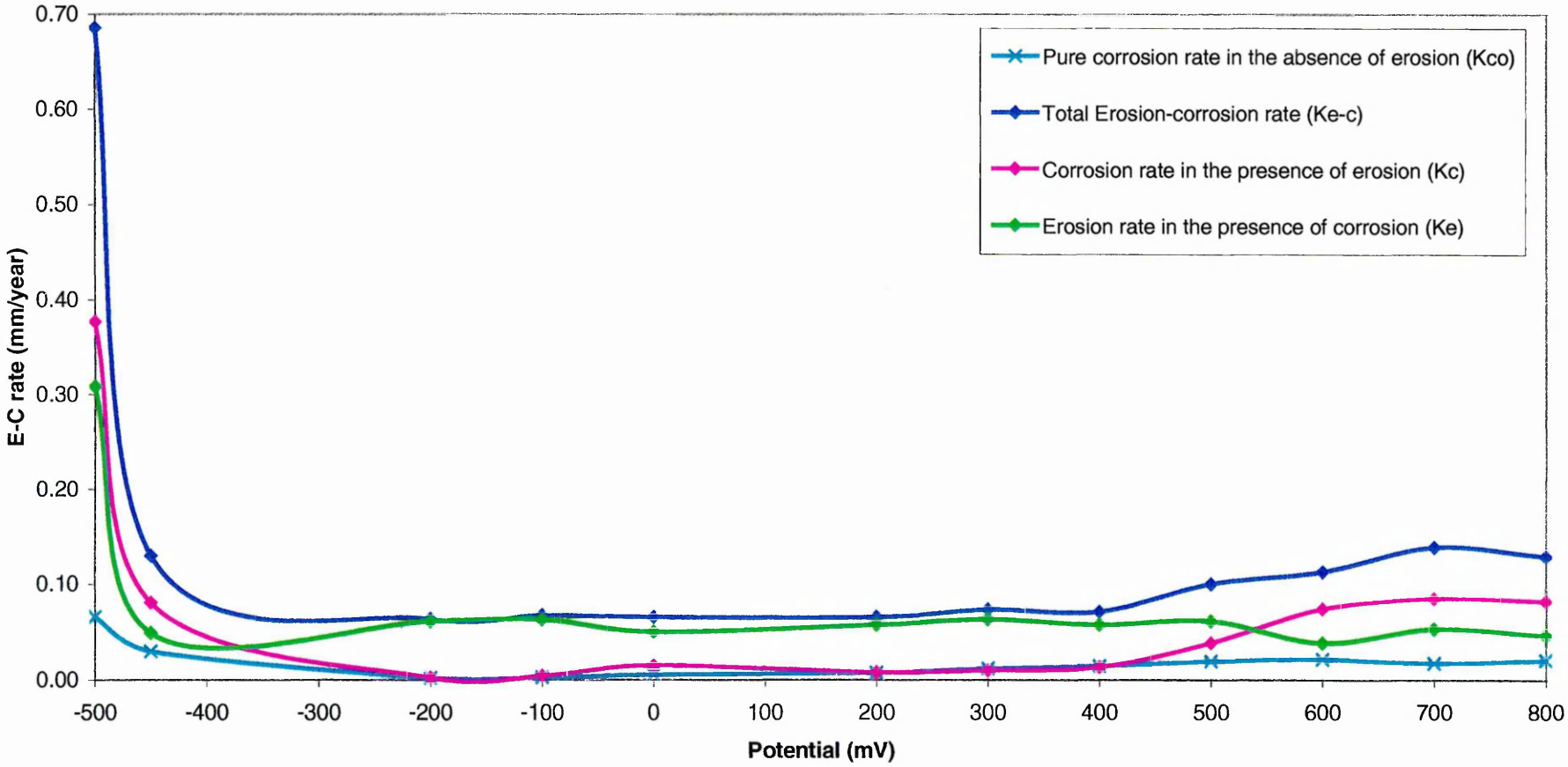

Table **13.5** Shows the current density values at different potential in the passive region of the duplex stainless steel at a range of fluid velocities.

Potential (mV)	Velocity (m/s)	Figure. No	Current density for total erosion-corrosion rate (micro A/sq.cm)	Current density for corrosion rate in the presence of erosion (micro A/sq.cm)	Pure corrosion rate current density (micro A/sq.cm)
300	**8.5**	7.4, 7.7	7.4	1.0	1.2
400			6.9	1.4	1.5
700			14.0	8.6	1.8
300	**7.9**	7.4, 7.9	6.0	1.4	1.2
400			8.5	1.7	1.5
700			13.0	5.2	1.8
300	**7.5**	7.4, 7.11	1.6	0.6	1.2
400			1.5	0.8	1.5
700			2.5	1.7	1.8
300	**7.2**	7.4, 7.12	1.9	0.8	1.2
400			1.5	1.6	1.5
700			2.9	2.3	1.8

Table 13.6 Show the current density (CD) values, erosion rate, corrosion rate, and erosion-corrosion rate in millimeter per year at 8.5 m/s fluid flow velocity

Potential (mV)	CD for fluid flow only (K_c)	CD for 3grams of sand (K_{e-c})	CD for pure corrosion rate (K_{co})	Corrosion rate in the presence of erosion (Kc) in mm/year	Pure corrosion rate in the absence of erosion in mm/year (K_{co})	Erosion rate in the presence of corrosion (K_e)	Total Erosion-corrosion rate in mm/year
-500	37.07	6.79	6.60	0.38	0.07	0.31	0.69
-450	8.10	3.11	3.00	0.08	0.03	0.05	0.13
-200	0.25	6.44	0.23	0.003	0.002	0.06	0.06
-100	0.45	6.75	0.27	0.005	0.003	0.06	0.07
0	1.54	6.59	0.56	0.02	0.01	0.05	0.07
200	0.81	6.58	0.76	0.01	0.01	0.06	0.07
300	1.02	7.44	1.23	0.01	0.01	0.06	0.07
400	1.37	7.17	1.50	0.01	0.02	0.06	0.07
500	3.90	10.10	1.97	0.04	0.02	0.06	0.10
600	7.49	11.43	2.20	0.07	0.02	0.04	0.11
700	8.59	14.00	1.80	0.09	0.02	0.05	0.14
800	8.30	13.00	2.10	0.08	0.02	0.05	0.13

In the narrow range of –500 mV to –440 mV (transition region) in the active dissolution region, the erosion-corrosion rate was maximum and dominated by anodic dissolution. There was some enhancement of erosion by corrosion (i.e. the corrosion rate in the presence of erosion was greater than the erosion rate in the presence of corrosion region). The erosion-corrosion rate peak at –500 mV (SCE) was consistent with the additional contribution of metal dissolution to the overall metal loss at such potential.

A transition from dissolution-dominated to erosion-passivation-dominated behaviour could be achieved as stated by Stack et al[160] as a result of application of an external voltage to raise the surface potential into the passive range. The variation of erosion-corrosion rate with applied potential showed a transition in erosion-corrosion process from dissolution-dominated behaviour at potentials less than –500 mV (SCE), to regimes in which erosion of the metal was affected by active dissolution and passivation.

In the passive state, the small increase in metal loss was consistent with the contribution of corrosion as measured by integrating the current densities over the exposure period. When passivation occurred, the erosion-corrosion rate decreased sharply and in the passivation regime of the duplex stainless steel, the contribution of corrosion to erosion-corrosion was relatively small, which coincided with the base line pure corrosion rate in the absence of erosion.This resulted in the erosion-corrosion rate being dominated by the erosion process enhanced by corrosion.

With the increase in the potential beyond 400 mV (SCE), the erosion-corrosion rate again was dominated by the corrosion process. Although corrosion processes were accelerated by erosion, this could suggest that the mechanical process of erosion was not affected by dissolution or passivation regions.

The regime in the range of 400 mV (SCE) to 900 mV (SCE) were erosion-corrosion processes dominated by erosion-passivation. Above 900 mV (SCE) dissolution corrosion process was dominant.

When considering the erosion-corrosion process as a function of fluid velocity at a fixed potential this would effect a transition from dissolution-dominated behaviour in the active region to erosion-passivation dominated behaviour, and in the passivation region, repassivation-dominated changed to erosion-passivation dominated behaviour.

At three selected potentials of 300 mV (SCE), 400 mV (SCE), 700 mV (SCE) and four velocities from 8.5 m/s to 7.2 m/s, the pure corrosion rate, corrosion rate in the presence of erosion, erosion rate in the presence of corrosion, and total erosion-corrosion rate, were measured. This selection of potentials was due to the study research interest in the duplex stainless steel passive and delta ferrite pitting regions.

In figures **13.8** and **13.9**, there was some synergistic effect from corrosion enhancement, and the erosion-corrosion rate was not identical to the sum of the pure corrosion rate in the absence of erosion and the erosion rate in the presence of corrosion. Apparently, at 300 mV (SCE) and 400 mV (SCE) potentials, the corrosion reactions involvement in the erosion- corrosion process was stable with low values as the fluid velocity increases.

This could result in no synergistic effect from the erosion rate in the presence of corrosion. However, the corrosion was enhanced significantly under erosion conditions and the corrosion rate increased drastically with the introduction of sand particles. There was no significant corrosion enhancement to erosion in the passive region. The total erosion-corrosion was the sum of the corrosion rate in the presence of erosion and the erosion rate in the presence of corrosion.

At 700 mV (SCE), as shown in figure **13.10**, a transition from passive to ferrite phase pitting region, the corrosion rate increases with fluid velocity because of the number of impacts and the area of the passive film ruptured by each individual impact increased with velocity[160]. Zhou et al[97] conveyed Eisenberg study which showed that corrosion enhancement was minimised by formation of the passive film, although the corrosion rate in the passive region under erosion conditions was not negligible, especially at higher velocities, and increased with potential.

However, there is a certain amount of synergistic effect because of total erosion-corrosion rate was consistently greater than the sum of pure corrosion and the erosion rate in the presence of corrosion. The synergism of corrosion as a function of potential at fluid velocity of 8.5 m/s, is shown in figure **13.12** and table **13.7**. There was a considerable synergistic effect from accelerated corrosion under erosion conditions. The trend of corrosion enhancement was the same as that of the corrosion rate, with maximum enhancement at the dissolution peak of –500 mV (SCE) where corrosion was predominant.

The values of the synergism in table **13.7** are calculated as a percentage of the total erosion-corrosion rate. In the narrow potential range of –500 mV to –400 mV (active to passive transition regime), evidence of corrosion affecting erosion was detected. The synergistic effect of corrosion (ΔK_c) dissolution regimes at this velocity was 38.5% and the passivation regime was 48.6%, as shown in figure **13.11**.

However, synergism has found to increase with corrosion tendency, and the magnitude of enhancement of erosion in many situations has been much larger than that of corrosion.

In general, it was important to evaluate the contribution of erosion rate and corrosion rate to the total erosion-corrosion rate, since it is useful in understanding the overall erosion-corrosion mechanism. The result shows that, at lower potentials, active dissolution is the predominant wastage process and therefore transitions from dissolution to erosion dominated behaviour is a function of increasing fluid velocity. Hence, the metal loss due to corrosion decreases with increasing the applied potential, as the transition from active to passive behaviour occurs.

Figure 13.8 Erosion, Corrosion and Erosion-corrosion rates of duplex stainless steel at 300 mV (SCE) as a function of fluid velocity

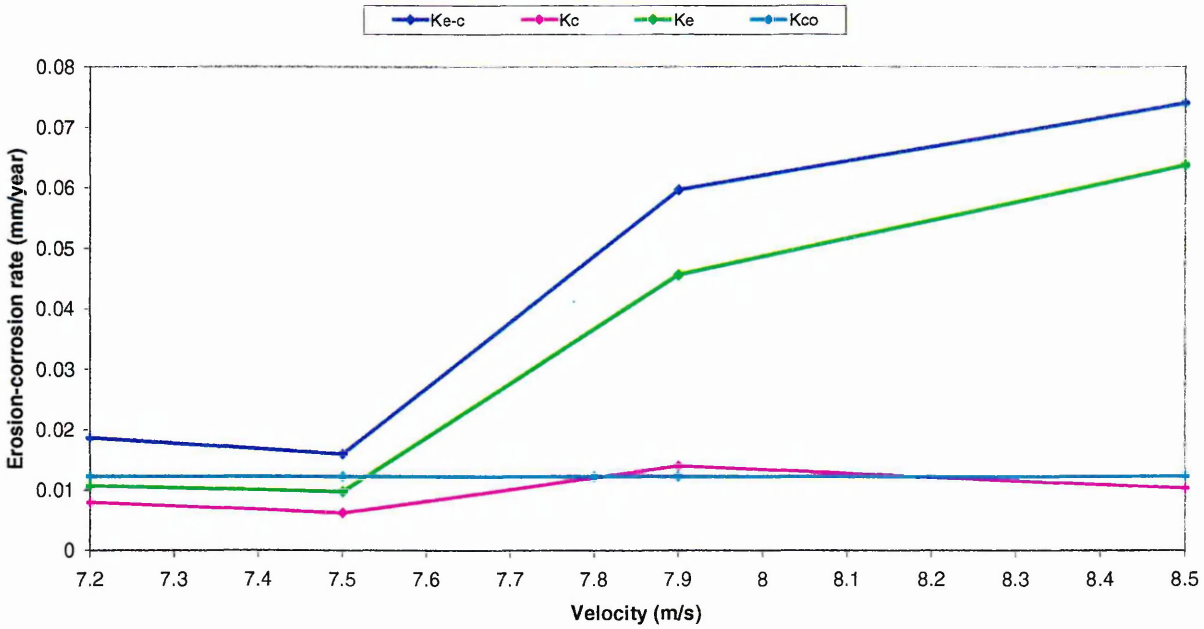

Figure 13.9 Erosion, corrosion and erosion-corrosion rates of duplex stainless steel at 400 mV (SCE) as a function of fluid velocity

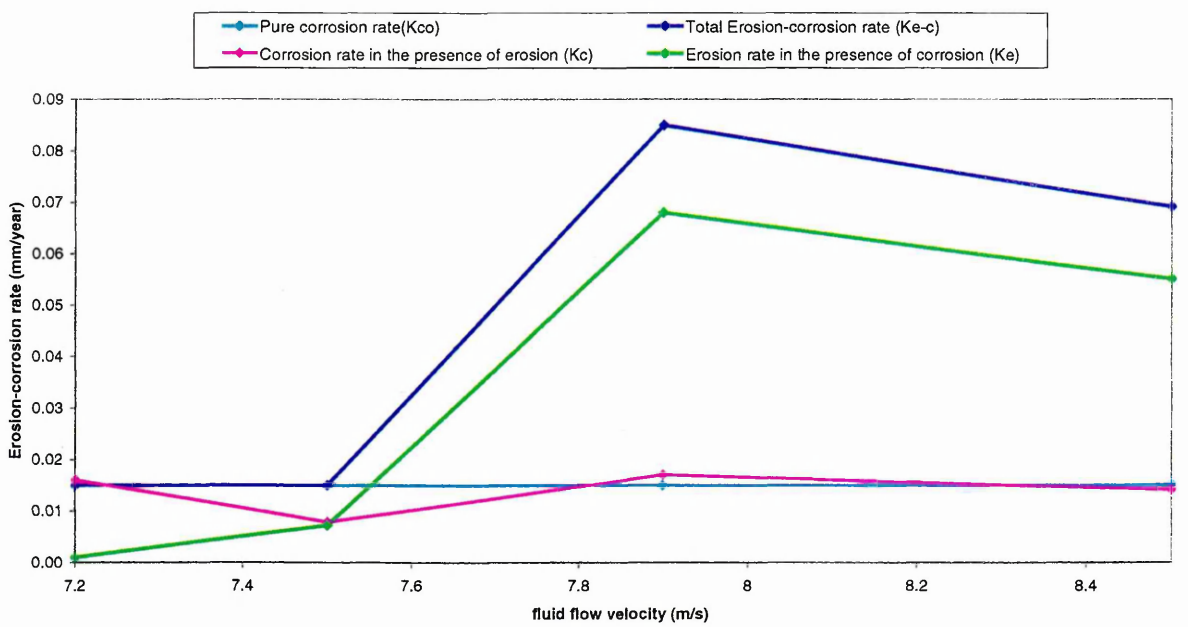

Figure 13.10 Erosiion, corrosion and erosion-corrosion rates of duplex stainless steel at 700 mV (SCE) as a function of fluid velocity

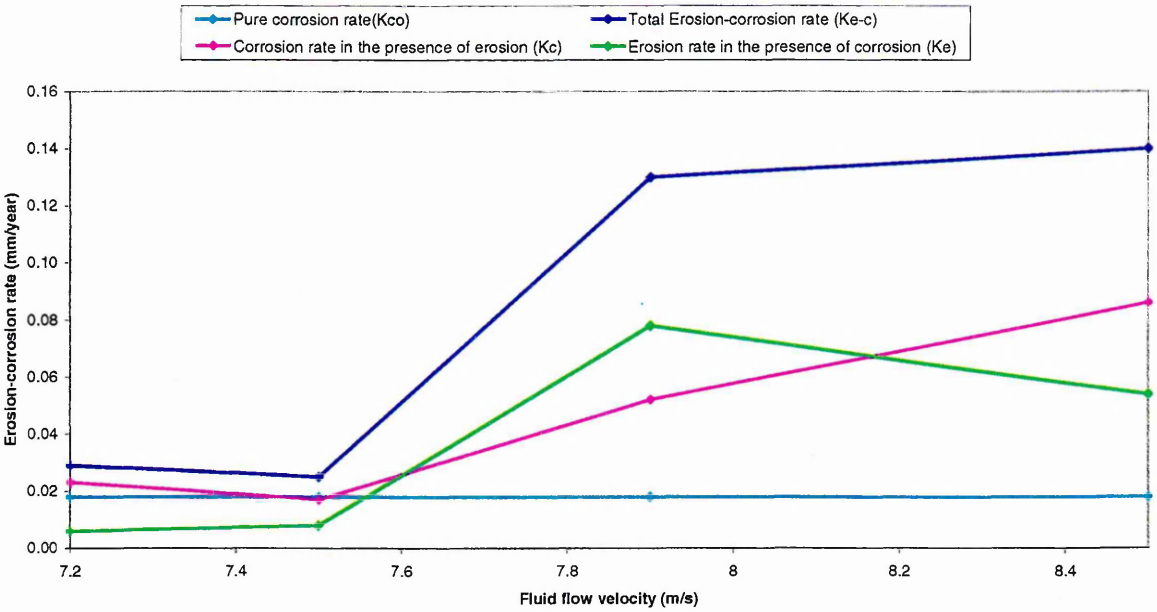

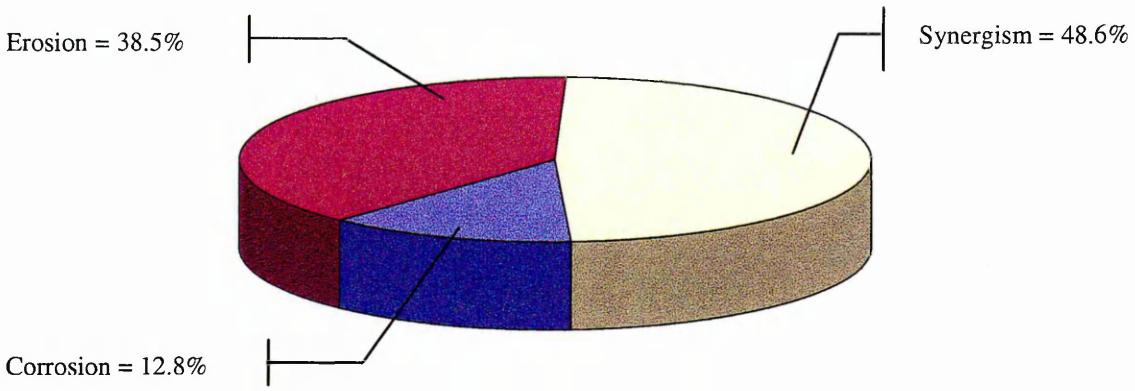

Figure **13.11** Shows the relative amounts of erosion, corrosion, and synergism for duplex stainless steel. Test conditions: 24 °C, 8.5 m/s, 3 grams of sand in seawater solution.

Figure 13.12 Corrosion synergy effect of duplex stainless steel at 8.5 m/s as a function of potential

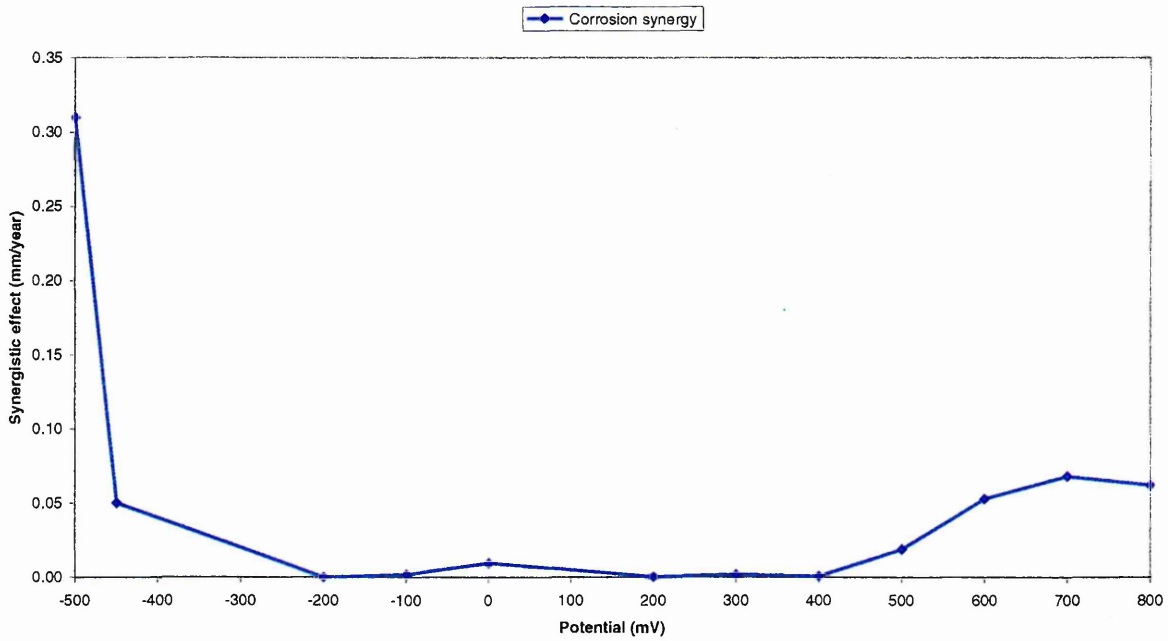

Table **13.7** Show the synergistic effect of corrosion in the presence of erosion at 8.5 m/s fluid flow velocity

Potential (mV)	Corrosion synergy in mm/year	Corrosion synergy percentage
-500	0.31	35
-450	0.05	38.5
-200	0.00	0.3
-100	0.00	2.7
0	0.01	15.0
200	0.01	0.8
300	0.00	2.7
400	0.00	1.4
500	0.02	19.0
600	0.05	48.0
700	0.07	48.6
800	0.06	48.0

After demonstrating the contribution of the synergism effect of erosion and corrosion rate to the total erosion-corrosion rate, the sand particle cutting mechanism was raised. Therefore, an assumption of two possible cases of sand particle cutting action were elaborated. First, *removal of the oxide film down to the substrate but no machining of the substrate*, and second, *removal of the oxide film and machining or ploughing action of the sand particles into the surface of the substrate.*

Figure **13.13** illustrates the first cutting mechanism. At normal fluid flow conditions with entrained sand particles, the impact of sand particles will rupture and remove the protective oxide layer that forms on the surface of the duplex stainless steel combined with plastic indentation but no metal loss due to machining or ploughing effect occurred to the material. Apparently, the oxide film on the duplex stainless steel is adherent and fast forming, since the passivation of the oxide film persists even at the maximum fluid velocity of 8.5 m/s and sand concentration of 4 grams to grow back to normal thickness.

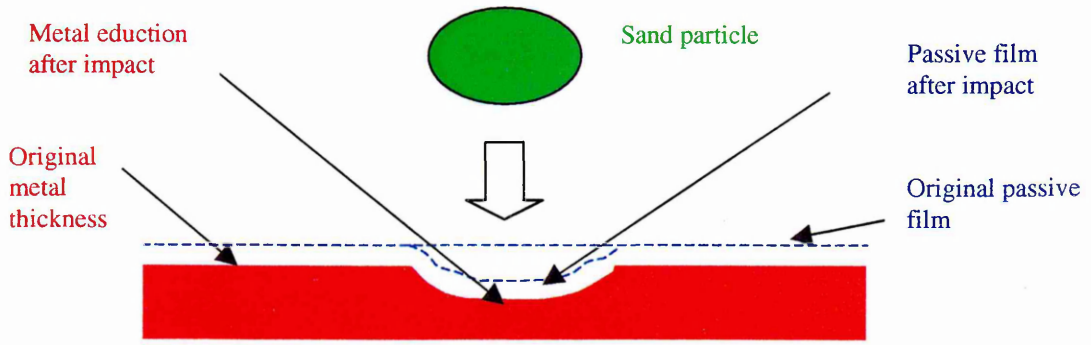

Figure **13.13** Shows the small indentation of the metal surface due to sand impact

With this cutting mechanism the applied force is assumed to have passed the elastic limit of the material, which resulted in plastic deformation. This leaves a thin film intact on the surface at all times. The increase in current density developed during polarisation measurements before the ferrite phase breakdown was mainly current caused by repassivation of bare metal at the point of impact of the sand particles.

This current density was mainly current to regrow the oxide film. The metal loss from the substrate was finite to contribute in the electrochemical reaction to reform the oxide film, hence the rate of removal was dependent on the percentage of sand concentration and the applied fluid flow velocity. In the passive range of the duplex stainless steel, the constant current density developed was mainly due to a continuous repassivation of impact sites, which were exposed to less frequent sand particle impact.

In turn, a second case was considered where the force of the impact exceeded the ultimate tensile strength of the material, consequently resulting in some metal loss by machining or ploughing to the specimen, as shown in figure **13.14**.

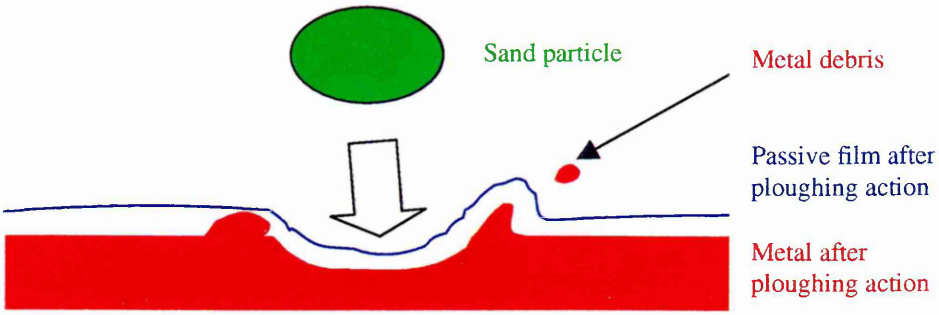

Figure **13.14** Shows the cutting mechanism of ploughing action effect on the surface of the material

With the impacted sand particles deforming the surface by ploughing, finite metal debris breaks away from the metal surface as metal loss. The oxide surface will repassivate again the metal debris transforms to oxidation products in the solution. These oxidation products are not adherent to the base metal, therefore they do not promote any passivation current. The reason behind this assumption was that the metal loss was finite and could not be detected by Telesurf profile and weight loss measurements in this study.

To determine which cutting mechanism assumption applies to the SAF2205 duplex stainless steel case on particle cutting action, a mathematical approach was developed by calculating the stress caused by the particle impacts on the surface, then comparing the calculated stress with the yield strength and tensile strength of the SAF2205 duplex stainless steel. Also scanning electron microscopy was implemented to show the surface crater of the impacted areas on the specimen and to assist in defining the mechanism of cutting.

Using equation (1) the calculated kinetic energy of each particle is

$$= \frac{1}{2} \times 1.4 \times 10^{-8} \times 8.5^2$$
$$= 5 \times 10^{-7} \text{ Joules}$$

Assuming that all the kinetic energy is lost on impact by deforming the substrate, then the area under the curve of the duplex stainless steel stress-strain curve represents the work done and the energy lost on impacting the material.

Therefore, the force exerted by the particle impact in machining the substrate can be estimated by the force to exceed fracture (σ_{uts}) for the UNS31803 duplex stainless steel,

$$\textit{i.e. Force} = \sigma_{uts} \times \text{Area of impact} \qquad (8)$$
$$= 680 \times 10^6 \times 1.0 \times 10^{-10}$$
$$F = 0.07 \text{ N}$$

Area under the = Force of particle × Displacement occurred in the material stress - strain curve
= Kinetic energy of particle

$$5 \times 10^{-7} = 0.07 \times \text{Displacement} \qquad (9)$$

$$\text{Displacement} = \frac{5 \times 10^{-7}}{0.07} = 7.0 \ \mu\text{m}$$

From the results of the calculation, it was concluded that machining or ploughing action of the surface occurred by the sand impact. This mechanism is depicted in four stages:

1- When the sand particle impacted the surface of the duplex stainless steel, a complete removal of the oxide film on the impacted area occurred down to the metal substrate, due to the force exerted by the sand particle impact and the kinetic energy imparted from the particle.

2- As the impacted sand particle calculation suggests, the mean kinetic energy of the particles is sufficient to exert a stress in the substrate equal to the tensile strength of the duplex stainless steel and produce an impact crater of 7 μm in depth. This value is only approximate due to the complexity of the stress field at the point of impact. In practice, the craters observed on the surface from the optical measurement were close to 2 μm in average depth (see figure **13.15**).

3- In this stage, regrowth of the oxide film back to equilibrium thickness occurs. Supportive evidence of repassivation process was the existence of partly clear surroundings sites close to the craters as seen in figure **13.15**. This can be explained by one site being impacted then simultaneously repassivated, at the same time other site has already been impacted and is still repassivating. Further evidence is the existence of 33 nm experimental film thickness.

4- It would appear that not all the kinetic energy of the particles was lost during the impacts but some kinetic energy was recovered in a partially elastic collision and fractured the sand particle. However, the force exerted on the substrate would be sufficient to exceed the tensile strength of the material and mechanical removal is to be expected.

From the polarisation diagrams electrochemical metal loss was accounted for within the calculation of average passive current density (I_{pass}) using Faraday's law, which gave a value of 0.07 to 0.08 mm/year. Evidence of mechanical erosion process occurred and the oxide film was removed down to the substrate level then regrowth of thin oxide film over a time scale of 1 hour. This indicated was by a pale interference colour as seen in the passive film optical measurement in sections **9.1.1**, **9.1.2** figures **9.2** and **9.7**. The oxide film thickness in the stagnation region at fluid flow, with and without sand addition, was 150 nm and reduced down to 33 nm, with changes in colour orders from second to first.

Therefore, if the substrate was exposed by the particle impacts then both erosion and corrosion processes will occur. This would indicate the fact that the produced average passive current density did not repassivate bare substrate only. Thus, it must be regrowing the passive film back to equilibrium thickness.

General summary shows that during sand impact there is a reduction in passive film thickness and metal loss in one area of the specimen while other sites will already be repassivated. This occurred due to the existence of a relatively large mean time between impact of particles. Overall conclusion revealed that the process appears to be mechanical erosion of the passive film and substrate, followed by electrochemical repassivation or, more probably at low fluid velocities and low impact sand energies, simple oxide film thickening.

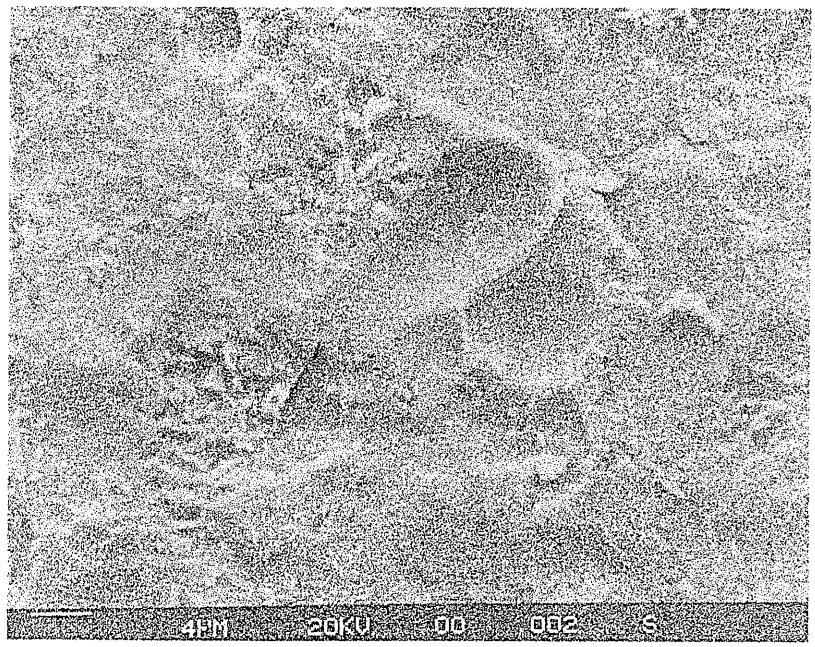

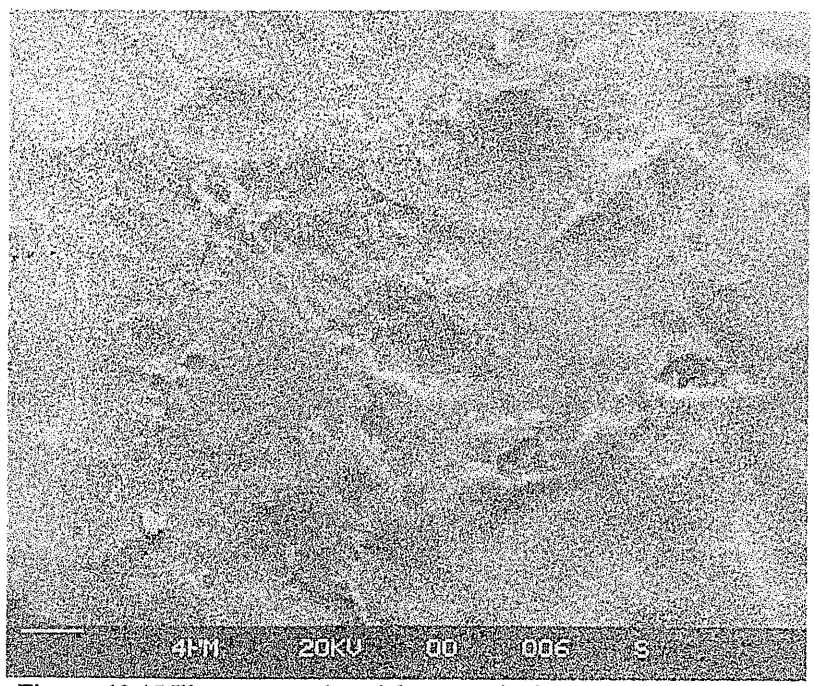

Figures **13.15** Illustrates sand particle craters in the stagnation region and the oxide film repassivation effect. Mag x 2100, x 2000

14.0 CONCLUSIONS

In the marine industry UNS 31803 duplex stainless steel is widely used, especially in seawater cooling systems and offshore pipelines. This is because it exhibits a good protective resistance against corrosion due to the existence of oxide film on its surface. This study produced both quantitative data regarding duplex stainless steel behaviour and qualitative information regarding the attack mechanism in seawater.

1.0 Electrochemical polarisation scans and optical film thickness measurements were utilised to measure the rate of repair of the passive film while varying the fluid flow velocity in seawater with and without the addition of sand particles. The passive current density value revealed the severity of the attack, as the fluid velocity was changed on the surface. The material was shown to have a good resistance to erosion corrosion, due to the low electrochemical metal loss value of 80 μm/y.

2.0 The electrochemical mechanism of attack follows the process of promoting the anodic reaction while the cathodic reaction stayed unchanged. The intersection of both reaction curves resulted in a polarisation diagram with high passive current density and more active rest potential. In the presence of sand particles entrained in the solution, further damage occurred to the metal and similar erosion corrosion mechanism applied, but with a higher current density and more negative rest potential.

3.0 Erosion corrosion was accompanied by a double breakdown of the passive film. The first was caused by pitting of the ferrite phase at 400 mV. The second, by breakdown of the austenitic phase at 900 mV. With the presence of sand particles, the average passive current density was enhanced significantly and increased up to 7.5 $\mu A/cm^2$ for 3 grams at 8.5 ms^{-1}. The average current density value stayed constant as the sand concentration increased to 4 grams as the fluid velocity decreased to 7.9 ms^{-1}. In general, the passive film produced an interface colour of the first or second order.

4.0 Oxide film thickness measurements showed that at velocities used in this study erosion corrosion occurred by particle impacts thinning the passive film. There was mechanical erosion of the metal substrate and the measured current density corresponded to that required to re-grow the film to its equilibrium thickness.

5.0 Microscopic observation and quantitative scanning electron microscopy showed that the attack mode on duplex stainless steel is potential dependent. Ferrite and austenite phases were shown to be preferentially degraded at potentials on the active and noble ranges. Comets of different sizes were initiated from pits and surface inclusions.

6.0 Overall, the study of duplex stainless steel SAF2205 concluded that the metal loss was strongly influenced by the fluid velocity and by the amount of solids suspended in the seawater. The measured electrochemical metal loss of 70 μm/year to 80 μm/year calculated from the average current density was in agreement with the

modelled depth of attack on the basis of a relationship between passive film thickness and sand particle energy from the water jet impingement system and polarisation scans.

7.0 The total erosion-corrosion rate was the sum of pure corrosion rate and erosion rate in the presence of corrosion. The mechanism of erosion on corrosion depends on the applied potential and the corrosion rate was enhanced by the presence of erosion. In the active region the dissolution rate increased at –500 mV (SCE) and the value of corrosion rate in the presence of erosion (K_c) was larger than erosion rate in the presence of corrosion (K_e). In the passive region, the corrosion was accelerated by breakdown of the passive film by the impact of sand particles.) and the value of corrosion rate in the presence of erosion (K_c) was less than erosion rate in the presence of corrosion (K_e).

8.0 The synergism between the erosion and corrosion rates in the total erosion-corrosion process at low fluid flow velocity can be account for just under one and half third while the erosion and corrosion processes are just over one third and less than half third of the total erosion-corrosion process. Therefore, the synergistic effects are very important in regard to the erosion corrosion of the duplex stainless steel material.

9.0 However, if a higher fluid velocity was used beyond the maximum utilised velocity of 8.5 m/s, a higher kinetic energy of sand impact will be produced. This in turn increases the metal loss and affects the resistance of the material and will shorten its service life in ships power plants and offshore piping. The increase in sand concentration is proportional to the tendency to depassivate rather than repassivate the surface of this material. Thus, special care should be taken when using the material in marine systems having higher fluid velocities and entrained solids in suspension.

15.0 FUTURE WORK

The following items should be considered for future work:

1- Specific Electrochemical erosion corrosion study

- Further study is required on crevice corrosion prevention on duplex stainless steel.
- Measuring the current density at different sizes and various sand particle concentrations to reveal accurately the depassivation/ repassivation process occurring on the surface of the duplex stainless steel.
- Investigate the effect of salt air atomisation on the erosion corrosion behaviour of duplex stainless steel with crude oil deposits on the surface, especially for material situated above the splash zone area of a marine structure.
- Make use of Reynolds number (Re) to identify the passive film thickness in every region of the flow.
- Relate shear stresses in every hydrodynamic region to the thickness of the passive film and the colour fringes formation.
- Identify the hydrodynamic region with the severest damage, when only air bubbles impact the material surface and the air works an as air cushion.
- Measuring the kinetic energy lost in both sand particle elastic rebound condition and sand particle fracture due to impact condition.
- Effect of varying the electrolyte temperature on the erosion corrosion process at the applied fluid velocities.
- Further investigation is required on measuring the finite metal loss due to erosion corrosion at those fluid velocities.

2- Passive film optical thickness

- Produce erosion corrosion tables for the optical film thickness of the alloy at different fluid velocities, sand concentrations and temperatures.
- Determine in the relationship between individual passive film colour fringes and chemical composition using both a Michel Levy chart and an optical image analyser.
- Study the effect of elevating the temperature on the characteristic of the passive film colour fringes in seawater.

- The effect of natural mechanical vibrations on the passive film growth and formation.

- Relate the electrochemical colours developed in the comet tail to the variation in fluid flow velocity and the amount of corrosion deposit produced outside the pit.

- The effect of surface roughness on passive film colour fringes formation.

3- Sand particle measurements

- Consider both particle sizes of 250 microns and 300 microns in the erosion model instead of 275 microns and the depth of a single impact point.

4- Correlation to an industrial flow pipeline

- Compare the erosion corrosion results obtained for the same specimen with real erosion corrosion from similar material pipelines, by placing the specimen in a flowing system.

16.0 APPENDIX

Table **6.3** Measured fluid flow rate data (ml/15 second)

Manometer Reading (mm)	Measured fluid flow rate data (ml/15sec)					Average fluid flow rate (ml/15 Sec)	Standard deviation of measured flow rate	
	1	2	3	4	5			
14	2500	2750	2510	2520	2300	2520	± 160	(6.0%)
13.5	2340	2440	2350	2230	2300	2330	± 77.0	(3.0%)
13	2300	2180	2340	2380	2300	2300	± 77.0	(3.0%)
12.5	2180	2240	2250	2250	2100	2200	± 65.0	(3.0%)
12	1940	2090	2090	2270	2190	2120	± 123	(6.0%)

Table **6.4** Measured fluid flow rate data (litre/minutes)

Manometer Reading (mm)	1	2	3	4	5	Average flow rate (l/minutes)	Standard deviation of measured flow rate	
14	10.0	11.0	10.0	10.0	9.2	10.0	± 0.64	(6.0%)
13.5	9.4	9.8	9.4	8.9	9.2	9.0	± 0.33	(4.0%)
13	9.2	8.7	9.4	9.5	9.2	9.0	± 0.31	(3.0%)
12.5	8.7	9.0	9.0	9.0	8.4	9.0	± 0.27	(3.0%)
12	7.8	8.4	8.4	9.1	8.8	9.0	± 0.49	(5.0%)

Table **6.5** Measured fluid flow rate data (ms^{-1})

Manometer reading	Measured fluid flow rate data (ms^{-1})					Average fluid flow rate (ms^{-1})	Standard deviation of flow rate data	
	1	2	3	4	5			
14	8.5	9.3	8.5	8.6	7.8	8.5	± 0.53	(6.0%)
13.5	8.0	8.3	8.0	7.6	7.8	7.9	± 0.26	(3.0%)
13	7.8	7.4	8.0	8.1	7.8	7.8	± 0.27	(4.0%)
12.5	7.4	7.6	7.7	7.6	7.1	7.5	± 0.24	(3.0%)
12	6.6	7.1	7.1	7.7	7.4	7.2	± 0.41	(6.0%)

Note:- The percentage values are calculated by dividing the standard deviation by the average fluid flow rate.

Table **8.1** Elemental weight percentage and standard deviation of figure **8.** values for duplex stainless steel (batch **A**) for various impingement regions held at 900 mV (SCE) for 18 hours under fluid flow condition

Element type	Stagnation region	Error	High turbulence region	Error	Low turbulence region	Error
Si	0.70	± 0.07	0.70	± 0.07	0.80	± 0.07
Mn	3.40	± 0.20	3.50	± 0.20	2.90	± 0.2
Cr	23.70	± 0.28	24.00	± 0.28	23.80	± 0.28
Ni	5.60	± 0.24	5.30	± 0.24	5.60	± 0.24
Mo	2.60	± 0.66	3.40	± 0.66	2.80	± 0.66
P	0.04	± 0.10	0.01	± 0.10	0.20	± 0.10
S	0.50	± 0.31	0.20	± 0.31	0.40	± 0.31
Cu	0.50	± 0.19	0.50	± 0.19	0.40	± 0.19
Co	0.20	± 0.22	0.20	± 0.22	0.20	± 0.22

Figure 10.1 Number of particle impacts for 4 grams sand concentration at various fluid flow velocities with vertical and horizontal bandwidth values at fluid flow velocity of 8.5 m/s

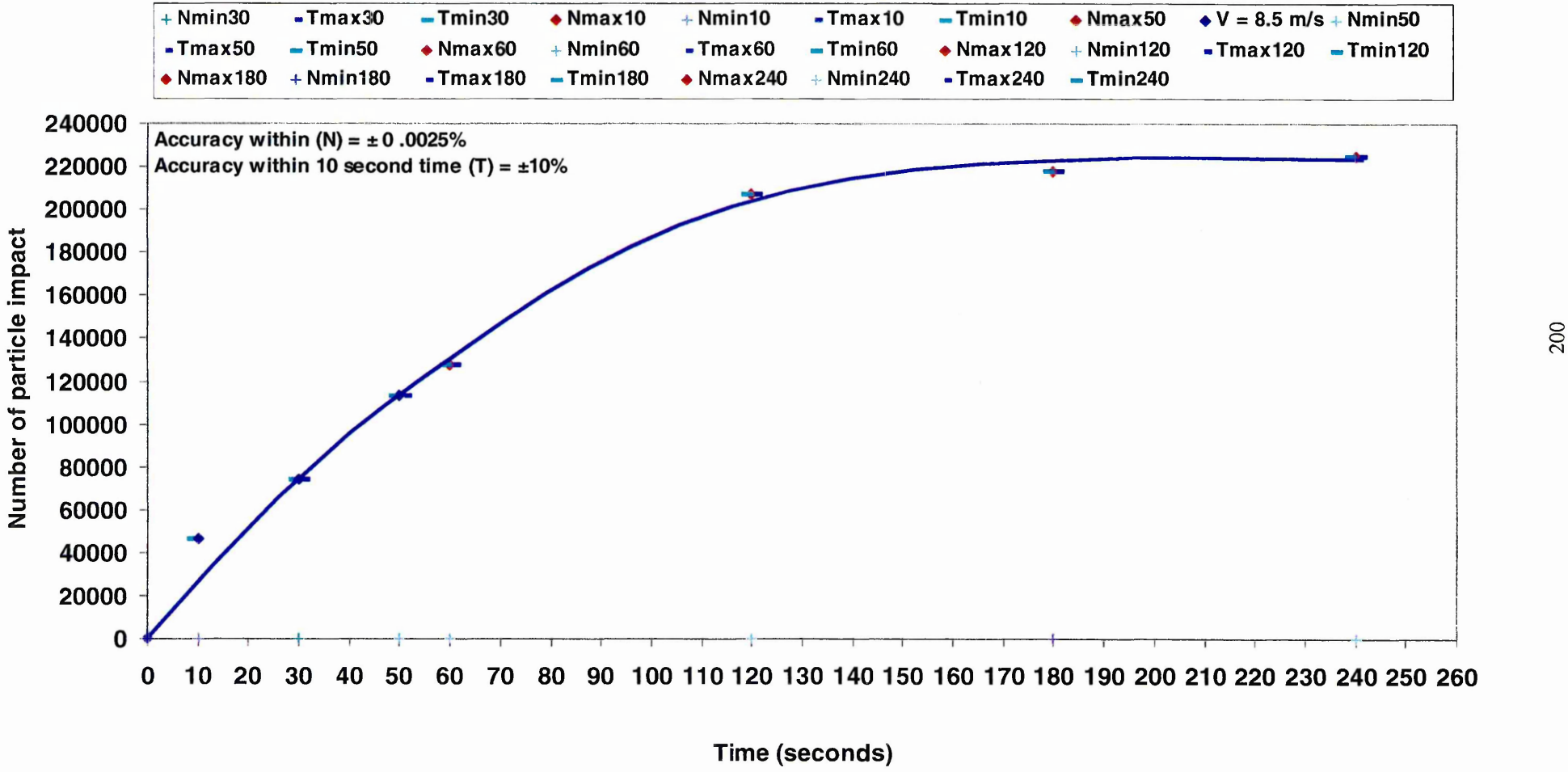

Figure 10.2 Number of particle gradients with ± 10 % bandwidth accuracy for 4 grams sand concentration at various fluid flow velocities

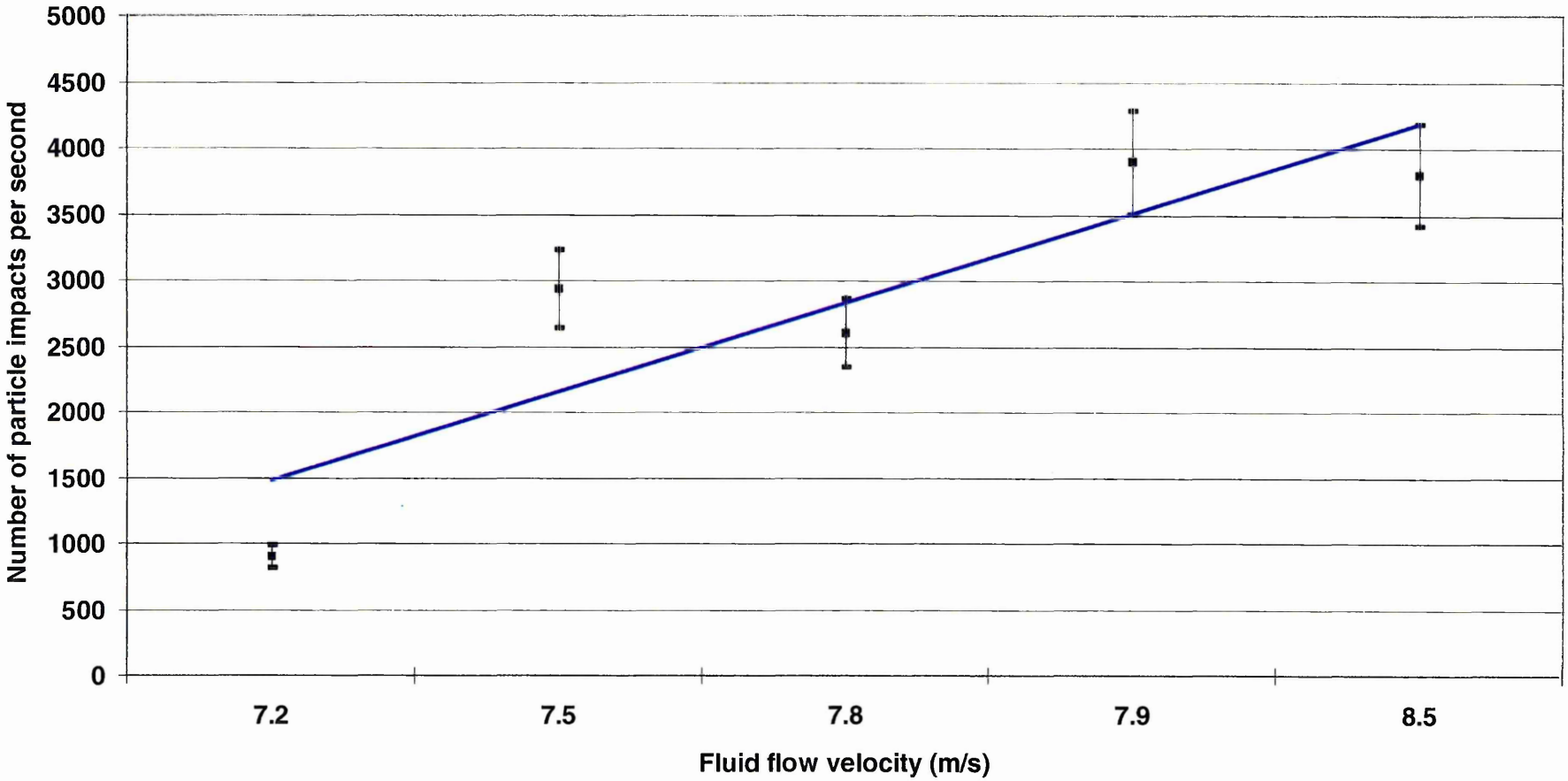

Figure 10.3 Shows fluid flow rate percentage vesus number of particle impacts at 10 and 50 second time periods

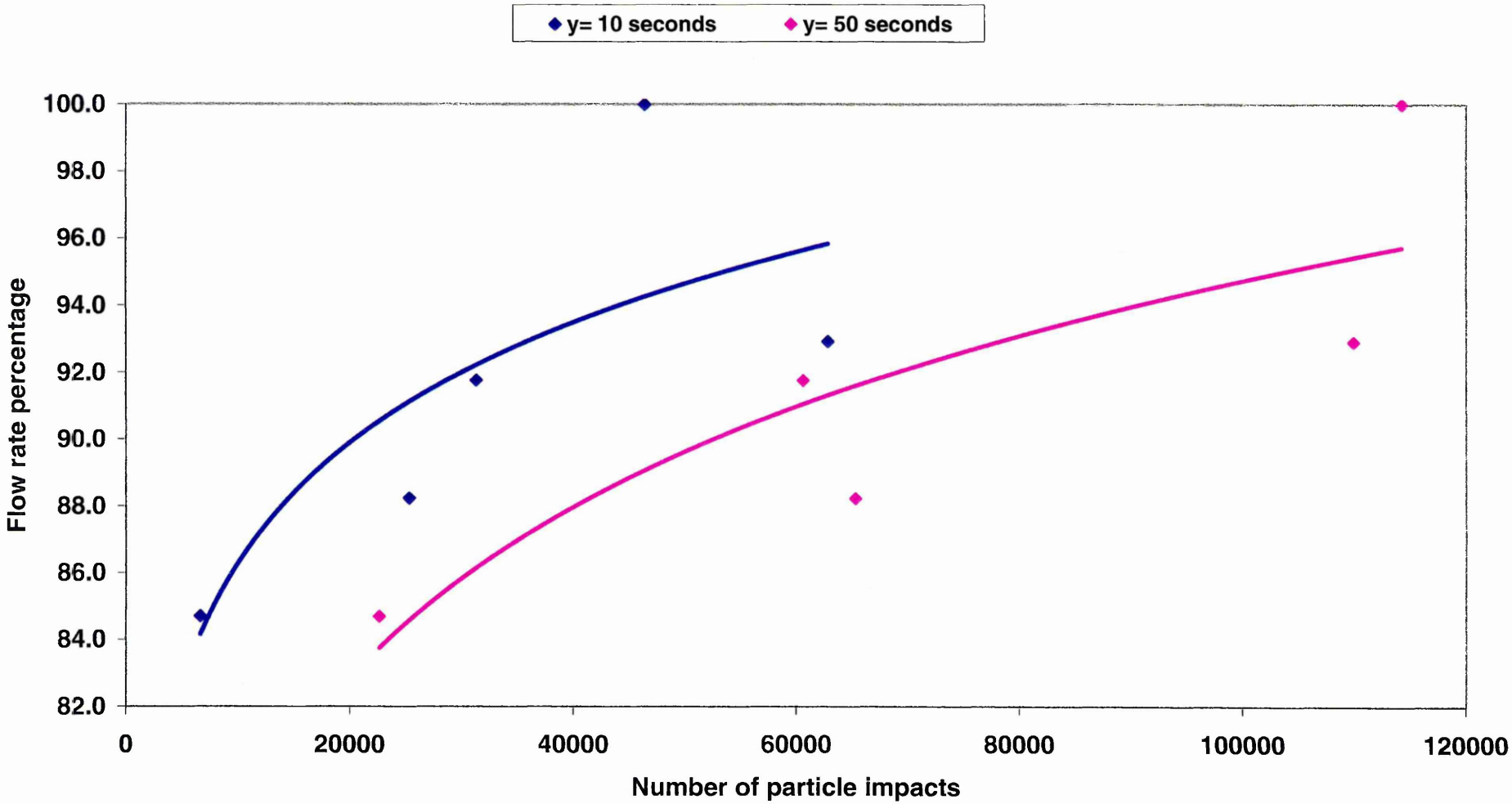

Nikon MICROSCOPY

Powered by
MOLECULAR EXPRESSIONS

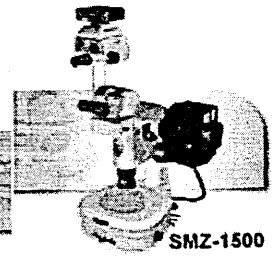

SEARCH
colour >GO

MicroscopyU Forum

Small World Contest

Interactive Tutorials

Microscopy Museum

Featured Microscopist

Digital Movie Gallery

Knowledge Database

Screen Savers

JAVA tutorial of the week:
Basic Microscope Ergonomics
Proper Microscope Posture

Welcome to Nikon's ***MicroscopyU*** website, designed to provide an educational forum for all aspects of optical microscopy, digital imaging, and photomicrography. Together with the scientists and programmers at **Molecular Expressions**, Nikon microscopists and engineers are providing the latest state-of-the-art information in microscope optics and imaging technology including specialized techniques such as fluorescence, differential interference contrast (DIC), phase contrast, reflected light microscopy, and microscopy of living cells. We invite you to explore our website and discover the exciting world of optics and microscopy.

Confocal Microscopy Image Gallery - The Nikon MicroscopyU Confocal Image Gallery features digital image sequences captured using a Nikon PCM-2000 confocal microscope scanning system coupled to an Eclipse E-600 upright microscope. Successive serial optical sections were recorded along the optical axis of the microscope over a range of specimen planes. These sequences are presented as interactive Java tutorials that allow the visitor to either "play" the series of sections automatically, or to utilize a slider to scroll back and forth through the images.

Nikon's Small World 2000 Competition

2000 Small World Contest Winners - Visit Small World gallery to view prize winners of the 2000 Small World contest. Specimens entered into the competition included plastic bubble wrap, a mangrove leaf, bamboo, soap, a canine eye, a mouse tongue, medusa worm skin, chemcial crystals, bovine arterial cells, zebrafish gills, and a human umbilical cord. Judges for the 26th annual contest included Dr. Kenneth R. Spring (National Heart, Lung, and Blood Institute), Martin L. Scott (Scientific Imaging), Dr. Nancy Kedersha (Harvard Medical School), and Michael W. Davidson (Florida State University).

Nikon MICROSCOPY

Powered by MOLECULAR EXPRESSIONS

Explore the World of Optics and Imaging Technology

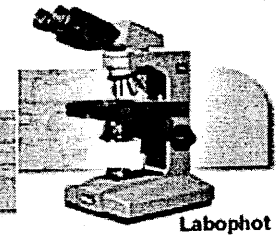

SEARCH
Go
MicroscopyU Forum
Small World Contest
Interactive Tutorials
Microscopy Museum
Featured Microscopist
Digital Movie Gallery
Knowledge Database
Screen Savers
JAVA tutorial of the week:
Basic Microscope Ergonomics
Proper Microscope Posture

Search Engine

Search our Website for information and/or the images that you need. Enter keyword(s) in the text box below and use the mouse cursor to either search for the keyword(s) by clicking on the search button or clear the text box. If you need help with the context of our search engine, use the link at the right of the text box to obtain tips about the search.

Search for: Tips for searching

Any Keywords

Use these words exactly (no additional wildcards).

Search only within the returned results.

Clear Search

MICROSCOPY U

Showing 1 - 2 of 2 matches for
colour OR chart**

Understanding Your Search Results

Nikon MicroscopyU: Michel-Levy Birefringence Chart

Abstract: The birefringence of a material observed in a polarized light microscope may be estimated if the interference color is of low enough order for its position in the color scale to be recognized on a Michel-Levy chart and if the thickness of the grain is known.

Size: 3.08 Kb, 6/26/2001 5:58:33 PM EST

Nikon MicroscopyU: Introduction to Polarized Light Microscopy

Abstract: Although much neglected and undervalued as an investigational tool, polarized light microscopy provides all the benefits of brightfield microscopy and yet offers a wealth of information simply not available with any other technique.

Size: 30.29 Kb, 6/26/2001 5:58:33 PM EST

Michel-Levy Interference Color Chart

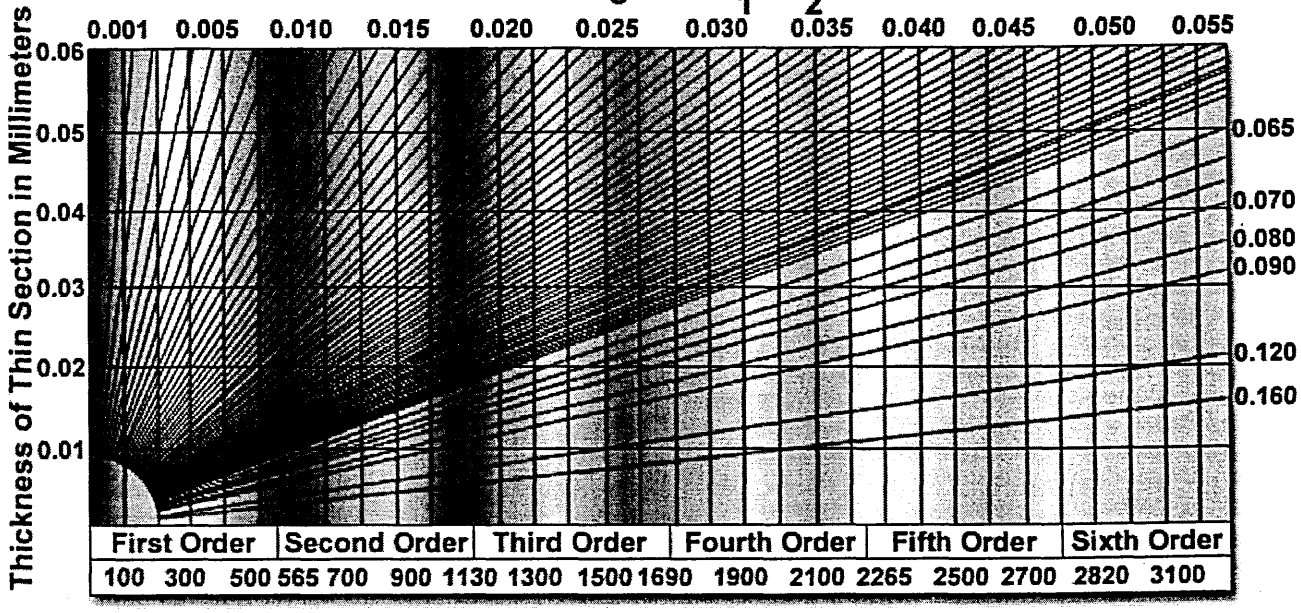

The birefringence of an isotropic material can be estimated when observed and/or photographed in a polarized light microscope. A relationship between interference color and retardation can be graphically illustrated in the classical Michel-Levy interference color chart, presented above. This graph plots retardation on the abscissa and specimen thickness on the ordinate. Birefringence is determined by a family of lines that emanate radially from the origin, each with a different measured value of birefringence corresponding to thickness and interference color.

The Michel-Levy chart is utilized by comparing the highest-order interference colors displayed by the specimen in the microscope to those contained on the chart. Once the appropriate color has been located, the nearest vertical line along the interference color is followed to the nearest horizontal line representing the known thickness. Birefringence is determined by selecting the diagonal line crossing the ordinate at the intersection of the specimen interference color and thickness value.

Authors

Phillip C. Robinson - Department of Ceramic Technology, Staffordshire Polytechnic, College Road, Stroke-on-Trent, ST4 2DE United Kingdom.

Michael W. Davidson - National High Magnetic Field Laboratory, 1800 East Paul Dirac Dr., The Florida State University, Tallahassee, Florida, 32310.

17.0 REFERENCES

1- Levy, Alan., *Solid particle erosion and erosion-corrosion of materials*, Pub: ASM International, Material Park, OH, USA, July 1995.

2- Mingwei, T., The mechanism chemical colouring of stainless steels-I. Calculation of the colouring initiation time, *Corrosion Science*, Vol. 33, No. 6, 1992, pp. 873-878.

3- Sedriks, A. J., *Corrosion of stainless steels*, Pub: John Willey & Sons, New York, 1979.

4- McLoone, J. D., Crevice corrosion of austenitic and duplex stainless steels, M.Sc Thesis, Cranfield Institute of Technology, 1987.

5- Atamert, S. and King, J. E., Super duplex stainless steels. Part 1: Heat affected zone, Microstructure, *Material Science and Technology*, Vol. 8, October 1992, pp.896-911.

6- Varol, I., Lipod, J. C. and Baeslack, III. W. A., 'Welding of duplex stainless steels'.In: *Ferrous alloy weldments*, Olson, D. L., and North, T. H (Eds)., Pub: Trans. tech., Switzerland, 1992.

7- Charles, J., Super duplex stainless steels: Structure and properties, *Conf. Proc. Duplex Stainless Steels '91*, France 28-30 October 1991, Pub: Les editions de physique, Vol. 1, pp.4-48, 3-48.

8- Charles, Jacques., Duplex stainless steel for chemical tankers, *MariChem 95, Conference –Road, Rail, River, Sea*, Kolnmesse, Germany, Nov 28-30, 1995, Vol. 1, pp. 191-204.

9- Gunn, R. N., *Duplex Stainless Steel*, Abington Publishing, Cambridge, England, 1997.

10- Stansbury, E. E., Ludin, C. D. and Pawel, Sensetion behavior of cast stainless steels subjected to simulated weld repair, S. J., SCRATA Research Division- *29th Annual Conference 1984 [Conf. Proc],* Nottingham, UK 20-21 June 1984, Pub: Werkstoffe und Korrosion, Germany.

11- Galvele, J. R., Lumsden, J. B. and Staehle, R. W., Effect of molybdenum on the pitting potential of high purity 18% chromium ferritic stainless steels, *J. Electrochemical science and technology*, Vol. 125, No. 8, August 1978, pp. 1204-1208.

12- Skoog, D. A., West, D. M., and Holler, F. J., *Analytical Chemistry an introduction*, Philadelphia, Saunders, 1994, 6th Ed, pp. 41.

13- Mitrovic, V., Scepanovic., MacDougall, B. and Graha, M. J., Nature of passive films on Fe-26Cr alloy, *Corrosion Science*, Vol. 24, No. 5, 1984, pp. 479- 490.

14- Kruger, J., Nature of passive film on iron and ferrous alloys, *Corrosion Science*, Vol. 29, No. 2/3, 1989, pp. 149-162.

15- Farah, L., Lemaitre, C. and Beranger, G., Passive film evolution on stainless steel with the medium composition: Electrochemical studies in the presence pf chloride and molybdate ions, In: *Modifications of Passive Films [Proc. Conf]*, Paris, France, Feb 15-17, 1993, Pub: The Institute of Materials, London, UK, 1994.

16- Beccaria, A. M., Poggi, G., Tartacca, E. and Castello, P., The effect of hydrostatic pressure on the modification of passive films on 316L stainless steel in sea water, *Modification of Passive Films [Proc. Conf]*, Paris, France, Feb 15-17, 1993, Pub: The Institute of Materials, London, UK, 1994.

17- Efird, K. D., Wright, E. J., Bros, J. A. and Hailey, T. G., Correlation of steel corrosion in pipe flow with jet impingement and rotating cylinder tests, *Corrosion*, Vol. 9, No.12, December 1993, pp. 992-1003.

18- Bjordal. M., Bardal. E., Rogne. T., Eggen. T. G., Erosion and corrosion properties of WC coatings and duplex stainless steel in sand containing synthetic seawater, *Wear*, Vol. 186-187, 1995, pp. 508-514.

19- Neville, A., Hodgkiess, T., Dallas, J. T., A study of the erosion-corrosion behavior of engineering steels for marine pumping applications, *Wear*, Vol. 186-187, 1995, pp. 497-507.

20- Neville, A., Hodgkiess, T. and Destriau, X., Initiation and propagation of localized corrosion on stainless steels in seawater containing high biocide concentrations, *Corrosion Sc*ience, Vol. 4-5, May 1998, pp. 715-730.

21- Kwok, C. T., Man, H. C. and Cheng, T. T., Cavitation erosion of duplex and super duplex stainless steels, *Scripta Materialia*, Vol. 39, No. 9, 1998, pp. 1229-1236.

22- Dawson, J. L., Shih, C. C., Electrochemical testing of differential flow induced corrosion using jet impingement rigs "*Corrosion/87*. March 9-13, 1987, Paper no. 453, Pub: NACE International, Houston, TX.

23- Postlethwaite, J., Effect of chromate inhibitor on the mechanical and electrochemical components of erosion-corrosion in aqueous slurries of sand, *Corrosion*, NACE, Vol. 37, No. 1, January 1981, pp. 1-5.

24- Haynes, A. G., Duplex and high alloy corrosion resistance steels, paper No.6, London, *Lloyd's Register Technical Association*, Report 000245, session 1990-91.

25- Gojkovic', S. L. J., Zec'evic', S. K., Obradovic', M. D. and Drazic', D. M., Oxygen reduction on a duplex stainless steel, *Corrosion Science*, Vol. 40, No. 6, 1998, pp. 849-860.

26- Koren, M. and Hochortler, G., Properties of ferritic austenitic steel X3 CrMnNi MoN 2564, *Stahl und Eisen*, Vol. 102, No. 10, 17 May 1982, pp.509-513.

27- Karimi, A., Cavitation erosion of a duplex stainless steel, *Mater. Sci. Eng.* Vol. 86, No. 1-2, 1987, pp.191-203.

28- Newman, R. C., Wong, W. P., Ezuber, H. and Garner, A., Pitting of stainless steel by thiosulfate ions, *Corrosion Science,* Vol. 45, No 4, April 1989, pp. 282-287.

29- Yue, Z., Zhou, P., Shi, J., *Proc.* Some factors influencing corrosion-erosion performance of materials, *Conf.. Wear of Materials*, Vol. 2, Houston, Texas, USA, 5-9 Apr. 1987, Pub: ASME, NY, 1987, pp. 763-768.

30- Stott, F. H., Stack, M. M. and Wood, G. C., The role of oxides in the erosion-corrosion of alloys under low velocity conditions, *Proc. 4th Berkeley. Conf. on Corrosion-Erosion-Wear of materials at elevated temperatures*, Jan. 31- Feb2, 1990, California, Levy, A. V, (Ed), Pub: NACE International, Houston, TX. Houston, TX, 1989, paper 544.

31- Angelini, E., Bianco, P. and Plassa, M., Instability of stainless steel reference weights due to corrosion phenomena, *Corrosion Science*, Vol. 40, 1998 pp. 1139-1148

32- Charles, J., Structure and mechanical properties of duplex stainless steels, *Conf. Proc. Duplex stainless steels '94*, Vol. 1: Materials and properties, Paper KI, Nov 1994, Glasgow, Pub: Abington, UK, 1995.

33- Liljas, M., Qvarfort, R., Influence of nitrogen on weldments in UNS S31803, Acom, Vol. 1, No. 2, 1986, pp. 2-12.

34- Redjaimia, A., Metauer, G., Gantois, M., Decomposition of delta ferrite in an Fe-22Cr-5Ni-3Mo-0.03C duplex stainless steel: A morphological and structural study, Conference: *Proc. Conf. Duplex Stainless Steels '91*, Beaune, France, 28-30 Oct, 1991, Pub: Les editions de physique, 1991, Vol. 1, 119-126.

35- Yutaka, S., Sato, Y. S. and Kokawa, Hiroyuki., Preferential precipitation of sigma phase in duplex stainless steel weld metal, *Scripta Materilia*, Vol. 40, No. 6, 1999, pp. 659- 663,.

36- Francis, R., Duplex stainless steels state of the art and future developments, *UK Corrosion 91*,Vol 2, Manchester, 22-24 October. 1991, Pub: Institute of Corrosion, Birmingham (UK), 1991, pp. 19.

37- Rashel, D. M., Petit, F. S., and Birks, N., Some principle mechanisms in the simultaneous erosion and corrosion attack of metals at high temperature, paper 16, *Proceedings of Conference on Corrosion Erosion-Wear of Materials at Elevated Temperatures*. Levy, A. V. (Ed), Pub: NACE/ EPRI.LDOE-FE, Berkeley, CA, 31 January-2 February 1990.

38- Miura, R. and Sakuraba, M., Clad steel pipe for corrosive gas transportation, *27th annual Offshore Technology Conference,* Pub: OTC 7790, Houston, Texas, USA, 1-4 May, 1995.

39- Hashimoto, K., Asami, K. and Teramoto, K, An X Ray Photo-Electron spectroscopy study on the role of molybdenum in increasing the corrosion resistance of ferritic stailess steels in HCl, *Corrosion Science*, Vol. 19, No. 1, 1979, pp. 3-14.

40- Olefjord, I., Borx, B. and Jelvestam, U., Surface composition of stainless steels during anodic dissolution and passivation studies by ESCA, *Journal of the Electrochemical Society*, Vol.132, No. 12, Dec 1985, pp. 2854-2861.

41- Sedriks, A. J, Metallurgical aspects of passivation of stainless steels, *Conf. Proc. Stainless Steels '84*, Goteborg, Sweden, 3-4 Sept. 1984, Institute of Metals, London, 1985, 125- 133, Pub: Werkstoffe und Korrosion, Germany, 1985.

42- Carranza, R. M. and Alvarez, M. G., The effect of temperature on the passive film properties and pitting behavior of A Fe-Cr-Ni alloy, *Corrosion Science*, Vol. 38, No. 6, 1996, pp. 909-925.

43- Ravindranath, K. and Malhotra, S. N., The influence of aging on the intergranular corrosion of 22 chromium-5 nickel duplex stainless steel, *Corrosion Science*, Vol. 37, No. 1, 1995, pp. 121-132.

44- Wanklyn, J. N., The role of molybdenum in the crevice corrosion of stainless steels, *Corrosion Science*, Vol. 21, No. 3, 1981, pp. 211-225.

45- Asami, K., Naka, M., Hashimoto, K. and Masumoto, T., Effect of molybdenum on the anodic behavior of amorphous Fe-Cr-Mo-B alloys in Hydrochloric acid, *J. Electrochem. Soc*, Vol. 127, No. 10, Oct. 1980, pp. 2130-2138.

46- Ansell, R. O., Dickenson, T. and Povey, A. F., An X Ray photo electron spectroscopic study of the films on coloured stainless steel and coloured 'Nilomag' alloy 771. *Corrosion Science*, Vol.18, 1978, pp. 257-259.

47- Belfrouh, A., Masson, C., Vouagner, D., Becdelievre, A. M. De., Prakash, N. S. and Audouard, J. P., The cumulative effect of alloying elements nitrogen, tungsten, molybdenum, an copper on the corrosion behavior of 17Cr-13Ni stainless steel in 2M H sub 2SO sub 4, *Corrosion Science*, Vol. 38, No. 10, Oct. 1996, pp. 1639-1648.

48- Stephen, E., and Alkire, R. C., The role of inclusions on initiation of crevice of stainless steel. I-Experimental studies, *J. Electrochemical society*, Vol. 136, No. 4, April 1989, pp. 973-979.

49- Denpo, K. and Ogawa, H., Effects of nickel and chromium on corrosion rate of line pipe steel, *Corrosion Science*, Vol. 35, No 1-4, 1993, pp. 285-288.

50- Cristofaro, N. De., Piantini, M. and Zacchetti, N. The influence of temperature on the passivation behavior of a super duplex stainless steel in a Boric-Borate buffer solution, *Corrosion Science*, Vol. 39, No. 12, 1997, pp. 2181-2191.

51- Hong, T., Ogushi, T. and Nagumo, M., The effect of chromium enrichment in the film formed by surface treatments on the corrosion resistance of type 430 stainless steel, *Corrosion Science*, Vol. 38, No. 6, 1996, pp. 881- 888.

52- Johnsen, R., North sea experience with the use of stainless steels in seawater applications, The Institute of Materials, Marine corrosion of stainless steels: Chlorination and Microbial Effects (UK), 1993, 30 Sep-20 Oct, pp. 48-58, Pub: The Institute of Materials, London, 1993.

53- Kotecki, D. J., Siewert, T. A; WRC-1992 Constitution diagram for stainless steel weld metals: A modification of the WRC-1988 diagram, *Welding Research (USA)*, Vol. 71, No. 5, May 1992, pp.171s-178s.

54- Kosel, T. H., Solid particle erosion, *ASM Handbook*, Vol. 18, Friction, lubrication and wear technology, Pub: ASM International (USA), Material Park, Ohio, Henry, S. D., (ed), 1992.

55- Solomon, H. D., Levinson, L. M., Mossbauer effect study of 475 embrittlement of duplex and ferritic stainless steels, *Acta Metallurgica,* Vol. 26, 1978, pp. 429-442.

56- Endo, S., Nage, M., Fujita, S. and Hirano, O., New line pipe resists preferential corrosion at welds, *Oil & Gas journal*, March 17, 1997, pp. 92-102.

57- NACE Standards International 50th Anniversary, *NACE Standard Test Method*: Method of conducting controlled velocity laboratory corrosion tests, TM0270-72, Dynamic corrosion testing of metals in high temperature water, TM0274-74, Abrasion resistance testing of thin film baked coatings and linings using the failing sand method TM0375-86, NACE 1972.

58- Nagano, H., Kudo, T., Inaba, Y., Harada, M; Highly corrosion resistance duplex stainless, *Metaux Corrosion Indusrie*, Vol. 667, Mar.1981, pp.81-88.

59- Kim, K. Y., Zhang, P. W., Ha, T. H. and Lee, Y. H., Electrochemical and stress corrosion properties of duplex stainless steels modified with tungsten addition, *Corrosion*, Vol. 54, No. 11. November 1998.

60- Nilsson, J. O., Wilson, A., Influence of isothermal phase transformations on toughness and pitting corrosion of super duplex stainless steel SAF2507, *Materials Science and Technology*, Vol. 9, No. 9, July 1993, pp. 545-554.

61- Okamoto, H., Tsuda, K., Azuma, S., Ueda, M., Ogawa, K., Igarashi, M., Advance performance of 2% tungsten bearing superduplex stainless steel DP3W, *Proc. 4th Int. Conf Duplex Stainless steels*, paper no 91, Glasgow, Scotland 13-16 Nov. 1994, Cambridge, England: Abington publishing for Woodhead publishing Ltd 1995.

62- Montemor, M. F., Simoes, A. M. P., Ferreira, M. G. S., Da Cunha Belo, M., The role of molybdenum in the chemical composition and semiconductive behavior of oxide films formed on stainless steels, *Corrosion Science*, Vol. 41, 1999, pp. 17-34.

63- Sugimoto, K., Sawada, Y., Role of molybdenum additions to austenitic stainless steel in the inhibition of pitting in acid chloride solutions, *Corrosion Science*, Vol. 17, No. 5, 1977, pp. 425-445.

64- Tan, M. W., Akiyama, E., Kawashima, A., Asami, K., Hashimoto, K., The effect of air exposure on the corrosion behavior of amorphous Fe-8Cr-Mo-13P-7C alloys in 1 M HCl, *Corrosion Science*, Vol. 37, No. 8, 1995, pp.1289-1301.

65- Zhiming, Y., Zheng, Y., The influence of applied potential on the erosion-corrosion behavior of AISI321 stainless steel in acidic slurry medium, *Wear*, Vol. 186- 187, 1995, pp. 568-572

66- Constable, F. H., *Proceeding of the Royal Society of London*, series A, Vol. 115, 1927, pp. 570-589.

67- King, R. J., Downs, M. J., Raine, K. W. and Talim, S. P., A comparison of methods for accurate film thickness measurement, *Journal of Physics E*: Scientific Instruments, Volume 5, 1972, pp. 445-449.

68- Breslin, C. B., Chen, C. and Mansfeld, F., The electrochemical behavior of stainless steels following surface modification in cerium-containing solutions, *Corrosion Science*, Vol. 39, No.6, 1997, pp. 1061-1071.

69- Gardner, S., Hayes and Baboian, Robert., laboratory corrosion tests and standards, *Symposium by ASTM committee G-1 on corrosion of metals*, Harbour. B., FL, 14-16 Nov. 1983, ASTM special technical publication, Texas instruments ncorportated, (Eds), Philadelphia.

70- Chance, J., Coop, W., Gradwell, K. J., Roscoe, C. V; Structure property relationships in a 25Cr-7Ni-2Mo duplex stainless steel casting alloy, *Conf. Proc. Duplex Stainless Steels '82*, St. Louis, USA, 25-28 Oct. 1982, Pub; ASM, Metals Park, Ohio, USA, 1982, pp. 371-398.

71- Roscoe, C. V., Gradwell, K. J., Lorimer, G. W; Structure property relationships in a series of duplex stainless steels, *Conf. Proc. Stainless steels '84,* Goteborg, Sweden, 3-4 Sept. 1984, Pub; The Institute of Metals, London, 1984, pp.563-577.

72- Chin, D. T. and Tsang, C. H., Mass transfer to an impinging jet electrode, *J. Electrochem Soc*, Vol.125, 1978, pp. 1461-1470.

73- Guha P, Clark CA; Properties and applications of high chromium duplex stainless steels, *Conf. Proc. Duplex stainless steels '82*, St. Louise, Mo, USA, 25-28 Oct 1982, Pub: ASM 1984, Metals Park, Ohio, pp.355-369.

74- Pini, G., Weber, J; Materials for pumping seawater and media with high chloride content, *Sulzer Technical Review*, Vol. 61, No. 2, 1979, pp. 69-80.

75- Heubner, U., Rockel, M. B., Wallis, E, The corrosion behavior of copper-alloyed stainless steels in reducing acids, *ATB. Metall*, Vol. 2, 1985, pp.235-241.

76- Okamoto, H., Effect of tungsten and molybdenum on the performance of super duplex stainless steel, Conf. Proc. *Applications of Stainless Steel' 92,* Stockholm, Sweden, Pub: Jernkontoret, 1992, Vol. 1, pp.360-369.

77- Burstein, G. T., and Sasaki, K., The birth of corrosion pits as stimulated by slurry erosion, *Corrosion Science*, Vol. 42, No. 5, May 2000, pp. 841-860.

78- Shalaby, H. M., Attari, S. A., Riad, W.T. and Gouda, V. K., Erosion-corrosion behavior of some cast alloys in seawater, *Corrosion*, Vol. 48, No. 3, March 1992, pp. 206-217.

79- Nilsson, J. O., Jonsson, P., Wilson, A; Formation of secondary austenite in super duplex stainless steel weld metal and its dependence on chemical composition, *Conf. Proc. Duplex stainless steels '94,* Glasgow, Scotland, 13-16 Nov.1994, Gooch, T. G, (Ed), Pub: Abington, Cambridge, UK, 1995.

80- Campbell, H. S., The Campbell condenser tube test apparatus, *The British Non-Ferrous Metals Research Association* (BNFMRA), Miscellaneous publication No. 577, Feb. 1973, pp. 1-9.

81- Bui, N., Irhzo, A., Dabosi, F., Limouzin, Y., Marie, On the mechanism for improved passivation by additions of tungsten to austenitic stainless steels, *Corrosion*, Vol. 39, No. 12, 1983, pp. 491-496.

82- Rishel, D. M., Petit, F. S., and Birks, N., The erosion-corrosion behavior of nickel in mixed oxidant atmospheres, *Proceedings of Corrosion and Particle Erosion at High Temperature*, Srinivasan, V., and Vedula, K. (Eds), Pub: TMS-AIME, 1989, pp. 265-313.

83- Kim, J.C., Heo, N. H., Na, J. G., Woo, J. S. and Kim, G. M., Effects of silicon addition on grain boundary segregation behaviors and mechanical properties in α iron, *Scripta Materialia*, Vol. 38, No.7, 1998, pp.1071-1076.

84- Hakkarainen, T., A method to avoid crevice corrosion in electrochemical determination of pitting potentials, *Laboratory tests and standards, a symposium by ASTM STP 866*, Haynes, G. S. and Boboian, R. (Eds), Pub: American Society for testing and materials, Philadelphia, 1985, pp-91-107.

85- Lu, Y.C. and Ives, M. B., Chemical treatment with cerium to improve the crevice corrosion resistance of austenitic stainless steel, *Corrosion Science*, Vol. 37, No. 1, (1995), pp. 145-155.

86- Robinson, Phili. C., Dept of technology, Staffordshire Polytechnic, College road, Stoke-on-Trent, ST4 2DE and Davidson, Michael. W., National High Magnetic Field Laboratory, 1800 East Paul Dirac Dr, The Florida State University, Tallahassee, Florida, 32310.(*www.microscopyu.com*) (see appendix, pages 203-205).

87- Horn, E.M., Lewandowski, I., Savakis, S., Schmitt, G; Corrosion performance of duplex stainless steels in caustic solutions, *Werkstoffe und korrosion*, Vol. 42, No. 10, Oct. 1991, pp. 511-519.

88- Smialowska, Szklarska. Z., *Pitting Corrosion of Metals*, Pub: National Association of Corrosion Engineer, Houston, Texas 77084, USA, 1986.

89- Frankenthal, R. P. and Kruger, J., Passivity of Metals, *Conf. 4th Int. Sym. on passivity*, Va, USA, Oct. 17-21 1977, Pub: The Electrochemical Society, Princeton, NJ.

90- MacDougal, B., Role of oxide defect sites in the breakdown of NiO films, *J. Electrochem. Soc*, Vol. 125, No. 11, Nov. 1978, pp. 1883-1885.

91- Oltra, R. and Keddam, Electrochemical response after a mechanical breakdown of thin protective surface films: relation with intiation of localized corrosion, *Modification of passive films*, Marcus. P., Baroux, B. & Keddam (Eds), Paris, France, The Institute of Metal, London 1994, European Federation of Corrosion, Pub. No. 12, 1994.

92- Oltra, R., Gabrielli, C., Huet, F., Keddam, M., Electrochemical investigation of locally depassivated iron: A comparison of various techniques, *Electrochim. Acta*, Vol. 31, No. 12, Dec. 1986, pp. 1501, 1986.

93- Rosenfeld, I. L., Danilov, I. S. and Oranskaya, R. N., Breakdown of the passive state and repassivation of stainless steels, *J. The Electrochemical Society*, Vol. 125, No. 11, Nov 1978, pp. 1729-1735..

94- Frankel, G. S., Pitting corrosion of metals, *J. Electrochem. Soc.*, Vol. 145, No. 6, June 1998, pp. 2186-2198.

95- Oltra, R. and Keddam, M., Depassivation of iron by straining and by abrasion: an A. C. Impedance study, *Corrosion Science*, Vol. 23, No. 4, 1983, pp. 441-451.

96- Hoar, T. P., et al., Relationship between anodic passivity, brightening and pitting, *Corrosion Science*, Vol. 5, No. 4, April 1965, pp. 279-289.

97- Zhou, S., Stack, M. M. and Newman, R. C., Characterization of synergistic effects between erosion and corrosion in an aqueous environment using electrochemical techniques, *Corrosion science*, Vol. 52, No. 12, Dec 1996, pp. 934-946.

98- Burstein,G. T. and Mattin, S. P., The nucleation and stages of growth of corrosion pits, In: *Critical factors in localized corrosion II*, Natishan, P. M., Kelly, R. J., Frankel, G. S. and Newman, R.C. (Eds), Chicago, Illinois, USA, 9-11 Oct 1995, Pub: The Electrochemical Society Proceedings Series, Pennington, NJ 1995.

99- Zhang, T.C., Jing, X. X., Li, S. Z., Acceleration of corrosive of duplex stainless steel by chloride in 69% H3PO4 solution, *Wear*, Vol.199, 1996, pp. 253-259.

100- Lu, Y. C. and Ives, M. B., Electrode reaction inhibition by surface modification and localized of corrosion resistance of stainless steels in aqueous solution, *Modification of passive films*, Paris, France, 15-17 Feb 1993, Pub: The Institute of Metal, London, UK, London, 1994, pp. 168-172.

101- Bjordal. M., Bardal. E., Rogne. T., Eggen. T. G., Combined erosion and corrosion of thermal sprayed WC and CrC coatings, *Surface and coatings Technology*, Vol. 70, 1995, pp. 215-220.

102- Solomon, H. D., Transgranular, Granulated, and Intergranular stress corrosion cracking in AISI 304 SS, *Corrosion*, Vol. 40, No.2, 1984, pp. 493-506.

103- Laycock, N. J., Stewart, J. and Newman, R.C., The initiation of crevice corrosion in stainless steels, *Corrosion Science*, Vol. 39, No.10-11, 1997, pp. 1791-1809.

104- Oldfield, J. W. and Sutton, W. H., New technique for predicting the performance of stainless steels in sea water and other chloride containing environments, *British Corrosion Journal*, 1980, Vol. 15, No.1 pp31-34.

105- Liu, G., Tree, D. A. and High, M. S., Relationships between rotating disk corrosion measurements and corrosion in pipe flow, *Corrosion Science*, Vol. 50, No. 8, August 1994, pp. 584-593.

106- Symniotis, E., Galvanic effects on the active dissolution of duplex stainless steels, *Corrosion*, NACE, Vol. 46, No.1. January 1990, pp.2-12.

107- Turnbull, A., Prevention of crevice corrosion by coupling to more noble material, *Corrosion Science*, Vol. 40, No. 4/5, 1998, pp. 843-845.

108- Oldfield, J. N. and Sutton, W. H., Crevice corrosion of stainless steel, II- Experimental studies, *British Corrosion*, Vol.13, No.1. 1978, pp.13-22.

109- Burstein, G. T., Ashley, G. W., Early steps in the anodic oxidation of iron in aqueous solution, *Corrosion*, NACE, Vol. 39, No.6, June 1983, pp. 241-247.

110- Fontana, M. G. and Greene, N. D., *Corrosion Engineering*, Pub: MacGraw- Hill series in materials science and engineering, NY, 1978.

111- Jones, D. A., *Principle and Prevention of corrosion*, Johnstone, D, (Ed), Pub: Macmillan, NY, 1992.

112- Masters, G. L., Crevice corrosion of austenitic and duplex stainless steel in seawater, PhD Thesis, Cranfield University, 1994.

113- Hirooka, S., The electrochemical behavior of austenitic stainless steel during erosion corrosion in flowing 3.5% NaCl solution containing sand particles, M.Phil Thesis, Cranfield University, October 1996.

114- Burstein, G. T., Marshall, P. I., Growth of passivating films on scratched 304L stainless steel in alkaline solution, *Corrosion Science*, Vol. 23, No. 4, 1983,

115- Poulson, B., *Corrosion Science*, Electrochemical measurements in flowing solutions, Vol. 23, No. 4, 1983, pp. 391-430.

116- Elbiache, A. and Marcus, P., The role of molybdenum in the dissolution and the passivation of stainless steels with adsorbed sulphur, *Corrosion Science*, Vol. 33, No. 2, 1992, pp. 261-269.

117- Ambrose, J. R., Kruger, J., Tribo-Elipsometry- A new technique to study the relationship of repassivation kinetics to stress corrosion, *Corrosion*, Vol. 28, No. 1, Jan. 1972, pp. 30-35.

118- Gelder, K. Van., Erlings, J. G., Damen, J., and Visser, A., The stress corrosion of duplex stainless steel in H2S/CO2/Cl- environments, *Corrosion Science*, Vol. 27, No. 10/11, 1987, pp. 1271-1279.

119- Lu, Y. C. and Ives, M. B., Inhibition of electrode kinetic for crevice corrosion resistance, *Proc. Critical factors in localised corrosion II*, Pub: The electrochemical society, Chicago, Illinois, USA, 9-11 Oct 1995, Vol. 95-15, pp.253-265.

120- Wang, J., Uggowitzer, P. J., Magdowski, R., and Speidel, M. O, Nickel free duplex stainless steels, *Scripta Materialia*, Vol. 40, No 1, 1999, pp. 123-129.

121- Lindsley, B. A. and Marder, A. R., Solid particle erosion of an Fe-Fe_3-C metal matrix composite, *Metallurgical and Materials Transactions*, Vol. 29A, March 1998, pp.1071-1079.

122- Angelini, E., Benedetti, B. De., Maizza, G., and Rosalbino, F., Sensitization phenomena on aged SAF 2205 duplex stainless steel and their control using the electrochemical potentiokinetic reactivation test. *Corrosion-* Vol. 55, No. 6, June 1999, pp.606-614.

123- MacDougall, B., Breakdown of oxide films on nickel, *J, Electrochem. Soc*: Electrochemical Science and Technology, Vol. 124, Aug. 1977, pp. 1185-1190.

124- Farrar, J. C. M., Welding castings of duplex stainless steel, *Welding design and fabrication*, USA, Vol. 65, No. 11, 1992, pp. 48-51.

125- De Castro, M. A. C., and Wilde, B. H., The corrosion and passivation of iron in the presence of Halide ions in aqueous solution, *Corrosion*, Vol. 19, No. 11, 1979, pp. 923-936.

126- Landolt, D., Measurement methods and the composition of passive oxide films, *Modification of passive films, Modification of Passive Films [Proc. Conf]*, Paris, France, Feb 15-17, 1993, Pub: The Institute of Materials, London, UK, 1994.

127- Pou, T. E., Murphy, O. J., Young, V., Bockies, J. O. M., Tongson, L. L., Passive films on iron: The mechanism of breakdown in chloride containing solutions, *J. Electrochem. Soc*, Vol. 131, No. 6, June 1984, pp. 1243-1251.

128- Oranowska, H., Szklarska-Smialowska, z., Effect of thickness and physical properties of oxide films grown o Ni at 100-400C in air on the susceptibility of the metal to the local breakdown of passivity, *Corrosion Science*, Vol. 16, No. 6, 1976, pp. 363-370.

129- Burstein, G. T., Ashley, G. W., Marshall, P. I. and Misra, R. D. K., Corrosion of metals under conditions of erosive wear, *Proc. 6th. Conf. On Erosion by liquid and solid impact*, Cambridge, England, 5-8 Sept 1983, pp.49-1 to 49- 8, Pub: Cavendish laboratory, Cambridge, England, 1983.

130- Frankenthal, R. P., Passivation of Fe in Borate buffer solution, *Electrochim. Acta*, Vol. 16, No. 11, Nov. 1971, pp. 1845-1857.

131- Foley, C. L., Kruger, J., Becholdt, C. J., Electron diffraction studies of active, passive, and transpassive oxide films formed on iron, *J. Electrochem. Soc*, Vol. 114, No. 10, Oct.1967, pp. 994-999.

132- Garner, A, Corrosion of high alloy austenitic stainless steel weldments in oxidizing environments, *Material Performance*, Vol. 21, Aug. 1982, No. 8, pp. 9-14.

133- Potgieter, J., AND Visser, Potentiostatic etching of duplex stainless steels and high chromium white cast irons, *Materials Science and Technology*, Vol. 9, April 1993.

134- Habazaki, H., Kawashima, A., Asami, K., and Hashimoto, K., The effect of molybdenum on the corrosion behavior of amorphous Fe-Cr-Mo-P-C alloys in hydrochloric acid, *Material Science and Engineering*, Vol. A134, 1991, pp. 1033-

135- Gartland, P. O., Aspects of testing stainless steels for seawater applications, The Institute of Materials, Marine Corrosion of Stainless Steels: Chlorination and Microbial Effects, (UK) 1993, pp. 134- 148. Pub: The Institute of Materials, London

136- Boese, E., Rothig, J., Schmidtchen, Grarz I. Und. H., Tribocorrosion of stainless steel, *Materials and Corrosion*, Vol. 49, 1998, pp. 98-107.

137- Finnie, I., Levy, A. and Mcfadden, D. H., Fundemental mechanisms of the erosive wear of ductile metals by solid particles, Erosion: Prevention and useful applications, *ASTM STP 664*, Adler, W. F.(Ed), Pub: American Society for Testing and Materials, 1979, pp.36-58.

138- Bardal, E., Drugli, J., and Gartland, P. The behavior of corrosion resistance steels in seawater: A review, *Corrosion Science*, Vol. 35, No 1-4, 1993, pp. 257-267.

139- Asami, K. and Hashimoto, K., An XPS study of the surfaces on Fe-Cr, Fe-Co and Fe-Ni alloys after mechanical polishing, *Corrosion Science*, Vol. 24, No. 2, 1984, pp. 83-97.

140- Tan, M. W., Akiyama, E., Kawashima, A., Asami, K. and Hashimoto, K., The influence of molybdenum addition and air exposure on the corrosion behavior of amorphous Fe-8Cr- 13P-7C alloy in de-aerated 1 M HCl, *Corrosion Science*, Vol.38, 1996, pp.349-365.

141- Habazaki, H., Kawashima, A., Asami, K., The effect of tungsten on the corrosion behavior of amorphous Fe-Cr-W-P-C alloys in 1M HCl, *J. Electrochem. Soc.*Vol. 138, No. 1, Jan. 1991, pp. 76-81.

142- Seo, M. and Sato, N., In depth profiles of anodic oxide films on Fe-Ni alloy in Boric acid-Sodium Borate solutions, *Corrosion Science*, Vol. 18, 1978, pp. 577-589.

143- Tretheway, K. R. and Chamberlin, J., *Corrosion: for students of science and engineering*, Pub: Longman Scientific and Technical, NY, 1988.

144- Finnie, I., Erosion of surface by solid particulates, *Wear*, Vol. 3, 1960, pp. 87-103.

145- Finnie, I., Some reflections on the past and future of erosion, *Wear*, 186-187 1995, pp.1-10.

146- Vyas, Brijes., Erosion-Corrosion, *treatise on materials science and technology*, Vol.16, Pub: Academic press, UK, 1979, pp. 357-394.

147- Levin, B. F., Dupont, J. N., Marder, A. R., Solid particle erosion resistance of ductile wrought super alloys and their weld overlay coatings, *J. of. Materials Science*, Vol. 33, 1998, pp.2153-2163.

148- Furneaux, R. C., Thompson, G. E. and Wood, G. C., The coloured film formed on stainless steel in hot chromic/suphuric acid solution, *Corrosion Science*, Vol.21, No. 1, 1981, pp.23-29.

149- Asami, K., Hashimoto, K. and Shimodaira, S., XPS (X-Ray Photo-Electron Spectroscopy) Determination of compositions of alloy surfaces and surface oxides on mechanically polished Fe-Cr alloys, *Corrosion Science*, Vol. 17, No. 9, 1977, pp. 713-723.

150- Bitter, J. G. A., A study of erosion phenomena, Part II, *Wear*, Vol. 6, 1963, pp.169-190.

151- Evans, T. E., Hart, A. C. and Sledgell, A. N., Nature of the film on coloured stainless steel, *Trans. Inst. Metal Finishing*, Vol. 51, No. 3, 1973, pp.108-112.

152- Neville, A., Hodgkiess, T., An assessment of the corrosion behavior of high grade alloys in seawater at elevated temperature and under a high velocity impinging flow, *Corrosion Science*, Vol. 38, No. 6, 1996, pp. 927-1056.

153- Shreir, L. L., *Corrosion: Vol.2. Corrosion Control*, Pub: Newnes-Butterworths, London and Boston, 1976, N.P.

154- Gupta, M. K., Chakrabarti, A/. K., Basak, A., Erosive and erosive-corrosive wear behavior of cast nitrogenated stainless steels, *Wear*, Vol. 199, 1996, pp. 33-35.

155- Evans, U. R., *The corrosion of metals*, London, Pub: Edward Arnold & Co, London, 1924.

156- Madsen, W. B., Measurement of erosion-corrosion synergism with a slurry wear test apparatus, *Wear,* Vol.123, 1988, pp.127-142.

157- Fontana, M. G., Greene, N. D., *Corrosion Engineering*, 3rd edition, NY; Pub: McGraw- Hill,1986.

158- Lee, T.S., Seawater velocity effects on corrosion behavior of materials, *Sea technology*, November 1983, pp. 51-59.

159- Evans, U. R., Metallic corrosion Passivity and Protection, London, Pub: Edward Arnold & CO, 1946.

160- Stack, M. M., Zhou, S., Newman, R. C., Identification of transitions in erosion-corrosion, regimes in aqueous environments, *Wear*, Vol.186-187, 1995, pp. 523-532.

161- Umemura, F., Matukura, S. and Kawamoto, K., Electrochemcial study of erosion-corrosion, in carbon and stainless steels, *J. Corros. Eng*, Vol. 36, No. 10, 1987, pp. 569-578.

162- Heymann, F., Liquid erosion impingement erosion, *ASM Book*, Vol. 18, *Friction, Lubrication and wear technology*, Pub: ASM International (USA), Material Park, Ohio, Henry, S. D., (Ed), 1992, pp. 221-232.

163- Esteban, J. M., Hickey, G.S. and Orazem, M.E., The impinging jet electrode: Measurement of the hydrodynamic constant and its use for evaluating film persistency, *Corrosion*, Vol. 46, No. 11, Nov. 1990, pp. 896-901.

164- Efird, K. D., Effect of fluid dynamics on the corrosion of Cu-base alloys in sea water, *Corrosion*, Vol. 33, No. 1, January 1977, pp. 3-8.

165- Worsfold, M., The control of localized corrosion on ageing aircraft, *PhD Thesis*, Cranfield University, 1996.

166- Frankel, G. S., Stockert, L., Hunkeler, F., Boehni, H., Metastable pitting of stainless steel, *Corrosion*, NACE, Vol. 43, No. 7, July 1987, pp. 429-436.

167- Defranoux, J. M., Mechanism of the action of molybdenum and of nickel on the behavior of stainless steels in industrial chemical media, *Aciers spec*, Vol. 31, 1975, pp.8-1.

168- Postlethwaite, J. and Nesic, S., Erosion in disturbed liquid-particle pipe flow: Effects of flow geometry and particle roughness, *Corrosion*-October, Vol. 49, No.10, Oct.1993, pp. 850-857.

169- Kim, J. J., Park, S. K., Solid particle erosion of AISI 403 stainless steel, *J. Materials Science Letters*, 17, 1998, pp.1503-1506.

170- Chang, S. L., Petit, F. S., and Birks, N., Effects of angle of incidence on the combined erosion-oxidation attack of nickel and cobalt, *Oxidation of metals*, Vol. 34, No. 1 / 2, 1989, pp. 47-70.

171- Masden, B. W., A study of parameters using a new constant wear rate slurry test, *Proc. Int. Conf. on wear of materials,* American Society of Mechanical Engineers, 1985, pp 345-354, New York.

172- Matsumura, M., Oka, Y., Hiura, H. and Yano, M., The role of passivating film in

preventing slurry erosion-corrosion of austenitic stainless steel, *ISIJ Int*, Vol. 31, No. 2, 1991, pp. 168-176.

173- Weber, S., Liebe, R., Heitz, E: Erosion corrosion and erosion of various materials in high velocity flows containing particles, In: Corrosion / 90, Sym, Flow induced corrosion; Fundamental studies and industry experience, Kennelley, J., Hausler, R. H., Silvermanm, D. C. (Eds), NACE, 1991, TX.

174- Blatt, W., Kohley, T., Heitz, E., Lotz, U., The influence of hydrodynamics on erosion-corrosion in two phase liquid particle flow, *Corrosion*, Vol. 45 No. 10, 1989, pp.793-804.

175- Nash, B. K. and Kelly, R.G., Characterization of the crevice solution chemistry of 304 stainless steel, *Corrosion Science*, Vol. 35, No 1-4, 1993, pp.817-825.

176- Clark, H. and Wong, K., Impact angle, particle energy and mass loss in erosion by dilute slurries, *Wear*, Vol.186-187, 1995, pp.454-464.

177- Suleiman, M. I., Ragault, I. and Newman, R. C., The pitting of stainless steel under a rust membrane at very low potentials, *Corrosion Science*, Vol. 36, No. 3, 1994, pp.79-486.

178- Chevallier, P., Vannes, A. B., Forner, A., New parameters in erosion for study of bulk materials and coatings, *Wear*, Vol. 186-187, 1995, pp.210-214.

179- Evans, T. E., Film formation on stainless steel in a solution containing CrO_3 and H_2SO_4, *Corrosion Science*, Vol. 17, No.2, 1977, pp.105-124.